A PRACTICAL METHOD FOR UNDERSTANDING AND EVALUATING SEMICLASSICAL VIBRATIONAL RESPONSE FUNCTIONS

A Dissertation

Presented to the Faculty of the Graduate School

of Cornell University

in Partial Fulfillment of the Requirements for the Degree of

Doctor of Philosophy

by

Scott Matthew Gruenbaum

May 2010

A PRACTICAL METHOD FOR UNDERSTANDING AND EVALUATING SEMICLASSICAL VIBRATIONAL RESPONSE FUNCTIONS

Scott Matthew Gruenbaum, Ph.D.

Cornell University 2010

Vibrational response functions may be used to predict the results of linear and nonlinear spectroscopic measurements. As quantum response theory is numerically impractical for large systems and as classical response functions can be qualitatively incorrect, there is a need for a method to calculate spectroscopic response functions semiclassically. Previously, the semiclassical Herman-Kluk propagator has been applied to the calculation of the linear and third-order vibrational response functions. In this approach, the response function is expressed as multiple phase-space integrals over pairs of classical trajectories and their associated stability matrices. This procedure can be quantitatively accurate, but the calculations are computationally challenging due to a highly oscillatory semiclassical phase and a time-divergent prefactor.

Here we analyze the structure of the semiclassical response function and discuss how the Herman-Kluk approximation is able to accurately describe quantum coherence effects. For coupled anharmonic oscillator systems, interference between pairs of classical trajectories results in a quantization condition on the classical action variables of the system. A pair of trajectories only contributes near phase space recurrences, and quantum coherence effects result from a summation over all possible recurrence topologies. By treating this interference analytically, we develop a mean trajectory approximation to the linear and nonlinear response functions that requires the propagation of classical trajectories

linked by quantized transitions in action. This mean trajectory treatment accurately reproduces quantum coherence effects in the linear and third-order response functions for coupled anharmonic systems at a significant reduction of the numerical cost of full Herman-Kluk dynamics, and thus represents a practical method for the calculation of nonlinear vibrational response functions.

For large systems such as biological molecules, semiclassical methods are currently impractical, but mixed quantum/classical techniques can be used for the calculation of response functions. We have implemented molecular dynamics simulations and a quantum/classical model to calculate the absorption and vibrational echo spectra for several spectroscopic states of carbonmonoxy horseradish peroxidase. While our simulations do agree with several experimental observations, our predicted spectra are not in good agreement with experiment, likely due to either an inaccurate force field or starting structures that are not fully at equilibrium.

BIOGRAPHICAL SKETCH

Scott Gruenbaum was born in Kettering, Ohio, where he lived with his parents John and Carolyn Gruenbaum and sister Jayna until seventh grade, when they moved to Westerville, Ohio. Scott attended Westerville North High School, where he was active in the marching and jazz bands, the Boy Scouts, the school trivia team, and in student government. He graduated from high school in 2001, and then started at Miami University, majoring in chemistry and mathematics. During undergrad, he worked with Professor Shouzhong Zou, investigating the surface-enhanced Raman spectroscopy of isocyanides bound to various transition metal nanoparticles and roughened metal surfaces, as well as surface-enhanced fluorescence of dye molecules bound to nanoparticles. He also spent a summer at the University of Kansas working for Professor Shih-I Chu studying pseudospectral methods for the calculations of high-order harmonic generation in hydrogen. After graduating from Miami in 2005, Scott spent a summer backpacking in New Zealand, and then started graduate work at Cornell University. His experience at Kansas influenced him to continue in theoretical chemistry at Cornell, and he joined the lab of Professor Roger Loring in the winter of 2005. In the Loring group, Scott works in the general area of nonequilibrium statistical mechanics, spending most of his time studying semiclassical vibrational response functions. He has also had a brief foray into molecular dynamics simulations and vibrational echo calculations in proteins. He spends his free time gardening and watching his pet hermit crabs and the occasional praying mantis. In graduate school, Scott met his fiancee Doris Pun, and in the summer of 2010 he will join her in the chemistry department at the University of Wisconsin, Madison as a postdoc in the lab of Professor Jim Skinner.

To my family and to Doris

ACKNOWLEDGEMENTS

Many people deserve my thanks for their help and encouragement during the past few years. First and foremost, I want to thank my family—my parents John and Carolyn Gruenbaum and my sister Jayna—for their support and for many phone conversations that helped wile away the daily walk to lab. They've always encouraged me from elementary up through graduate school, and I am grateful. I'm sure they will take great joy in reading aloud from this dissertation in times to come. I would also like to thank my advisor, Professor Roger Loring, for allowing me to work in his group. He has been a wonderful advisor, always helpful and happy to work with me as I learned so much about theoretical chemistry and semiclassics. I've had a great five years working in his group, and I will miss it. My committee members, Professor Greg Ezra and Professor Garnet Chan, also deserve much thanks, both for reading this dissertation, and also for being great teachers. I am grateful to Professor Ben Widom, both for his skill as a teacher, and also for a massive amount of delicious Saturday pizza. My group members—Anne, Paolo, Maicol, Swapna, and Ben—have taught me a lot and have been great company. My roommate Seán was a great guy to stay with, and I learned far more than I ever wanted to know about biochemistry from him! Thanks Emily, Brenda, Elliott (I will miss the bunnies...), Paulina, Rob, Kevin, and everyone else for keeping my entertained when I was bored! And to the Chan group– Jon, Debashree, Eric, and all the rest– thanks for the many hours of study on elastic scattering of spinning particles, aka ping pong. Finally, I would like to thank Doris, without whom these last five years would have been much less joyful than they were—you were the best part of graduate school! I also want to acknowledge the National Science Foundation for supporting this research through Grants No. CHE0413992 and CHE0743299.

TABLE OF CONTENTS

LIST OF TABLES

LIST OF FIGURES

CHAPTER 1

TIME-DEPENDENT QUANTUM AND SEMICLASSICAL METHODS

1.1 Who cares about time?

In introductory quantum mechanics, students learn about the Schrödinger equation, stationary states, and energy levels, but time is typically given very little attention. This is unfortunate, since most chemical processes and the methods for learning about such processes depend strongly on time. In a scattering experiment, molecules collide with one another, perhaps exchange energy, and end up in a different quantum state from the initial one. Chemical reaction kinetics depend on the dynamics of a nuclear wavefunction on a potential energy surface. All the spectroscopic methods which are used to determine the identity and probe the properties of chemical species depend on the interaction between the molecule of interest and an applied field. This applied field typically induces transitions between stationary states, generating a time-dependent signal which is Fourier transformed to give the usual frequency domain spectrum. [1]

The time dynamics of a superposition of stationary state wavefunctions (a wavepacket) provide an intuitive method for understanding experiments such as optical absorption spectroscopy. An ultraviolet laser pulse first excites the vibrational ground state for a system to an excited electronic energy surface. As the resulting wavepacket is no longer a stationary state on the new potential, it oscillates within the excited state potential well in a manner that is sometimes strikingly similar to classical mechanics. The wavepacket eventually decays back to the ground state through, for example, a non-adiabatic transition,

but the wavepacket oscillations generate a time-dependent signal which can be measured. The Fourier transform of this signal results in an absorption spectrum. Even though we typically think about spectroscopy as involving transitions between discrete quantum energy levels, it is equally valid to think about spectroscopy in terms of the motions of a wavepacket.

Time-dependence in quantum mechanics is also invaluable by providing a link between the quantum and classical realms. While stationary states and energy levels do not have close classical analogs, it is easy to see the connection between the motion of a wavepacket in a potential and the motion of a classical particle in the same potential. The wavepacket will have a finite width, and the shape of the wavepacket can change with time, but for reasonably well localized initial states, the center of the wavepacket will follow essentially classical dynamics for short times. The dynamics on a potential energy surface of large particles such as nuclei more massive than hydrogen will very closely resemble classical motion in many cases.

In the remainder of this chapter, we will first discuss general time-dependent quantum mechanics for both wavefunctions and the density matrix in Sections 2 and 3 respectively. Linear and nonlinear vibrational spectroscopy will be discussed in Section 4, while Section 5 will focus on the application of time-dependent quantum mechanics to vibrational spectroscopy— response theory. An example of both quantum and classical response functions is investigated in Section 6. Finally, semiclassical methods for time propagation will be presented in Section 7, and we summarize in Section 8. Semiclassical approximations to linear and nonlinear response functions and to wavepacket dynamics will be the focus of Chapters 2, 3, and 4, while Chapter 5 will focus on a mixed

quantum/classical approximation to response functions as applied to carbon monoxide bound in heme proteins.

1.2 The time-dependent Schödinger equation

The time dependence of a non-relativistic quantum system is described by the time dependent Schödinger equation,

$$\frac{\partial}{\partial t}\,|\Psi(t)\rangle = -\frac{i}{\hbar}\,\hat{H}\;|\Psi(t)\rangle \tag{1.1}$$

where $\hat{H}$ is the system Hamiltonian. For an initial state $|\Psi(0)\rangle$, Eq. (1.1) can in principle be integrated to generate the state at a future time t. For systems where energy is conserved, the Hamiltonian is independent of time, and the energy eigenstates (stationary states) can be found from the time-independent Schödinger equation,

$$\hat{H}\;|\phi_k\rangle = \epsilon_k\,|\phi_k\rangle\;. \tag{1.2}$$

As the energy eigenstates $|\phi_k\rangle$ form an orthonormal, complete basis in the Hilbert space of the system, the time dependence of an arbitrary initial state is given by

$$|\Psi(t)\rangle = \sum_k c_k\, e^{-i\epsilon_k t/\hbar}\;|\phi_k\rangle \equiv \hat{K}(t,0)\;|\Psi(0)\rangle \tag{1.3}$$

where $c_k \equiv \langle\phi_k|\Psi(0)\rangle$, and $\hat{K}(t,0)$ is known as the propagator or time evolution operator because it propagates a state from time 0 to time t. So long as the Hamiltonian is independent of time, the propagator simply has the form of an exponential of $\hat{H}$,

$$\hat{K}(t,0) = e^{-i\hat{H}t/\hbar} \equiv 1 - \frac{it}{\hbar}\hat{H} + \frac{1}{2!}\left(-\frac{it}{\hbar}\right)^2 \hat{H}\hat{H} + \frac{1}{3!}\left(-\frac{it}{\hbar}\right)^3 \hat{H}\hat{H}\hat{H} + \cdots\;. \tag{1.4}$$

When a system exchanges energy with its environment by, for example, interacting with an applied field, the Hamiltonian may depend on time. In this case, calculating the propagator is more challenging. The partial differential equation satisfied by $\hat{K}$ is

$$\frac{\partial}{\partial t}\hat{K}(t,0) = -\frac{i}{\hbar}\,\hat{H}(t)\,\hat{K}(t,0)\,, \tag{1.5}$$

which can be integrated, resulting in an integral equation for the propagator,

$$\hat{K}(t,0) = 1 - \frac{i}{\hbar}\int_0^t d\tau\,\hat{H}(\tau)\,\hat{K}(\tau,0)\,. \tag{1.6}$$

Eq. (1.6) can be solved by iteration, and the propagator is then written as an infinite sum,

$$\hat{K}(t,0) = 1 + \sum_{n=1}^{\infty}\left(-\frac{i}{\hbar}\right)^n \int_0^t d\tau_n \cdots \int_0^{\tau_3} d\tau_2 \int_0^{\tau_2} d\tau_1\,\hat{H}(\tau_n)\,\hat{H}(\tau_{n-1})\cdots\hat{H}(\tau_1) \tag{1.7}$$

$$\equiv \exp_+\left(-\frac{i}{\hbar}\int_0^t d\tau\,\hat{H}(\tau)\right) \tag{1.8}$$

where $\exp_+$ is known as the time-ordered exponential. [2] Despite the similarities, the time-ordered exponential is distinct from the standard Taylor expansion of an exponential due to the time-ordering in the integration variables of Eq. (1.7).

The expression for the propagator in Eq. (1.8) is exact, but it is not very useful since truncation of Eq. (1.7) at finite n will lead to qualitatively incorrect long time behavior for the propagator. For Hamiltonians which naturally separate into a dominant time-indepedent term and a "small" time-dependent term,

$$\hat{H}(t) = \hat{H}_0 + \hat{H}_1(t)\,, \tag{1.9}$$

the propagator can be rewritten in a more useful form in the interaction representation. [2] Note that the interaction representation does not necessarily require that $\hat{H}_1(t)$ be small or be dependent on time, but all Hamiltonians dealt

with in this dissertation shall be of this form. Specifically, $\hat{H}_0$ will usually represent the system Hamiltonian, and $\hat{H}_1(t)$ will represent the interaction between the system and an applied electromagnetic field.

For Hamiltonians of the form in Eq. (1.9), the full propagator $\hat{K}$ factors into a zeroth-order propagator $\hat{K}_0$ and the interaction propagator $\hat{K}_{int}$,

$$\begin{aligned}\hat{K}(t,0) &= \hat{K}_0(t,0)\,\hat{K}_{int}(t,0) \\ &\equiv e^{-i\hat{H}_0 t/\hbar}\,\exp_+\left(-\frac{i}{\hbar}\int_0^t d\tau\,\hat{H}_{int}(\tau)\right)\end{aligned} \tag{1.10}$$

where the interaction Hamiltonian $\hat{H}_{int}$ is given by $\hat{H}_{int}(t) \equiv \hat{K}_0^\dagger(t,0)\hat{H}_1(t)\hat{K}_0(t,0)$. As the zeroth-order Hamiltonian is independent of time, $\hat{K}_0$ is simpler to calculate than the full propagator. Inserting the definition of the interaction Hamiltonian into Eq. (1.10) and writing the time-ordered exponential as an infinite sum yields

$$\begin{aligned}\hat{K}(t,0) = \hat{K}_0(t,0) + \sum_{n=1}^{\infty}\left(-\frac{i}{\hbar}\right)^n \int_0^t d\tau_n \cdots \int_0^{\tau_2} d\tau_1 \hat{K}_0(t,\tau_n)\hat{H}_1(\tau_n)\hat{K}_0(\tau_n,\tau_{n-1})\hat{H}_1(\tau_{n-1})\cdots \\ \times\ \hat{K}_0(\tau_2,\tau_1)\hat{H}_1(\tau_1)\hat{K}_0(\tau_1,0)\,.\end{aligned} \tag{1.11}$$

If $\hat{H}_1$ is small in some sense compared to $\hat{H}_0$, we can truncate Eq. (1.11) at finite order and obtain a full propagator that is accurate for a moderate range of times. Other approximations such as a cumulant approximation (the Magnus expansion) can also be used to compute $\hat{K}(t,0)$. [2] By truncating the full propagator in Eq. (1.11) rather than in Eq. (1.8), the system evolves with correct zeroth-order dynamics along with approximate dynamics due to $\hat{H}_1(t)$.

1.3 Time-dependence of the density matrix

For isolated systems such as a single molecule, the wavefunction formalism presented in the previous section suffices to describe the state of the system. In general, however, a subsystem which interacts with its environment cannot be described by a single wavefunction $|\Psi\rangle$. Instead, the state of the system is given by the density operator $\hat{\rho}$, defined in the spectral representation as

$$\hat{\rho} = \sum_j p_j \left|\Psi_j\right\rangle \left\langle\Psi_j\right| \tag{1.12}$$

where p_j is the probability of finding the system in state $|\Psi_j\rangle$. If p_j is equal to unity and all other $p_{i\neq j} = 0$, then the system is in a pure state and has a definite wavefunction $|\Psi_j\rangle$. Otherwise, the system is in a mixed state. This is the usual case for a subsystem of a macroscopic ensemble of interacting particles. For both pure and mixed states, the density operator is useful because the expectation value for any observable $\hat{A}$ is found by taking the trace of $\hat{A}$ with $\hat{\rho}$,

$$\left\langle \hat{A} \right\rangle_\rho = \mathrm{Tr}\left(\hat{\rho}\,\hat{A}\right) . \tag{1.13}$$

In an orthonormal, complete basis $|a\rangle$, the diagonal matrix elements of $\hat{\rho}$ will be real and non-negative. These diagonal elements are known as populations, while the complex off-diagonal elements are called coherences.

The equation of motion for the density operator is found by applying the time-dependent Schrödinger equation to Eq. (1.12),

$$\frac{\partial}{\partial t}\,\hat{\rho}(t) = -\frac{i}{\hbar}\left[\hat{H},\,\hat{\rho}(t)\right] \equiv -\frac{i}{\hbar}\mathcal{L}(t)\,\hat{\rho}(t) . \tag{1.14}$$

$\mathcal{L}$ is the Liouvillian (super)operator, [2] and it acts on an operator $\hat{A}$ by taking the commutator of $\hat{A}$ with the Hamiltonian. Eq. (1.14) is the quantum Liouville equation, and it is analogous to the classical Liouville equation which describes

the time evolution of a classical phase space distribution function. Eq. (1.14) can be solved in terms of the wavefunction propagator $\hat{K}$ or its density operator counterpart $\hat{\mathcal{K}}$,

$$\hat{\rho}(t) = \hat{K}(t,0)\,\hat{\rho}(0)\,\hat{K}^{\dagger}(t,0) \equiv \hat{\mathcal{K}}(t,0)\,\hat{\rho}(0)\,. \tag{1.15}$$

As in Eq. (1.4), the density propagator $\hat{\mathcal{K}}$ is formally given by

$$\hat{\mathcal{K}}(t,0) = \exp\left(-i\mathcal{L}t/\hbar\right) \tag{1.16}$$

for time-independent Hamiltonians.

As with the wavefunction propagator $\hat{K}$, when the Hamiltonian is given by Eq. (1.9), the Liouvillian splits into a dominant time-independent part $\mathcal{L}_0$ and a time-dependent perturbation $\mathcal{L}_1(t)$,

$$\mathcal{L}(t) = \mathcal{L}_0 + \mathcal{L}_1(t)\,. \tag{1.17}$$

The density propagator then factors into a relatively simple zeroth-order propagator and a more complicated time-ordered exponential,

$$\hat{\mathcal{K}}(t,0) = \hat{\mathcal{K}}_0(t,0)\exp_+\left(-\frac{i}{\hbar}\int_0^t d\tau\;\mathcal{L}_{int}(\tau)\right) \tag{1.18}$$

$$\hat{\mathcal{K}}_0(t,0) = e^{-i\mathcal{L}_0 t/\hbar} \tag{1.19}$$

$$\mathcal{L}_{int}(t) \equiv \hat{\mathcal{K}}_0^{\dagger}(t,0)\mathcal{L}_1(t)\hat{\mathcal{K}}_0(t,0) \tag{1.20}$$

where $\mathcal{L}_{int}$ is the interaction Liouvillian. If the propagator in the interaction representation is expanded in an analogous manner to Eq. (1.11), a series expansion for the time-dependent density operator is generated in powers of the interaction Liouvillian,

$$\hat{\rho}(t) = \hat{\rho}^{(0)} + \hat{\rho}^{(1)}(t) + \hat{\rho}^{(2)}(t) + \cdots \tag{1.21}$$

where

$$\hat{\rho}^{(n)} = \left(-\frac{i}{\hbar}\right)^n \int_0^t d\tau_n \int_0^{\tau_n} d\tau_{n-1} \cdots \int_0^{\tau_2} d\tau_1 \; \mathcal{L}_{int}(\tau_n) \cdots \mathcal{L}_{int}(\tau_2) \; \mathcal{L}_{int}(\tau_1) \, \hat{\rho}(0) \, . \tag{1.22}$$

As each factor of $\mathcal{L}_{int}$ introduces a commutator with the Hamiltonian $\hat{H}_1(t)$, the nth-order density operator in Eq. (1.22) is nth-order in $\hat{H}_1$. We shall use this expansion for the density operator to calculate the response of a material system to an applied electric field. This analysis will form the basis for an understanding of linear and nonlinear vibrational spectroscopy.

1.4 Linear and nonlinear vibrational spectroscopy

Spectroscopy describes the process by which molecules or materials interact with an applied radiation field, resulting in quantum transitions. For example, ultraviolet light causes transitions in the electronic state of a molecule, while low frequency radio waves result in transitions in the nuclear spin degrees of freedom, as in NMR spectroscopy. For the remainder of this dissertation, we shall focus on vibrational infrared (IR) spectroscopy on a single electronic potential energy surface. The formalism developed is applicable to both IR and Raman spectroscopies, though we shall typically concentrate on the IR case.

In order to discuss spectroscopy, we must first write the Hamiltonian which describes the interaction of matter with a radiation field. In the non-relativistic limit, the Hamiltonian describing a system of N particles interacting with a field is [2,3]

$$\hat{H} = \sum_{i=1}^{N} \frac{1}{2m_i}\left(\hat{p}_i - \frac{q_i}{c}\hat{A}(\hat{r}_i)\right)^2 + \hat{V}(\hat{r}_i) + \hat{H}_{rad} \tag{1.23}$$

where $\hat{A}$ is the vector potential of the radiation, m_i, q_i, $\hat{p}_i$, and $\hat{r}_i$ are the mass, charge, momentum operator, and position operator of particle i, and $\hat{H}_{rad}$ is the Hamiltonian for the radiation field. The distortion in the charge density of a material in the presence of an applied electric field is described by the polarization $P(\mathbf{r})$ which acts as a source term in Maxwell's equations. For most applications, the applied field consists of many photons, and the field can therefore be treated classically. The Hamiltonian then reduces to

$$\hat{H} = \hat{H}_{sys} - \int d\mathbf{r}\, P(\mathbf{r}) \cdot E(\mathbf{r}, t) \tag{1.24}$$

where $E(\mathbf{r}, t)$ is the classical (transverse) electric field. If we assume that the wavelength of E is large compared to the scale of the system (a molecule), then we can make the electric dipole approximation and neglect the $\mathbf{r}$ dependence of E and P,

$$\hat{H} = \hat{H}_{sys} - \hat{\mu} \cdot E(t) + \cdots . \tag{1.25}$$

In Eq. (1.25), $\hat{\mu}$ is the electric dipole operator, and we have neglected the electric quadrupole, magnetic dipole, and other higher order terms. Note that if we were interested in Raman spectroscopy, the relevant operator that couples the field to the system is the polarization operator $\hat{\alpha}$.

In a standard linear IR absorption measurement, a sample is irradiated with infrared light, and the absorption spectrum is plotted as a function of frequency ω. Absorption peaks correspond to frequencies such that $\hbar\omega = \Delta E_{i,f}$ where $\Delta E_{i,f}$ is the difference in energy between a pair of initial and final states. Within the dipole approximation, the peak intensity depends on the absolute square of the dipole matrix element $\hat{\mu}_{i,f}$. If $\hat{\mu}_{i,f} = 0$ due to the symmetry of the initial and final states, the transition is termed dipole forbidden, and either no peak or a very

weak peak will appear in the IR spectrum. Also note that spectra can be equivalently plotted and interpreted in the time domain. This is perhaps most useful in the condensed phase, when interactions between molecules result in peak broadening and thus lower frequency resolution. In the next section we shall discuss the time domain signal for the IR absorption spectrum and its relation to the dipole autocorrelation function $\langle \hat{\mu}(t)\, \hat{\mu}(0) \rangle$.

In addition to linear spectroscopy, there are many coherent nonlinear techniques possible which provide information about a system that is unobtainable from an absorption spectrum. [4–9] In nonlinear experiments, the system typically interacts with multiple laser pulses, where the frequency, wavevector, time delay between pulses, and the pulse shape itself can be tuned for different applications. For example, second-order techniques such as sum-frequency and second-harmonic generation allow surface selective measurements, while third-order techniques such as two dimensional infrared spectroscopy (2D-IR) yields information on correlations between vibrational modes. Other nonlinear techniques include vibrational echoes, pump-probe and transient grating experiments, and coherent anti-Stokes Raman, among many others. [2] These nonlinear experiments are closely analogous to nonlinear or multidimensional NMR spectroscopy, where different (radio wave) pulse shapes allow the determination of, for example, through-bond and through-space correlations. [10–12]

In coherent nonlinear spectroscopy, the spectroscopic signals that correspond to different processes are emitted from the sample at distinct, well-defined wavevectors. For example, in a vibrational echo experiment, three IR laser pulses are applied to the sample with wavevectors $\mathbf{k}_1$, $\mathbf{k}_2$, and $\mathbf{k}_3$. The echo signal is then emitted along the rephasing wavevector $\mathbf{k}_{echo} = -\mathbf{k}_1 + \mathbf{k}_2 + \mathbf{k}_3$. Other

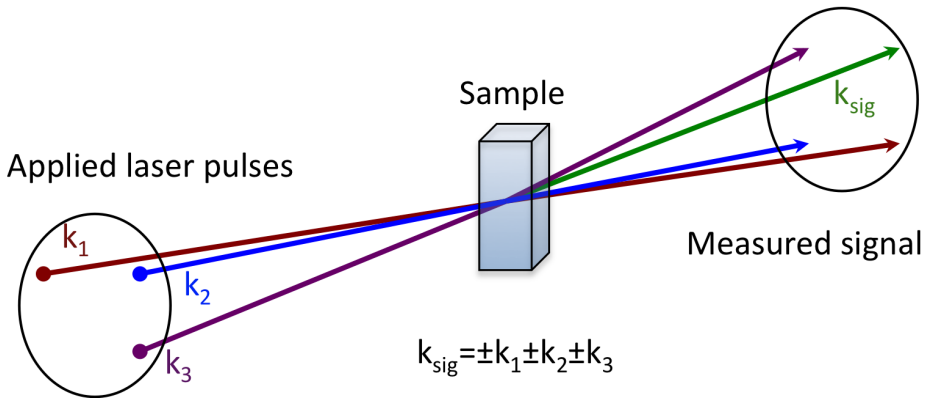

Figure 1.1: Diagram depicting a general four-wave mixing experiment. Distinct signals are emitted at linear combinations of the applied laser pulse wavevectors.

nonlinear signals are also emitted along other linear combinations of wavevectors. Each of these nonlinear signals is associated with a collection of double-sided Feynman diagrams that provide a visual representation for the perturbation and time evolution of the ket and bra sides of the density matrix. [2, 13] These diagrams are useful for calculating specific nonlinear spectroscopic signals and are discussed more fully in Appendix D. The vibrational echo and other experiments that involve three interactions between the incoming laser pulses and the system are termed four-wave mixing spectroscopy. A schematic diagram of this process is shown in Figure 1.1.

For real experimental systems, vibrational absorption peaks are not infinitely narrow but are instead typically broadened into a Gaussian or Lorentzian line shape. For low pressure gas phase systems, the peaks may be quite sharp, while for liquids, absorption lines are typically broad. There are several different mechanisms which result in line broadening. For example, lifetime broadening due to the finite lifetime of the vibrationally excited state leads to a Lorentzian lineshape. This is an example of homogeneous broadening. Homogeneous

broadening is the result of interactions or processes which are fast on the time scale of the experiment, typically femto- to picoseconds for molecular vibrations. During the experiment, each molecule being probed by the IR radiation samples a range of frequencies, resulting in an inherent, homogeneous linewidth.

In the other limit, an experiment could average over a static distribution of molecular frequencies. This inhomogeneous limit results when molecules in a sample experience different local environments which change slowly on the time scale of the experiment. Examples include experiments on biological molecules, where proteins can undergo slow (nano- and microsecond), conformational changes. [14] Inhomogeneous processes usually result in Gaussian lineshapes and can be an experimental problem because they tend to obscure the natural, homogeneous lineshape. A particular third-order vibrational experiment known as the vibrational echo can be used to reduce or even eliminate inhomogeneous broadening. [13, 15, 16] This technique will be discussed more fully in Chapter 5. Also note that broadening can occur on the same time scale as an experiment. This is known as spectral diffusion, and it can be used to measure, for example, molecular connectivity and vibrational energy transfer [17] or protein conformational changes that take place on the picosecond time-scale. [18]

1.5 Vibrational response functions

For classical electromagnetic fields and within the dipole approximation, the polarization P is given by the expectation value of the dipole operator $\hat{\mu}$,

$$P(t) = \mathrm{Tr}\left\{\hat{\mu}\,\hat{\rho}(t)\right\} \tag{1.26}$$

where $\hat{\rho}(t)$ is the full time-dependent density operator in the presence of the applied field. For a particular configuration of applied laser pulses $E(t)$, the equation of motion for $\hat{\rho}$, Eq. (1.14), can be solved directly, and the polarization calculated from Eq. (1.26). The difficulty in this procedure, in addition to the challenging numerical problem of solving for the density operator, is that it is difficult to extract a particular spectroscopic signal from the full polarization. $P(t)$ in Eq. (1.26) contains contributions from both linear and all nonlinear processes. Therefore the calculations must typically be run for a range of applied field strengths and the results carefully extrapolated to generate a specific linear or nonlinear signal. [19, 20]

An alternate method for calculating spectroscopic signals is to expand the density operator and the polarization in powers of $\hat{H}_1(t)$ and thus in powers of the applied field,

$$P(t) = P^{(0)}(t) + P^{(1)}(t) + P^{(2)}(t) + \cdots \tag{1.27}$$

$$P^{(n)}(t) = \mathrm{Tr}\left\{\hat{\mu}\,\hat{\rho}^{(n)}(t)\right\}. \tag{1.28}$$

The nth-order density operator is obtained from Eq. (1.22) by using the definition of the interaction Liouvillian in Eq. (1.20),

$$\begin{aligned}\hat{\rho}^{(n)}(t) = &\left(-\frac{i}{\hbar}\right)^n \int_0^t d\tau_n \int_0^{\tau_n} d\tau_{n-1} \cdots \int_0^{\tau_2} d\tau_1\, \hat{\mathcal{K}}_0(t,\tau_n)\,\mathcal{L}_1(\tau_n)\,\hat{\mathcal{K}}_0(\tau_n,\tau_{n-1})\,\mathcal{L}_1(\tau_{n-1})\cdots \\ &\times\, \hat{\mathcal{K}}_0(\tau_2,\tau_1)\,\mathcal{L}_1(\tau_1)\,\hat{\mathcal{K}}_0(\tau_1,0)\,\hat{\rho}(0)\,. \end{aligned} \tag{1.29}$$

Within the dipole approximation, the interaction of the field with the system is

$$\hat{H}_1(t) = -\hat{\mu}\, E(t)\,. \tag{1.30}$$

For a system that begins in equilibrium at a temperature T, the density operator at $t = 0$ is the canonical density,

$$\hat{\rho}(0) = \hat{\rho}^{(0)} = \frac{1}{\mathcal{Z}} e^{-\beta \hat{H}_0}\,, \tag{1.31}$$

where $\mathcal{Z}$ is the canonical partition function, and $\beta \equiv 1/k_B T$ where k_B is Boltzmann's constant. Defining $t_k \equiv \tau_{k+1} - \tau_k$ to be the delay time between laser pulses, and inserting Eqs. (1.30) and (1.31) into Eq. (1.28) allows the nth-order polarization to be written as the convolution of n factors of the applied field with a response function $R^{(n)}$,

$$\begin{aligned} P^{(n)}(t) = \int_0^\infty dt_n \int_0^\infty dt_{n-1} \cdots \int_0^\infty dt_1\, R^{(n)}(t_n, t_{n-1}, \cdots, t_1) \\ \times\; E(t - t_n) E(t - t_n - t_{n-1}) \cdots E(t - t_n \cdots - t_1)\,. \end{aligned} \tag{1.32}$$

The nth-order response function $R^{(n)}(t_n, \cdots, t_1)$ contains all the system-specific information necessary for the treatment of any coherent n-photon process on a single electronic surface. If the response function is known for a system, any combination of applied fields can be used in Eq. (1.32) to calculate the resulting polarization. $R^{(n)}$ has the form of a set of nested commutators,

$$\begin{aligned} R^{(n)}(t_n, t_{n-1}, \cdots, t_1) = \left(\frac{i}{\hbar}\right)^n \mathrm{Tr}\Big\{\hat{\mu}\hat{K}_0(t_n)\Big[\hat{\mu}, \hat{K}_0(t_{n-1})\Big[\cdots\Big[\hat{\mu}, \hat{K}_0(t_1)\Big[\hat{\mu}, \hat{\rho}(0)\Big] \\ \times\; \hat{K}_0^\dagger(t_1)\Big]\cdots\Big]\hat{K}_0^\dagger(t_{n-1})\Big]\hat{K}_0^\dagger(t_n)\Big\} \end{aligned} \tag{1.33}$$

where $\hat{\rho}(0)$ is the initial equilibrium state of the system, each factor of $\hat{\mu}$ indicates an interaction with the field, and in between these $n+1$ interactions, the density operator evolves according to the propagator in the absence of the field, $\hat{K}_0$.

By expanding the commutators in Eq. (1.33), response functions can also be written as a sum of 2^n dipole correlation functions with n time arguments divided by a power of $\hbar$. For example, the linear response is given by

$$R^{(1)}(t) = \frac{i}{\hbar}\left\{\langle\hat{\mu}(t)\,\hat{\mu}(0)\rangle - \langle\hat{\mu}(0)\,\hat{\mu}(t)\rangle\right\} = -\frac{2}{\hbar}\,\mathrm{Im}\,\langle\hat{\mu}(t)\,\hat{\mu}(0)\rangle \tag{1.34}$$

where the brackets $\langle\ \rangle$ indicate a trace with the canonical density operator $\hat{\rho}(0)$. The time dependence of each correlation function reflects interference among quantum phases, [21–26] and the response function additionally includes interference effects between correlation functions. Note that in the short-pulse limit for $E(t)$, the Fourier transform of $R^{(1)}(t)$ is proportional to the absorption spectrum.

Classical mechanical response functions may also be defined by either performing classical time-dependent perturbation theory, or by taking the $\hbar \to 0$ limit of Eq. (1.33). The linear and nth-order classical vibrational response functions are given by [27]

$$R^{(1)}_{cl}(t) = \frac{\beta}{m}\langle q(t)\,p(0)\rangle = \int dz\, q(t)\,p(0) f_{cl}(z) \tag{1.35}$$

$$R^{(n)}_{cl}(t_n,\cdots,t_1) = \int dz \left(\frac{\partial^n q(t_1+\cdots+t_n)}{\partial p(t_1+\cdots+t_{n-1})\cdots\partial p(0)}\right) f_{cl}(z) \tag{1.36}$$

where the brackets $\langle\ \rangle$ in Eq. (1.35) represent a classical canonical phase space average, $f_{cl}(z)$ is the classical canonical distribution function, q, p, and m are the coordinate, momentum, and mass of the active chromophore degree of freedom, and we have assumed the dipole μ is linear in coordinate q. Classical response functions have been extensively studied for a variety of systems, [28–39] and it has been found that in some cases the classical response is qualitatively incorrect. For one-dimensional anharmonic systems, the nonlinear classical response can grow without bound for certain combinations of time arguments, [28,32,40]

while the quantum response is bounded. This unphysical growth reflects the linear growth the classical stability matrix elements, and it indicates that truncation of the expansion for the polarization in powers of the electric field is only valid for a limited range of times within classical mechanics.

1.6 Response functions of anharmonic oscillators

In order to illustrate the similarities and differences between quantum and classical response functions, as well as to motivate the use of semiclassical and mixed quantum-classical methods, we shall calculate the linear and third-order response functions for a thermal ensemble of non-interacting, one-dimensional anharmonic Morse oscillators. The classical and quantum mechanics for both the harmonic and Morse oscillator systems is discussed more fully in Appendix A. As was done for classical response functions, we shall assume that the dipole operator and thus the interaction between the system and the applied field is linear in the coordinate operator, $\hat{\mu} \propto \hat{x}$. The case where the dipole is quadratic in $\hat{x}$ is discussed by Sahrapour and Makri. [41] In addition to the linear response function $R^{(1)}(t)$, we shall also discuss the third-order nonlinear response function $R^{(3)}(t_3, t_2, t_1)$. The second-order (and all even-order) response functions vanish for isotropic systems. Second-order experiments are thus useful for measuring spectroscopy at interfaces and surfaces. However, we shall not consider even-order response theory here.

For harmonic systems, the spacing between any two adjacent energy levels is the same, and thus the linear response function for a harmonic system with frequency ω is simply $R^{(1)}(t) \propto \sin(\omega t)$. If the coupling between the system and the

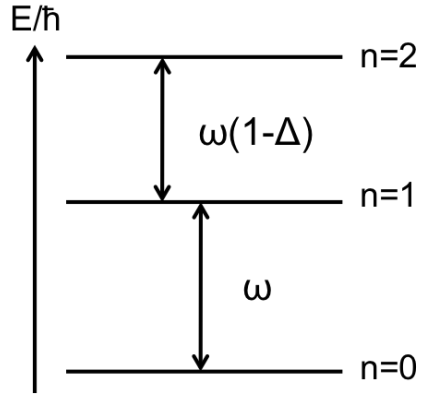

Figure 1.2: Energy level diagram for a typical three-level anharmonic system. The frequency difference between the $0,1$ and $1,2$ coherences is given by $\omega\Delta$.

radiation is linear in the coordinate operator, all nonlinear response functions for harmonic systems vanish. If a harmonic system is quadratically coupled to radiation, then the nonlinear response may be non-zero. For anharmonic systems, the linear and nonlinear response functions are typically characterized by the frequencies shown in Figure 1.2 for a generic three-level anharmonic system. The $n = 0$ to $n = 1$ ground to first excited state coherence frequency determines the dominant frequency of the response function. For nonlinear response functions at zero temperature, and for linear response functions at elevated temperatures, the frequency of the $n = 1$ to $n = 2$ transition also contributes. This $1,2$ coherence frequency is shifted from the $0,1$ coherence frequency by an anharmonicity Δ.

The Morse oscillator potential is defined as

$$V(q) = D\left(1 - e^{-q\sqrt{\frac{m\omega^2}{2D}}}\right)^2 \tag{1.37}$$

with energy eigenvalues $\epsilon_n = (n+1/2)\hbar\omega - (n+1/2)^2\hbar^2\omega^2/2D$. The dimensionless linear response function $m\omega R^{(1)}(t)$ is expressed as a function of ωt and depends on only two dimensionless parameters βD and $\beta\hbar\omega$. The quantum linear re-

sponse can be calculated exactly as discussed in Appendix A, or we can approximate $R^{(1)}$ by evaluating the response in the energy representation and replacing the thermal density operator and the coordinate matrix elements with their harmonic limits. The quantum linear response then takes the form

$$R^{(1)}(t) = \frac{\left(1 - e^{-\beta\hbar\omega}\right)^2}{\left(1 - 2e^{-\beta\hbar\omega}\cos(\Delta\omega t) + e^{-2\beta\hbar\omega}\right)^2}\Big[\sin\left((1-\Delta)\omega t\right) - 2e^{-\beta\hbar\omega}\cos\left(\omega t\right) + e^{-2\beta\hbar\omega}\sin\left((1+\Delta)\omega t\right)\Big] \tag{1.38}$$

where $\Delta \equiv \hbar\omega/4D$ is the dimensionless anharmonicity depicted in Figure 1.2. The quantum response contains frequencies ω and $\omega(1 \pm \Delta)$, and thus has recurrences with a period of $2\pi/\omega\Delta \propto \hbar^{-1}$ which becomes infinite in the classical limit. We can obtain the classical linear response either numerically by integrating Eq. (1.35), or by taking the $\hbar \to 0$ limit of Eq. (1.38),

$$R_{cl}^{(1)}(t) = \frac{\left(1 - (\omega t/2\beta D)^2\right)\sin\omega t - (\omega t/\beta D)\cos\omega t}{\left(1 + (\omega t/2\beta D)^2\right)^2}\,. \tag{1.39}$$

Eq. (1.39) decays as t^{-2} for long times, in contrast to the quantum linear response which is periodic in time. Quantum and classical linear response functions for the Morse oscillator system are depicted in both the time and frequency domain in Figure 1.3.

The dimensionless third-order response function $m^2\omega D R^{(3)}(t_3, t_2, t_1)$ can also be calculated in both the quantum and classical cases, as depicted in Figure 1.4. The quantum response for $t_1 = t_3 = t$ and $t_2 = 0$ is composed of a frequency 2ω corresponding to twice the fundamental frequency of the Morse oscillator and a slow frequency $\Delta\omega$ which derives from the anharmonicity of the oscillator. The classical response on the other hand is qualitatively different. Though the quantum and classical results agree for short times, for longer times the classical third-order response $R_{cl}^{(3)}(t, 0, t)$ diverges linearly with time. [27, 40, 42–46]

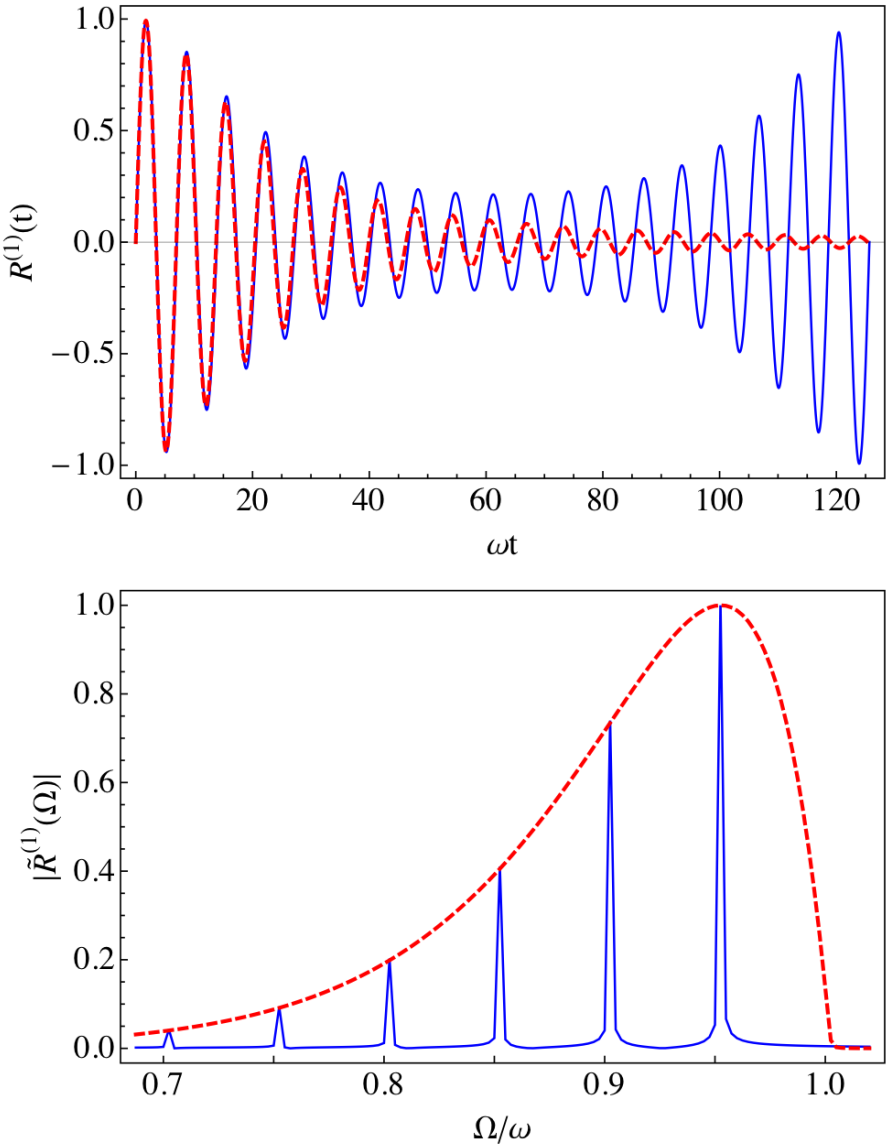

Figure 1.3: Quantum (blue) and classical (red, dashed) linear response functions for a Morse oscillator system with $\beta\hbar\omega = 1$ and $\beta D = 10$, calculated using Eq. (1.38) and (1.39). The top panel depicts the response as a function of time, $R^{(1)}(t)$, while the bottom panel shows the absolute magnitude of the Fourier transform of the response, $|\tilde{R}^{(1)}(\Omega)|$.

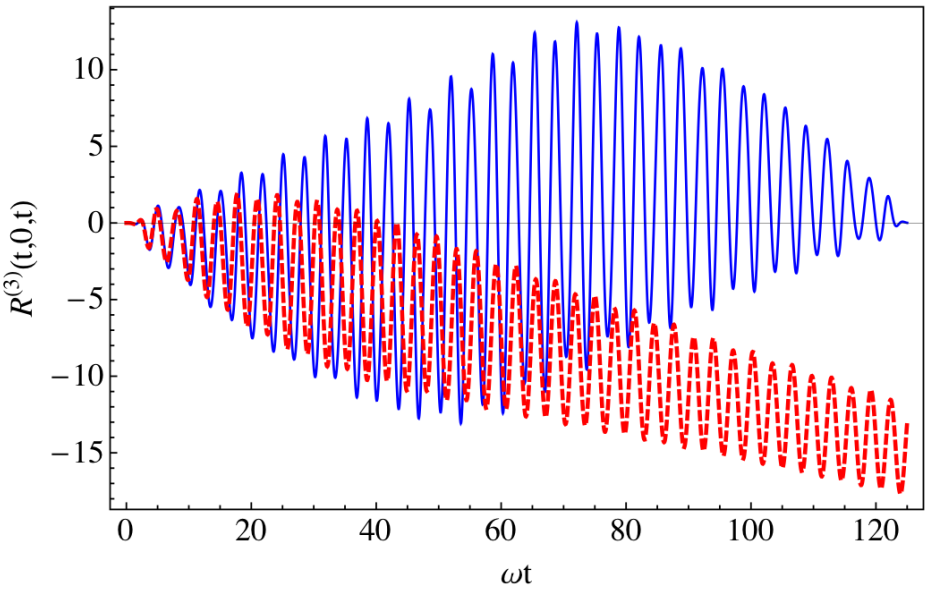

Figure 1.4: Quantum (blue) and classical (red, dashed) third-order response function $R^{(3)}(t, 0, t)$ for an ensemble of uncoupled Morse oscillators with $\beta\hbar\omega = 5$ and $\beta D = 50$.

To understand this divergence, we note that in the quantum third-order response, there is a term proportional to $\sin(\Delta\omega t)$ due to the system anharmonicity. For small $\hbar$, Δ is small, and this sine function is expanded in power of of Δ, $\sin(\Delta t) \approx \Delta\omega t$. [47] The time divergence of the classical nonlinear response function thus results from taking an $\hbar \to 0$ limit prior to taking the $t \to \infty$ long time limit.

The effects of temperature and anharmonicity can also be visualized in the two-dimensional plots of $R^{(3)}(t_3, 0, t_1)$ in Figure 1.5. The cyan background of Figure 1.5 indicates areas of small absolute magnitude, while red and purple regions indicate large positive and negative values for the response function. For fixed anharmonicity, panels (a) and (b) display the low and high temperature behavior of the response function. For low temperatures, the response has a checkerboard pattern, with a slow recurrence frequency along the t_3 axis due

to the system's anharmonicity. For high temperatures, the response is shaped like an 'X', with large magnitudes along the diagonals. In panel (c), the anharmonicity is increased, with a corresponding decrease in the period of the slow oscillations of the response function. Finally, panel (d) approximates the small $\hbar$ classical limit. As in Figure 1.4, the classical response function diverges without bound along the $t_1 = t_3$ diagonal.

While relatively simple to calculate, the classical response functions are qualitatively incorrect for even simple anharmonic systems. For systems with fast dephasing, perhaps due to interactions with a heat bath, the response functions decay to zero on a finite time scale, and the classical results may agree more closely with the quantum response. [48, 49] Calculations of the quantum response for nonlinear response functions and for systems with multiple coupled degrees of freedom quickly become very challenging, however. One method to circumvent this problem is to treat part of the system with quantum mechanics, and treat the remainder classically. For example, a single anharmonic degree of freedom may be weakly coupled to a bath of off-resonant modes, as occurs in the case of carbon monoxide bound in the active site of a heme protein. [50–52] In this case, the chromophore (the CO) is treated as a quantum system, while the effects of the protein are included only approximately. An example of this method is discussed more fully in Chapter 5. An alternative which treats all degrees of freedom equivalently is to use semiclassical methods to calculate the response. This will be the topic of the next section, as well as Chapters 2–4.

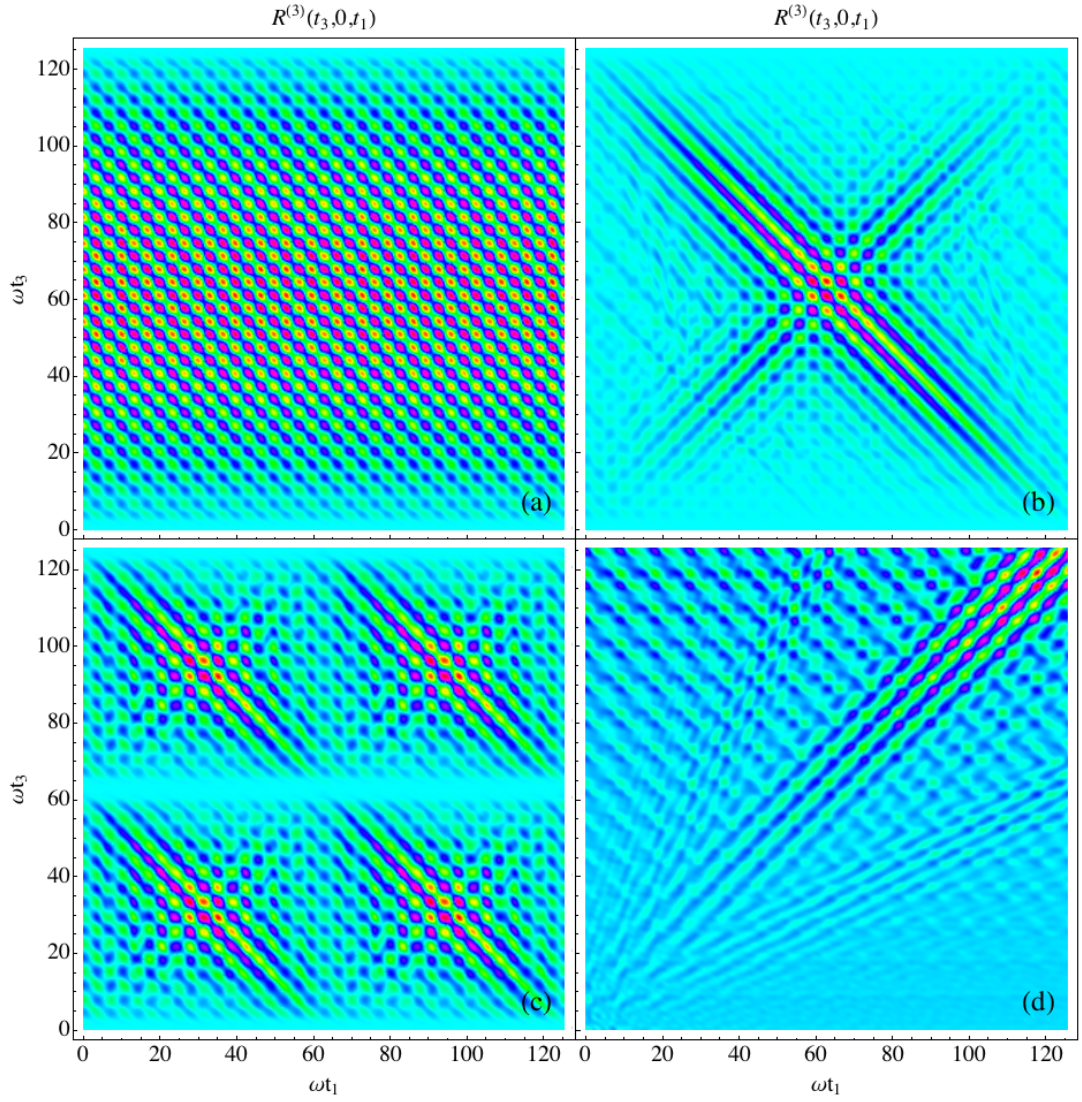

Figure 1.5: The quantum third-order response function $R^{(3)}(t_3, 0, t_1)$ is plotted for a thermal ensemble of one-dimensional Morse oscillators with parameters (a) $\beta\hbar\omega = 10$, $\beta D = 100$, (b) $\beta\hbar\omega = 1$, $\beta D = 10$, (c) $\beta\hbar\omega = 2$, $\beta D = 10$, and (d) $\beta\hbar\omega = 0.1$, $\beta D = 10$. Panel (d) is essentially equivalent to the classical third-order response function for the time range plotted.

1.7 Semiclassical propagators

As mentioned in the previous section, quantum calculations on coupled systems with multiple degrees of freedom quickly become challenging. Semiclassical techniques refer to a variety of methods which attempt to approximate quantum mechanics with only classical information, such as the motion of trajectories in phase space. Quantum and classical mechanics become equivalent for large enough energies, large masses, or "small $\hbar$" (really, the limit where a dimensionless quantity proportional to $\hbar$ goes to zero), and so we expect that classical ideas will be useful in this "semiclassical" limit. In practice, semiclassical techniques can generate surprisingly accurate approximations to wavefunctions, the density of states, and propagators even in the case of small quantum numbers.

The origin of semiclassical methods goes back to the earliest days of the old quantum theory. The WKB (Wentzel, Kramers, and Brillouin) method [53] allows the approximate solution to the time-independent Schrödinger equation in the large quantum number limit. Though WKB wavefunctions fail near classical turning points, they can be surprisingly accurate for a variety of one-dimensional systems such as the bound states of an anharmonic oscillator. The constraint that WKB wavefunctions be normalizable generates a quantization condition on the classical action integral,

$$\frac{1}{2\pi}\int p\, dq = n\hbar \tag{1.40}$$

where p and q are the momentum and coordinate of the system, n is an integer (or half-integer), and the integral is taken over one period of motion. Eq. (1.40) is known as the Bohr-Sommerfeld quantization condition, and it was generalized

to quasiperiodic systems with multiple degrees of freedom by Einstein, Brillouin, and Keller, among others. [54–56] Bohr-Sommerfeld and the more general EBK semiclassical quantization, as well as Gutzwiller's theory for semiclassical quantization in the chaotic regime, [57–59] are discussed more fully in Appendix C.

One can also make a semiclassical approximation to the quantum propagator $\hat{K}$. Feynman showed that the propagator $K(x_1, x_2, t) \equiv \langle x_1|\hat{K}(t)|x_2\rangle$ could be expressed as a sum over all possible paths connecting x_1 to x_2 in time t with a weight given by $\exp[iS(x_1, x_2, t)/\hbar]$ where S is the action (Hamilton's principal function) for the path, [53, 60]

$$S(x_1, x_2, t) = \int_0^t d\tau \left(p(\tau)\dot{q}(\tau) - H(p(\tau), q(\tau)) \right). \tag{1.41}$$

For small $\hbar$, only paths where the phase $S/\hbar$ is nearly stationary with respect to variations in the path will contribute to the propagator. These paths correspond to the classically allowed paths between x_1 and x_2 in time t. Within this stationary phase approximation, the propagator for a system with f degrees of freedom is given by

$$K_{VV}(x_1, x_2, t) = (2\pi i\hbar)^{-f/2} \sum_r \frac{e^{iS(x_1,x_2,t)/\hbar - i\pi\nu_r/2}}{|\det(\partial x_2/\partial p_1)|^{1/2}} \tag{1.42}$$

where the sum over r corresponds to a sum over all classical trajectories that start at x_1 and end at x_2 in time t, and ν_r is an integer known as the Maslov (Morse) index which changes discontinuously at caustics when $\det(\partial x_2/\partial p_1) = 0$. [59, 61] Eq. (1.42) is known as the Van Vleck (VV or VVG) semiclassical propagator after J. H. Van Vleck who first formulated a version of it in 1928 as an asymptotic solution to the Schrödinger equation as $\hbar \to 0$. [62]

The Van Vleck propagator presents several numerical difficulties that make

it challenging to use in practice. Eq. (1.42) is written as a double-sided boundary problem, where all possible classical trajectories connecting two coordinates must be determined. As the number of such trajectories may become large for long times or for multi-dimensional systems, this is a difficult root search problem. In addition, for each trajectory, the Maslov index must be calculated. Most importantly, at caustic points the denominator of the VV propagator goes to zero and K_{VV} becomes infinite. This is a fundamental, not a numerical, problem which causes the VV approximation to break down for certain combinations of x_1, x_2, and t — the VV propagator is not a uniform semiclassical approximation. [63]

One method to circumvent the root search problem is to use an initial value representation (IVR) for the semiclassical propagator. [21, 23, 64–74] The IVR writes the propagator as an integral over initial conditions rather than through boundary conditions,

$$K_{VV}^{IVR}(x_1, x_2, t) = \frac{1}{(2\pi i\hbar)^{f/2}} \int dp \int dq\, \delta(x_2 - q(t))\, |\det(\partial q(t)/\partial p)|^{1/2} \times\ e^{iS(q,p,t)/\hbar - i\pi\nu/2}\, \delta(x_1 - q)\,. \tag{1.43}$$

The VV-IVR propagator in Eq. (1.43) can also be reformulated in the momentum basis. [68] The IVR method removes the troublesome root search problem as well as moves the factor $\det(\partial q(t)/\partial p)$ to the numerator of the propagator. At caustics, Eq. (1.43) therefore does not diverge, but instead equals zero. Thus, the Van Vleck propagator in either representation is not accurate for some coordinates x and times t.

An alternative, and at first glance unrelated, method was developed by Heller for the propagation of wavepackets. [75, 76] In the thawed Gaussian ap-

proximation, [77] the initial state Ψ is expressed as a complex Gaussian

$$\psi(q,t) \propto \exp\Big[-\frac{\alpha_t}{2\hbar}(q-q_t)^2 + \frac{i}{\hbar}p_t(q-q_t) + \frac{i}{\hbar}\phi_t \Big] \tag{1.44}$$

where the complex width α_t and the phase ϕ_t can vary with time. The Gaussian wavepacket will obey classical equations of motion for short times and in harmonic potentials by Ehrenfest's theorem. As the width of Ψ will be very narrow when $\hbar$ is small, the potential can be expanded to quadratic order around the center of the wavepacket. However, even though the shape of the Gaussian in Eq. (1.44) changes with time, wavepackets propagating in an anharmonic potential will not remain Gaussian for long. Thus, the thawed Gaussian approximation fails for long times, though it is useful for quantities which only depend on short-time dynamics. [77] The frozen Gaussian approximation [76] on the other hand constrains the width of the Gaussian wavepacket to be constant in time. To allow for wavepacket spreading, this approximation expresses the initial state as a sum over many frozen Gaussians, each of which propagates in time according to classical equations of motion and accumulates a phase $\exp(iS(t)/\hbar)$ as in the Van Vleck propagator. The sum of these complex, frozen Gaussians generates the wavepacket at future times t. This approximation has been applied, for example, to electronic transitions in solutions [78] and is reasonably accurate for short times.

Herman and Kluk (HK) used the frozen Gaussian idea to derive an alternative expression for the semiclassical propagator in an initial value representation. [79, 80] The initial state was expanded in a frozen Gaussian (coherent state) [81] basis $|z\rangle$, where

$$\langle x|z\rangle = \left(\frac{\gamma}{\pi}\right)^{f/4} \exp\left[-\frac{\gamma}{2}(x-q)^2 + \frac{i}{\hbar}p\cdot(x-q)\right] \tag{1.45}$$

and γ is a constant that is inversely proportional to $\hbar$. In a harmonic system, the

coherent states are those states whose motion in time most closely resembles classical mechanics. These coherent states are then propagated forward in time with the Van Vleck propagator, Eq. (1.42), and several integrals are performed by stationary phase. The resulting propagator $K_{HK}(x_1, x_2, t)$ has the form

$$K_{HK}(x_1, x_2, t) = \iint \frac{dq\, dp}{(2\pi\hbar)^f} \langle x_2|z(t)\rangle\, C(z,t)\, e^{iS(z,t)/\hbar} \langle z|x_1\rangle \tag{1.46}$$

where the Herman-Kluk prefactor $C(z,t)$ is given by

$$C(z,t) \equiv \sqrt{\det \frac{1}{2}\left[M_{qq}(z,t) + M_{pp}(z,t) - i\hbar\gamma M_{qp}(z,t) + \frac{i}{\hbar\gamma} M_{pq}(z,t)\right]} \tag{1.47}$$

and the monodromy (stability) matrix elements [59] are defined as

$$M_{ab}(z,t) \equiv \left(\frac{\partial a(t)}{\partial b(0)}\right)_{a(0)} \tag{1.48}$$

with a and b either q or p. The HK expression in Eq. (1.46) differs from Heller's frozen Gaussian approximation due to the HK prefactor $C(z,t)$. This prefactor is vital for ensuring that the semiclassical propagator is unitary within the stationary phase approximation. [82] Note that the phase of the prefactor is easily determined by continuity.

Though there was initially some controversy over the nature of the HK propagator, [83, 84] Eq. (1.46) has since be re-derived in a number of different manners. Miller [85] obtained the HK propagator from the VV-IVR propagator thorough an Filinov integral conditioning method, while Shalashilin and Child showed that the the exact coherent state expression for the propagator is equivalent to the HK approximation within linearization and a local quadratic approximation. [86] Grossmann and Xavier derived the HK result from the path integral form for the propagator within a stationary phase approximation. [87] Miller [88] and Deshpande and Ezra [89, 90] have started from the Schrödinger equation and demonstrated the approximations necessary to arrive at the HK

propagator. Specifically, the main approximation in addition to a local quadratic expansion of the potential is that the HK prefactor is a weak function of the initial point in phase space. Finally, Kay has derived the HK propagator (as well as several other related semiclassical propagators) as an asymptotic solution to the Schrödinger equation in the limit of small $\hbar$. [68,91] Kay has also shown that the HK expression can be converted into the VV propagator within a stationary phase approximation to the integrals. [91]

The HK propagator in Eq. (1.46) has many advantages over the VV propagator of Eq. (1.42). As a semiclassical initial value representation for the propagator, there are no boundary condition root-search problems. The Maslov index ν does not appear explicitly in the HK propagator, though as is discussed in Chapter 4, the phase of the HK prefactor plays the same role. Most importantly, the HK prefactor does not diverge or go to zero for any values of q and p. Thus the HK propagator is finite for all times and is potentially more accurate than the VV propagator. Kay has shown that the HK propagator is a uniform semiclassical approximation, unlike the VV approximation, and corrections to HK to order $\hbar^2$ have been developed. [68] In addition to these numerically advantageous properties, the HK propagator is also exact for potentials up to quadratic order.

The HK propagator has been applied to many problems such as wavepacket propagation in anharmonic [80, 92, 93] and in chaotic [94–96] potentials, the calculation of photodissociation spectra, [97] and tunneling through one-dimensional barriers. [98] A surface hopping generalization of the HK method has been used to study nonadiabatic problems on several model systems. [99–101] The HK propagator has also been applied to correlation functions [102]

and by the Loring and Ezra groups to linear and nonlinear vibrational response functions. [27, 45, 47, 103, 104] In each case, the semiclassical HK treatment has performed well compared to classical or VV treatments. Though the HK propagator is unable to describe deep tunneling, [98, 105] it does accurately capture quantum coherence effects in response functions as well as quantization of energy in the density of states for simple anharmonic oscillator systems. Due to an exponential growth of the HK prefactor with time for chaotic classical trajectories, the unmodified HK propagator is numerically unable to deal with chaotic systems. Various filtering methods have been suggested to remedy this problem. [94, 96, 106, 107] In the next three chapters of this dissertation, we shall be concerned with the application of the HK method to response functions as well as to wavepacket dynamics. Our goal will be to analyze and understand the mechanism by which the HK approximation generates accurate, quantum results using only classical inputs.

1.8 Summary

In this chapter we have introduced the vibrational response function formalism that is used to interpret the results of linear and multidimensional infrared spectroscopic measurements. Both quantum and classical response theory are useful for different types of systems, but these two methods may exhibit qualitative differences such as a classical time divergence. This was demonstrated for a thermal ensemble of one-dimensional anharmonic oscillators. Semiclassical methods in principal may allow for the accurate calculation of response functions using only classical information. We have reviewed several semiclassical techniques, and in Chapters 2, 3, and 4 we will use the Herman-Kluk approx-

imation to the propagator to calculate linear and nonlinear response functions. Mixed quantum-classical methods are useful when the system of interest separates into a quantum chromophore coupled to a classical bath of motions. This approach will be considered in Chapter 5.

CHAPTER 2

THE SEMICLASSICAL LINEAR RESPONSE FUNCTION

2.1 Introduction

The calculation of linear and nonlinear vibrational response functions provides a method for the interpretation of the observables in linear and multidimensional infrared spectroscopy. [2, 108–112] Response functions may be calculated both quantum mechanically as well as classically, and quantum and classical results agree for short times and for systems where quantum coherences dephase on the experimental time scale. For other systems such as weakly coupled anharmonic oscillators or coupled oscillators at relatively low temperatures, the quantum and classical linear and nonlinear response functions may be qualitatively different. Classical response functions fail to reproduce quantum recurrences, and nonlinear classical response functions may unphysically diverge for certain combinations of the time arguments. [27, 40, 42–45] However, quantum response functions rapidly become impractical to calculate for multidimensional coupled systems.

Semiclassical approximations have the potential to more accurately reproduce the quantum response function from purely classical information. As discussed in the previous chapter, we will use the Herman-Kluk approximation, an initial value representation of the quantum propagator in the coherent states basis. [79,80] The Herman-Kluk approximation is only exact for harmonic systems,

*Reprinted with permission from S. M. Gruenbaum and R. F. Loring, J. Chem. Phys., 128, 124106 (2008) and from S. M. Gruenbaum and R. F. Loring, J. Chem. Phys., 131, 204504 (2009), Copyright 2008 and 2009, American Institute of Physics.

but as we will show, it accurately reproduces the linear response function even for anharmonic oscillator systems. However, though the semiclassical response is accurate, numerical computations are challenging due to an oscillatory integrand — the sign problem that so often plagues semiclassical dynamics. In addition, HK calculations require the propagation of the classical monodromy matrix, the elements of which diverge with time for anharmonic systems.

This sign problem has been dealt with in other contexts with a variety of approximate methods. The linearized semiclassical propagator is based on the assumption that trajectory pairs are close in phase space, and thus it eliminates the semiclassical phase entirely. [113–117] Herman and Coker [102] have applied the HK propagator to correlation functions and analyzed the resulting semiclassical structure within a linearization approximation. The forward-backward methods of Makri et.al. and Miller et.al. [21–26] combine a pair of quantum propagators into a single semiclassical operator and therefore reduce the oscillatory nature of the integrand. Various integral filtering methods similarly decrease the integrand's oscillations. [106] Each of these methods, however, can eliminate quantum coherence information in the response function. The result is a loss of quantum recurrences, as is the case for the classical response function.

Rather than attempt to eliminate the semiclassical phase, we will use approximate dynamics for pairs of classical trajectories to investigate the structure of the phase and the semiclassical linear response function. The primary goal of this chapter is thus to analyze the mechanism by which the HK approximation reproduces the quantum recurrence structure, and then to use these insights to simplify the numerical computations. We show that by analytically but approximately integrating over trajectory difference variables, we can simplify the HK

linear response function into a quasiclassical form where single classical trajectories are propagated with quantized values of the classical action variables. This mean trajectory approximation is shown to be highly accurate and numerically efficient.

In Section 2, we introduce the Herman-Kluk approximation to the linear and nonlinear response function, as well as demonstrate its numerical accuracy. In Section 3, the structure of the semiclassical phase is analyzed for a one-dimensional anharmonic oscillator, and this structure is used in Section 4 to approximately integrate over difference variables, resulting in a simplified form for the semiclassical linear response function. The pairs of classical trajectories which contribute to the response at time t, as well as the time-dependent nature of the action quantization condition derived in Section 4, are discussed in Section 5. In Section 6 we generalize the mean trajectory treatment to multiple coupled oscillator systems. Numerical tests of the mean trajectory approximation are shown in Section 7, and we summarize our conclusions in Section 8.

2.2 Herman-Kluk response functions

The nth-order vibrational response function describes coherent n photon processes on a single electronic potential energy surface. As derived in Chapter 1, $R^{(n)}(t_n, \cdots, t_1)$ is given by

$$R^{(n)}(t_n, \ldots, t_1) = \left(\frac{i}{\hbar}\right)^n \mathrm{Tr}\left\{\hat{q}_a \hat{K}(t_n)\Big[\hat{q}_a, \hat{K}(t_{n-1})\Big[\hat{q}_a, \cdots \right. \\ \left. \times \Big[\hat{q}_a, \hat{K}(t_1)\Big[\hat{q}_a, \hat{\rho}\Big]\hat{K}^\dagger(t_1)\Big]\cdots\Big]\hat{K}^\dagger(t_{n-1})\Big]\hat{K}^\dagger(t_n)\right\} \tag{2.1}$$

where we have taken the interaction with the radiation field to be linear in a vibrational coordinate $\hat{q}_a$. While there may be many degrees of freedom in the

system, we assume that only the coordinate labeled a couples to the field. As discussed previously, $\hat{K}$ is the quantum propagator, and $\hat{\rho}$ is the equilibrium canonical density operator.

The Herman-Kluk approximation to the quantum propagator is given for f degrees of freedom by [79, 80]

$$\hat{K}_{HK}(t) = (2\pi\hbar)^{-f} \int d\mathbf{z}\, |\mathbf{z}(t)\rangle\, C(\mathbf{z},t)\, e^{iS(\mathbf{z},t)/\hbar}\, \langle \mathbf{z}| \tag{2.2}$$

where $C(\mathbf{z},t)$ is the HK prefactor, $S(\mathbf{z},t)$ is Hamilton's principal function, and $|\mathbf{z}\rangle$ is a coherent state [81] with coordinates $\mathbf{q}$ and momenta $\mathbf{p}$,

$$C(\mathbf{z},t) \equiv \sqrt{\det\left(\mathbf{\Gamma}\mathbf{M}_{\mathbf{qq}}(t) + \mathbf{M}_{\mathbf{pp}}(t)\mathbf{\Gamma} - i\hbar\mathbf{\Gamma}\mathbf{M}_{\mathbf{qp}}(t)\mathbf{\Gamma} + \frac{i}{\hbar}\mathbf{M}_{\mathbf{pq}}(t)\right) / (2\det\mathbf{\Gamma})} \tag{2.3}$$

$$S(\mathbf{z},t) \equiv \int_0^t d\tau\, (\mathbf{p}(\tau)\dot{\mathbf{q}}(\tau) - H(\mathbf{p}(\tau),\mathbf{q}(\tau))) \tag{2.4}$$

$$\langle \mathbf{r}|\mathbf{z}\rangle \equiv \left(\frac{\det\mathbf{\Gamma}}{\pi}\right)^{f/4} \exp\left[-(\mathbf{r}-\mathbf{q})\cdot\frac{\mathbf{\Gamma}}{2}\cdot(\mathbf{r}-\mathbf{q}) + \frac{i}{\hbar}\mathbf{p}\cdot(\mathbf{r}-\mathbf{q})\right]. \tag{2.5}$$

For f degrees of freedom, each monodromy matrix element such as $\mathbf{M}_{\mathbf{qp}} \equiv (\partial\mathbf{q}(t)/\partial\mathbf{p})_{\mathbf{q}}$ is an $f \times f$ matrix, and the coherent states are specified by a diagonal $f \times f$ matrix $\mathbf{\Gamma}$. Kay has investigated generalizations for complex symmetric and time-dependent matrices $\mathbf{\Gamma}(t)$. [63] The diagonal elements of $\mathbf{\Gamma}$ are inversely proportional to $\hbar$ but are otherwise arbitrary in principle. We shall take the diagonal elements of $\mathbf{\Gamma}$ to have their harmonic values $\Gamma_{\alpha\alpha} = m_\alpha\omega_\alpha/\hbar$ where m_α and ω_α are the effective mass and frequency of mode $\alpha = a, b, c, \cdots$. Noid et.al. [27] have investigated the effects of varying $\mathbf{\Gamma}$ on the linear response function, and have shown that while alternate values for $\mathbf{\Gamma}$ affect numerical convergence properties, the final results are essentially independent of $\mathbf{\Gamma}$ for a range of $\mathbf{\Gamma}$ near its harmonic value.

Substitution of the HK propagator into Eq. (2.1) yields the linear and nth-

order response functions,

$$R^{(1)}_{HK}(t) = \frac{1}{m_a k_B T (2\pi\hbar)^f} \int d\mathbf{z}_1 \int d\mathbf{z}_2 \; f_{cl}(\bar{\mathbf{z}}_{12}) A_{12}(t) P_{a,12} Q_{a,21}(t) \tag{2.6}$$

$$\begin{aligned} R^{(n)}_{HK}(t_n, \cdots, t_1) = & \frac{1}{m_a^n \omega_a^{n-1} \hbar^{n-1} k_B T (2\pi\hbar)^{f(2n-1)}} \int d\mathbf{z}_1 \cdots \int d\mathbf{z}_{2n} f_{cl}(\bar{\mathbf{z}}_{12}) \\ & \times A_{12}(t_1) A_{34}(t_2) \cdots A_{2n-1,2n}(t_n) \\ & \times O_{1234}(t_1) O_{3456}(t_2) \cdots O_{2n-3,2n-2,2n-1,2n}(t_{n-1}) \\ & \times P_{a,12} \left[P_{a,34} - P^*_{a,12}(t_1) \right] \left[P_{a,56} - P^*_{a,34}(t_2) \right] \cdots \\ & \times \left[P_{a,2n-1,2n} - P^*_{a,2n-3,2n-2}(t_{n-1}) \right] Q_{a,2n,2n-1}(t_n) \end{aligned} \tag{2.7}$$

where Eq. (2.7) is valid for $n \geq 2$ and the quantities in Eqs. (2.6) and (2.7) are defined as

$$A_{jk}(t) \equiv \left| \langle \mathbf{z}_j | \mathbf{z}_k \rangle \langle \mathbf{z}_k(t) | \mathbf{z}_j(t) \rangle \right| C(\mathbf{z}_j, t) C^*(\mathbf{z}_k, t) e^{i\psi_{jk}} \tag{2.8}$$

$$\hbar\psi_{jk} \equiv S(\mathbf{z}_j, t) - S(\mathbf{z}_k, t) - \bar{\mathbf{p}}_{jk}(t) \cdot \Delta\mathbf{q}_{jk}(t) + \bar{\mathbf{p}}_{jk} \cdot \Delta\mathbf{q}_{jk} \, . \tag{2.9}$$

The manipulations required to obtain Eqs. (2.6) and (2.7) are discussed by Noid, et.al., [27] and are briefly reviewed in Appendix B. The magnitude of the coherent state overlap is a Gaussian in the phase space distance $\Delta\mathbf{z}_{jk}$ between a propagating pair of trajectories $\mathbf{z}_j$ and $\mathbf{z}_k$,

$$\left| \langle \mathbf{z}_j | \mathbf{z}_k \rangle \right| = \exp\left(- \Delta\mathbf{z}^2_{jk}/2 \right) \tag{2.10}$$

$$\Delta\mathbf{z}^2_{jk} = \sum_\alpha \left(\frac{1}{2m_\alpha} \Delta p^2_{\alpha,jk} + \frac{\omega^2_\alpha m_\alpha}{2} \Delta q^2_{\alpha,jk} \right) / \omega_\alpha \hbar \tag{2.11}$$

and the ratio of coherent state overlaps is given by

$$\begin{aligned} O_{jklm}(t) \equiv & \frac{\langle \mathbf{z}_k(t) | \mathbf{z}_m \rangle \langle \mathbf{z}_l | \mathbf{z}_j(t) \rangle}{\langle \mathbf{z}_k(t) | \mathbf{z}_j(t) \rangle \langle \mathbf{z}_l | \mathbf{z}_m \rangle} \\ = & \prod_\alpha \exp\Big[- \frac{m_\alpha \omega_\alpha}{2\hbar} \left(Q_{\alpha,lm} - Q^*_{\alpha,jk}(t) \right)^2 \\ & - \frac{1}{2\hbar m_\alpha \omega_\alpha} \left(P_{\alpha,lm} - P^*_{\alpha,jk}(t) \right)^2 \Big] \, . \end{aligned} \tag{2.12}$$

The coherent state matrix elements of coordinates and momenta are given by

$$Q_{\alpha,jk} \equiv \frac{\langle \mathbf{z}_j | \hat{q}_\alpha | \mathbf{z}_k \rangle}{\langle \mathbf{z}_j | \mathbf{z}_k \rangle} = \bar{q}_{\alpha,jk} - \frac{i}{2m_\alpha \omega_\alpha} \Delta p_{\alpha,jk} \tag{2.13}$$

$$P_{\alpha,jk} \equiv \frac{\langle \mathbf{z}_j | \hat{p}_\alpha | \mathbf{z}_k \rangle}{\langle \mathbf{z}_j | \mathbf{z}_k \rangle} = \bar{p}_{\alpha,jk} + \frac{i m_\alpha \omega_\alpha}{2} \Delta q_{\alpha,jk} \tag{2.14}$$

$$\bar{\mathbf{z}}_{jk} \equiv (\mathbf{z}_j + \mathbf{z}_k)/2, \quad \Delta \mathbf{z}_{jk} \equiv \mathbf{z}_j - \mathbf{z}_k \, . \tag{2.15}$$

In the final expressions for the linear and nth-order HK response functions, Eqs. (2.6) and (2.7), we have made a high temperature approximation to the coherent state matrix element of the density operator,

$$\langle \mathbf{z}_j | \, \hat{\rho} \, | \mathbf{z}_k \rangle \approx (2\pi\hbar)^f \langle \mathbf{z}_j | \mathbf{z}_k \rangle f_{cl}(\bar{\mathbf{z}}_{jk}) \tag{2.16}$$

where $f_{cl}(\bar{\mathbf{z}}_{jk})$ is the classical canonical Boltzmann distribution with temperature T. The distribution could also be treated semiclassically at the same level as the propagator, [73, 118] or evaluated analytically for a harmonic system. [119] However, we will demonstrate numerically that for most temperatures and anharmonicities studied, the quantum effects in the equilibrium distribution function are not as important as quantum effects in the dynamics for both linear and nonlinear response functions. The use of Eq. (2.16) produces accurate response functions even for relatively low temperatures, though in the $T \to 0$ limit a better approximation for the distribution is required.

In order to calculate $R^{(n)}$, n pairs of classical trajectories are propagated on an electronic surface, along with the corresponding monodromy matrices. Each pair of trajectories $\mathbf{z}_j$ and $\mathbf{z}_k$ accumulates a phase $\psi_{jk}(t)$, and trajectory pairs are connected by ratios of coherent state overlaps O_{jklm} and momentum and coordinate coherent state matrix elements. This structure is depicted in Figure 2.1, with horizontal lines indicating classical trajectories, and dashed vertical lines indicating interactions between the trajectories, and it is discussed in de-

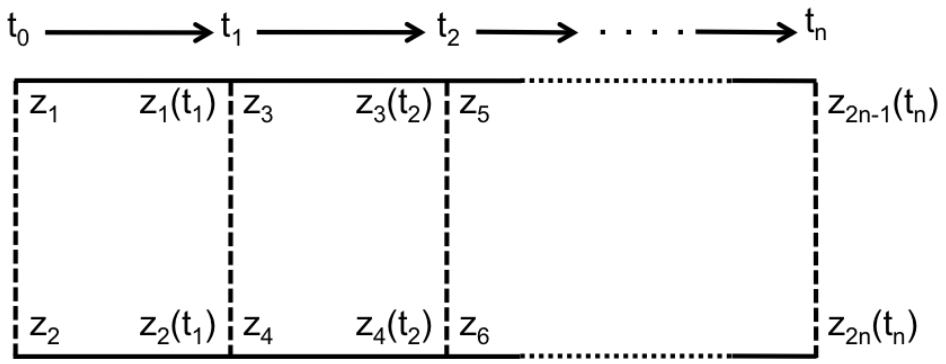

Figure 2.1: The structure of the semiclassical nth-order response function is depicted schematically. Solid, horizontal lines indicate classical trajectories, while dashed, vertical lines indicate interactions between trajectories.

tail by Noid, et.al. [27] In numerical calculations, the integrals over trajectory pairs are performed by Monte Carlo integration, with initial trajectories sampled according from the distribution $f_{cl}(\bar{\mathbf{z}}_{12})\left|\langle \mathbf{z}_1|\mathbf{z}_2\rangle\right|$. Classical trajectories and the associated monodromy matrix elements are propagated using the velocity Verlet algorithm.

Both the linear and third-order response functions within the HK approximation have been calculated numerically for a thermal ensemble of noninteracting Morse oscillators. [27, 45, 103] Figure 2.2 compares the HK result of Eq. (2.6) to the exact quantum linear response function $m\omega R^{(1)}(t)$ for both low (top panel) and high temperatures (bottom panel). The HK response function accurately reproduces the periodic recurrences which are the hallmark of the quantum response, as discussed in Chapter 1. The quantum and HK linear response functions have been compared for a variety of parameters with similar accuracy. For very low values of the temperature (large β), the high-temperature approximation to the density operator breaks down, and the resulting HK linear response function loses some accuracy. Also, Noid et.al. [45] have calculated

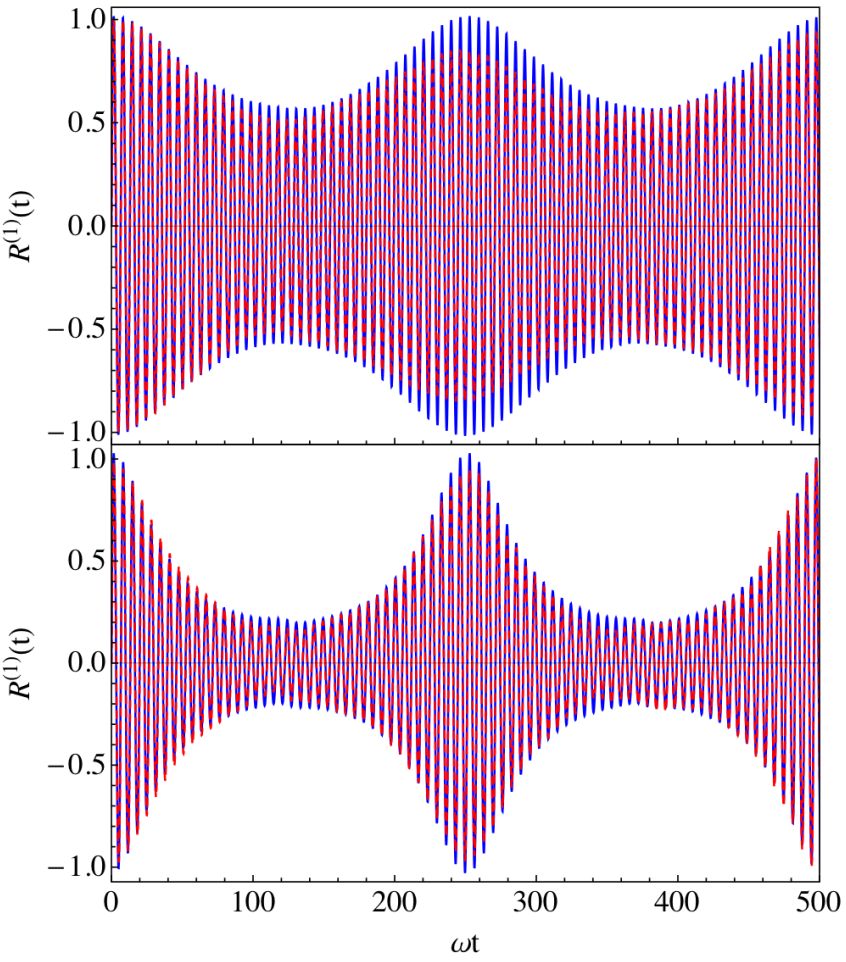

Figure 2.2: The quantum (blue) and HK (red, dashed) linear response functions are depicted for a thermal ensemble of noninteracting Morse oscillators with parameters $\beta D = 40$, $\beta\hbar\omega = 2$ (top panel) and $\beta D = 20$, $\beta\hbar\omega = 1$ (bottom panel). The discrepancy in the magnitude of the recurrence for the case of low temperatures (top panel) is likely due to the high temperature approximation to the coherent state matrix element of the canonical density operator, Eq. (2.16).

the third-order response function for the same system as in Figure 2.2. While the calculation was numerically quite challenging, they demonstrated that the HK nonlinear response function is quantitatively accurate as well.

The HK approximation to the linear response function in Eq. (2.6) has also been tested for a thermal ensemble of one-dimensional oscillators with quartic anharmonicities. The two potentials used are a quartically perturbed harmonic oscillator, Eq. (2.17), and a purely quartic oscillator, Eq. (2.18),

$$V(q) = \frac{m\omega^2}{2}q^2 + aq^4 \tag{2.17}$$

$$V(q) = aq^4 \, . \tag{2.18}$$

Figure 2.3 compares the quantum linear response to Eq. (2.6) for a quartically perturbed harmonic oscillator system at both low and high temperatures. The HK result qualitatively reproduces the complicated quantum structure of the response function, but it is not as accurate as it is for the Morse oscillator system. Nonetheless, the HK approximation to the response function is far more accurate than the classical response, which decays irreversibly to zero and shows no quantum recurrences.

Similarly, Figure 2.4 shows the quantum and HK linear response functions $m\omega_0 R^{(1)}(t)$ for the quartic oscillator system in Eq. (2.18). The time axis is scaled by an effective frequency $\omega_0 \equiv (a/\beta m^2)^{1/4}$. Again, the HK result qualitatively captures both the low and high temperature behavior of the response, but it is not quantitatively accurate. The cause for this inaccuracy can be more easily seen in the frequency domain, as is shown in the bottom panel of Figure 2.4. While the HK response function quantitatively yields the correct high-frequency components to the response, the lowest frequency component due to trajectories near the bottom of the quartic well is shifted to a higher frequency within the HK approximation. The reason for this frequency shift is discussed in Section 4.

As final test, the HK linear response function was calculated for a bilinearly

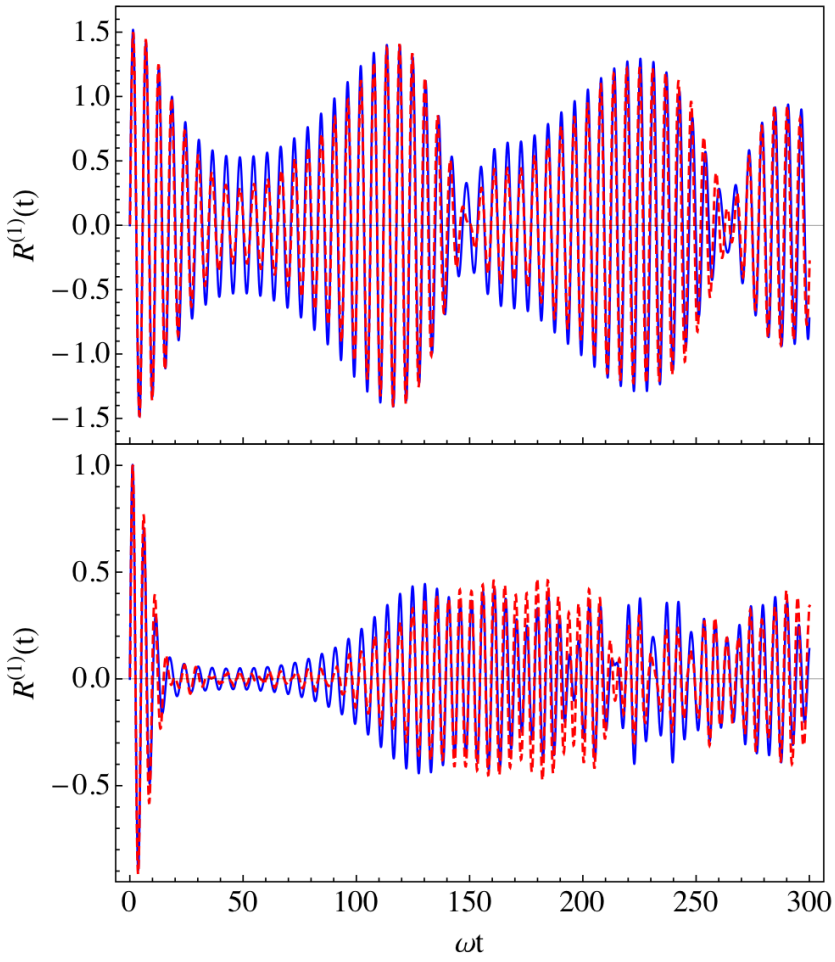

Figure 2.3: The quantum (blue) and HK (red, dashed) linear response functions are plotted for a thermal ensemble of oscillators with the potential of Eq. (2.17) with parameters $\beta\hbar\omega = 1$ and $(a/\beta m^2\omega^4)^{1/4} = 0.398$ (top panel) and $\beta\hbar\omega = 0.25$ and $(a/\beta m^2\omega^4)^{1/4} = 0.562$ (bottom panel).

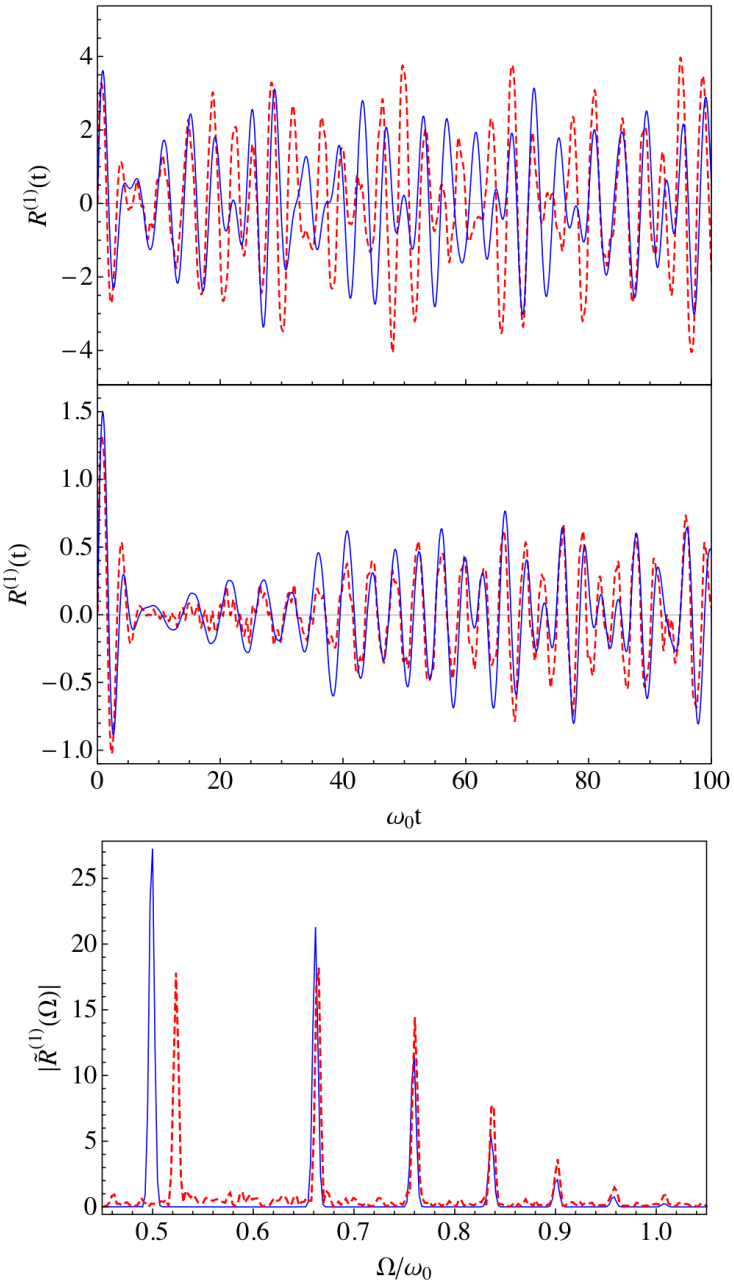

Figure 2.4: The quantum (blue) and HK (red, dashed) linear response functions are compared for an ensemble of quartic oscillators with $(\hbar^4 a\beta^3/m^2)^{1/4} = 0.473$ (top) and $(\hbar^4 a\beta^3/m^2)^{1/4} = 0.167$ (middle). In the bottom panel, the absolute magnitude of the Fourier transform of the quantum and HK linear response functions is compared for the same parameters as the top panel.

coupled anharmonic oscillator system with the potential

$$V(\mathbf{q}) = \sum_{\alpha} V_{\alpha} + \sum_{\alpha>\beta} c_{\alpha\beta} \frac{\sqrt{m_{\alpha} m_{\beta}} \omega_{\alpha} \omega_{\beta}}{2} q_{\alpha} q_{\beta} \tag{2.19}$$

where the index $\alpha = a, b, c, \cdots$ sums over f vibrational modes. In Figure 2.5, we have taken V_a to be a Morse potential coupled to one harmonic mode b with parameters $\beta D_a = 40$, $\beta\hbar\omega_a = 2$, $\omega_b = 0.9\omega_a$, $m_a = m_b$, and $c_{ab} = 0.1$. The frequencies of these coupled oscillators were chosen so that energy transfers between the normal modes, but that there are no low order resonances at low energies. The high frequency oscillations in Figure 2.5 are due to the dominant ω_a frequency, while the slow oscillations with frequency $\sim 250\omega_a^{-1}$ are due to the anharmonicity in mode a, as was the case for uncoupled oscillators. The intermediate frequency, however, is due to the frequency difference $\omega_a - \omega_b$ between the coupled oscillators. Once again, the HK result accurately reproduces the quantum structure of the response function.

For a variety of simple systems, the linear and nonlinear HK response functions agree well with exact quantum results. However as noted above, the calculations for nonlinear response functions are numerically challenging and are impractical for large, coupled systems or for higher order nonlinear response functions. The principal reason for this is the highly oscillatory semiclassical phase that results from interference between pairs of classical trajectories. The calculation of the nth-order response function requires $2n$ integrals over n such phase factors. This sign problem is common in semiclassical applications, and presents a numerical problem for Monte Carlo integration. [45] The other numerical difficulty for HK calculations is the time-divergence of the HK prefactor $C(\mathbf{z}, t)$. For regular (nonchaotic) systems with f degrees of freedom, the prefactor diverges as $t^{f/2}$, while for chaotic systems, the monodromy matrix elements and thus the prefactor diverge exponentially with time. [37–39, 120] Therefore,

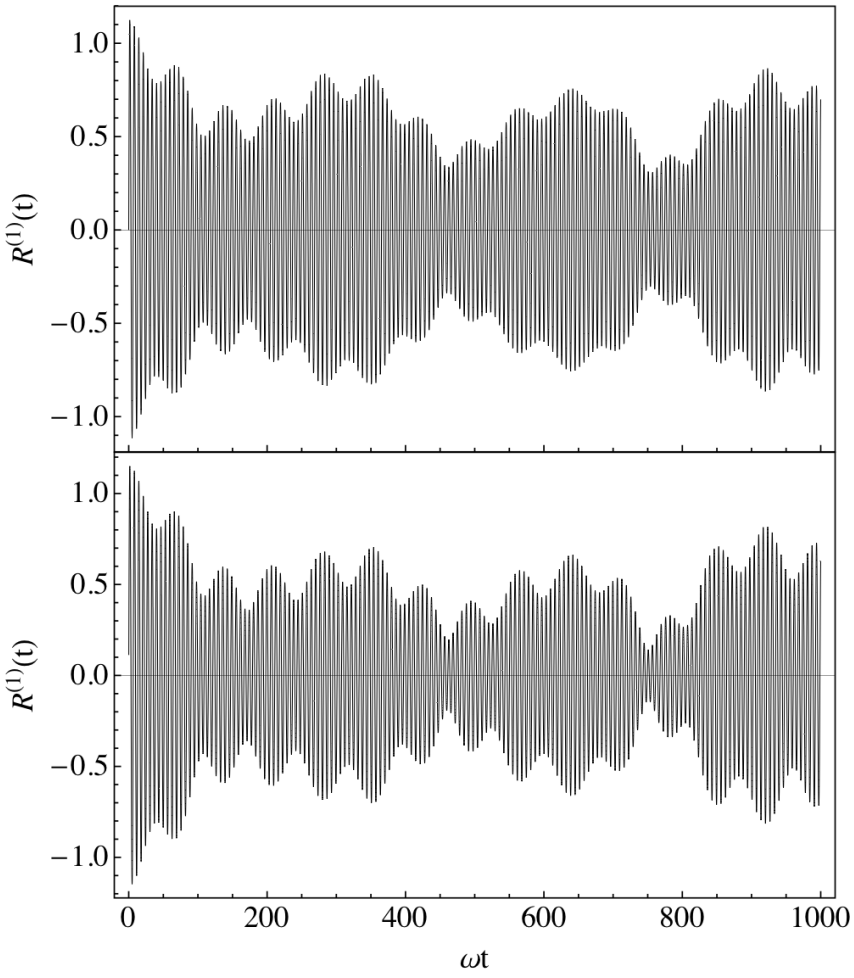

Figure 2.5: The quantum (top panel) and HK (bottom panel) linear response functions are plotted for a thermal ensemble of a chromophore Morse oscillator bilinearly coupled to a dark harmonic oscillator with parameters $\beta D_a = 40$, $\beta\hbar\omega_a = 2$, $\omega_b = 0.9\omega_a$, $m_a = m_b$, and $c_{ab} = 0.1$.

the semiclassical calculation of a response function requires multiple integrals over a diverging, oscillating integrand. In the remainder of this chapter, we shall analyze the various components of the HK linear response function in Eq. (2.6) and thereby elucidate the mechanism by which semiclassical response functions can reproduce quantum effects. This analysis will enable us to propose a numerically simplified semiclassical linear response function.

2.3 The semiclassical phase

For an ensemble of noninteracting anharmonic oscillators, the principal quantum effects in the linear response function are quantum recurrences with a frequency inversely proportional to $\hbar$. We will show that these recurrences are primarily due to the structure of the semiclassical phase. In the harmonic limit, the phase of the coherent state overlaps in Eq. (2.9) exactly cancels the classical action difference $\Delta S_{jk}(t)$, and the harmonic phase ψ_{jk} is thus equal to zero for any pair of trajectories. Similarly, if we assume that only trajectory pairs that start very close together in phase space will contribute to the response function, we can linearize the time-dependent difference coordinates and momenta,

$$\begin{aligned}
\Delta\mathbf{q}_{jk}(t) &\approx \mathbf{M}_{\mathbf{qq}}(\bar{\mathbf{z}}_{jk}, t)\cdot\Delta\mathbf{q}_{jk} + \mathbf{M}_{\mathbf{qp}}(\bar{\mathbf{z}}_{jk}, t)\cdot\Delta\mathbf{p}_{jk} \\
\Delta\mathbf{p}_{jk}(t) &\approx \mathbf{M}_{\mathbf{pq}}(\bar{\mathbf{z}}_{jk}, t)\cdot\Delta\mathbf{q}_{jk} + \mathbf{M}_{\mathbf{pp}}(\bar{\mathbf{z}}_{jk}, t)\cdot\Delta\mathbf{p}_{jk}\,.
\end{aligned} \tag{2.20}$$

Within this linearization approximation, the phase ψ_{jk} is also exactly equal to zero. [27,113–117] Linearization of the difference variables in fact leads analytically to the classical limit for the linear response function, as is discussed more fully in Appendix B. We have observed numerically that taking the harmonic or linearized limit for the phase results in the complete loss of quantum recur-

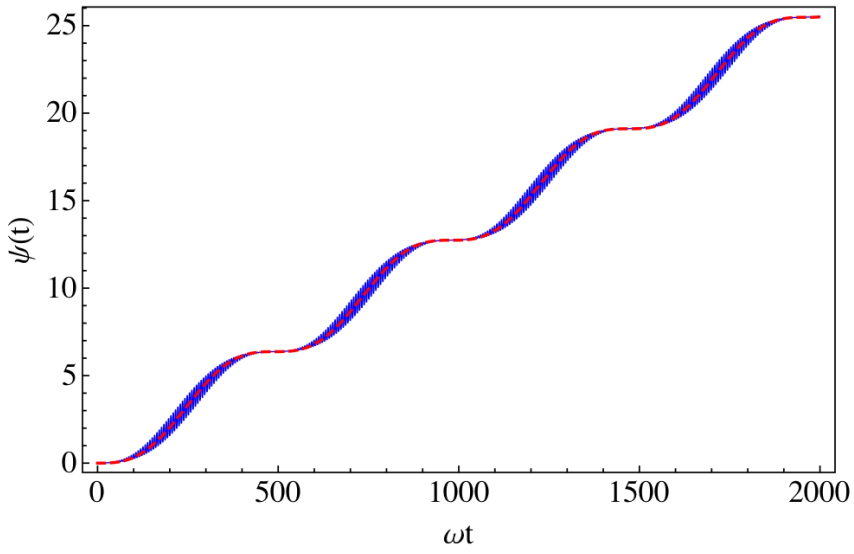

Figure 2.6: The semiclassical phase ψ (blue) and the approximation to the phase in Eq. (2.28) (red, dashed) are plotted for a pair of trajectories propagating in a Morse potential with initial conditions $\bar{E}_{12}/D = \hbar\omega$, $\Delta E_{12}/D = \hbar\omega$, and $\phi_1 = \phi_2 = 0$.

rences. Taking the harmonic approximation for the magnitude of the HK prefactor, $|C(\mathbf{z}, t)| \to 1$, results in the irreversible time decay of the response function, but partial recurrences are observed.

The semiclassical phase ψ_{jk} for a pair of classical trajectories propagating in a one-dimensional Morse oscillator potential is plotted as a function of time in Figure 2.6. This phase displays rapid oscillations superimposed on a slowly varying staircase-like structure with periodic inflection points. These inflection points are points of nearly stationary phase that dominate the integrals in the response calculation. Around each stationary point, the phase ψ_{jk} is approximately a cubic function of time. The overall linear growth of the phase with time is a reflection of the linear growth of the classical action $S(z, t)$ for an anharmonic system. We shall show that the structure of the semiclassical phase can be understood in terms of recurrences in phase space for the propagating pair of

trajectories. When the two trajectories are close in phase space, their phase space separation $\Delta z_{jk}(t)$ will be at a minimum, and the phase will be nearly stationary.

In order to analyze the structure of the semiclassical phase, we first rewrite Eq. (2.9) as an expansion in powers of the time-dependent coordinate difference between the trajectories $\mathbf{z}_j$ and $\mathbf{z}_k$,

$$\hbar\psi_{jk} = \sum_{r=3,5,\ldots} \left(\frac{r-1}{2^{r-1}r!}\right) \int_0^t d\tau \left(\Delta\mathbf{q}_{jk}(\tau) \cdot \nabla_{\bar{\mathbf{q}}_{jk}(\tau)}\right)^r V(\bar{\mathbf{q}}_{jk}(\tau)) \,. \tag{2.21}$$

Here $V(\mathbf{q})$ is the total potential energy. In this discussion, we shall focus on an ensemble of noninteracting, one-dimensional Morse oscillators. However, our general conclusions about the structure of the phase will hold for other one-dimensional anharmonic oscillator systems. The generalization for multiple coupled degrees of freedom is discussed in Section 6.

For the one-dimensional Morse oscillator system, we have found numerically that truncating Eq. (2.21) at the lowest order $r = 3$ term yields an accurate approximation to the response function,

$$\hbar\psi_{jk} \approx \frac{\varepsilon}{12} \int_0^t d\tau \; V^{(3)}(\bar{q}_\tau) \, (\Delta q_\tau)^3 \tag{2.22}$$

$$\approx \frac{\varepsilon}{12} \int_0^t d\tau \left(V^{(3)}(0) + \varepsilon \bar{q}_{jk}(\tau) V^{(4)}(0)\right) \left(\Delta q_{jk}(\tau)\right)^3 \tag{2.23}$$

where ε is a dimensionless anharmonicity parameter. In Eq. (2.23), $V^{(3)}(q)$ has been linearized about $q = 0$. Note that the expansion in Eqs. (2.21) and (2.23) is in some sense an expansion in anharmonicity ε. The $r = 5$ term in Eq. (2.21) and the $V^{(5)}(0)$ term in Eq. (2.23) contribute to order ε^3 and higher terms to the phase.

In order to proceed, we next use classical action-angle perturbation theory as discussed in Appendix A to derive approximate dynamics to order ε for the

coordinate and momentum $q(t)$ and $p(t)$ for an anharmonic oscillator,

$$q(t) = \sqrt{\frac{2J}{m\omega}}\cos\phi(t) + \varepsilon\frac{V^{(3)}(0)J}{\omega^3 m^2}\Big(\cos\left(2\phi(t)\right) - 3\Big)$$
$$p(t) = -\sqrt{2m\omega J}\sin\phi(t) - \varepsilon\frac{4V^{(3)}(0)J}{m\omega^2}\cos\phi(t)\sin\phi(t) \tag{2.24}$$

where J is the classical action variable and ϕ is the angle. [121] In Eq. (2.24), the exact time-dependent coordinate and momentum have been expanded to first order in the anharmonicity ε, and the time dependence of the angle is given by $\phi(t) = \phi + \lambda(J)\omega t$, where $\lambda(J)\omega$ is the exact action-dependent frequency as discussed in Eqs. (A.15) and (A.26) of Appendix A. Note that λ contains all orders in ε, so Eq. (2.24) is not strictly perturbative.

The expressions for the coordinates and momenta in Eq. (2.24) are next inserted into the expression for the phase in Eq. (2.23) and the integrand expanded to second order in the anharmonicity ε. Because the phase shown in Figure 2.6 is dominated by a slow frequency staircase-like structure and a linear time divergence, we shall concentrate on only the slowest frequency components of the phase. To zeroth-order in anharmonicity, the phase ψ_{jk} is equal to zero, as was noted above for a harmonic system. The first-order term (and in fact all odd-order terms) only generate high frequency contributions to the phase. The second-order term, however, contains both a linear time dependence as well as slow frequency contributions,

$$\hbar\psi_{jk} \approx \varepsilon^2\frac{3(2m\omega^2 V^{(4)}(0) - 5V^{(3)}(0))}{2m^3\omega^5}\Big(\bar{J}_{jk}\Delta J_{jk}\omega t$$
$$- \frac{\Delta J_{jk}\sqrt{\bar{J}_{jk}^2 - \Delta J_{jk}^2/4}}{\Delta\lambda_{jk}}\Big(\sin\Delta\phi_{jk}(t) - \sin\Delta\phi_{jk}\Big)\Big) \tag{2.25}$$

with average and difference action-angle variables given by

$$\bar{J}_{jk} \equiv (J_j + J_k)/2, \quad \Delta J_{jk} \equiv J_j - J_k$$
$$\bar{\phi}_{jk} \equiv (\phi_j + \phi_k)/2, \quad \Delta\phi_{jk} \equiv \phi_j - \phi_k. \tag{2.26}$$

For the Morse oscillator system, the third and fourth derivatives of the potential at $\bar{q}_{jk} = 0$ are

$$V^{(3)}(0) = -\frac{m^{3/2}\omega^3}{\sqrt{8D}} \ , \quad V^{(4)}(0) = \frac{7m^2\omega^4}{48D} \ . \tag{2.27}$$

If we further assume that the mean action $\bar{J}_{jk}$ is large compared to the action difference ΔJ_{jk}, the phase can be written simply as

$$\psi_{jk} = \frac{\bar{J}_{jk}}{\hbar}\Big(-\eta_{jk} + \big(\sin\left(\Delta\phi_{jk}(t)\right) - \sin\left(\Delta\phi_{jk}\right)\big)\Big) \tag{2.28}$$

$$\eta_{jk} \equiv \Delta J_{jk}\omega^2 t/2D \tag{2.29}$$

where the time dependence of the difference angle $\Delta\phi(t)$ is given by

$$\Delta\phi_{jk}(t) = \Delta\phi_{jk} + \Delta\lambda_{jk}\omega t = \Delta\phi_{jk} - \eta_{jk} \tag{2.30}$$

and the frequency $\lambda_j\omega$ is defined in Eq. (A.15) of Appendix A. The approximation for the phase in Eq. (2.28) quantitatively reproduces the linear growth and the slow-frequency stationary points that dominate the exact phase. This is shown numerically in Figure 2.6, where the dashed red line is Eq. (2.28) and the solid blue line is the exact phase as discussed previously.

Using Eq. (2.28), the stationary points in the phase are given by

$$\eta_{jk} - \Delta\phi_{jk} = 2\pi k \tag{2.31}$$

for integer k. As η_{jk} is proportional to both time t and the action difference ΔJ_{jk}, the phase will exhibit stationary points in both time for fixed ΔJ_{jk}, and in the difference action for fixed time. Around the kth stationary point, the phase is locally cubic in both $\delta\eta_{jk} \equiv \eta_{jk} - \Delta\phi_{jk} - 2\pi k$ and $\Delta\phi_{jk}$. The phase accumulated between the kth and $(k+1)$th stationary point is proportional to the mean action $\bar{J}_{jk}$ of trajectories z_j and z_k.

2.4 Analysis of the linear response function

In addition to the semiclassical phase, the calculation of the linear response function in Eq. (2.6) requires knowledge of both the coherent state overlaps and the HK prefactors for a propagating pair of trajectories. For a one-dimensional Morse oscillator system, we can use the same approximate dynamics as in Eq. (2.24) to generate an approximation for these factors. The coherent state overlap is given to zeroth-order in ε in the same sense as Eq. (2.24) by

$$\left|\langle z_j|z_k\rangle\langle z_k(t)|z_j(t)\rangle\right| = \exp\left[-\frac{\bar{J}_{jk}}{\hbar}\Big(2 - \cos(\Delta\phi_{jk}(t)) - \cos(\Delta\phi_{jk})\Big)\right] . \tag{2.32}$$

Note that for harmonic systems, Eq. (2.32) is independent of time. For anharmonic systems, peaks in the coherent state overlap correspond to small phase space separations $\Delta z_{jk}^2(t)$. These minima in $\Delta z_{jk}^2(t)$ correspond to times such that $\eta_{jk} = \Delta\phi_{jk} + 2\pi k$ — the stationary condition for the semiclassical phase in Eq. (2.28)!

Similarly, the monodromy matrix elements can be approximated using perturbation theory in action-angle variables, and the product of the HK prefactor for trajectories z_j and z_k is written as

$$C(z_j, t)C^*(z_k, t) = \varepsilon^2\left(\frac{\bar{J}_{jk}\omega^2 t}{2D}\right)e^{i\eta_{jk}/2} . \tag{2.33}$$

The magnitude of the product of two HK prefactors is proportional to both the mean action $\bar{J}_{jk}$ and to time for a one-dimensional anharmonic system. For short times and for purely harmonic systems, the magnitude of $C(z_j, t)$ is unity. Thus, Eq. (2.33) is a long-time approximation. The phase of the prefactor is linear in time and is proportional to the action difference for the trajectory pair. The approximate form for the prefactor in Eq. (2.33) is compared to the exact result in the complex plane as a parametric function of time in Figure 2.7 for a pair of

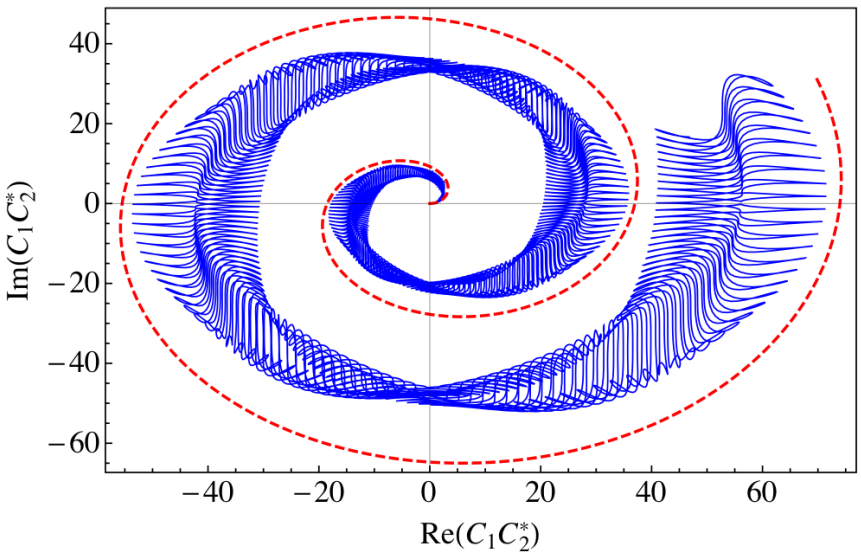

Figure 2.7: The HK prefactor $C(z_1,t)C^*(z_2,t)$ is plotted in the complex plane as a parametric function of time for a pair of trajectories propagating in a Morse potential with initial conditions $\bar{E}_{12}/D = 3\hbar\omega/2$, $\Delta E_{12}/D = \hbar\omega/2$, and $\phi_1 = \phi_2 = 0$. The blue curve is the exact result, while the red, dashed curve is the approximate Eq. (2.33).

trajectories with initial conditions $\bar{E}_{12}/D = 3\hbar\omega/2$, $\Delta E_{12}/D = \hbar\omega/2$, and $\phi_1 = \phi_2 = 0$. While incorrect for short times and lacking the rapid oscillations of the exact prefactor, our approximate form quantitatively captures both the phase and the linear time divergence of the HK prefactor.

The approximate forms for the phase, coherent state overlaps, and HK prefactor in Eqs. (2.28), (2.32), and (2.33) can now be used to approximately compute the linear response function for a one-dimensional anharmonic oscillator. The exponent of $A_{12}(t)$ in Eq. (2.6) can be written as

$$F \equiv \ln\left(\frac{A_{12}(t)}{|C(z_1,t)\,C^*(z_2,t)|}\right) \tag{2.34}$$

$$\approx N_{12}\left(-2 - i\eta_{12} + e^{i\Delta\phi_{12}} + e^{-i(\Delta\phi_{12}-\eta_{12})}\right) + \frac{i}{2}\eta_{12} \tag{2.35}$$

where $N_{12} \equiv \bar{J}_{12}/\hbar$ measures the mean action in units of $\hbar$. The $\frac{i}{2}\eta_{12}$ term in Eq.

(2.35) derives from the phase of the HK prefactors in Eq. (2.33). Next we expand F around each stationary point of the phase in powers of $\delta\eta_{12} \equiv \eta_{12} - (\Delta\phi_{12} + 2\pi k)$ and $\Delta\phi_{12}$. To cubic order in the deviation from a particular stationary point, F becomes

$$\begin{aligned} F_k \approx\ & 2\pi i k\,(N_{12} - 1/2) + \frac{i}{2}(\delta\eta_{12} + \Delta\phi_{12}) \\ & - \frac{N_{12}}{2}(\delta\eta_{12}^2 + \Delta\phi_{12}^2) - i\frac{N_{12}}{6}(\delta\eta_{12}^3 + \Delta\phi_{12}^3)\,. \end{aligned} \tag{2.36}$$

In order to evaluate Eq. (2.6) for $R^{(1)}(t)$, the integral over trajectory differences Δz_{12} can be transformed into action-angle variables with unit Jacobian, $dz_1 dz_2 \to d\bar{z}_{12} d\Delta J_{12} d\Delta\phi_{12}$, and then the integral over action differences can be changed into an integral over η_{12},

$$|C\,(z_1, t)\,C^*\,(z_2, t)|\,d\Delta J_{12} = \hbar N_{12} d\eta_{12}\,. \tag{2.37}$$

It should be emphasized that while $|C\,(z_1, t)\,C^*\,(z_2, t)|$ diverges linearly in t, this time divergence is exactly canceled by the Jacobian for the transformation of ΔJ_{12} to η_{12}. [103] Thus the principal contribution of the magnitude of the HK prefactors to the response function is to cancel a time decay resulting from integration of the semiclassical phase factor over action differences.

We can now use Eqs. (2.36) and (2.37) to integrate $A_{12}(t)$ over difference variables. This integral will be dominated by contributions near each stationary point k in η_{12},

$$\begin{aligned} & \iint \frac{d\Delta J_{12} d\Delta\phi_{12}}{(2\pi\hbar)}\,|C\,(z_1, t)\,C^*\,(z_2, t)|\,e^F \\ & \quad = \sum_k e^{2\pi i k(N_{12} - 1/2)} \iint \frac{d\delta\eta_{12} d\Delta\phi_{12}}{(2\pi\hbar)} e^{\frac{i}{2}(\delta\eta_{12} + \Delta\phi_{12}) - \frac{N_{12}}{2}(\delta\eta_{12}^2 + \Delta\phi_{12}^2) - i\frac{N_{12}}{6}(\delta\eta_{12}^3 + \Delta\phi_{12}^3)} \\ & \quad = G(N_{12})\,\sigma_{1/2}(N_{12}) \end{aligned} \tag{2.38}$$

where $\sigma_{1/2}(N_{12})$ is given in the long time limit by

$$\sigma_{1/2}(N_{12}) \equiv \sum_{k=-\infty}^{\infty} e^{2\pi i k(N_{12}-1/2)} = \sum_{n=-\infty}^{\infty} \delta\left(N_{12} - 1/2 - n\right) \ . \tag{2.39}$$

In Eq. (2.38), $G(N_{12})$ is a slowly varying function of the mean action, and for $N_{12} \geq 1$, G is of order unity. We therefore set $G = 1$. The factor $\sigma_{1/2}(N_{12})$ is composed of a contribution from each stationary point in η_{12}, and in the long time limit, there will be a large number of stationary points. The effect of $\sigma_{1/2}$ is to quantize the mean actions N_{12} at half-integer values $n + 1/2$. The $1/2$ in Eq. (2.39) comes directly from the phase of the HK prefactor. For intermediate times, $\sigma_{1/2}$ is composed of a sum of only a few terms, and the quantization condition on N_{12} in Eq. (2.39) will be relaxed. At very short times, only a single stationary point is accessible, resulting in a classical distribution for the actions. This is consistent with the agreement between classical and quantum response functions for short times.

In addition to $A_{12}(t)$, the linear response function in Eq. (2.6) also depends on the complex coordinate and momentum of the vibrational mode, P_{12} and $Q_{12}^*(t)$. As is shown below, these additional terms result in an integer, rather than a half-integer, quantization of the mean action N_{12}. The complex coordinate and momentum are approximated by

$$Q_{12} = \bar{q}_{12} - i\frac{1}{2m\omega}\Delta p_{12} \approx q_{12}\, e^{i\Delta\phi_{12}} \tag{2.40}$$

$$P_{12} = \bar{p}_{12} + i\frac{m\omega}{2}\Delta q_{12} \approx p_{12}\, e^{i\Delta\phi_{12}} \tag{2.41}$$

where the phase space variables q_{12} and p_{12} are distinct from the mean phase space variables of trajectories z_1 and z_2, but to zeroth-order in anharmonicity are related by $\bar{q}_{12} \approx q_{12}\cos\Delta\phi_{12}$ and $\bar{p}_{12} \approx p_{12}\cos\Delta\phi_{12}$. Inserting the stationary phase

condition from Eq. (2.31) into Eqs. (2.40) and (2.41) yields

$$P_{12}\, Q^*_{12}(t) \approx p_{12}\, q_{12}(t)\, e^{i\pi k}\, e^{i(\Delta\phi_{12} - \delta\eta_{12})/2} \,. \tag{2.42}$$

The exponent of Eq. (2.42) contains a factor of $i\pi k$. With this extra k dependence inserted into Eq. (2.36), the integral over difference variables in Eq. (2.38) generates an integer, rather than a half-integer, quantization condition on the mean action N_{12},

$$\sigma_1(N_{12}) \equiv \sum_{n=-\infty}^{\infty} \delta\left(N_{12} - n\right) \,. \tag{2.43}$$

The full integral over difference variables for $R^{(1)}(t)$ then is given by

$$\iint \frac{d\Delta J_{12} d\Delta\phi_{12}}{2\pi\hbar}\, A_{12}(t)\, P_{12}\, Q^*_{12}(t) = p_{12}\, q_{12}(t)\, \sigma_1(N_{12}) \,, \tag{2.44}$$

where we have again set $G = 1$. This results in a simple final form for the semiclassical linear response function,

$$R^{(1)}_{MT}(t) = \frac{\beta}{m} \iint dz\; p(0)\, q(t)\, \sigma_1(N)\, f_{cl}(z) \,. \tag{2.45}$$

We refer to Eq. (2.45) as the mean-trajectory (MT) approximation to the linear response function because the calculation of $R^{(1)}_{MT}(t)$ only requires the phase space integration over a single propagating classical trajectory. [47,103] The initial conditions for the trajectories are chosen to have integer-quantized classical actions N and are weighted according to a classical Boltzmann distribution. Note that Eq. (2.45) is structurally very similar to the classical linear response function defined in Eq. (1.35). The action quantization condition $\sigma_1(N)$ however results in a quasiclassical [42, 122, 123] expression for the response.

We can evaluate Eq. (2.45) analytically by approximating $p(0)$ and $q(t)$ as having harmonic dynamics with an anharmonic frequency $\lambda(J)$. If we also make

a harmonic approximation to the classical distribution, $f_{cl}(z) \approx (\beta\omega/2\pi)\exp(-\beta E)$, the mean trajectory response function is given by

$$\begin{aligned} R^{(1)}_{MT}(t) &\approx \frac{\beta^2\omega}{2\pi m}\sum_{n=1}^{\infty}\int dN\delta(N-n)e^{-\beta E(N)}\int\frac{d\phi}{2\pi}p(0)q(t) \\ &\approx \frac{\beta^2\omega\hbar}{2\pi m}\sum_{n=1}^{\infty} n\, e^{-\beta E_n}\sin\left(\lambda_n\omega t\right). \end{aligned} \tag{2.46}$$

Evaluating the sum over n in Eq. (2.46) results in an approximation for the linear response function that has the same time dependence as the approximation to the quantum linear response function in Eq. (1.38). The two expressions differ slightly in the static normalization factors but agree to order $(\beta\hbar\omega)^2$. This discrepancy is due to the normalization of the classical distribution function $f_{cl}(z)$, followed by quantization of the action variables.

The quantization of mean action condition in Eq. (2.45) is simply the Bohr-Sommerfeld semiclassical quantization condition for a one-dimensional anharmonic system without the usual Maslov factor of 1/2. [53] As was shown above, the additional phase of the complex coordinate and momentum cancel the half-integer quantization that results when the phase of the HK prefactor is taken into account. This quantization condition generates the exact quantum energy eigenvalues for harmonic and Morse oscillator systems, but it is not exact in general. For a quartic oscillator, the action is proportional to the 3/4 power of the energy, $J \propto E^{3/4}$. The quantized values for the energy in the mean trajectory approximation thus scale as $n^{4/3}$. While this is correct for large n, the Bohr-Sommerfeld quantization condition is incorrect near the bottom of the quartic well. This discrepancy results in the frequency shift noted in the HK calculation of the linear response for a quartic oscillator in Figure 2.4. For a harmonic oscillator with a quartic perturbation, as in Figure 2.3, the quantization of the action is nearly correct for small n, and the semiclassical response function is

more accurate.

2.5 Time-dependent quantization and the classical limit

In this section we wish to analyze which classical trajectory pairs are most important for the calculation of the HK linear response function, as well as how quantization of action occurs as a function of time. As was noted earlier, we expect that a trajectory pair will contribute to the linear response function in Eq. (2.6) primarily when the pair of trajectories is close in phase space, $\Delta z_{12}^2(t) \approx 0$. The magnitude of the coherent state overlap at the initial time, $|\langle z_1|z_2\rangle|$, constrains a pair of trajectories to start relatively close in phase space, which for fixed values of the actions, implies $\Delta\phi_{12} \approx 0$. We have observed numerically that the complete omission of the magnitude of the coherent state overlaps in Eq. (2.6), $|\langle z_1|z_2\rangle\langle z_2(t)|z_1(t)\rangle| \to 1$, still results in a qualitatively correct response function. This in turn suggests that the stationary points in the semiclassical phase $\psi_{12}(t)$ are sufficient to enforce quantization of action and the convergence of the integral over difference variables.

The trajectory energies that contribute to the linear response function at time t can be determined numerically by examining the density $r(\bar{\epsilon}, \Delta\epsilon; t)$, defined as

$$r(\bar{\epsilon}, \Delta\epsilon; t) \equiv \left| \frac{\beta}{m} \iint \frac{dz_1 dz_2}{2\pi\hbar}\, f_{cl}(\bar{z}_{12})\, P_{12}\, Q_{12}^*(t)\, e^{-(\Delta z_i^2 + \Delta z^2)/2} e^{i\psi_{12}} \right.$$
$$\left. \times\, \delta(\bar{E}_{12} - \bar{\epsilon})\delta(\Delta E_{12} - \Delta\epsilon) \right| . \tag{2.47}$$

The integrand in Eq. (2.47) differs from the full linear response function in Eq. (2.6) due to the omission of the HK prefactors $C(z_1, t)C^*(z_2, t)$. With the prefactors, the density Eq. (2.47) would represent the magnitude of the contribution

to the response function from all pairs of trajectories with fixed mean and difference energies $\bar{\epsilon}$ and $\Delta\epsilon$. The HK prefactors have been omitted because their linear time divergence partially obscures the time dependence in $r(\bar{\epsilon}, \Delta\epsilon; t)$.

The density $r(\bar{\epsilon}, \Delta\epsilon; t)$ is plotted in Figure 2.8 as a function of $\Delta\epsilon$ and t for a one-dimensional Morse oscillator with the same parameters as in the top panel of Figure 2.2. The mean energy is fixed at $\bar{\epsilon} = 3/2\hbar\omega$, but varying $\bar{\epsilon}$ has no qualitative effect on the structure of $r(\bar{\epsilon}, \Delta\epsilon; t)$. Lighter regions in Figure 2.8 indicate larger magnitudes of the density. For fixed time t, the large density region around $\Delta\epsilon = 0$ is due to the stationary point in the phase with $k = 0$ in Eq. (2.31). A pair of trajectories that starts very close in phase space will remain close in phase space for intermediate times and will thus contribute constructively towards the linear response function. The high density regions centered at nonzero $\Delta\epsilon$ for time t correspond to pairs of trajectories at the $k = \pm 1, \pm 2, \cdots$ stationary points. Note that for nearly harmonic systems, the energy difference $\Delta\epsilon$ is approximately proportional to an action difference ΔJ. The value of $\Delta\epsilon$ that corresponds to each type of stationary point, e.g. $k = 2$, falls off as t^{-1}. Note that for very short times, a wide range of energy differences contribute to the $k = 0$ classical term of the response function. Figure 2.8 demonstrates graphically that for a given time, there is no one pair of trajectories that dominates the response function. Rather, we must integrate over a range of action differences, as well as integrate over all possible angle differences, in order to obtain the correct semiclassical linear response.

As discussed in Section 4, integration of the semiclassical phase over difference variables ΔJ_{12} and $\Delta\phi_{12}$ results in the quantization of the mean action N_{12}. As this quantization requires integrating over an infinite number of stationary

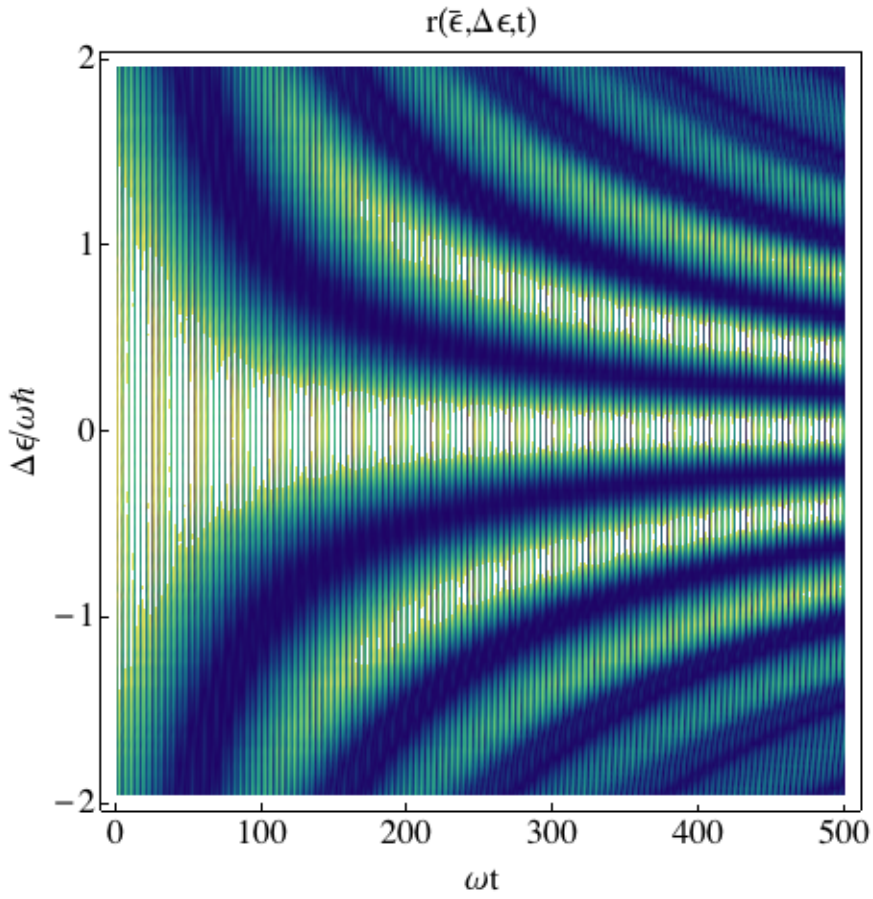

Figure 2.8: The density $r(\bar{\epsilon}, \Delta\epsilon; t)$ shows the contribution to the linear response function from a pair of trajectories with fixed mean energy $\bar{\epsilon} = 3\hbar\omega/2$ as a function of the energy difference $\Delta\epsilon$ and of time for a one-dimensional Morse oscillator. Light regions correspond to a large absolute magnitude.

points, it is a long time approximation. For short times, summing over a finite number of stationary points will result in only a partial quantization condition on the mean action. This time-dependent quantization can be investigated numerically with the density of mean energy $f_{HK}(\bar{\epsilon}, t)$, defined as

$$f_{HK}(\bar{\epsilon}, t) \equiv \frac{1}{t}\int_0^t d\tau \left| \frac{\beta}{m} \iint \frac{dz_1 dz_2}{2\pi\hbar}\, f_{cl}(\bar{z}_{12}) P_{12}\, Q_{12}^*(\tau)\, A_{12}(\tau) \delta(\bar{E}_{12} - \bar{\epsilon}) \right| . \qquad (2.48)$$

For nearly harmonic systems, both P_{12} and Q_{12} scale as $\bar{E}_{12}^{1/2}$, and so we expect $f_{HK}(\bar{\epsilon}, t)$ to look like $\bar{\epsilon}\, e^{-\beta\bar{\epsilon}}$ superimposed with peaks in the mean energy (action)

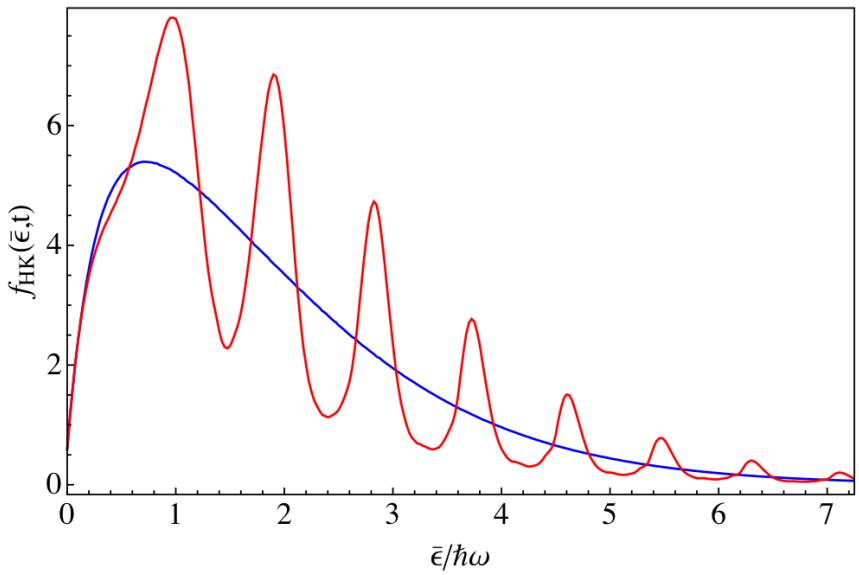

Figure 2.9: The density $f_{HK}(\bar{\epsilon}, t)$ shows the contribution to the linear response function from trajectory pairs as a function of mean energy $\bar{\epsilon}$ for fixed times $\omega t = 10$ (blue) and $\omega t = 200$ (red).

that get sharper as time progresses. This is observed numerically in Figure 2.9 for a one-dimensional Morse oscillator with the same parameters as in Figure 2.8. For short times, as for $\omega t = 10$ (blue curve), the mean energy density is simply the classical result. As only the $k = 0$ stationary point is accessible, there are no peaks in the mean energy distribution. For intermediate times as for $\omega t = 200$ (red curve), several stationary points are possible, and the mean energy is peaked.

Rather than integrate over an infinite number of stationary points in Eq. (2.39), the quantization condition on the mean action can also be written in terms of a finite sum,

$$\sigma_1(N; k_{max}) = 1 + 2\sum_{k=1}^{k_{max}} \cos(2\pi k N) \tag{2.49}$$

where k_{max} in general increases as time progresses. The response function for a

finite k_{max} is then given by

$$R^{(1)}_{MT}(t; k_{max}) = \frac{\beta}{m} \iint dz\; p(0)\; q(t)\; \sigma_1(N; k_{max})\; f_{cl}(z)\; . \tag{2.50}$$

The classical limit is easily extracted from Eq. (2.50) by taking $k_{max} = 0$ and thus $\sigma_1(N; 0) = 1$. The only trajectory pairs that contribute in the classical limit at time t are those for which $\Delta z_{12}(t)$ is still near its initial minimum value. While all trajectory pairs satisfy this condition as $t \to 0$, for long times only trajectory pairs that start very close in phase space will still be near the $k = 0$ stationary point in the phase. This is consistent with the linearization scheme which was used by Noid, et.al. [27] to derive the classical limit for the linear response function within the HK approximation.

As the index k in Eq. (2.50) labels temporal recurrences for a pair of trajectories, we can systematically improve the linear response function for longer times by increasing k_{max}. While an infinite sum over k results in exact mean action quantization, a finite sum is sufficient to calculate an accurate response function for finite time. If our one-dimensional anharmonic oscillator were coupled to an off-resonance bath as in a condensed phase system, the linear response function would decay to zero on a finite time scale due to dephasing. In this case, truncating the sum in Eq. (2.50) may result in an accurate response function.

It should be noted that for harmonic systems, the manipulations which led to integration over stationary points in the semiclassical phase and the subsequent quantization of the mean action are qualitatively incorrect. For a harmonic oscillator, the phase $\psi_{12}(t) = 0$; there are no stationary points. This is because the frequency for a trajectory is independent of action. As a result, the phase space separation $\Delta z^2_{12}(t)$ is a constant (for harmonic $\gamma = m\omega/\hbar$), and trajectory pairs do not have temporal recurrences. Thus, the mean action N_{12} in the response func-

tion is not quantized on any time scale for harmonic systems, and the integral of $A_{12}(t)$ over difference variables is simply a constant. However, as must be the case, it can be shown that the response function within the HK approximation is exact for harmonic systems. [27]

2.6 Linear response for coupled oscillator systems

In this section we will simplify the HK linear response function as was done previously in Sections 3 and 4, but now for a thermal ensemble of coupled anharmonic and harmonic oscillators. One anharmonic mode labeled a couples directly to the radiation, and other modes labeled $b, c, \cdots$ are taken to be bilinearly coupled to mode a and to each other with coupling constants $c_{\alpha\beta}$,

$$H = \sum_{\alpha} H_{\alpha} + \sum_{\alpha>\beta} c_{\alpha\beta} \left(\frac{\omega_{\alpha}\omega_{\beta}}{2} \right) \sqrt{m_{\alpha} m_{\beta}}\, q_{\alpha} q_{\beta} \tag{2.51}$$

$$H_{\alpha} \equiv \frac{p_{\alpha}^2}{2m_{\alpha}} + V_{\alpha}(q_{\alpha}) \,. \tag{2.52}$$

In Eq. (2.52), V_{α} is the potential for mode α, and m_{α} and ω_{α} are the mass and frequency of mode α. We shall typically take V_a to be a Morse potential with dissociation energy D_a. The linear response function within the Herman-Kluk approximation was calculated for this model, as shown previously in Figure 2.5.

In order to analyze the structure of the semiclassical linear response function, we require approximate dynamics for $q_{\alpha}(t)$ and $p_{\alpha}(t)$. We first transform Eq. (2.51) from local modes $\mathbf{q}$ to normal modes $\mathbf{x}$ that would be uncoupled for harmonic V_{α},

$$q_{\alpha} = \sum_{\beta} \kappa_{\alpha\beta} x_{\beta} \,. \tag{2.53}$$

With anharmonicity, the Hamiltonian contains cubic and higher order coupling terms in the normal mode coordinates,

$$H = \sum_{\alpha} h_\alpha + \varepsilon V_3 + \varepsilon^2 V_4 + \cdots \tag{2.54}$$

$$h_\alpha \equiv \frac{\pi_\alpha^2}{2\mu_\alpha} + \frac{\Omega_\alpha^2 \mu_\alpha}{2} x_\alpha^2 \tag{2.55}$$

where V_n contains all terms that are nth order in $\mathbf{x}$, μ_α and Ω_α are the mass and frequency of normal mode α, π_α is the momentum of mode α, and ε is the dimensionless anharmonicity as discussed previously. For two coupled oscillators a and b, the cubic anharmonicity parameters γ are defined as

$$V_3 = \gamma_a x_a^3 + \gamma_{ab} x_a^2 x_b + \gamma_{ba} x_a x_b^2 + \gamma_b x_b^3 \,. \tag{2.56}$$

For general coupled anharmonic systems, the dynamics of $x_\alpha(t)$ are quite complicated. For multiple coupled anharmonic oscillators, there are often regions of phase space where the dynamics are chaotic (ergodic). These chaotic regions typically become more prevalent at high energies. [124, 125] For small enough energies and anharmonicities, however, the dynamics of $x_\alpha(t)$ may be quasiperiodic (or in rare cases, periodic). [126, 127] In both periodic and quasiperiodic f-dimensional systems, the dynamics are characterized by f action and angle variables. For regions of phase space away from resonances, the true action variables can be described as perturbations from the actions for uncoupled oscillators. Methods other than perturbation theory must be employed to find the action variables when low-order resonances exist. [128, 129]

Using action-angle perturbation theory as discussed in Appendix A, $x_\alpha(t)$ is given to first order in anharmonicity by

$$\begin{aligned} x_\alpha &= \xi_{10,\alpha} \cos(\phi_\alpha) + \varepsilon \left[\xi_{00,\alpha} + \xi_{20,\alpha} \cos(2\phi_\alpha) \right. \\ &+ \left. \xi_{02,\alpha} \cos(2\phi_\beta) + \xi_{11,\alpha} \cos(\phi_\alpha + \phi_\beta) + \xi_{1-1,\alpha} \cos(\phi_\alpha - \phi_\beta) \right] \end{aligned} \tag{2.57}$$

where the $\xi_{ij,\alpha}$ are the Fourier coefficients, and the angle ϕ_α and action J_α are the good angle and action for the coupled system. Eq. (2.57) is a generalization of $q(t)$ for a one-dimensional anharmonic system, Eq. (2.24). For non-degenerate oscillators, the anharmonicity parameters γ_a and γ_b in Eq. (2.56) determine the slowest frequency components of the phase ψ_{jk}, while the coupling parameters γ_{ab} and γ_{ba} only contribute to rapid oscillations in the phase. We therefore make an "independent oscillator approximation" to Eq. (2.57) and set $\gamma_{ab} = \gamma_{ba} = 0$. Within this independent oscillator approximation, a normal mode coordinate is given in first order in anharmonicity by

$$x_\alpha = \sqrt{\frac{2J_\alpha}{\Omega_\alpha \mu_\alpha}} \cos(\phi_\alpha) + \varepsilon \frac{\gamma_\alpha J_\alpha}{\Omega_\alpha^3 \mu_\alpha^2} \Big(\cos(2\phi_\alpha) - 3 \Big) . \tag{2.58}$$

This expression has the form of Eq. (2.24) for one degree of freedom, except J_α and ϕ_α are the action and angle for the fully coupled system.

Using these approximate dynamics, we can express the semiclassical phase, coherent state overlaps, and HK prefactor as was done for a one-dimensional anharmonic system,

$$\hbar \psi_{jk} = \sum_\alpha \bar{J}_{\alpha,jk} \Big(-\eta_{\alpha,jk} + \big(\sin(\Delta\phi_{\alpha,jk}(t)) - \sin(\Delta\phi_{\alpha,jk}) \big) \Big) \tag{2.59}$$

$$\Big| \langle \mathbf{z}_j | \mathbf{z}_k \rangle \langle \mathbf{z}_k(t) | \mathbf{z}_j(t) \rangle \Big| = \prod_\alpha \exp \left[-\frac{\bar{J}_{\alpha,jk}}{\hbar} \Big(2 - \cos(\Delta\phi_{\alpha,jk}(t)) - \cos(\Delta\phi_{\alpha,jk}) \Big) \right] \tag{2.60}$$

$$C(\mathbf{z}_j, t) C^*(\mathbf{z}_k, t) = \prod_\alpha \left(\frac{\bar{J}_{\alpha,jk} \Omega_\alpha^2 t}{2 D_\alpha} \right) e^{i\eta_{\alpha,jk}/2} \tag{2.61}$$

$$\eta_{\alpha,jk} \equiv \Delta J_{\alpha,jk} \Omega_\alpha^2 t / 2 D_\alpha \, . \tag{2.62}$$

In Figure 2.10(a), the two terms in Eq. (2.59) that constitute the phase for a pair of bilinearly coupled Morse oscillators a and b are separately plotted. Each curve has stationary points at $\eta_{\alpha,jk} = \Delta\phi_{\alpha,jk} + 2\pi k_\alpha$ for integer k_α. The sum of these terms is shown in Figure 2.10(b) as the red, dashed curve. The exact HK phase for the

same initial conditions is shown as the solid blue curve. Our approximate form for the phase in Eq. (2.59) quantitatively reproduces the significant features of the exact phase, as was demonstrated previously for a one-dimensional anharmonic system. As was discussed before, the stationary points in the phase for coupled oscillators occur at times when the phase space separation of the propagating pair of trajectories is at a minimum. In Figure 2.10(c), the approximate coherent state overlap, Eq. (2.60), is plotted against the exact HK coherent state overlap for the same pair of trajectories as in panel (a). The approximate form once again captures the slow-frequency structure of the coherent state overlaps, and maxima in the overlap correspond to stationary points in the phase.

For f coupled oscillators, Eq. (2.61) indicates that the HK prefactor scales as t^f for quasiperiodic dynamics. For chaotic trajectories [37–39] the monodromy matrix, and hence the HK prefactor, diverges exponentially. We do not consider this ergodic regime here. For nonchaotic regions of phase space, Eq. (2.61) quantitatively matches the divergence and phase of the exact prefactor for long times. This is shown in Figure 2.10(d), where the magnitude of the exact HK prefactor is plotted against the approximate prefactor in Eq. (2.61) for the same pair of trajectories as in panels (a)–(c). As for the one-dimensional case, the rapid oscillations in the prefactor contribute little to the final response function. It should also be noted that Eq. (2.33) is not valid as $t \to 0$. For harmonic systems or at short time for anharmonic ones, the HK prefactor has a value of unity. Thus the square of the magnitude of the prefactor for a coupled non-chaotic system of f_a anharmonic oscillators and f_b harmonic oscillators will start out at one and then increase as t^{f_a} for intermediate times. If we introduce a very small anharmonicity into the f_b harmonic modes, the magnitude of the HK prefactor will eventually cross over from t^{f_a} to $t^{f_a+f_b}$ growth at long times.

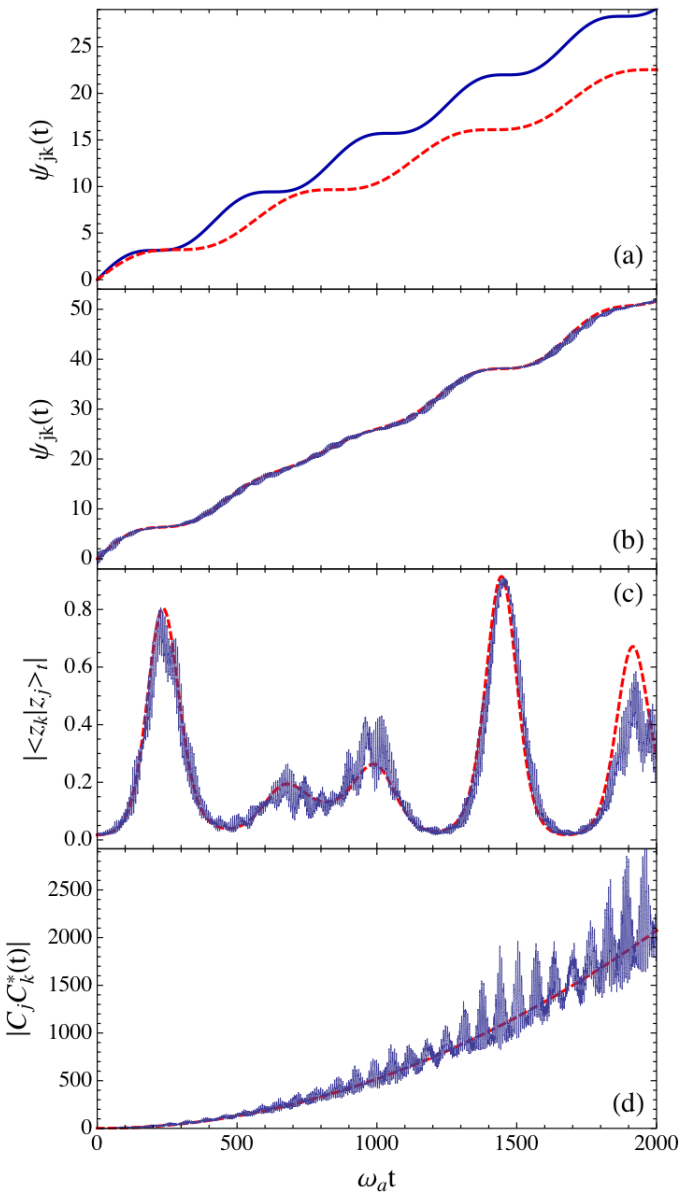

Figure 2.10: The semiclassical phase, coherent state overlap, and HK prefactors are shown for two coupled Morse oscillators with $\hbar\omega_a/D_a = 0.05$, $D_a = D_b$, $m_a = m_b$, $\omega_b = 0.9\omega_a$, and $c_{ab} = 0.1$. The pair of propagating trajectories $\{\mathbf{z}_j, \mathbf{z}_k\}$ have action and angle variables given by $J_{a,j} = 0.7\hbar$, $J_{b,j} = 0.75\hbar$, $J_{a,k} = J_{b,k} = 1.3\hbar$, $\phi_{a,j} = \phi_{b,j} = 0$, and $\phi_{a,k} = \phi_{b,k} = \pi$. Panel (a) shows the terms $\alpha = a$ (blue, solid) and $\alpha = b$ (red, dashed) for the phase ψ_{jk} in Eq. (2.59). Panel (b) shows the total phase ψ_{jk}, while panel (c) depicts the magnitude of the coherent state overlap, and panel (d) displays the magnitude of the HK prefactors. In panels (b)-(d), the blue, solid curve indicates the exact result, while the red, dashed curve is the independent oscillator result.

Using the approximate dynamics for the coupled oscillator system in Eqs. (2.59)–(2.61), we can now calculate the linear response function by analytically integrating over difference variables $\Delta\mathbf{J}_{12}$ and $\Delta\phi_{12}$. The computation is quite similar to the one-dimensional case, so only the important differences shall be emphasized. As before, $A_{12}(t)$ from Eq. (2.6) is given within our independent oscillator approximation by

$$F \equiv \ln\left(\frac{A_{12}(t)}{|C(\mathbf{z}_1,t)\,C^*(\mathbf{z}_2,t)|}\right) = \sum_\alpha F_\alpha \tag{2.63}$$

$$F_\alpha = N_{\alpha,12}\left(-2 - i\eta_{\alpha,12} + e^{i\Delta\phi_{\alpha,12}} + e^{-i(\Delta\phi_{\alpha,12}-\eta_{\alpha,12})}\right) + \frac{i}{2}\eta_{\alpha,12} \tag{2.64}$$

where $N_{\alpha,12} \equiv \bar{J}_{\alpha,12}/\hbar$ measures the mean action of mode α in units of $\hbar$. The magnitude of the HK prefactor again serves to cancel a time decay due to the $d\Delta\mathbf{J}_{12} \to d\boldsymbol{\eta}_{12}$ Jacobian, and the integral of $A_{12}(t)$ over difference variables generates as before a half-integer quantization condition on each mean action variable $N_{\alpha,12}$,

$$\iint \frac{d\Delta\mathbf{J}_{12}d\Delta\phi_{12}}{(2\pi\hbar)^f}\,|C(\mathbf{z}_1,t)\,C^*(\mathbf{z}_2,t)|\,e^F = G(\mathbf{N}_{12})\prod_\alpha \sigma_{1/2}(N_{\alpha,12})\,. \tag{2.65}$$

For $N_{\alpha,12} \geq 1$, G is a slowly varying function of action that approaches a value of unity. As with the one-dimensional anharmonic system, we therefore set $G = 1$.

The complex coordinate and momentum for the chromophore local mode a also contribute $\Delta\mathbf{J}_{12}$ and $\Delta\phi_{12}$ dependence to the integrand of the linear response function. These additional terms result in integer quantization for one normal mode action, while all other normal mode actions remain half-integer quantized. This should be contrasted to the one-dimensional case, where the mean action N_{12} had integer values only. To complete the calculation, we expand the

complex phase space variables in normal mode coordinates,

$$P_{a,12}Q^*_{a,12}(t) = \sum_{\alpha,\beta} \kappa_{a\alpha}\kappa_{a\beta}\Pi_{\alpha,12}X^*_{\beta,12}(t) \tag{2.66}$$

where the complex normal mode coordinate and momentum $X_{\alpha,12}$ and $\Pi_{\alpha,12}$ are given by

$$X_{\alpha,12} \equiv \bar{x}_{\alpha,12} - \frac{i}{2\mu_\alpha\Omega_\alpha}\Delta\pi_{\alpha,12} \approx x_{\alpha,12}e^{i\Delta\phi_{\alpha,12}} \tag{2.67}$$

$$\Pi_{\alpha,12} \equiv \bar{\pi}_{\alpha,12} + \frac{i\mu_\alpha\Omega_\alpha}{2}\Delta x_{\alpha,12} \approx \pi_{\alpha,12}e^{i\Delta\phi_{\alpha,12}} \, . \tag{2.68}$$

As before, the phase space variables $x_{\alpha,12}$ and $\pi_{\alpha,12}$ are distinct from the mean phase space variables $\bar{x}_{\alpha,12}$ and $\bar{\pi}_{\alpha,12}$. Inserting the stationary phase condition $\eta_{\alpha,12} = \Delta\phi_{\alpha,12} + 2\pi k_\alpha$ into Eqs. (2.67) and (2.68) yields

$$\Pi_{\alpha,12}X^*_{\beta,12}(t) \approx \pi_{\alpha,12}\, x_{\beta,12}(t)\, e^{i\pi k_\beta} e^{i(\Delta\phi_{\alpha,12} - \delta\eta_{\beta,12})/2} \, . \tag{2.69}$$

The exponent in Eq. (2.69) contains an additional term $i\pi k_\beta$ that when inserted into Eq. (2.65) results in the integer quantization of the action for mode β. All other normal mode actions remain half-integer quantized.

The linear response function can thus be decomposed into a sum of contributions from pairs of normal modes,

$$R^{(1)}_{MT}(t) \;\; = \;\; \sum_{\alpha,\beta} \kappa_{a\alpha}\kappa_{a\beta}\, R^{(1)}_{\beta\alpha}(t) \tag{2.70}$$

with each component given by

$$R^{(1)}_{\beta\alpha}(t) = \frac{1}{m_a k_B T} \int d\mathbf{z} f_{cl}(\mathbf{z})\, \pi_\alpha(0)\, x_\beta(t)\, \sigma_1(N_\beta) \prod_{\gamma\neq\beta} \sigma_{1/2}(N_\gamma) \, . \tag{2.71}$$

The semiclassical mean trajectory linear response function in Eq. (2.70) generalizes the mean trajectory treatment for the linear response presented in Eq. (2.45). In the uncoupled limit, $\kappa_{a\gamma} = 0$ for $a \neq \gamma$. Thus, only $R^{(1)}_{aa}(t)$ contributes to the response, and the action for the chromophore mode a is integer quantized.

2.7 Numerical results

The mean-trajectory approximation to the linear response function in Eqs. (2.46) and (2.70) is numerically simpler to implement compared to the Herman-Kluk response function in Eq. (2.6). The HK response for f degrees of freedom requires $2f$ phase space integrals over a rapidly oscillating, diverging integrand. By approximately performing the integrals over difference variables, the mean trajectory result requires only f phase space integrals. Furthermore, the mean trajectory integrand in Eq. (2.70) no longer has an oscillatory phase factor, and the computation of the classical monodromy matrix elements is unnecessary. Consequently, numerical computation of the mean trajectory linear response function is several orders of magnitude faster than HK calculations. This numeric savings grows for coupled oscillator systems, as well as for the nonlinear response, as shall be discussed in Chapter 3.

In order to implement the mean trajectory method, the relations between the good action and angle variables for the system of interest and the corresponding coordinates and momenta must be computed. For the harmonic, Morse, and quartic oscillator systems, these relations are known analytically. [130, 131] For general Hamiltonians, classical action-angle perturbation theory may be used, as discussed in Appendix A. For the coupled oscillator calculations presented below, perturbation theory to second order in the anharmonic coupling was used to find initial coordinates and momenta. For weakly coupled, nonresonant systems, the action J_α can also be accurately approximated by

$$\langle E_\alpha(t) \rangle = J_\alpha \Omega_\alpha + O(\varepsilon^2) \tag{2.72}$$

where $\langle E_\alpha(t) \rangle$ is the time average of the energy of normal mode α, defined as

$$E_\alpha(t) \equiv \frac{\pi_\alpha^2}{2\mu_\alpha} + \frac{\mu_\alpha \Omega_\alpha^2}{2} x_\alpha^2 + \varepsilon \gamma_\alpha x_\alpha^3(t) + \cdots . \tag{2.73}$$

For nonzero anharmonic coupling, $E_\alpha(t)$ varies in time as energy is transferred among oscillator modes, but its time average is roughly proportional to the action of oscillator α. This condition can be used to check the action quantization for a classical trajectory. In our calculations, trajectories with time-averaged energies that were not correctly quantized after propagation were discarded.

As a test of the mean trajectory method, the quantum and mean trajectory response functions for a thermal ensemble of uncoupled Morse oscillators are compared in Figure 2.11 for the same parameters as the top panel of Figure 2.2. The mean trajectory response function is quantitatively correct on all time scales of interest, as well as for a wide range of parameters. Even though the exact quantization of mean action in Eq. (2.38) is a long time approximation, the resulting response function is correct even for short times. Also note that even though the manipulations which led to the mean trajectory result are qualitatively incorrect for a purely harmonic system, the application of Eq. (2.70) to a harmonic system is quantitatively correct.

The effect of finite k_{max} in Eq. (2.50) is shown in Figure 2.12 for an ensemble of uncoupled Morse oscillators with the same parameters as in Figure 2.11. The $k_{max} = 0$ classical limit is given by the red, dotted curve. As expected, it decays to zero without any quantum recurrences. When $k_{max} = 1$ (green, dashed curve), the first quantum recurrence is qualitatively recovered, but then the response decays to zero for longer times. For $k_{max} = 2$, the second recurrence is also recovered. When $k_{max} \to \infty$, the mean trajectory result in Figure 2.11 is recovered.

In Figure 2.13 we compute the mean trajectory linear response functions for

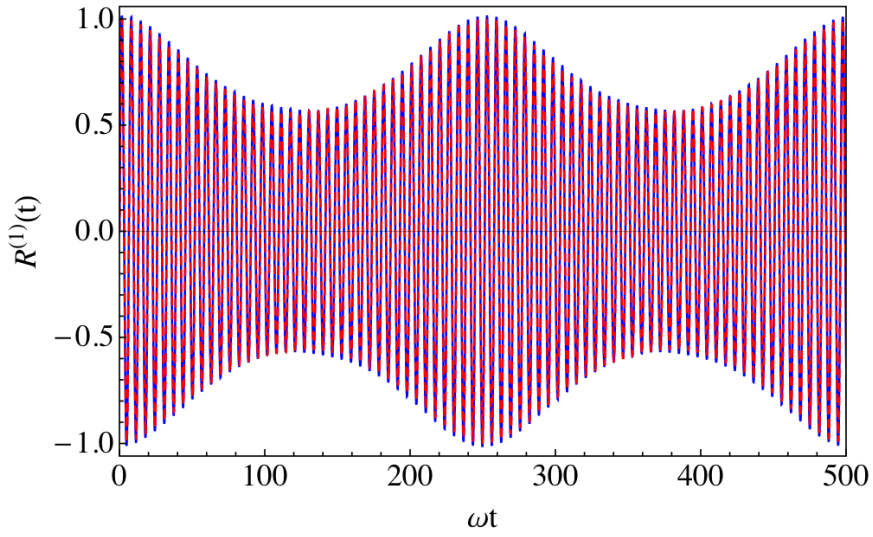

Figure 2.11: The quantum (blue) and semiclassical mean trajectory (red, dashed) linear response functions are plotted for an ensemble of uncoupled Morse oscillators with parameters $\beta D = 40$ and $\beta\hbar\omega = 2$.

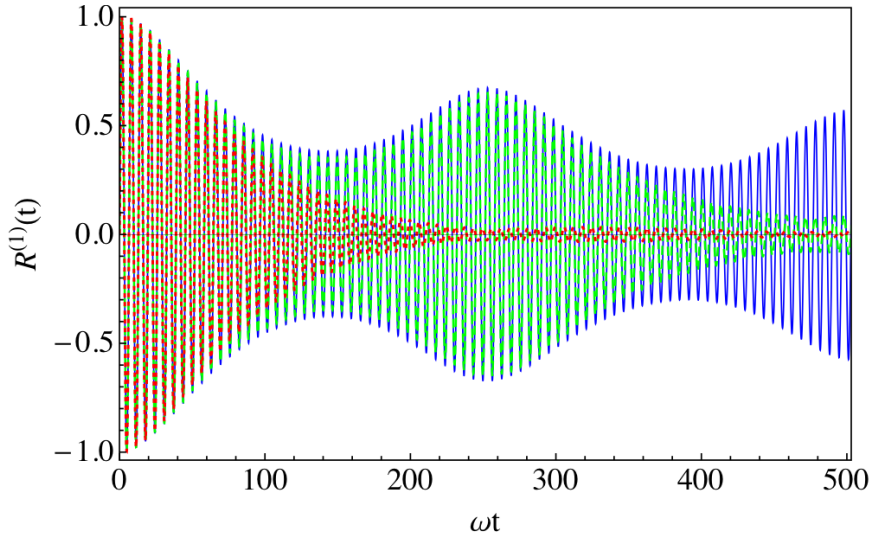

Figure 2.12: The linear response function $R^{(1)}_{MT}(t; k_{max})$ is plotted for an ensemble of uncoupled Morse oscillators with parameters $\beta D = 40$ and $\beta\hbar\omega = 2$ for $k_{max} = 0$ (red, dotted), $k_{max} = 1$ (green, dashed), and $k_{max} = 2$ (blue, solid).

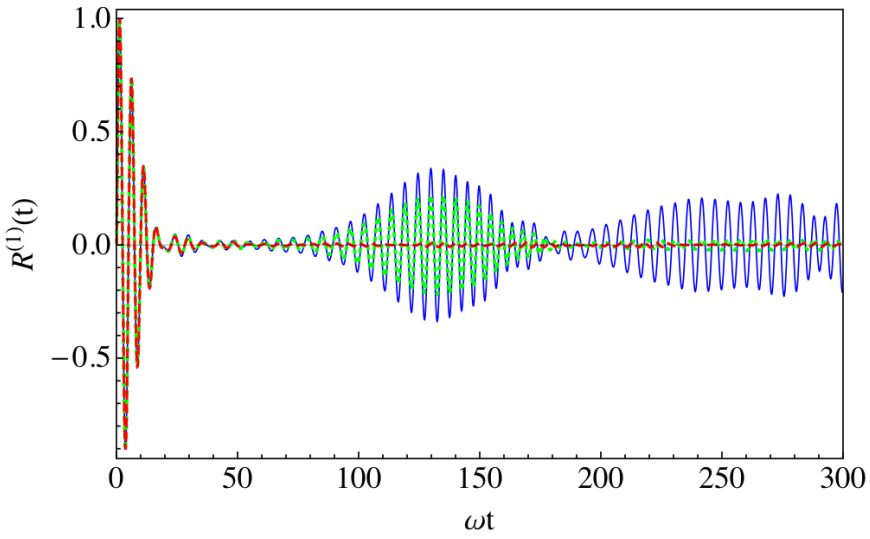

Figure 2.13: The linear response function $R^{(1)}_{MT}(t;k_{max})$ for an ensemble of quartically perturbed harmonic oscillators with parameters $\beta\hbar\omega = 0.25$ and $(a/\beta m^2\omega^4)^{1/4} = 0.562$ is plotted for $k_{max} = 0$ (red, dashed), $k_{max} = 1$ (green, dashed), and $k_{max} \to \infty$ (blue, solid). The quantum result for the same system is shown in the bottom panel of Figure 2.3.

an ensemble of quartically perturbed harmonic oscillators for the same parameters as in Figure 2.3. The blue curve is the $k_{max} \to \infty$ mean trajectory result, the red, dashed curve corresponds to the classical $k_{max} = 0$ case, and the green, dotted curve is the $k_{max} = 1$ result. As for the Morse oscillator system, increasing k_{max} results in a response function that is accurate for longer and longer times. However, as the quantization of the action variables does not result in the exact quantum frequencies for quartic oscillator systems, the mean trajectory response function is not quantitatively accurate even as $k_{max} \to \infty$.

Finally, the linear response for a chromophore Morse oscillator bilinearly coupled to a dark harmonic degree of freedom is plotted in Figure 2.14. When compared to the quantum and HK results in Figure 2.5, the mean trajectory response function accurately reproduces the main quantum features, including

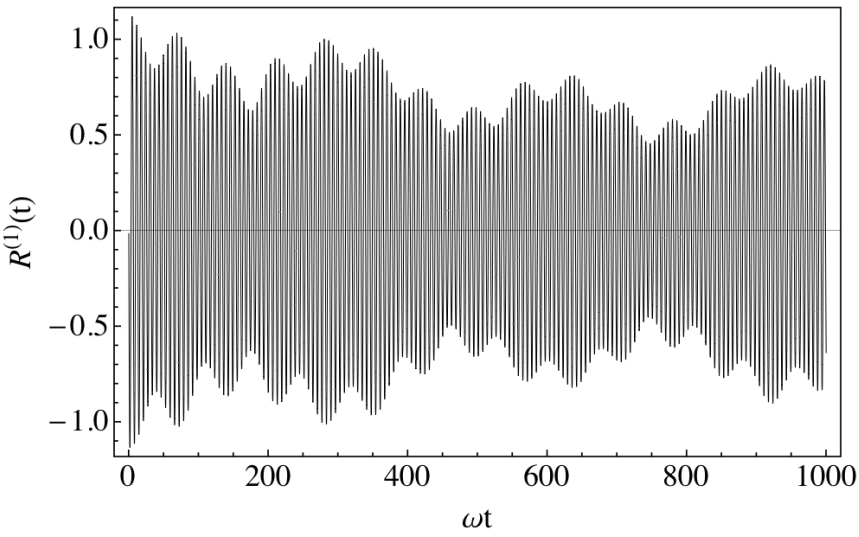

Figure 2.14: The mean trajectory linear response function for a thermal ensemble of a chromphore Morse oscillator bilinearly coupled to a harmonic oscillator is plotted for the same parameters as in Figure 2.5.

the intermediate frequency that results from energy transfer between oscillator modes. This calculation has been repeated for the case where the coupling constant c_{ab} is five times as large as in Figure 2.14. While the accuracy does decline somewhat, the mean trajectory method is still qualitatively correct. The mean trajectory method can also be applied to larger coupled systems such as an anharmonic chromophore oscillator bilinearly coupled to a bath of off-resonance modes. Such a system will be considered in Chapter 3 for the third-order response function.

2.8 Summary

In this chapter, we have analyzed the vibrational linear response function within the Herman-Kluk approximation to the propagator. Our semiclassical approx-

imation to the response function, Eq. (2.6), accurately reproduces the quantum result for a variety of anharmonic oscillator systems. In each case, the semiclassical response reproduces quantum recurrences that are qualitatively missed by the classical linear response. However, these semiclassical calculations are numerically challenging due to a divergent, oscillating integrand. For nonlinear response functions or for strongly coupled oscillator systems, this sign problem makes the HK calculation numerically impractical.

In order to understand the mechanism by which the semiclassical response reproduces the quantum result, we have adopted approximate dynamics for the phase space variables using action-angle perturbation theory. With these dynamics, we have generated approximate but accurate expressions for the semiclassical phase, coherent state overlap, and HK prefactor. The phase exhibits periodic stationary points that occur when a pair of trajectories comes close in phase space. The integral over trajectory difference variables is dominated by contributions near each stationary point. These approximations allowed us to analytically integrate over trajectory differences, resulting in a time-dependent quantization condition on the mean action for the pair of trajectories. The resulting mean trajectory semiclassical linear response function, Eq. (2.70), is numerically efficient to calculate due to the lack of an oscillatory phase factor. The cost associated with eliminating the sign problem is that we must determine the classical action variables, which may be difficult or impossible for strongly coupled systems. For systems where we can determine the actions, we have shown that the mean trajectory treatment accurately reproduces the quantum response for a variety of anharmonic oscillator systems. In the next chapter, we will extend the mean trajectory treatment to nonlinear response functions.

CHAPTER 3

SEMICLASSICAL NONLINEAR RESPONSE FUNCTIONS

3.1 Introduction

While the linear vibrational response function discussed in the previous chapter suffices for the interpretation of linear infrared absorption measurements, multidimensional vibrational spectroscopy requires the calculation of nonlinear response functions. The nth-order response function describes coherent n photon processes on a single electronic surface and can be expressed as a sum of n-time correlation functions divided by a power of $\hbar$. As discussed in Chapter 1, nonlinear response functions can be calculated both quantum mechanically and classically, but for anharmonic systems, classical response functions may be qualitatively incorrect. In Chapter 2 we investigated semiclassical linear response functions within the Herman-Kluk approximation for the propagator. This semiclassical treatment is accurate, but numerical computations are challenging due to an oscillatory semiclassical phase— the sign problem. [45] While a number of methods such as linearization, [102, 113] forward-backward schemes, [25,26] and integral filtering [106] have been proposed for dealing with this problem, each of these methods results in the loss of quantum coherence information in the linear response function.

Instead of trying to reduce the oscillations of the response function integrand, we have instead developed approximations to the semiclassical phase

[†]Reprinted with permission from S. M. Gruenbaum and R. F. Loring, J. Chem. Phys., 129, 124508 (2008) and from S. M. Gruenbaum and R. F. Loring, J. Chem. Phys., 131, 204504 (2009), Copyright 2008 and 2009, American Institute of Physics.

and other response function components that allow us to analytically integrate over difference variables for a pair of propagating trajectories. We have shown that integration over all stationary points in the semiclassical phase results in a quantization condition on the mean action for a pair of trajectories. In this chapter, we seek to extend this treatment to nonlinear response functions. Our analysis will result in a mean trajectory approximation for the nth-order response function for a coupled anharmonic oscillator system. This mean trajectory treatment requires integration over n classical trajectories propagating on the potential energy surface, and these n trajectories are connected by quantized jumps in action variables for fixed values of the angle. This mean trajectory treatment requires the existence of good action and angle variables and is thus not applicable to chaotic systems. [47, 103]

In Section 2 of this chapter, we analyze the semiclassical third-order response function for a thermal ensemble of uncoupled anharmonic oscillators. Using the same methodology as in Chapter 2, we focus on the differences between the nonlinear and linear semiclassical response functions. Section 3 generalizes this treatment to the nth-order response function for coupled oscillator systems with f degrees of freedom. In Section 4, we derive a mean trajectory treatment for spatially phase-matched components of the third-order response function. These components correspond to the total nonlinear signal propagating in a particular wavevector. [33] In Section 5 we analyze the structure of the mean trajectory response functions and connect the semiclassical expressions to the appropriate double-sided Feynman diagrams. Finally, the mean trajectory treatment is tested numerically in Section 6, and we summarize our findings in Section 7.

3.2 $R^{(3)}(t_3, t_2, t_1)$ for one-dimensional anharmonic systems

In this section, we shall analyze the third-order semiclassical response function for a thermal ensemble of one-dimensional anharmonic oscillators. We will use the same strategy as for the linear response function and write the integrand of $R^{(3)}_{HK}$ using approximate phase space dynamics $q(t)$ and $p(t)$. Certain aspects of the analysis will be quite similar to the linear response calculation, and we shall therefore focus on the additional complications that arise for the nonlinear case.

As discussed in Chapter 2, the third-order vibrational response function within the Herman-Kluk approximation for a one-dimensional system is given by

$$\begin{aligned} R^{(3)}_{HK}(t_3, t_2, t_1) = & \frac{\beta}{m^3\omega^2\hbar^2(2\pi\hbar)^5} \int d\mathbf{z}_1 \cdots \int d\mathbf{z}_6 \; f_{cl}(\bar{\mathbf{z}}_{12}) \\ & \times A_{12}(t_1) O_{1234}(t_1) A_{34}(t_2) O_{3456}(t_2) A_{56}(t_3) \\ & \times P_{12} \left[P_{34} - P^*_{12}(t_1) \right] \left[P_{56} - P^*_{34}(t_2) \right] Q^*_{56}(t_3) \end{aligned} \tag{3.1}$$

where $A_{jk}(t)$ and the complex coordinates and momenta Q_{jk} and P_{jk} are defined in Eqs. (2.8)–(2.15). Unlike the linear response function, the calculation of the semiclassical nonlinear response function requires the ratio of coherent state overlaps defined in Eq. (2.12),

$$O_{jklm}(t) = \exp\Big[-\frac{m\omega}{2\hbar} \Big(Q_{lm} - Q^*_{jk}(t) \Big)^2 - \frac{1}{2\hbar m\omega} \Big(P_{lm} - P^*_{jk}(t) \Big)^2 \Big] . \tag{3.2}$$

This ratio couples the trajectory pair $\{z_j(t), z_k(t)\}$ at time t to the trajectory pair $\{z_l, z_m\}$ at $t = 0$. We shall see that it is this coupling which constrains the mean action and angle of trajectory pair j, k at time t, N_{jk} and $\bar{\phi}_{jk}(t)$, relative to the mean action and initial angle of trajectory pair l, m. This constraint, discussed below, will result in only certain allowed transitions in the mean action variable between two pairs of trajectories.

As for the linear response function, the phase space dynamics for the one-dimensional Morse oscillator can be approximated with classical action-angle perturbation theory as described in Appendix A,

$$\begin{aligned} q(t) &= \sqrt{\frac{2J}{m\omega}}\cos\phi(t) - \varepsilon\frac{J}{\sqrt{8Dm}}\Big(\cos\left(2\phi(t)\right) - 3\Big) \\ p(t) &= -\sqrt{2m\omega J}\sin\phi(t) + \varepsilon\frac{2m^{1/2}\omega J}{\sqrt{2D}}\cos\phi(t)\sin\phi(t)\,. \end{aligned} \tag{3.3}$$

The semiclassical phase, HK prefactors, and the coherent state overlap can then be approximated as in Eqs. (2.28), (2.32), and (2.33),

$$\psi_{jk} = \frac{\bar{J}_{jk}}{\hbar}\Big(-\eta_{jk} + \Big(\sin\left(\Delta\phi_{jk}(t)\right) - \sin\left(\Delta\phi_{jk}\right)\Big)\Big) \tag{3.4}$$

$$C\left(z_j,t\right)C^*\left(z_k,t\right) = \varepsilon^2\left(\frac{\bar{J}_{jk}\omega^2 t}{2D}\right)e^{i\eta_{jk}/2} \tag{3.5}$$

$$\left|\langle z_j|z_k\rangle\langle z_k(t)|z_j(t)\rangle\right| = \exp\Big[-\frac{\bar{J}_{jk}}{\hbar}\Big(2 - \cos(\Delta\phi_{jk}(t)) - \cos(\Delta\phi_{jk})\Big)\Big] \tag{3.6}$$

where η_{jk} is defined in Eq. (2.29). The complex ratio of coherent states $O_{jklm}(t)$ is given within the same approximate dynamics as

$$\begin{aligned} O_{jklm}(t) = \exp\Big[&-\frac{\bar{J}_{lm}}{\hbar}\,e^{i\Delta\phi_{lm}} - \frac{\bar{J}_{jk}}{\hbar}\,e^{-i\Delta\phi_{jk}(t)} \\ &+ \frac{2\sqrt{\bar{J}_{lm}\bar{J}_{jk}}}{\hbar}\,\cos\left(\bar{\phi}_{lm} - \bar{\phi}_{jk}(t)\right)e^{i(\Delta\phi_{lm}-\Delta\phi_{jk}(t))/2}\Big]. \end{aligned} \tag{3.7}$$

Note that for harmonic systems, Eq. (3.7) depends on time only through the $\cos\left(\bar{\phi}_{lm} - \bar{\phi}_{jk}(t)\right)$ term and is peaked for $\bar{\phi}_{lm} \approx \bar{\phi}_{jk}(t)$. In general, we also expect this ratio of coherent states to constrain the initial difference angle of trajectory pair l,m to be close to the difference angle for trajectory pair j,k at time t, $\Delta\phi_{jk}(t) \approx \Delta\phi_{lm}$.

In analogy to our derivation in Eq. (2.34), we define the exponent F_{1234} as

$$A_{12}(t_1)O_{1234}(t_2)A_{34}(t_2) \equiv \left|C(z_1,t_1)C^*(z_2,t_1)C(z_3,t_2)C^*(z_4,t_2)\right|\,e^{F_{1234}(t_1,t_2)} \tag{3.8}$$

where for simplicity we start by analyzing only two pairs of trajectories $\{z_1, z_2\}$ and $\{z_3, z_4\}$. We will later generalize to the case of three and then n pairs of trajectories. F_{1234} is composed of contributions from two semiclassical phases ψ_{12} and ψ_{34}, as well as contributions from the coherent state overlaps and the new ratio of overlaps,

$$F_{1234}(t_1, t_2) = \frac{1}{\hbar}\Big(\psi_{12}(t_1) + \psi_{34}(t_2)\Big) - \frac{1}{2}\Big(\Delta z_{12}^2(t_1) + \Delta z_{12}^2 + \Delta z_{34}^2(t_2) + \Delta z_{34}^2\Big) - \frac{m\omega}{2\hbar}\left(Q_{34} - Q_{12}^*(t_1)\right)^2 - \frac{1}{2\hbar m\omega}\left(P_{34} - P_{12}^*(t_1)\right)^2 \ . \tag{3.9}$$

Within the approximations to $A_{jk}(t)$ and $O_{jklm}(t)$ in Eqs. (3.4)–(3.7), F_{1234} can be written as

$$\begin{aligned} F_{1234}(t_1, t_2) = {} & N_{12}(e^{i\Delta\phi_{12}} - 2) + N_{34}(e^{i(\eta_{34} - \Delta\phi_{34})} - 2) \\ & - i\eta_{12}(N_{12} - 1/2) - i\eta_{34}(N_{34} - 1/2) \\ & + 2\sqrt{N_{12}N_{34}}\,\cos\left(\bar{\phi}_{12}(t_1) - \bar{\phi}_{34}\right) e^{i(\Delta\phi_{12}(t_1) - \Delta\phi_{34})} \end{aligned} \tag{3.10}$$

where as before $N_{jk} \equiv \bar{J}_{jk}/\hbar$ measures the mean action of trajectory pair $\{z_j, z_k\}$ in powers of $\hbar$. While η_{34} in Eq. (3.10) still has stationary points at $\eta_{34} = 2\pi k + \Delta\phi_{34}$ for integer k, as in the linear response function, it is important to note that the ratio of coherent state overlaps $O_{1234}(t_1)$ has completely eliminated all stationary points in η_{12}. Thus, while we might expect that integration over η_{34} will yield a quantization condition on the mean action N_{34}, it is not immediately apparent if there is a similar quantization condition for N_{12}.

To clarify the structure of F_{1234}, we substitute into Eq. (3.10) the stationary point condition for η_{34}, and then make use of the constraint between the difference angle for the trajectory pairs,

$$\eta_{34} \to \Delta\phi_{34} + 2\pi k + \delta\eta_{34} \tag{3.11}$$

$$\Delta\phi_{34} \to \Delta\phi_{12}(t_1) + \delta\Delta\phi_{34} \ . \tag{3.12}$$

Near each stationary point in η_{34}, we expect that $\delta\eta_{34}$ and $\delta\Delta\phi_{34}$ will be small quantities. We further make a change of variables,

$$\eta_{12} \to \Delta\phi_{12} + \eta'_{12} \,. \tag{3.13}$$

As η_{12} does not have stationary points any longer, there is no reason to expect η'_{12} to be a small quantity. With these substitutions, F_{1234} can be expanded in powers of $\delta\eta_{34}$, $\delta\Delta\phi_{34}$, and $\Delta\phi_{12}$,

$$\begin{aligned} e^{F_{1234}} \approx \left|\langle z_{12}(t_1)|z_{34}\rangle\right|^2 \exp\Big[&2\pi i\, k\, (N_{34} - 1/2) \\ &- i\,\eta'_{12}(N_{12} - N_{34}) + F''(\delta\eta_{34}, \delta\Delta\phi_{34}, \Delta\phi_{12})\Big] \end{aligned} \tag{3.14}$$

where F'' is dominated by quadratic terms in $\delta\eta_{34}$, $\delta\Delta\phi_{34}$, and $\Delta\phi_{12}$. The exact functional form of F'' is unimportant, as we shall integrate it to yield a slowly varying function of action, as was the case for integration over $\delta\eta_{12}$ and $\Delta\phi_{12}$ in Eq. (2.38). Note that Eq. (3.14) has not been expanded in powers of η'_{12}. As with the linear response calculation, the mean trajectories z_{jk} in the coherent state overlap in Eq. (3.14) are distinct from the average trajectory $\bar{z}_{jk}$.

F_{1234} contains a term $2\pi ik(N_{34} - 1/2)$ as was the case for the linear response function. Therefore, integration of F_{1234} over each stationary point in η_{34} results in the half-integer quantization of N_{34}. As before, the $1/2$ comes from the phase of the HK prefactors. As noted above, there are no stationary points in η'_{12}. However, the factors in $O_{1234}(t_1)$ which cancel these stationary points also cancel all quadratic and cubic terms in η'_{12} in Eq. (3.14). Therefore the imaginary part of F_{1234} is purely linear in η'_{12} with a coefficient of $(N_{12} - N_{34})$. Integration of F_{1234} over η'_{12} will therefore yield a value of zero unless this coefficient equals zero, $N_{12} = N_{34}$. Quantization of the mean action N_{12} for the trajectory pair $\{z_1, z_2\}$ thus arises from a combination of the quantization of N_{34} as for the linear response

function, as well as the constraint between the value of $\Delta z_{12}(t_1)$ at time t_1 and the initial value of Δz_{34}.

The integrals over difference variables in Eq. (3.1) can be rewritten as before in terms of η_{12} and η_{34},

$$\begin{aligned}\Big|C(z_1,t_1)C^*(z_2,t_1)C(z_3,t_2)C^*(z_4,t_2)\Big|\, d\Delta z_{12}\, d\Delta z_{34} \\ \approx \bar{J}_{12}\bar{J}_{34}\, d\eta_{12}\, d\eta_{34}\, d\Delta\phi_{12}\, d\Delta\phi_{34}\end{aligned} \tag{3.15}$$

where the magnitude of the HK prefactors once again cancels a time decay that results from integration of the semiclassical phases over the difference actions ΔJ_{jk}. We can now integrate $A_{12}(t_1)O_{1234}(t_1)A_{34}(t_2)$ over difference variables to yield

$$\begin{aligned}&\iint \frac{d\Delta z_{12}\, d\Delta z_{34}}{(2\pi\hbar)^2}\, A_{12}(t_1)\, O_{1234}(t_1)\, A_{34}(t_2) \\ &\quad = (N_{12}N_{34})^{1/4} G(N_{12},N_{34})\, \sigma_{1/2}(N_{34})\, \Big|\langle z_{12}(t_1)|z_{34}\rangle\Big|^2\, \delta(N_{34}-N_{12})\end{aligned} \tag{3.16}$$

where, as in Eq. (2.38), G is a slowly varying function of the mean action which we set to unity. As with $R^{(1)}(t)$, the action of each mean trajectory is half-integer quantized in Eq. (3.16), and the mean action N_{12} is constrained to equal the mean action N_{34}. Furthermore, the mean trajectory coherent state overlap, $\Big|\langle z_{12}(t_1)|z_{34}\rangle\Big|^2$, will constrain the angle of trajectory z_{12} at time t_1 to be approximately equal to the inital angle for trajectory z_{34}.

Also as was the case with $R^{(1)}(t)$, the various combinations of P_{jk} and Q_{jk} in the nonlinear response function will alter the quantization condition for the action variables. For the third-order response, expansion of the integrand in Eq. (3.1) results in four combinations of the complex coordinates and momenta, while in general for the nth-order response there are 2^{n-1} combinations possible. To demonstrate the effect of these additional terms, we choose for the case of

two pairs of trajectories the combination $P_{12}P_{34}Q^*_{34}(t_2)$. As was done for the linear response calculation, we make use of the stationary point condition in η_{34} to approximate this term as

$$\begin{aligned} P_{12}P_{34}Q^*_{34}(t_2) &= p_{12}p_{34}q_{34}(t_2)\, e^{i(\Delta\phi_{12}+\Delta\phi_{34}-\Delta\phi_{34}(t_2))/2} \\ &\approx p_{12}p_{34}q_{34}(t_2)\, e^{i\pi k}\, e^{-i\eta'_{12}/2}\,. \end{aligned} \tag{3.17}$$

As in Eq. (2.42), the additional $i\pi k$ term in Eq. (3.17) results in the integer quantization of the mean action N_{34} when it is inserted into the integrand of Eq. (3.16). However, Eq. (3.17) also contains a term that is linear in η'_{12}. When this additional η'_{12} dependence is inserted into Eq. (3.14) for F_{1234}, the coefficient of η'_{12} becomes $(N_{12} - N_{34} + 1/2)$. Thus, integration over η'_{12} will constrain the action N_{12} to differ from N_{34} by $1/2$. If we had taken the $P_{12}P_{12}(t_1)Q^*_{34}(t_2)$ combination of complex coordinates and momenta instead, the "action jump" between N_{12} and N_{34} simply changes sign to $-1/2$. We should also note that the exponent in Eq. (3.17) contains additional $\delta\eta_{34}$, $\delta\Delta\phi_{34}$, and $\Delta\phi_{12}$ dependent terms which contribute to F'' in Eq. (3.14).

The absolute square of the coherent state overlap in Eq. (3.16) constrains the initial mean angle variable for a trajectory following a transition to be close to the final mean angle of the preceding trajectory. Therefore, we approximate the coherent state overlap by

$$\left|\langle z_{12}(t_1)|z_{34}\rangle\right|^2 \approx \frac{\sqrt{\pi}}{(N_{12}N_{34})^{1/4}}\,\delta(\bar{\phi}_{12}(t_1) - \bar{\phi}_{34})\,. \tag{3.18}$$

Within this additional approximation, we can extend the analysis that led to Eq. (3.16) to three pairs of trajectories, and thus write the mean trajectory third-order

response function as

$$R^{(3)}_{MT}(t_3,t_2,t_1) = \frac{\beta}{m^3\omega^2\hbar^4}\iiint dz_1 dz_2 dz_3\; f_{cl}(z_1)\,\sigma_1(N_1) \\ \times \delta(\phi_1(t_1)-\phi_2)\,\delta(\phi_2(t_2)-\phi_3) \\ \times p_1\,(p_2 D_1^+ - p_1(t_1)D_1^-)\,(p_3 D_2^+ - p_2(t_2)D_2^-)\,q_3(t_3) \tag{3.19}$$

where $D_j^{\pm}$ connects the action variable of mean trajectory z_j to that of z_{j+1},

$$D_j^{\pm} \equiv \delta(N_{j+1} - N_j \mp 1/2)\,. \tag{3.20}$$

The three trajectories which make up $R^{(3)}_{MT}(t_3,t_2,t_1)$ in Eq. (3.19) are connected by quantized half-integer jumps in action at fixed angle. We can rewrite Eq. (3.19) more compactly in terms of an average over a single phase space variable as

$$R^{(3)}_{MT}(t_3,t_2,t_1) = \frac{\beta}{m^3\omega^2\hbar^2}\Big\langle \sigma_1(N)\; p\,\Big[p_{t_1\uparrow}p_{t_1\uparrow t_2\uparrow}q_{t_1\uparrow t_2\uparrow t_3} + p_{t_1}p_{t_1\downarrow t_2}q_{t_1\downarrow t_2\downarrow t_3} \\ - p_{t_1\uparrow}p_{t_1\uparrow t_2}q_{t_1\uparrow t_2\downarrow t_3} - p_{t_1}p_{t_1\downarrow t_2\uparrow}q_{t_1\downarrow t_2\uparrow t_3}\Big]\Big\rangle \tag{3.21}$$

where the angular brackets indicate a phase space average over $f_{cl}(z)$ and the term $q_{t_1\uparrow t_2\downarrow t_3}$ for example indicates the coordinate after a process in which the system with initial phase point z is propagated for time t_1, the action is increased by $\hbar/2$, the trajectory is propagated for time t_2, the action is then decreased by $\hbar/2$, and the trajectory is finally propagated for time t_3.

In this section, we have shown how a quantization of action condition arises for each mean trajectory in the third-order response function for a one-dimensional anharmonic system. The ratio of coherent state overlaps $O_{jklm}(t)$ destroys the stationary points in the semiclassical phase for all but the final pair of trajectories. This final action variable N_{56} is integer quantized as with the linear response function. The remaining phase for the second pair of trajectories connects the mean action N_{34} to the action N_{56} by a half-integer quantized jump.

The mean action for the first pair of trajectories, N_{12} is similarly connected by a quantized jump to N_{34}. While the mean angle variables are not quantized, a coherent state overlap constrains the angle at a jump to remain approximately fixed, $\bar{\phi}_{12}(t_1) = \bar{\phi}_{34}$ and $\bar{\phi}_{34}(t_2) = \bar{\phi}_{56}$. In the next section, we shall extend this treatment to the nth-order response function for coupled anharmonic systems with f degrees of freedom.

3.3 The mean trajectory nth-order response function

In this section, we will derive a mean trajectory approximation to the nth-order vibrational response function for a system of f weakly coupled anharmonic oscillators. As in Eq. (2.19) of Chapter 2, the Hamiltonian for f bilinearly coupled oscillators is taken to be

$$H = \sum_{\alpha} H_{\alpha} + \sum_{\alpha>\beta} c_{\alpha\beta} \left(\frac{\omega_{\alpha}\omega_{\beta}}{2} \right) \sqrt{m_{\alpha} m_{\beta}}\, q_{\alpha} q_{\beta} \tag{3.22}$$

where $\alpha = a, b, c, \cdots$ labels each local mode, and H_{α} is the vibrational Hamiltonian for mode α. As before, we shall assume that only the chromophore mode labeled a couples to the radiation and that H_a is given by the Morse oscillator Hamiltonian. We again transform from local to normal modes with coordinates and momenta denoted x_{α} and π_{α}, with approximate dynamics given by Eq. (2.57).

Within the independent oscillator approximation, we can once again write the coherent state overlap, phase, HK prefactor, and the ratio of coherent state overlaps in the same forms as Eqs. (2.59)–(2.62). The multi-dimensional gener-

alization of Eq. (3.7) for $O_{jklm}(t)$ is given by

$$O_{jklm}(t) = \prod_{\alpha} \exp\Big[-\frac{\bar{J}_{\alpha,lm}}{\hbar}\, e^{i\Delta\phi_{\alpha,lm}} - \frac{\bar{J}_{\alpha,jk}}{\hbar}\, e^{-i\Delta\phi_{\alpha,jk}(t)} + \frac{2\sqrt{\bar{J}_{\alpha,lm}\bar{J}_{\alpha,jk}}}{\hbar}\, \cos\left(\bar{\phi}_{\alpha,lm} - \bar{\phi}_{\alpha,jk}(t)\right) e^{i(\Delta\phi_{\alpha,lm} - \Delta\phi_{\alpha,jk}(t))/2} \Big] \tag{3.23}$$

where $\boldsymbol{J}$ and $\boldsymbol{\phi}$ represent the good action and angle variables for the fully coupled system. Using these approximation, we can integrate over difference variables for n pairs of trajectories, as was done for the $n = 2$ case in Eq. (3.16), which results in the half-integer quantization of the mean actions for the nth pair of trajectories, as well as constraints on the the mean action for the previous pair of trajectories, $N_{\alpha,2n-1,2n} = N_{\alpha,2n-3,2n-2} = \cdots = N_{\alpha,12}$ for all vibrational modes α. Also as before, the final mean angle for a trajectory is constrained to be approximately equal to the initial mean angle of the subsequent trajectory by the absolute square of a coherent state overlap.

The 2^{n-1} combinations of complex local mode coordinates and momenta Q_a and P_a in Eq. (2.7) can be expanded in terms of the complex normal mode phase space variables X_α and Π_α, as was done for the linear response function. For the same $n = 2$ term treated in the previous section, this expansion is given by

$$P_{a,12}P_{a,34}Q_{a,43}(t_2) = \sum_{\alpha,\beta,\gamma} \kappa_{a\alpha}\kappa_{a\beta}\kappa_{a\gamma}\Pi_{\alpha,12}\Pi_{\beta,34}X^*_{\gamma,34}(t_2) \tag{3.24}$$

and the complex normal mode variables can then be approximated using the stationary point condition for η_{34},

$$\Pi_{\alpha,12}\Pi_{\beta,34}X^*_{\gamma,34}(t_2) = \pi_{\alpha,12}\,\pi_{\beta,34}\,x_{\gamma,34}(t_2)\, e^{i\pi k_\gamma}\, e^{-i\eta'_{\beta,12}/2}\,. \tag{3.25}$$

Once again, the combinations of complex phase space variables results in the integer quantization of a mean action variable— the mean action for trajectory pair $\{\mathbf{z}_3, \mathbf{z}_4\}$ in normal mode γ, $N_{\gamma,34}$. All other mean actions $N_{\epsilon,34}$ for $\epsilon \neq \gamma$ remain

half-integer quantized. In addition, the $\eta'_{\beta,12}$ dependence in Eq. (3.25) results in a jump in the mean action for the β degree of freedom between trajectory pairs $\{\mathbf{z}_1, \mathbf{z}_2\}$ and $\{\mathbf{z}_3, \mathbf{z}_4\}$. All other action variables remain fixed across this transition.

Generalizing the analysis in Eqs. (3.24) and (3.25) to arbitrary n allows the mean trajectory nth-order response function for a coupled system with f degrees of freedom to be written as

$$R^{(n)}_{MT}(t_n, t_{n-1}, \cdots, t_1) = \sum_{\alpha,\beta,\cdots,\xi,\zeta} \kappa_{a\alpha}\kappa_{a\beta}\cdots\kappa_{a\xi}\kappa_{a\zeta}\, R^{(n)}_{\zeta\xi\cdots\beta\alpha}(t_n, t_{n-1}, \cdots, t_1) \tag{3.26}$$

with each component of the response defined as

$$\begin{aligned} R^{(n)}_{\zeta\xi\cdots\beta\alpha}(t_n, t_{n-1}, \ldots, t_1) = \frac{1}{m_a^n \omega_a^{n-1} \hbar^{(f+1)(n-1)} k_B T} \int\cdots\int d\mathbf{z}_1 \cdots d\mathbf{z}_n \, f_{cl}(\mathbf{z}_1) \\ \times \sigma_1(N_{\zeta,n}) \prod_{\nu\neq\zeta} \sigma_{1/2}(N_{\nu,n}) \\ \times \prod_{\epsilon} \delta(\phi_{\epsilon,1}(t_1) - \phi_{\epsilon,2}) \cdots \delta(\phi_{\epsilon,n-1}(t_{n-1}) - \phi_{\epsilon,n}) \\ \times \pi_{\alpha,1}\left(\pi_{\beta,2} D^+_{\beta,1} - \pi_{\beta,1}(t_1) D^-_{\beta,1}\right) \cdots \\ \times \left(\pi_{\xi,n} D^+_{\xi,n-1} - \pi_{\xi,n-1}(t_{n-1}) D^-_{\xi,n-1}\right) x_\zeta(t_n) \,. \end{aligned} \tag{3.27}$$

In this expression, $D^\pm_{\alpha,j}$ denotes a jump in the α action variable by $\pm\hbar/2$,

$$D^\pm_{\alpha,j} \equiv \delta\left(N_{\alpha,j+1} - N_{\alpha,j} \mp 1/2\right) \prod_{\epsilon\neq\alpha} \delta\left(N_{\epsilon,j+1} - N_{\epsilon,j}\right). \tag{3.28}$$

while the action for all other modes remains fixed across the transition. Equations (3.26)-(3.28) give our final mean-trajectory expression for the nonlinear response of a coupled oscillator system. [47, 104]

In Eq. (3.26), the response function is expressed as an integral over n classical trajectories propagating on the exact potential energy surface. These trajectories are connected by discrete jumps in the good action variables for the coupled system, while the angle variables are held fixed between jumps. In order to

calculate $R^{(n)}_{MT}(t_n, \cdots, t_1)$ for a coupled multidimensional system, trajectories must be sampled from a thermal Boltzmann distribution with quantized values for the action variable. For each component of the response in Eq. (3.26), one vibrational mode has an integer action, while all others start as half-integers. The nth-order response function requires all possible combinations of jumps in the action to be summed. For weakly coupled or off-resonant systems, many components in Eq. (3.26) may be numerically unimportant, and a small set of terms may suffice for accurate response calculations.

3.4 Spatially phase-matched components

The nth-order response function in Eq. (2.1) gives the total response of a system to n interactions with an applied electric field, including all coherent signals that propagate in distinct spatial directions. We can determine the signal emitted at a particular wavevector through a Fourier transform of the total response function, but is is often more convenient to separate the response function into additive components which produce signals that propagate at different wavevectors. Each of these components is then associated with double-sided Feynman diagrams which provide a visual representation of the time dependence of that contribution to the total response. [2, 13] The two sides of these Feynman diagrams represent the perturbation and evolution of the ket and bra sides of the density matrix, as discussed in more detail in Appendix D. The value of each diagram is intrinsically quantum mechanical and diverges as $\hbar \to 0$. However, certain combinations of these diagrams have a well defined classical limit. These spatially phase-matched components correspond to "classical Feynman diagrams" and are associated with the total signal propagating in a given wavevector. [33]

As discussed by Noid, et.al., [33] these diagrams allow for the identification of the classical analogs of the quantum phase as well as quantum dephasing and rephasing.

In order to investigate these spatially phase-matched components to the response, we will decompose the response function by writing the coordinate $\hat{q}_\alpha$ as a sum of harmonic creation and annihilation operators,

$$\hat{q}_\alpha = \hat{q}_\alpha^+ + \hat{q}_\alpha^- , \qquad \hat{q}_\alpha^+ \equiv \sqrt{\frac{\hbar}{2m_\alpha\omega_\alpha}}\hat{a}_\alpha^\dagger , \qquad \hat{q}_\alpha^- \equiv (\hat{q}_\alpha^+)^\dagger . \tag{3.29}$$

Substitution of Eq. (3.29) into the quantum nth-order response function, Eq. (2.1), permits the total response function to be written as a sum of terms of the form $R^{y_i,y_j,\cdots,y_k}(t_n,\cdots,t_1)$, where the indices $y_j = +,-$ label either creation or annihilation operators. As an example, we examine a rephasing component of the third-order response, $R^{++-}(t_3,t_2,t_1)$, which is associated with a signal with wavevector $\mathbf{k}_1+\mathbf{k}_2-\mathbf{k}_3$ in a three-pulse vibrational echo measurement. The classical Feynman diagram representing this term is given as the $\hbar \to 0$ limit of a sum of the eight double-sided Feynman diagrams in Figure 2 of Ref. [33],

$$\begin{aligned} R^{++-}(t_3,t_2,t_1) = \left(\frac{i}{\hbar}\right)^3 \mathrm{Tr}\Big\{ & \hat{q}_a^- \hat{K}(t_3)\Big[\hat{q}_a^+,\hat{K}(t_2)\Big[\hat{q}_a^+,\hat{K}(t_1) \\ & \times \Big[\hat{q}_a^-,\hat{\rho}\Big]\hat{K}^\dagger(t_1)\Big]\hat{K}^\dagger(t_2)\Big]\hat{K}^\dagger(t_3)\Big\} . \end{aligned} \tag{3.30}$$

In order to calculate Eq. (3.30) with the Herman-Kluk approximation to the propagator, we require the coherent state matrix elements of $\hat{q}_\alpha^\pm$,

$$\begin{aligned} 2\langle \mathbf{z}_j|\hat{q}_\alpha^+|\mathbf{z}_k\rangle &= Q_{\alpha,j}^+\langle \mathbf{z}_j|\mathbf{z}_k\rangle \\ 2\langle \mathbf{z}_j|\hat{q}_\alpha^-|\mathbf{z}_k\rangle &= Q_{\alpha,k}^-\langle \mathbf{z}_j|\mathbf{z}_k\rangle \end{aligned} \tag{3.31}$$

$$Q_{\alpha,j}^\pm \equiv q_{\alpha,j} \mp i p_{\alpha,j}/m_\alpha\omega_\alpha \tag{3.32}$$

where Eq. (3.32) defines the complex coordinate $Q_\alpha^\pm$. Using Eq. (B.3) of Appendix B, the coherent state matrix element of the commutator of $\hat{q}_\alpha^\pm$ with the density operator $\hat{\rho}$ is given by

$$\frac{\langle \mathbf{z}_j|[\hat{q}_\alpha^\pm, \hat{\rho}]|\mathbf{z}_k\rangle}{\langle \mathbf{z}_j|\mathbf{z}_k\rangle} = \frac{i\hbar}{2}\Big(\frac{\partial}{\partial \bar{p}_{\alpha,jk}} \pm \frac{i}{m_\alpha \omega_\alpha}\frac{\partial}{\partial \bar{q}_{\alpha,jk}}\Big)\frac{\langle \mathbf{z}_j|\hat{\rho}\,|\mathbf{z}_k\rangle}{\langle \mathbf{z}_j|\mathbf{z}_k\rangle} \tag{3.33}$$

and we once again make the high-temperature approximation to the density matrix as in Eq. (2.16). The rephasing component to the third-order response function within the HK approximation is then given by

$$\begin{aligned} R_{HK}^{++-}(t_3,t_2,t_1) = \frac{-\beta}{2^4 m\hbar^2(2\pi\hbar)^5}\int d\mathbf{z}_1 \cdots \int d\mathbf{z}_6\; f_{cl}(\bar{\mathbf{z}}_{12}) \\ \times A_{12}(t_1) O_{1234}(t_1) A_{34}(t_2) O_{3456}(t_2) A_{56}(t_3) \\ \times Q_{a,2}^- \Big[Q_{a,3}^+ - Q_{a,2}^+(t_1)\Big]\Big[Q_{a,5}^+ - Q_{a,4}^+(t_2)\Big] Q_{a,5}^-(t_3) \end{aligned} \tag{3.34}$$

The structure of Eq. (3.34) has essentially the same form as the full third-order response function in Eq. (3.1), but with the complex coordinates and momenta P_a and Q_a replaced by the coordinates $Q_a^\pm$.

By carrying out the same analysis as was done with the full nonlinear response function, we can derive a mean trajectory approximation to the rephasing component of the response function,

$$R_{MT}^{++-}(t_3,t_2,t_1) = \sum_{\alpha,\beta,\gamma,\delta} \kappa_{a\alpha}\kappa_{a\beta}\kappa_{a\gamma}\kappa_{a\delta}\, R_{\delta\gamma\beta\alpha}^{++-}(t_3,t_2,t_1)\,. \tag{3.35}$$

The components of R^{++-} in Eq. (3.35) are given by

$$\begin{aligned} R^{++-}_{\delta\gamma\beta\alpha}(t_3,t_2,t_1) = \frac{i\omega_a}{2^4\hbar^{2(f+1)}k_BT}\iiint d\mathbf{z}_1 d\mathbf{z}_2 d\mathbf{z}_3 \; f_{cl}(\mathbf{z}_1) \\ \times \sigma_1(N_{\delta,n}) \prod_{\nu\neq\delta} \sigma_{1/2}(N_{\nu,n}) \\ \times \prod_{\epsilon} \delta(\phi_{\epsilon,1}(t_1) - \phi_{\epsilon,2}) \, \delta(\phi_{\epsilon,2}(t_2) - \phi_{\epsilon,3}) \\ \times X^-_{\alpha,1}\left(X^+_{\beta,2}D^+_{\beta,1} - X^+_{\beta,1}(t_1)D^-_{\beta,1}\right) \\ \times \left(X^+_{\gamma,3}D^+_{\gamma,2} - X^+_{\gamma,2}(t_2)D^-_{\gamma,2}\right) X^-_{\delta,3}(t_3) \end{aligned} \tag{3.36}$$

with the complex coherent state matrix element $X^{\pm}_{\alpha,j}$ defined as

$$X^{\pm}_{\alpha,i} \equiv x_{\alpha,i} \mp \frac{i\pi_{\alpha,i}}{\mu_\alpha \Omega_\alpha} \, . \tag{3.37}$$

and $D^{\pm}_{\alpha,j}$ defined in Eq. (3.28). Similar expressions for other phase-matched components can also be derived. The structure of Eqs. (3.35) and (3.36) is identical to that in Eqs. (3.26) and (3.27), with classical trajectories connected by quantized jumps in mean action variables at fixed values of the angle. In Eq. (3.36) however, the complex coordinates $X^{\pm}_{\alpha}$ select out only specific contributions to the response function. For R^{++-} and its complex conjugate R^{--+}, only rephasing double-sided Feynman diagrams are selected.

If the dynamics of each normal mode in a system are harmonic but with an action dependent frequency, as in the first term of Eq. (2.58), the integrand in Eq. (3.36) can be shown to be independent of the initial angle variable ϕ. As the system dynamics in general are anharmonically coupled, the integrand will depend on the initial angle, but this dependence will be significantly reduced from that of the total response function, Eq. (3.26). As a result, it is numerically more efficient to calculate R^{++-}_{MT} and other phase-matched components as compared to the full $R^{(3)}_{MT}$ by about an order of magnitude. By calculating each phase-matched component in this way, we can reconstruct the full response function if desired.

3.5 Structure of the third-order response function

The mean trajectory expressions for the nth-order response function, Eq. (3.26), and for spatially phase-matched components of the third-order response, Eq. (3.36), are expressed as integrals over n classical trajectories connected by discrete jumps in the good action variables for the system at fixed values for the angles. This structure is depicted for the third-order response function in Figure 3.1. Horizontal lines represent classical trajectories, while the dashed, vertical lines indicate discontinuous transitions either up or down in the action variable of one normal mode. The labels α, β, γ, and δ indicate the mode for which this transition occurs. Each classical trajectory that enters into the mean trajectory response function therefore follows a particular "path", with a certain set of action transitions either up or down.

Transitions in the action variables are semiclassical representations of harmonic dipole transitions in the quantum response function. Harmonically forbidden dipole transitions enter implicitly into the mean trajectory response in an uncontrolled fashion through additional frequency components in the propagating trajectories. We expect that the nth-order mean trajectory response function in Eq. (3.26) will remain valid so long as the anharmonicity is small enough that harmonically allowed transitions dominate the response. Note that if additional terms to higher order in anharmonicity were included in, for example, Eq. (3.25), a mean trajectory approximation with explicit harmonically forbidden transitions could be derived. In addition, the mean trajectory treatment requires the existence of f good action variables for an f coupled oscillator system. For large enough energies and anharmonicities, these action variables may not exist, and Eq. (3.26) will be invalid.

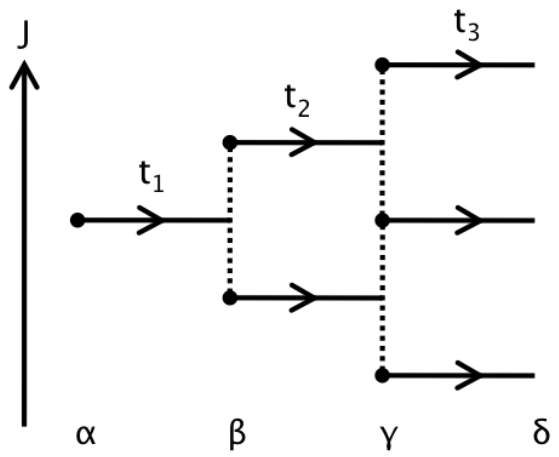

Figure 3.1: The classical trajectories needed for the calculation of the third-order response function $R^{(3)}_{MT}(t_3, t_2, t_1)$ are shown schematically in a diagram of action vs. time. The horizontal lines represent classical trajectories, and the vertical dashed lines indicate transitions in action at fixed angle. The labels α, β, γ, and δ identify the normal modes interacting with the radiation, as in Eq. (3.26).

For a one-dimensional, anharmonic system, we can gain additional insight into the structure of the mean trajectory approximation for the third-order response function by making a quasi-harmonic approximation to the phase space dynamics. As was done in relation to Eq. (2.46) for the linear response function, we assume the system dynamics are nearly harmonic with an action dependent frequency. If the classical distribution is approximated as its harmonic limit, the integrals over actions and angles in Eq. (3.27) can be performed, resulting in an analytic expression for $R^{(3)}_{MT}$,

$$\begin{aligned} R^{(3)}_{MT}(t_3, t_2, t_1) \approx & -\frac{\beta^2\hbar}{2m^2} \sum_{n=1}^{\infty} \sum_{r=n-1/2}^{n+1/2} \sum_{j=r-1/2}^{r+1/2} e^{-\beta\hbar\omega n} \sqrt{n}\,\sqrt{j} \\ & \times (\sqrt{n}\,\delta_{n,r+1/2} - \sqrt{r}\,\delta_{n,r-1/2})\,(\sqrt{r}\,\delta_{r,j+1/2} - \sqrt{j}\,\delta_{r,j-1/2}) \\ & \times \Big[\sin(\Omega_n t_1 - \Omega_j t_3) - \sin(\Omega_n t_1 + \Omega_j t_3) \\ & - \sin(\omega_n t_1 + 2\Omega_r t_2 + \Omega_j t_3) \Big] \end{aligned} \tag{3.38}$$

where the frequency Ω_n and the anharmonicity Δ are defined as

$$\Omega_n \equiv \omega(1 - n\Delta) \ , \qquad \Delta \equiv \hbar\omega/4D \, . \tag{3.39}$$

For a given value of n, each pair of values r and j correspond to one mean trajectory path from Figure 3.1. Within the same quasi-harmonic approximations we used in Eq. (3.38), we can analytically integrate Eq. (3.36) for $R_{MT}^{++-}(t_3, t_2, t_1)$ over action and angle variables to yield

$$\begin{aligned} R_{MT}^{++-}(t_3, t_2, t_1) \approx \frac{i\beta^2\hbar}{4m^2} e^{i\omega(t_1 - t_3)} \sum_{n=1}^{\infty} e^{-\beta\hbar\omega n} \Big\{ & (n+1)\sqrt{n(n+1/2)}\, e^{i\omega(n\Delta(t_3 - t_1) + \Delta t_3)} \\ & + n\sqrt{(n-1)(n-1/2)}\, e^{i\omega(n\Delta(t_3 - t_1) - \Delta t_3)} \\ & - (2n^2 + n/2)\, e^{i\omega n\Delta(t_3 - t_1)} \Big\} \, . \end{aligned} \tag{3.40}$$

This rephasing contribution to the response function is, as expected, independent of the time t_2, and at the echo condition $t_1 = t_3 = t$, the time dependence is independent of temperature. Numerical tests of the mean trajectory approximation to the full response function and to spatially phase-matched components of the response function are presented below in Section 6.

As is discussed in Chapter 1, the classical third-order response function for uncoupled anharmonic oscillators diverges linearly with time for the combination of times arguments $t_1 = t_3 = t$. [104] For $t_1 \neq t_3$, this unbounded growth is destroyed by thermal dephasing, but along the $t_1 = t_3$ diagonal, the time dependence of the rephasing contribution to the response function, Eq. (3.40), is independent of temperature and diverges in the $\hbar \to 0$ limit. This nonphysical time divergence is a result of the temporal growth of the classical monodromy matrix elements, and it indicates that the perturbation expansion for the classical response function is only valid for a finite range of temperatures. As a check on Eq. (3.38), we consider its $\hbar \to 0$ limit. Nonrephasing contributions to the

response are bounded in the classical limit, but the rephasing component of the response diverges, resulting in the quantitatively correct time divergence for the classical limit,

$$\lim_{t\to\infty}\lim_{\hbar\to 0} R^{(3)}_{MT}(t,0,t) = -\frac{t}{2m^2 D}\,. \tag{3.41}$$

The approximation to the mean trajectory response function, Eq. (3.38) is not exactly correct in the classical limit due to the quasi-harmonic approximation for the dynamics, but it does reproduce the correct unbounded temporal growth.

It is useful to interpret the mean trajectory approximation to the response function in terms of double-sided Feynman diagrams. As discussed in Appendix D, these diagrams provide a visual representation of the averaged polarization, with the two sides corresponding to the time dependence of the ket and bra sides of the density matrix. For the third-order response $R^{(3)}(t_3, t_2, t_1)$, there are four interactions between the system and the field, where the final interaction corresponds to the emission of the observed signal. Each of the first three interactions provides a factor of the normal mode momentum $\boldsymbol{\pi}$ in Eq. (3.27), while the emitted signal provides a factor of the coordinate $\mathbf{x}$. The jumps in action between $\{\mathbf{z}_1(t_1), \mathbf{z}_2\}$ and $\{\mathbf{z}_2(t_2), \mathbf{z}_3\}$ correspond to the second and third interactions. If mode β gains energy from the field at time t_1, the action N_β will increase by 1/2. Similarly, if mode γ loses energy to the field at time t_2, N_γ will decrease by 1/2.

Each combination of jumps in action corresponds to one "path" in Figure 3.1. Each of these paths represents the contribution to the response function from a collection of Feynman diagrams. [2, 13] In Figure 3.2 we show the "up-down" path corresponding to $N_{\beta,2} = N_{\beta,1} + 1/2$ and $N_{\gamma,3} = N_{\gamma,2} - 1/2$ for the third-order response function. Three double-sided Feynman diagrams that contribute

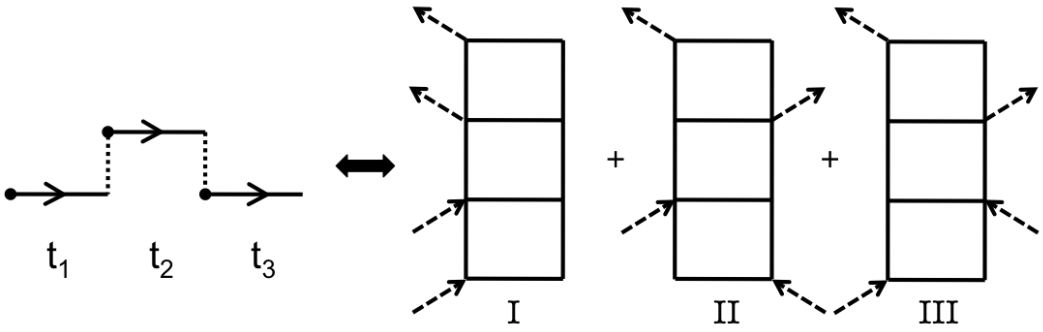

Figure 3.2: The "up-down" path from Figure 3.1 is depicted along with the corresponding double-sided Feynman diagrams. Diagrams I and III are non-rephasing, while diagram II is of the rephasing type. During time t_2, diagrams II and III describe a population, while diagram I represents a two-quantum coherence. Each possible path in Figure 3.1 contains contributions from these three types of diagrams.

to this path are also depicted. Diagram I is of the nonrephasing [48, 49] type with the system in a two-quantum coherence during time t_2. Diagram III is also nonrephasing but describes a population during t_2. Similarly, diagram II describes population dynamics during t_2 but is of the rephasing type. This mean trajectory path also contains diagrams where the first interaction with the field results in emission of a photon, rather than absorption.

The half- and full-integer quantization of action variables can be interpreted in terms of coherences and populations. When the action of mode α is integer quantized, the primary frequency of α corresponds to the frequency of a one-quantum coherence. For example, $N_\alpha = 1$ and $N_\alpha = 2$ correspond to the $0, 1$ and $1, 2$ coherences, respectively. Half-integer quantization such as $N_\alpha = 3/2$ corresponds to an average of the $0, 1$ and $1, 2$ frequencies. Therefore, half-integer quantization can be interpreted as one-half the frequency of a two-quantum coherence. To more clearly show this, we will examine the mean trajectory approximation to the third-order response function, Eq. (3.26), for a single chro-

mophore degree of freedom in the limit of small anharmonicity as was done in Eq. (3.38). This analysis will clearly demonstrate how each mean trajectory path in Figure 3.1 includes contributions from both rephasing and nonrephasing double-sided Feynman diagrams, as discussed in Figure 3.2.

For the "up-down" mean trajectory path depicted in Figure 3.2, the combination of normal-mode momenta and coordinates that enters into Eq. (3.27) is given by $\pi_1\ \pi_2\ \pi_2(t_2)\ x_3(t_3)$. To zeroth-order in anharmonicity ε, the dynamics of z_j are harmonic, and this product can be written as

$$\pi_1\ \pi_2\ \pi_2(t_2)\ x_3(t_3) \propto \sin(\phi_1)\sin(\phi_2)\sin(\phi_2(t_2))\cos(\phi_3(t_3))\,. \tag{3.42}$$

Integration over all angle variables then yields

$$\begin{aligned}\iiint d\phi_1 d\phi_2 d\phi_3\ \pi_1\ \pi_2\ \pi_2(t_2)\ x_3(t_3)\ \delta(\phi_3-\phi_2(t_2))\delta(\phi_2-\phi_1(t_1))&\\ \propto \sin(\lambda_1\omega t_1+\lambda_3\omega t_3)+\sin(\lambda_1\omega t_1+2\lambda_2\omega t_2+\lambda_3\omega t_3)&\\ -\sin(\lambda_1\omega t_1-\lambda_3\omega t_3)&\end{aligned} \tag{3.43}$$

where $\lambda_j\omega$ is the vibrational frequency of a mode with action N_j. The first two sine terms in Eq. (3.43) give the contribution to the response function from nonrephasing diagrams. The first term corresponds to the case of a population during time t_2 as in Diagram III in Figure 3.2, while the second term corresponds to a two-quantum coherence during t_2 as in Diagram I in Figure 3.2 The third sine function corresponds to the rephasing Diagram II in Figure 3.2.

All paths that contribute to $R^{(3)}_{MT}(t_3,t_2,t_1)$ generate these three sine functions upon integration over angle variables. The different action jumps in each path serve to alter the frequency $\lambda_j\omega$ in each trajectory z_j. As mentioned previously, integer quantization for the actions N_1 and N_3 generates frequencies in Eq. (3.43) corresponding to one-quantum coherences. The half-integer quantization for

N_2 on the other hand only enters into Eq. (3.43) in the second sine function as $2\lambda_2\omega t_2$. The factor of 2 in this expression results in a frequency during time t_2 that corresponds to a two-quantum coherence. To illustrate, we consider the "up-down" path from Figure 3.1 with $N_1 = 1$, $N_2 = 3/2$, and $N_3 = 1$. In this case, the action dependent frequencies are given by

$$\lambda_1\omega = \omega\,(1 - J_1\omega/2D) = \omega_{10} \tag{3.44}$$

$$\lambda_2\omega = \omega\,(1 - J_2\omega/2D) = \frac{1}{2}\omega_{20} \tag{3.45}$$

$$\lambda_3\omega = \lambda_1\omega = \omega_{10} \tag{3.46}$$

where ω_{ij} is the frequency of the i, j coherence. With these values for the actions, Eq. (3.43) becomes

$$\sin(\omega_{10}t_1 + \omega_{10}t_3) + \sin(\omega_{10}t_1 + \omega_{20}t_2 + \omega_{10}t_3) - \sin(\omega_{10}t_1 - \omega_{10}t_3)\,. \tag{3.47}$$

The first and third terms in Eq. (3.47) correspond to diagrams where the system is in the $1,1$ population during time t_2, while the second term corresponds to the $0,2$ coherence. For the "down-up" path in Figure 3.1 however, $N_2 = 1/2$ and ω_{20} in the second term of Eq. (3.47) is replaced by ω_{-11}. The mean trajectory approximation to the third-order response function thus contains a spurious contribution to $R^{(3)}_{MT}$ from photon emission from the ground state due to this $N_\alpha = 1/2$ term. While this unphysical term is numerically unimportant for the calculation of $R^{(3)}_{MT}(t_3, 0, t_1)$, it is non-negligible for $t_2 \neq 0$. We can correct for these spurious ground state emissions by breaking the total response function into phase-matched components as in Eq. (3.36), which facilitates their removal.

For f coupled oscillators, $R^{(n)}$ contains f^{n+1} terms $R^{(n)}_{\zeta\xi\ldots\beta\alpha}$, each of which has 2^{n-1} possible combinations of jumps in the action. For each of these terms, an average over angle variables and quantized actions must be performed. However,

as Eq. (3.27) does not contain any oscillatory phases or time divergences, this mean trajectory approach is far more computationally efficient than the original semiclassical Herman-Kluk response function. For $R^{(3)}(t, 0, t)$ of an ensemble of uncoupled anharmonic oscillators, the mean trajectory approximation is at least four orders of magnitude more numerically efficient than the Herman-Kluk calculation. For higher dimensional, coupled systems, the Herman-Kluk treatment is numerically impractical, while the mean trajectory treatment is only more difficult than in one dimension due to the requirement of identifying good action variables. We can additionally simplify Eq. (3.26) by noting that each component $R^{(n)}_{\zeta\xi\ldots\beta\alpha}$ carries a coefficient of $\kappa_{a\alpha}\kappa_{a\beta}\cdots\kappa_{a\xi}\kappa_{a\zeta}$, and many of these terms will be numerically insignificant if $\kappa_{a\epsilon}$ is small. This would be the case for a chromophore degree of freedom labeled a coupled to a mode labeled b that is far from resonance. Only when significant energy transfer between oscillator modes a and b occurs is it necessary to consider action jumps in the b degree of freedom.

3.6 Numerical results

As with the linear response function in Chapter 2, in order to calculate nonlinear mean trajectory response functions, we must propagate classical trajectories at fixed values of the good action variables. In addition, between trajectories we must execute jumps in action variables at fixed angle. While good action and angle variables may not exist for coupled systems with large anharmonicities and energies, for the systems investigated here, perturbation theory as discussed in Appendix A will suffice to determine approximate action and angle variables. For strongly coupled systems, or for systems with low order

resonances, alternate methods as discussed in Appendix C may become necessary. [127,128,132,133]

Rather than executing jumps at fixed values for the angle, there are several alternative methods which can be computationally useful for complicated systems where determining the good angle variable is challenging. For systems that are approximately harmonic, the coordinate and momentum at a jump can simply be scaled by a factor $\sqrt{1 \pm \hbar/2J_\alpha}$. Another alternative which is suggested by Eq. (3.16) is to choose the initial phase point of the $j+1$th trajectory relative to the jth trajectory by maximizing the coherent state overlap $|\langle \mathbf{z}_j(t_j)|\mathbf{z}_{j+1}\rangle|^2$ while constraining the action variables. For the systems investigated below, each of these methods for performing trajectory transitions results in qualitatively similar nonlinear response functions. For large values of anharmonicity, we expect that the harmonic rescaling of coordinate and momenta will fail.

As an initial test of the mean trajectory approximation for nonlinear response functions, we compare in Figure 3.3 the quantum and mean trajectory third-order response function with $t_2 = 0$, $R^{(3)}(t, 0, t)$, for a thermal ensemble of uncoupled Morse oscillators with parameters $\beta D = 40$, $\beta\hbar\omega = 2$. As discussed in Chapter 1, the third-order response is dominated by a fast frequency 2ω that is approximately twice the principal $0, 1$ coherence frequency of the Morse oscillator system. The slow recurrence frequency $\Delta\omega$ is due to the difference between the $0, 1$ and $1, 2$ coherence frequencies for the Morse oscillator. High frequency components in the response result from forbidden harmonic dipole transitions. Comparing panels (a) and (b) of Figure 3.3, the mean trajectory approximation is seen to quantitatively capture the main features of the quantum response function for both long and short times. The small differences in the envelope shape

between the quantum and mean trajectory response functions are primarily due to an effective temperature difference that results from the high temperature approximation to the coherent state matrix element of the density operator.

In panel (c) of Figure 3.3, we plot the third-order mean trajectory response function with $\sigma_1(N_1)$ in Eq. (3.26) set to its $k_{max} = 1$ value of $\Big(1 + 2\cos(2\pi N_1)\Big)$. Transitions between trajectories are still performed for quantized values of action at fixed angle. The result is an approximate response function which agrees with the quantum result for short times, but quickly becomes incorrect. Had we relaxed the transition in action condition in a similar manner, the resulting approximation to the response function would again be correct for short times, but would then decay to zero, as with the linear response in Chapter 2.

In Figure 3.4, the quantum and mean trajectory third-order response functions are compared for an ensemble of uncoupled Morse oscillators at high temperatures (a), large anharmonicity (b), and near the classical limit (c). As compared to the low temperature case in Figure 3.3, the higher temperature response function in panel (a) appears to decease linearly with time for $\omega t < 50$ before recurring with the same recurrence period as in Figure 3.3(a). Increasing the anharmonicity in panel (b) has the effect of reducing the recurrence period, while in the near-classical limit, panel (c), the recurrence period is pushed towards infinite time. In each case, the mean trajectory treatment accurately reproduces the important quantum features of the response function.

We further test the mean trajectory treatment in Figure 3.5 by computing $R^{(3)}_{MT}(t, 0, t)$ for a thermal ensemble of uncoupled quartically perturbed harmonic oscillators, as in Figure 2.13 of Chapter 2. Once again, the mean trajectory treatment is quantitatively accurate. We can also compute the two-time third-order

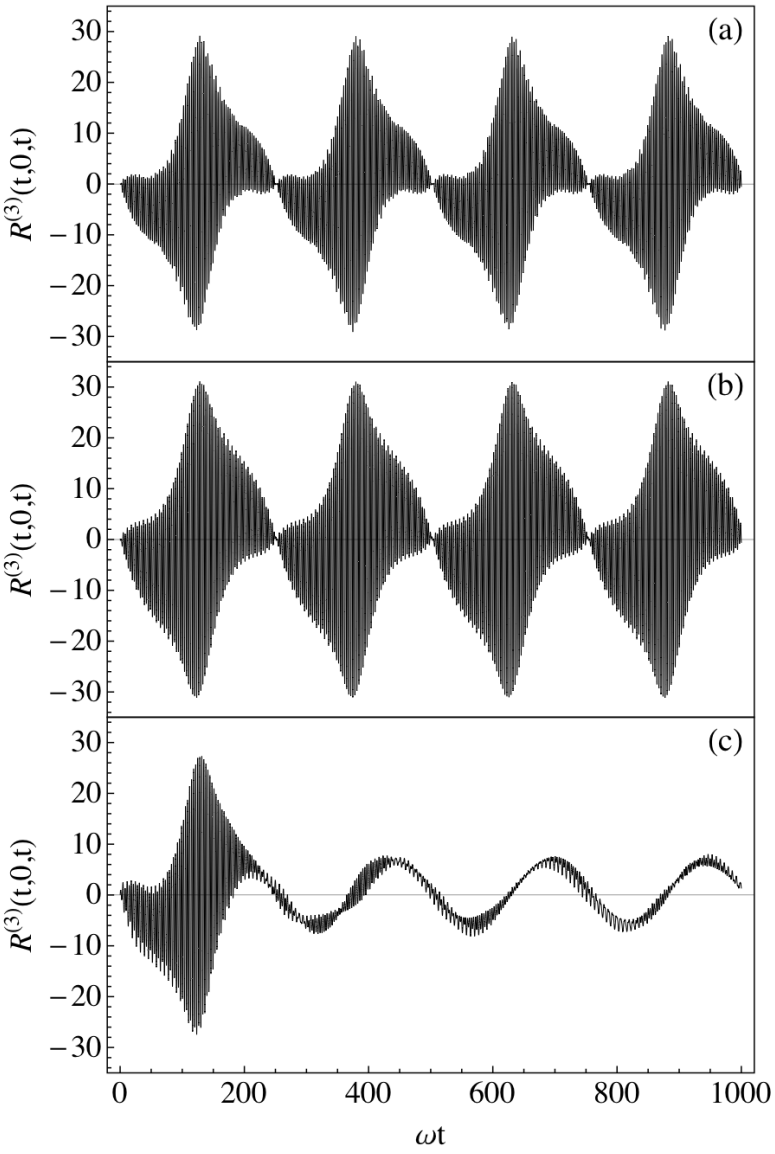

Figure 3.3: The quantum (a) and mean trajectory (b) third-order response functions for a thermal ensemble of uncoupled Morse oscillators with parameters $\beta D = 40$, $\beta\hbar\omega = 2$ are compared and are in quantitative agreement. Panel (c) shows the mean trajectory response with $k_{max} = 1$, as in Figure 2.12 of Chapter 2.

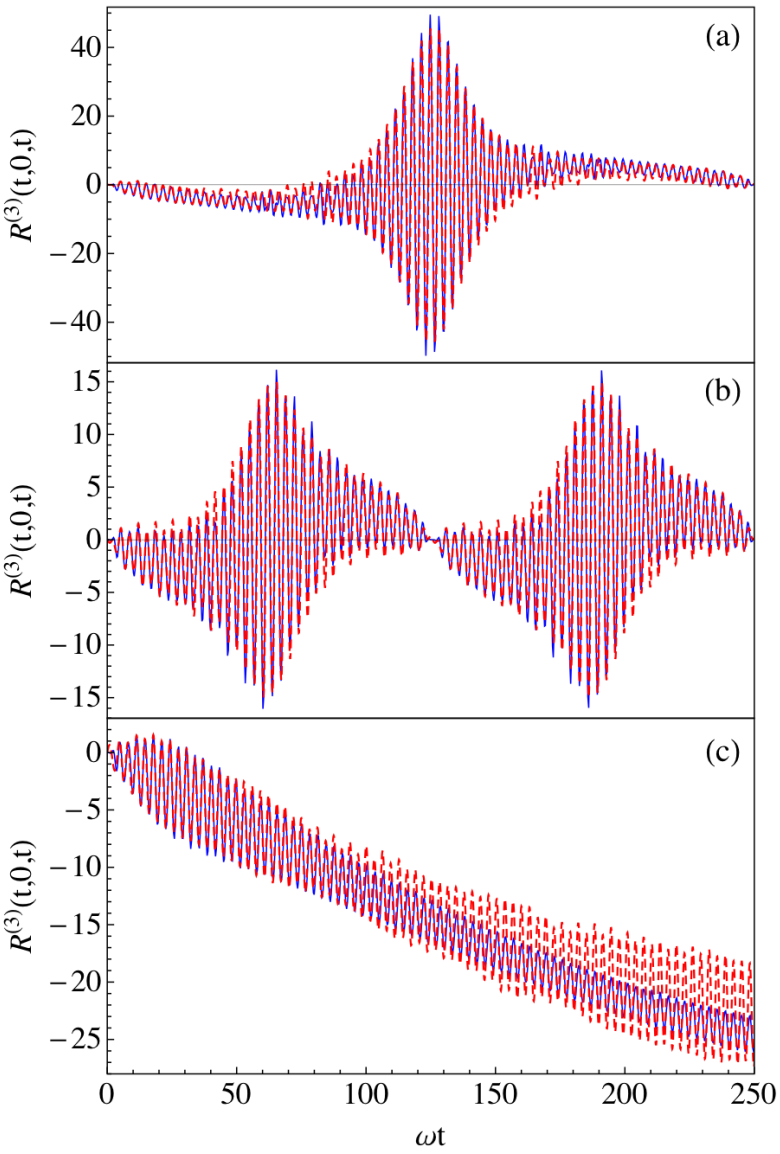

Figure 3.4: The quantum (blue) and mean trajectory (red, dashed) third-order response functions are compared for the same system as in Figure 3.3. Panel (a) shows a high temperature case, with $\beta D = 20$, $\beta\hbar\omega = 1$, while panel (b) has a larger anharmonicity, $\beta D = 20$, $\beta\hbar\omega = 2$. In panel (c), the anharmonicity is reduced with $\beta D = 40$, $\beta\hbar\omega = 2/5$, and the response trends towards the classical limit over the time scale plotted.

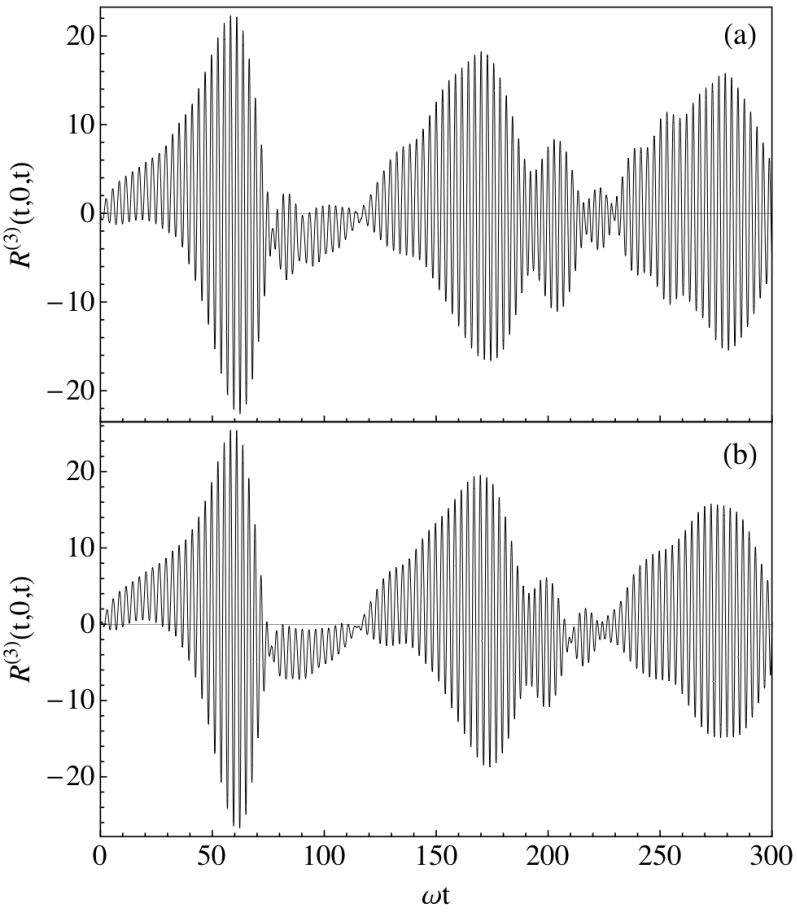

Figure 3.5: The quantum (a) and mean trajectory (b) third-order response functions are compared for a thermal ensemble of quartically perturbed harmonic oscillators with parameters $\beta\hbar\omega = 1$ and $(a/\beta m^2\omega^4)^{1/4} = 0.398$.

response function $R^{(3)}_{MT}(t_3, 0, t_1)$, as depicted in Figure 3.6 for an ensemble of uncoupled Morse oscillators with the same parameters as in Figure 1.5(b) of Chapter 1. The mean trajectory response accurately reproduces both the t_1 and t_3 dependence of the quantum response function.

Mean trajectory results for the third-order response function were calculated for a thermal ensemble of a chromophore Morse oscillator labeled *a* bilinearly

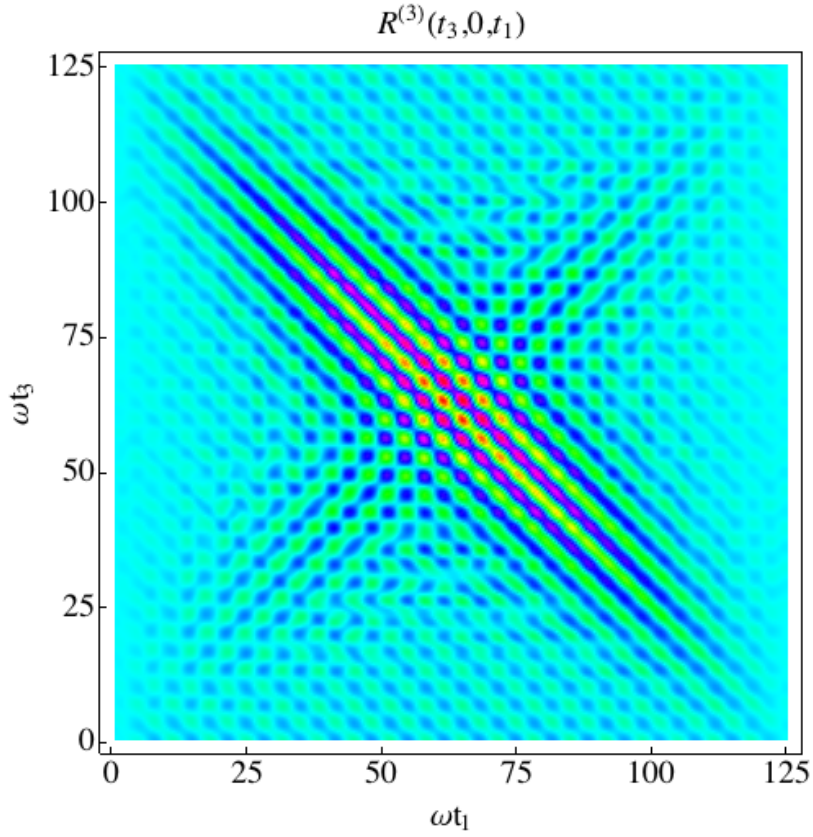

Figure 3.6: The mean trajectory third-order response function $R^{(3)}(t_3, 0, t_1)$ for an ensemble of Morse oscillators with parameters $\beta D = 10$, $\beta\hbar\omega = 1$ is plotted vs. both t_1 and t_3. The mean trajectory result compares well to the quantum result in panel (b) of Figure 1.5.

coupled to a harmonic oscillator b with parameters $D_a/k_BT = 40$, $\hbar\omega_a/k_bT = 2$, $m_a = m_b$, $\omega_b = 0.9\omega_a$, and $c_{ab} = 0.1$. As with the linear response calculation for the same system and parameters in Figure 2.14, the frequencies were chosen so that energy transfer between normal modes is numerically relevant, but there are no resonances at low energies. As in Figure 2.14, the intermediate frequency components seen in Figure 3.7 are due to the frequency difference between the two coupled oscillators, $\omega_a - \omega_b$. The very slow recurrence frequency results from the anharmonicity of the chromophore oscillator, as in the case of uncoupled Morse oscillators. It can be seen that even for coupled oscillator systems,

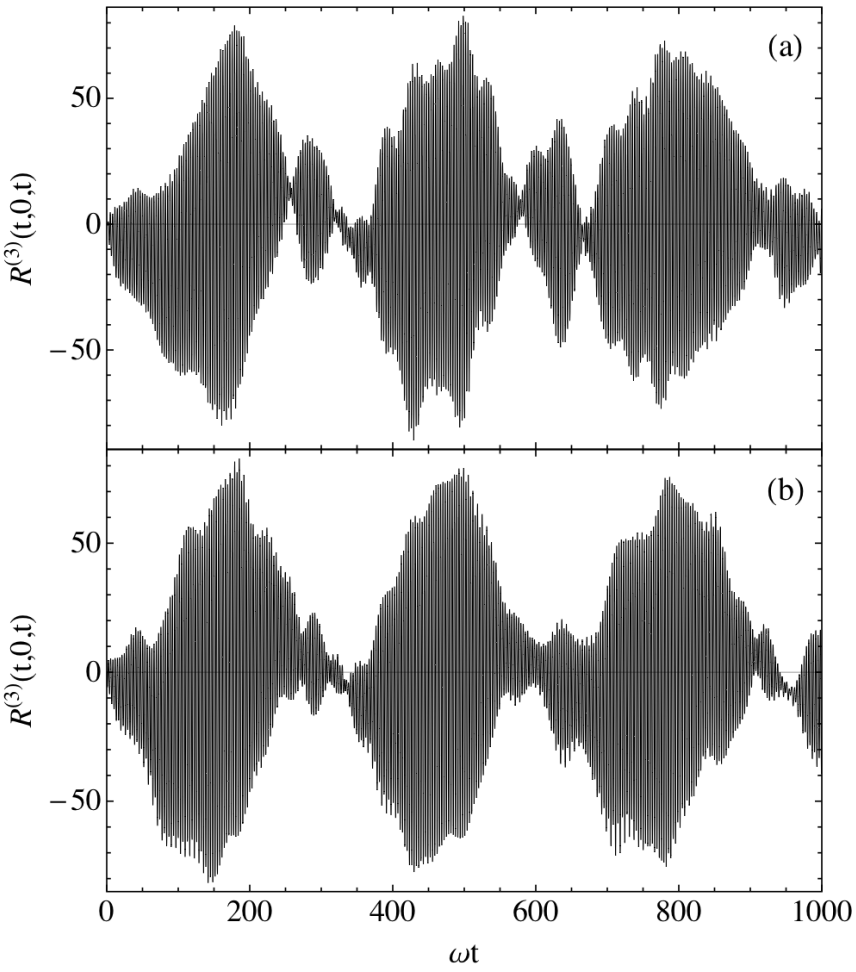

Figure 3.7: The third-order response function is shown for a thermal ensemble of a chromophore Morse oscillator labeled a bilinearly coupled to a harmonic oscillator b with parameters $D_a/k_BT = 40$, $\hbar\omega_a/k_bT = 2$, $m_a = m_b$, $\omega_b = 0.9\omega_a$, and $c_{ab} = 0.1$. Panel (a) displays the quantum result, while panel (b) is the mean trajectory result. These calculations have been repeated for larger coupling constants c_{ab} with similar accuracy.

the mean trajectory treatment accurately reproduces the main quantum features of the response function.

In Figure 3.8, we calculate the third-order response as a function of the wait-

ing time t_2 for fixed $\omega t_1 = 0$ and $\omega t_3 = 5$. As discussed in Section 5, the mean trajectory approximation to the response function contains an unphysical term due to emission from the ground state. This term results in a mean trajectory response function which does not agree well with the quantum result, as is seen by comparing the quantum result in panel (a) with the original mean trajectory result in panel (b). When the response function is split into phase-matched components and the spurious term removed, the resulting mean trajectory response function, depicted in panel (c), is in good agreement with the quantum result. These t_2 calculations can be carried out for other combinations of t_1 and t_3 with similar accuracy.

The real part of the rephasing phase-matched component of the third-order response function, $R^{++-}_{MT}(t, 0, t)$, is compared to the exact quantum results in Figure 3.9(a) for an ensemble of one-dimensional Morse oscillators with the same parameters as in Figure 3.3. This phase-matched component of the response is dominated by the slow frequency $\Delta\omega$ due to the anharmonicity of the Morse oscillator, as discussed in relation to Eq. (3.40). The fast frequency oscillations superimposed on the dominant slow oscillation are a result of harmonically forbidden dipole transitions. In panel (b) of Figure 3.9, the quantum and mean trajectory results for the rephasing contribution to the response function are compared for the quartically perturbed oscillator system in Figure 3.5. As with the linear and full third-order response functions, the mean trajectory approximation is not as accurate for this quartically perturbed system as for the Morse oscillator. Finally, $R^{++-}_{MT}(t, 0, t)$ is calculated in Figure 3.10 for the coupled oscillator system in Figure 3.7. For the coupled oscillator system, $R^{++-}(t, 0, t)$ contains intermediate frequencies due to energy transfer between the oscillator normal modes. Once again, the mean trajectory result accurately captures the principal

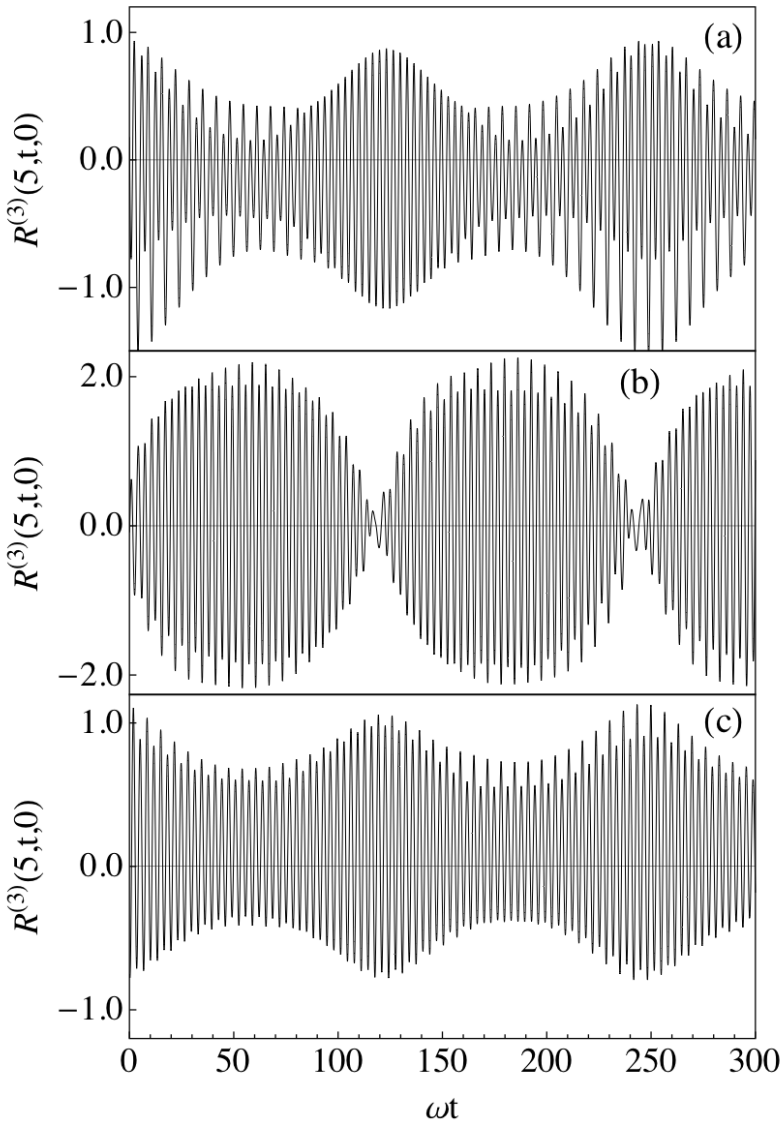

Figure 3.8: The t_2 dependence of the third-order response function at $\omega t_1 = 0$ and $\omega t_3 = 5$ is shown for a thermal ensemble of Morse oscillators with parameters $\beta D = 40$, $\beta\hbar\omega = 2$. The quantum result is shown in panel (a), while panel (b) is the mean trajectory result with the spurious ground state emission term included, and panel (c) is the mean trajectory response function with this incorrect term removed.

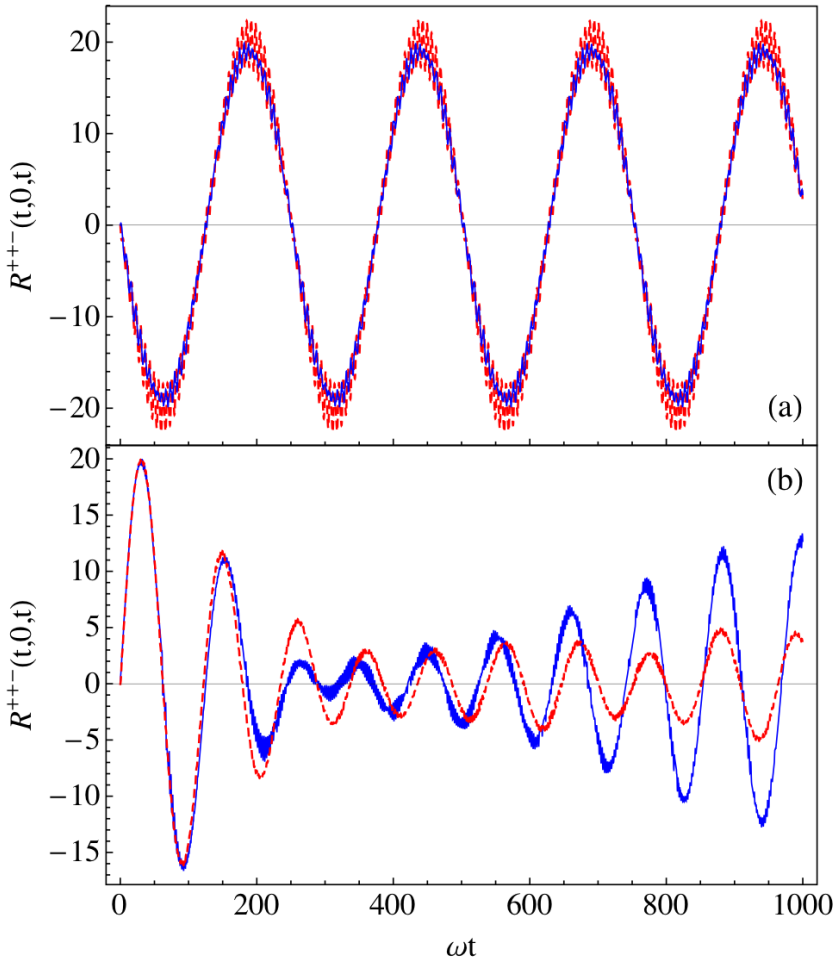

Figure 3.9: The real part of the spatially phase-matched component $R^{++-}(t, 0, t)$ is shown in panel (a) for a thermal ensemble of Morse oscillators with the same parameters as in Figure 3.3, and in panel (b) for an ensemble of quartically perturbed oscillators with the same parameters as in Figure 3.5. In both panels, the blue curve indicates the quantum result, while the red, dashed curve is the mean trajectory result.

features of the quantum rephasing response function.

The mean trajectory approximation to the nth-order response function, Eq. (3.26), can in principle be applied to any number of coupled oscillators. For

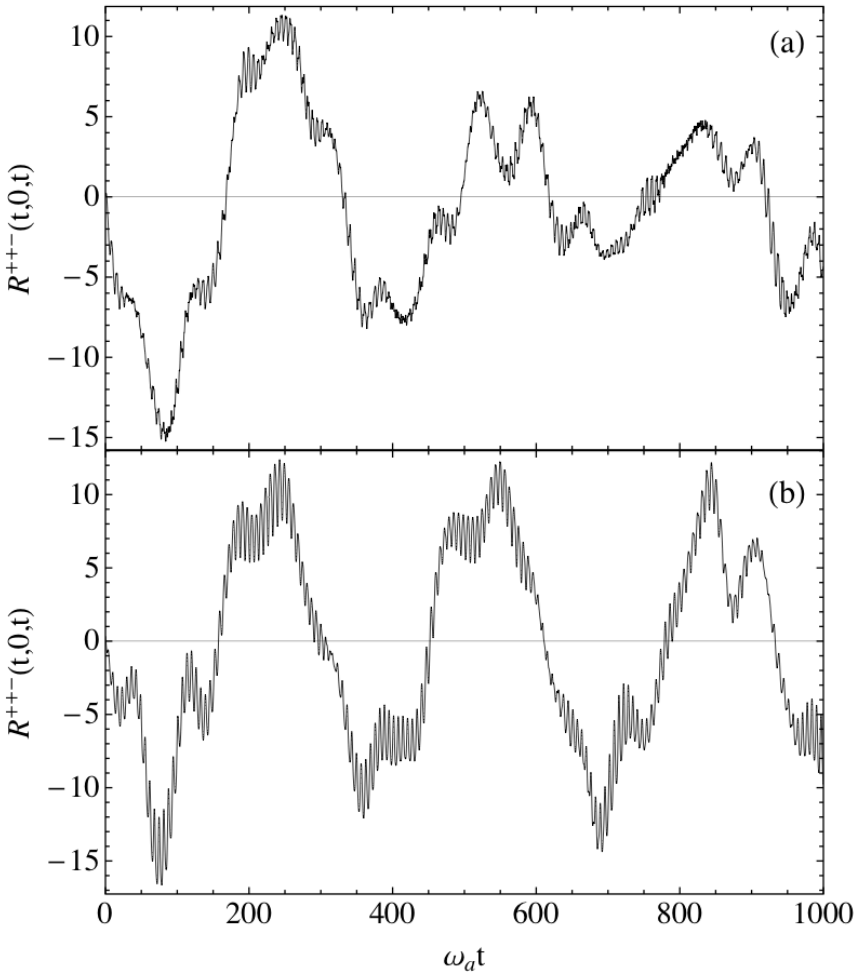

Figure 3.10: The quantum (a) and mean trajectory (b) results for the real part of the rephasing phase-matched component $R^{+++-}(t, 0, t)$ are shown for the same coupled oscillator potential and parameters as in Figure 3.7.

the case of a chromophore oscillator coupled to a bath of oscillators far from resonance however, we can simplify the calculation by noting that $\kappa_{a\beta}$ will be very small for $a \neq \beta$, provided the coupling is not too large. Thus in the pure dephasing limit, we can ignore all terms in Eq. (3.26) that involve transitions in the action variables of the bath. In addition, the bath actions will be very close to their zero-coupling, harmonic values. For the case of one slightly an-

harmonic chromophore weakly coupled to a classical harmonic bath, Akiyama and Loring [48, 49] (AL) have developed an analytic expression for the rephasing and nonrephasing components of the third-order vibrational response function. We use Eqs. (30)–(38) of Ref. [48] to calculate an approximate quantum third-order response function for one Morse oscillator bilinearly coupled to a harmonic bath. The bath oscillators are governed by an Ohmic density of states, and the chromophore oscillator coordinate obeys a generalized Langevin equation with a friction kernel given by [30, 31]

$$\eta(t) = \frac{2\eta_0}{\pi} \frac{\lambda}{\lambda^2 + t^2} \, . \tag{3.48}$$

In Figure 3.11, the AL (a) and mean trajectory (b) third-order response functions $R^{(3)}_{MT}(t, 0, t)$ are shown for a thermal ensemble of a chromophore Morse oscillator labeled a coupled to 19 low frequency harmonic oscillators with frequencies chosen uniformly from an Ohmic density of states. The Morse oscillator has parameters given by $D_a/k_BT = 40$ and $\hbar\omega_a/k_BT = 2$, while the bath is given by $\omega_a m_a \eta_0 = 0.5$ and $\omega_a \lambda = 100$. As expected, the interaction with the bath results in the decay of the response function on the timescale shown, as is captured by the mean trajectory treatment. Inspection of Figure 3.11(b) also shows that the mean trajectory response function contains additional rapid oscillations that are not present in the AL approximation. As in Figure 3.3, these additional frequencies arise from harmonically forbidden dipole transitions, which are absent in the AL result in Figure 3.11(a).

The effects of coupling can be more easily identified in the frequency domain. Figure 3.12 displays the absolute magnitude of the Fourier transform of the third-order response function with respect to t_1 and t_3 with the waiting time $t_2 = 0$, $|\tilde{R}^{(3)}_{MT}(\omega_3, 0, \omega_1)|$, for a Morse oscillator labeled a bilinearly coupled to a harmonic oscillator labeled b with parameters $D_a/k_BT = 50$, $\hbar\omega_a/k_bT = 7.5$,

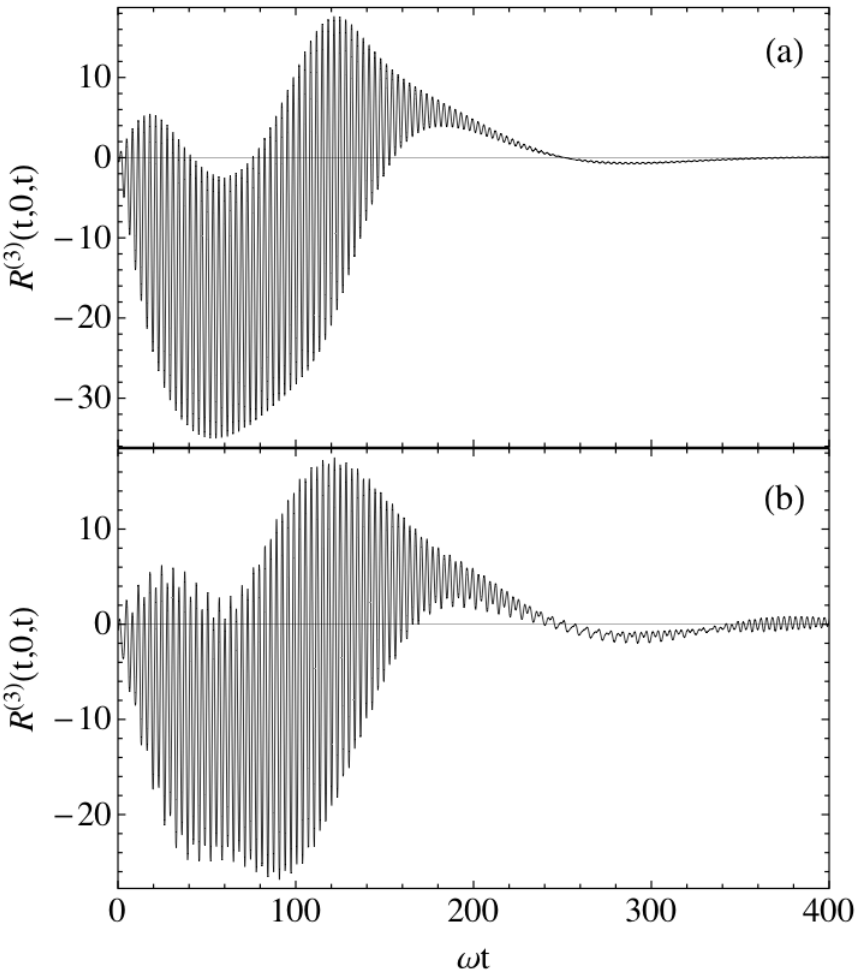

Figure 3.11: The third-order response function $R^{(3)}(t, 0, t)$ is shown for one chromophore Morse oscillator bilinearly coupled to a harmonic bath with an Ohmic density of states with $D_a/k_BT = 40$, $\hbar\omega_a/k_BT = 2$, $\omega_a m_a \eta_0 = 0.5$, and $\omega_a \lambda = 100$. Panel (a) is calculated from Eqs. (30)–(38) of Ref. [48], and panel (b) shows the mean trajectory result.

$m_a = m_b$, $\omega_b = 0.8\omega_a$, and $c_{ab} = 0.1$. Ω_a and Ω_b label the harmonic frequencies of the a and b normal modes. In panel (a), the quantum response function is shown, with blue regions corresponding to large amplitudes and blank regions corresponding to small amplitudes. The diagonal peaks A and C derive from the fundamental frequencies of the Morse a and harmonic b modes respectively. Peak C has nonzero intensity by virtue of the coupling of modes a and b. Peak B comes from contributions to the response function where the first interaction excites the chromophore oscillator to a $0,1$ coherence, and the third interaction produces the $1,2$ coherence. The frequency difference between A and B is the anharmonicity of the a oscillator. Similarly, the small splitting present in peak C is due to the coupling-derived anharmonicity in mode b. The peaks labeled D and the other unlabeled peaks are cross peaks between oscillators a and b, and are thus primary signatures of coupling.

For comparison purposes, the classical-mechanical response function [27,45] for the same coupled oscillator system is shown in Figure 3.12(b). Comparison of the quantum (a) and classical (b) results indicates that the classical response function is qualitatively incorrect for these parameters. For uncoupled Morse oscillators, the classical third-order response in the time domain diverges for $t_1 = t_3$. [40, 42–45] However, in the limit of high temperatures, or for systems with a bath that rapidly damps the response function, the classical result will increase in accuracy.

Panel (c) in Figure 3.12 shows the mean trajectory result for $\left|\tilde{R}^{(3)}_{MT}(\omega_3, 0, \omega_1)\right|$. The mean trajectory response function reproduces the main features of the quantum response in the frequency domain. In panel (d), a low frequency bath is added to the coupled Morse and harmonic oscillator system. The bath cou-

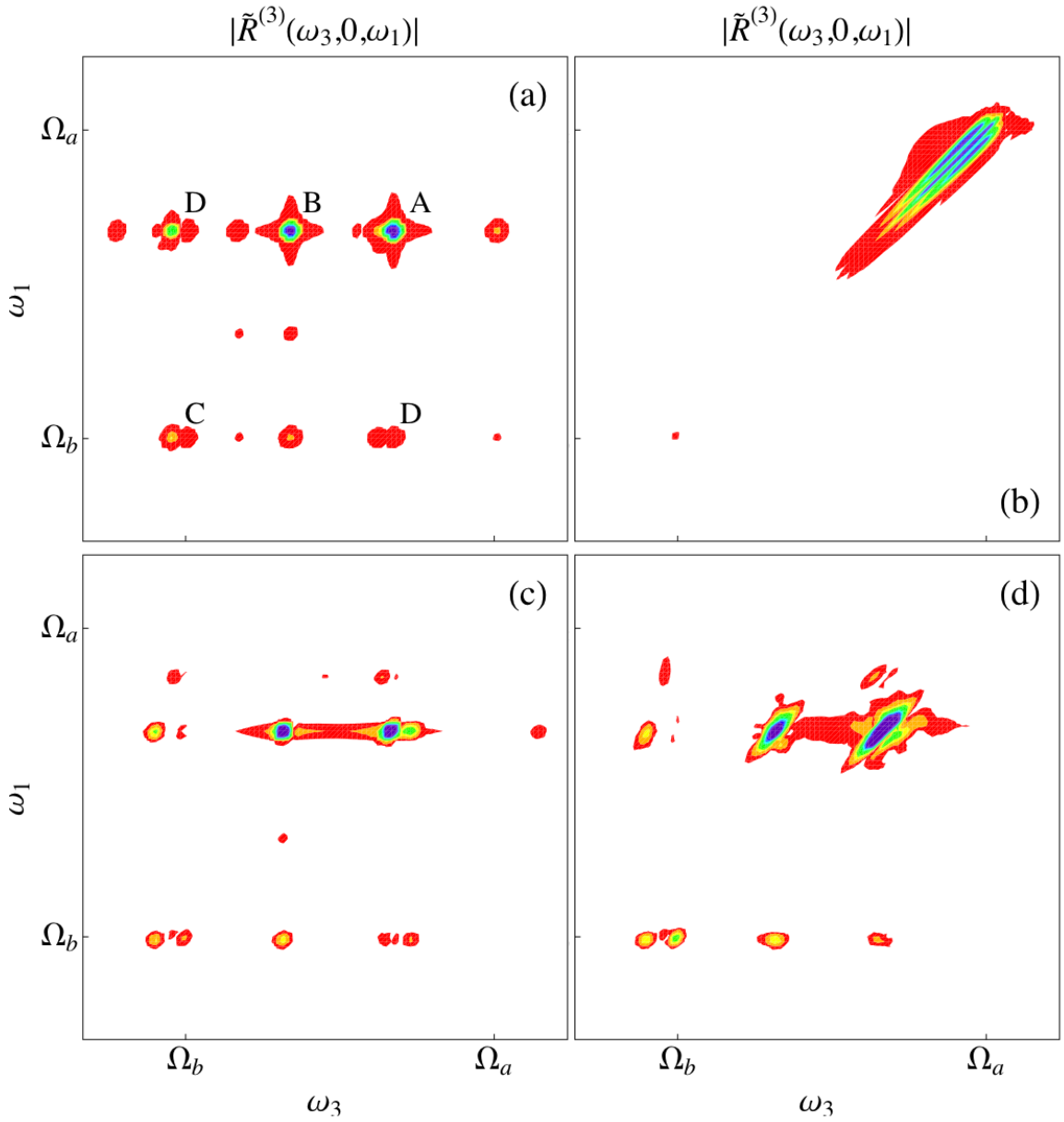

Figure 3.12: The absolute magnitude of the Fourier transform of the third-order response function, $\left|\tilde{R}^{(3)}(\omega_3, 0, \omega_1)\right|$, is shown for the two coupled oscillator system described in Figure 3.7 with $D_a/k_BT = 50$, $\hbar\omega_a/k_BT = 7.5$, $m_a = m_b$, $\omega_b = 0.8\omega_a$, and $c_{ab} = 0.1$. Panel (a) shows the quantum response, panel (b) shows the classical-mechanical response, and panel (c) is the mean trajectory result. In panel (d), a harmonic bath with $\omega_a m_a \eta_0 = 0.5$ and $\omega_a \lambda = 100$ is added to the two-oscillator system, broadening the spectral features.

ples to oscillator a and has an Ohmic density of states with $\omega_a m_a \eta_0 = 0.5$ and $\omega_a \lambda = 100$, as in Figure 3.11. As expected, the bath broadens the spectral features of the chromophore oscillator, stretching peaks 'A' and 'B' along the diagonal. For large values of η_0, the mean trajectory response begins to resemble the classical result in panel (b). For each case investigated here, the mean trajectory approximation has proven accurate. Unlike the original semiclassical response function based on HK dynamics in Eq. (2.7), the mean trajectory result is computationally tractable even for coupled systems.

3.7 Summary

In this chapter, we have analyzed the vibrational nonlinear response function within the Herman Kluk approximation to the propagator. As was the case for the linear response function in Chapter 2, integration of the semiclassical phase over stationary points in the action difference ΔJ for a pair of trajectories resulted in the quantization of mean action variables. However unlike the linear response function, the ratio of coherent state overlaps $O_{jklm}(t)$ in Eq. (3.2) alters the semiclassical phase for all but one pair of trajectories so that there are no longer any stationary points in ΔJ. Instead, the mean action and angle for a trajectory pair is connected to the mean action and initial angle for the subsequent trajectory pair by a quantized jump in action variables at fixed angle. The resulting mean trajectory approximation to the nth-order response function requires the integration over n classical trajectories propagating on the exact potential energy surface. We have also derived a mean trajectory approximation to spatially phase-matched components to the third-order response function associated with nonlinear signals propagating at specific wavevectors.

The mean trajectory method, developed here for response functions, could also be applied to other observables, such as time correlation functions, in which quantum coherence effects arise semiclassically from interference between classical trajectories. The notion of propagating classical trajectories with quantized action variables originates in the earliest conceptions of quantum mechanics and has been extensively applied numerically to problems in chemical dynamics. [122,123,126] Rather than starting with a "quasiclassical" approximation for the response function, however, we have established a connection between this venerable idea and the HK semiclassical propagator. Kryvohuz and Cao [42] have also derived quasiclassical expressions for response functions in the microcanonical ensemble by starting with the classical result and then quantizing the phase space around the energy surface.

We have numerically tested the mean trajectory approximation for both the entire third-order response function and its rephasing component for a variety of one-dimensional anharmonic systems, for coupled oscillator systems, and for a chromophore oscillator coupled to an off-resonance bath of harmonic modes. In each case, the mean trajectory treatment accurately reproduced the important quantum features in the response function. Mean trajectory calculations are numerically simple to implement due to the lack of an oscillatory semiclassical phase— at least four order of magnitude faster than the HK third-order response function for an ensemble of one-dimensional anharmonic oscillators. The associated cost, however, is the requirement of computing good action and angle variables for the system of interest. The mean trajectory method is therefore valid only in the regime of quasiperiodic motion. However, when applicable, it is a straightforward and practical semiclassical method that includes quantum coherence effects for nonlinear vibrational response functions.

CHAPTER 4

THE SEMICLASSICAL DENSITY OF STATES, WAVEPACKET PROPAGATION, AND CONNECTIONS TO RESPONSE FUCTIONS

4.1 Introduction

The quantum coherence effects of correlation functions and vibrational response functions arise from interference between pairs of quantum propagators $\hat{K}(t)$ and $\hat{K}^{\dagger}(t)$, as discussed in Chapters 2 and 3. The propagation of the wavefunction, on the other hand, only requires a single propagator $\hat{K}(t)$. The time propagation of the wavefunction or a wavepacket is an important problem in quantum mechanics due to its relevance to scattering, spectroscopic processes, photochemistry, and the calculation of vibrational bound states. [80, 134] Quantities such as the density of states can also be calculated from the trace of the quantum propagator. As was the case for response functions, fully quantum mechanical descriptions for wavepacket propagation are numerically challenging for large, coupled systems. As a result, semiclassical techniques as described in Section 7 of Chapter 1 have been employed to approximate the true quantum dynamics. [76, 92, 135, 136]

We have previously described how the nth-order vibrational response function within the Herman-Kluk approximation to the propagator accurately captures quantum coherence information. Integration over action differences between a pair of propagating trajectories produces a quantization condition on the mean action of the trajectory pair that is equivalent to Bohr-Sommerfeld quantization for the anharmonic oscillator systems studied. However, the anal-

ysis of semiclassical quantization with the older Van Vleck propagator has a long history. For example, Berry and Tabor [137,138] and Berry and Mount [53] discuss the structure of the density of states within the root-search formulation of the Van Vleck propagator given by Eq. (1.42) of Chapter 1. [139] We shall seek to connect these ideas to our recent analysis of Herman-Kluk response functions in Chapters 2 and 3. We shall also discuss the origin of quantization of frequency in the density of states and wavepacket propagation within the Herman-Kluk approximation. The Herman-Kluk propagator and similar semiclassical approximations have been numerically applied to propagate wavepackets, [92–94, 97] but the mechanism by which these approximations function is not fully understood. This analysis will thus allow us to compare and contrast the origins of quantization for both single and multiple propagator observables within the Herman-Kluk approximation.

In Section 2, we review the calculation of the density of states within the Van Vleck approximation to the propagator. Berry and Tabor [138] showed that the density of states could be written in the form of a topological sum of all possible periodic trajectories of energy E. In Section 3, we connect this topological sum idea to our previous analysis of the semiclassical response function in Chapters 2 and 3. We show that the quantization of actions in the mean trajectory approximation can be reinterpreted as a sum over all possible recurrence topologies for a pair of trajectories. In Section 4, we analyze the density of states within the Herman-Kluk approximation to the propagator, while in Section 5 we investigate the mechanism by which the Herman-Kluk propagator accurately propagates wavepackets. Finally, we summarize our findings in Section 6.

4.2 The Van Vleck density of states

For quantum systems, the density of states is typically calculated from the energy eigenvalue spectrum. Alternatively, the Fourier transform of the trace of the propagator is also proportional to the density of states $n(E)$,

$$\begin{aligned} n(E) &\equiv \mathrm{Tr}\,\delta(E-\hat{H}) \\ &= \mathrm{Re}\frac{1}{\pi\hbar}\int_0^\infty dt\, e^{iEt/\hbar}\,\mathrm{Tr}\hat{K}(t) \end{aligned} \tag{4.1}$$

where $\hat{K}(t)$ is the quantum propagator. [53] We will replace $\hat{K}$ with the Van Vleck semiclassical approximation to the propagator [139] and analyze its structure in order to determine the origin of quantization of energy in the density of states. This analysis follows that of Berry and Tabor, 1977. [138]

For a one-dimensional system, the trace over the propagator can be rewritten in the coordinate basis as

$$\mathrm{Tr}\hat{K}(t) = \int dq\, \langle q|\hat{K}(t)|q\rangle \equiv \int dq\, K(q,q;t) \tag{4.2}$$

where the Van Vleck semiclassical approximations to the propagator is given by

$$K(q_B,q_A;t) = \frac{1}{(2\pi i\hbar)^{1/2}}\sum_r |D_r|^{1/2}\exp\left[i\left(S_r/\hbar - \alpha_r\pi/2\right)\right]\,. \tag{4.3}$$

The sum over r represents all paths that connect q_A to q_B in time t. For long times, there may be many such paths. In order to evaluate the trace, we must sum over all paths that end where they started in time t — the periodic orbits. In Eq. (4.3), α_r is the number of caustics encountered during path r, D_r is a function of the monodromy matrix, and S_r is the classical action,

$$S_r(q_A,q_B;t) = \int_0^t p_r(\tau)\,\dot{q}_r(\tau)\,d\tau - E_r\,t \tag{4.4}$$

where E_r is the energy of the trajectory along path r.

For multiply periodic systems, we can define action and angle variables J and ϕ as discussed in Appendix A such that

$$\frac{\partial}{\partial t}\phi = \frac{\partial H(J)}{\partial J} = \omega(J) \ , \quad \frac{\partial}{\partial t}J = 0 \ . \tag{4.5}$$

Classical trajectories thus move on a constant action surface (the invariant torus) with an angle that is linear in time. The action S_r then can be written as

$$S(\phi_A, \phi_B; t) = J_r(t)\,(\phi_B - \phi_A) - H(J_r)\,t \tag{4.6}$$

$$J_r(t)\,(\phi_B - \phi_A) \equiv \int_0^t p_r(t)\,\dot{q}_r(t)\,dt \tag{4.7}$$

where $J_r(t)$ is equal to the action variable J_r when the time t is the period of motion. Similarly, D_r can be written in action-angle variables. [138] As the trace over q only allows contributions when $q_A = q_B$, and as the action J_r is invariant in time, we will only get contributions to the trace of the propagator when $\phi_A = \phi_B + 2\pi j$ for integer j. Therefore,

$$\mathrm{Tr}\,K(t) = \sum_j \int_0^{2\pi} d\phi\,K(\phi + 2\pi j, \phi; t) \ . \tag{4.8}$$

Note that the sum over j replaces an integral over action J, because for fixed time t, only a finite number of discrete actions J will result in the condition $\omega(J)t = 2\pi j$. Also, we have assumed that each path r corresponds to exactly one value of the action J_j. The generalization of this assumption is discussed by Berry and Tabor. [137] It is important to note that for a harmonic system, the frequency is independent of the action, $\omega(J) = \omega$, and this analysis will break down.

The jth component of the action S_j is given by

$$S_j(t) = 2\pi j J_j(t) - E_j t \ . \tag{4.9}$$

As S_j is independent of the initial angle ϕ, the angle integral in Eq. (4.8) simply generates a factor of 2π. Plugging our form for the action S_j into the density of states in Eq. (4.1) yields

$$n(E) = n_0(E) + \mathrm{Re}\frac{2}{(2\pi i\hbar)^{1/2}\hbar}\sum_j{}' \int_0^\infty dt|D_j|^{1/2}\, e^{i(2\pi jJ_j+(E-E_j)t)/\hbar}\, e^{-i\alpha_j\pi j/2} \tag{4.10}$$

where the prime in the sum indication $j \neq 0$. The term $n_0(E)$ is the smoothly varying Thomas-Fermi density of states, and it arises from the $j = 0$ paths of zero length. [53] The time integral in Eq. (4.10) can now be evaluated by stationary phase in time and the amplitude evaluated as in [138] to yield the final result

$$n(E) = n_0(E) + \frac{2}{\hbar^{1/2}}\sum_j{}' \frac{|j|^{1/2}}{|\omega(J_j)||K_j|^{1/2}} \cos\left(2\pi j(J_j/\hbar - \alpha_j/4) + \pi\beta_j/4\right) \tag{4.11}$$

where β_j is an integer, and K_j is the curvature of the energy contour. Note that J_j corresponds to a trajectory with topology j and energy E, and that the sum over j runs over the family of all trajectories with energy E.

In the derivation above, the important point is that only trajectories with certain specific values of the action J contribute at time t. These are the trajectories that have come back to where they started either zero, one, two, three, etc. times. Each such trajectory contributes a phase $e^{iS_j/\hbar}$ that is a function of the action J_j. The interference from all possible periodic trajectories results in peaks in the density of states that correspond to the semiclassical energy eigenvalues. As an example, consider a one-dimensional bound anharmonic oscillator system with $\alpha = -2$ and $\beta = 0$. If we ignore the slowly-varying prefactor of Eq. (4.11), the density of states is approximately given by

$$n(E) \propto \sum_j \cos\left(2\pi j(J(E)/\hbar + 1/2)\right)\ . \tag{4.12}$$

The sum over all topologies j reduces in one dimension to a sum over the number of windings $j = 0, 1, 2, 3, \cdots$ the trajectory makes. In multiple dimensions we would need to consider topologies such as a trajectory which goes around twice in coordinate a and three times in coordinate b, etc. Summing over the possible values of j then leads to the condition that $n(E)$ is sharply peaked when $J/\hbar$ is a half-integer. This is merely the Bohr-Sommerfeld condition for semiclassical quantization, as discussed in Appendix C.

4.3 Connection to the HK response function

We now wish to connect the "sum over periodic trajectories" idea that underlies Eq. (4.11) to the quantization of mean action that was derived for the linear response function $R^{(1)}(t)$ within the Herman-Kluk approximation. For a system with f degrees of freedom as described in Section 6 of Chapter 2, the linear response function can be written as

$$R^{(1)}_{HK}(t) = \sum_{\alpha,\beta} \kappa_{a\alpha}\kappa_{a\beta} R^{(1)}_{\beta\alpha}(t) \tag{4.13}$$

$$R^{(1)}_{\beta\alpha}(t) = \frac{1}{k_B T m} \int d\mathbf{z}_{12}\; f_{cl}(\mathbf{z}_{12})\, \pi_{\alpha,12}\, x_{\beta,12}(t)\, G_{\beta\alpha}(\mathbf{z}_{12}, t) \tag{4.14}$$

$$G_{\beta\alpha}(\mathbf{z}_{12}, t) \equiv |C(\mathbf{z}_1, t)C^*(\mathbf{z}_2, t)| \int \frac{d\Delta\mathbf{z}_{12}}{(2\pi\hbar)^f}\, \langle \mathbf{z}_1|\mathbf{z}_2\rangle\langle \mathbf{z}_2(t)|\mathbf{z}_1(t)\rangle\, e^{i(\Delta S(t)+\Phi_{\beta\alpha})/\hbar} \tag{4.15}$$

where $\Phi_{\beta\alpha}$ is an additional phase due to the HK prefactors and the complex coordinates and momenta $X_{\alpha,12}$ and $\Pi_{\beta,12}$,

$$C(\mathbf{z}_1, t)C^*(\mathbf{z}_2, t)\, \Pi_{\alpha,12}\, X^*_{\beta,12}(t) \equiv |C(\mathbf{z}_1, t)C^*(\mathbf{z}_2, t)|\; \pi_{\alpha,12}\, x_{\beta,12}(t)\, e^{i\Phi_{\beta\alpha}/\hbar} \tag{4.16}$$

and $z_{\alpha,12}$ differs from $\bar{z}_{\alpha,12}$ as discussed in relation to Eqs. (2.40) and (2.41). This phase $\Phi_{\beta\alpha}$ plays a similar role to the Maslov index in Eq. (4.3), resulting in an integer or half-integer offset to the quantization condition on $\bar{J}_\epsilon/\hbar \equiv N_\epsilon$.

Previously in Eq. (2.65), the integral over trajectory differences in Eq. (4.15) was shown to generate a quantization condition on the mean action,

$$\begin{aligned} G_{\beta\alpha}(z,t) &\approx \sigma_1(N_\beta) \prod_{\epsilon\neq\beta} \sigma_{1/2}(N_\epsilon) \\ &= \sum_{k_\beta=-\infty}^{\infty} e^{2\pi i k_\beta N_\beta} \prod_{\epsilon\neq\beta} \sum_{k_\epsilon=-\infty}^{\infty} e^{2\pi i k_\epsilon (N_\epsilon+1/2))} \qquad (4.17) \\ &= \sum_{n_\beta=-\infty}^{\infty} \delta(N_\beta - n_\beta) \prod_{\epsilon\neq\beta} \sum_{n_\epsilon=-\infty}^{\infty} \delta(N_\epsilon + 1/2 - n_\epsilon)\,. \qquad (4.18) \end{aligned}$$

The key step in the derivation of Eq. (4.17) is to recognize that the phase of $G_{\beta\alpha}$ is shaped like a staircase in both time and $\Delta\mathbf{J}$, as shown graphically in Figure 2.6 for a one-dimensional Morse oscillator system, with the flat steps (the stationary points) corresponding to times and action differences where the phase space separation of the pair of trajectories is minimized. The phase is locally cubic around each stationary point, and the integral over all stationary points generates both the sum in Eq. (4.17), as well as a $1/t^f$ time decay that is precisely canceled by the t^f time divergence of the magnitude of the HK prefactors.

In Eq. (4.17), the sum over $\mathbf{k}$ form for $G_{\beta\alpha}$ bears a striking resemblance to the density of states in Eq. (4.11). In Eq. (4.11), the sum over $\mathbf{j}$ runs over all possible windings (topologies) of a single trajectory, e.g. $j_\gamma = 0, 1, 2, \cdots$ for each component of $\mathbf{j}$, while in Eq. (4.17) the sum over $\mathbf{k}$ runs over all possible recurrences of a pair of trajectories in phase space, $k_\epsilon = 0, \pm 1, \pm 2, \cdots$, for each vibrational mode ϵ. The f-dimensional vector $\mathbf{k}$ thus labels the topology of the recurrences for a pair of trajectories in phase space. For example, $k_\alpha = 2$, $k_\beta = 1$, $k_{\epsilon\neq\alpha,\beta} = 0$ labels the recurrence for which the pair of trajectories has come together in phase space twice in mode α, once in mode β, and for all other modes the pair is still near its initial stationary point.

In both Eq. (4.11) and (4.17), the sum over all windings and recurrences re-

sults in interference that generates peaks in the density of states and mean action distribution respectively. The density of states is calculated by a Fourier transform of the trace of the propagator; therefore all possible windings will contribute due to the infinite upper limit of the time integral in Eq. (4.10). For response functions, there is no such time integral. Instead, the number of recurrence topologies summed over is a function of both the time and the action difference $\Delta\mathbf{J}$ for the propagating pair of trajectories. The infinite sum over $\mathbf{k}$ is Eq. (4.17) is therefore an infinite time approximation. For short times, only a few recurrences are possible, and the mean action distribution $G_{\beta\alpha}$ will more closely resemble the classical limit without any sharp peaks, as is demonstrated numerically in Figure 2.8.

We will now rewrite the expression for $G_{\beta\alpha}$ in order to make the connection to the stationary phase approximation that underlies Eq. (4.11) more clear. We will assume that the only contributions to $G_{\beta\alpha}$ occur when

$$\Delta\mathbf{z}^2(0) \approx \Delta\mathbf{z}^2(t) \tag{4.19}$$

where $\Delta\mathbf{z}$, defined in Eq. (2.11), measures the phase space separation of a pair of trajectories. Unlike the linearization approximation described in Appendix B, Eq. (4.19) does not imply that $\Delta\mathbf{z} \approx 0$, though clearly in this limit Eq. (4.19) will be satisfied for short enough times. As the action variables of the system are invariant in time, Eq. (4.19) is equivalent to assuming that

$$\Delta\phi_\epsilon(t) = \Delta\phi_\epsilon + \Delta\lambda_\epsilon(\mathbf{N})\omega_\epsilon t = \Delta\phi_\epsilon + 2\pi k_\epsilon \tag{4.20}$$

for all modes ϵ and integer k_ϵ. For fixed action, the only contributions to $G_{\beta\alpha}$ occur at times where the frequency difference $\Delta\lambda_\epsilon(\mathbf{N})\omega_\epsilon$ multiplied by the time is equal to an integer multiple of 2π. The distribution of mean action $G_{\beta\alpha}$ can

then be rewritten as

$$\begin{aligned} G_{\beta\alpha}(\mathbf{J},\phi,t) &\approx |C(\mathbf{z}_1,t)C^*(\mathbf{z}_2,t)| \int d\Delta\mathbf{z}_{12}\, e^{i(\Delta S(t)+\Phi_{\beta\alpha})/\hbar} \\ &\approx \sum_{\mathbf{k}} |C(\mathbf{z}_1,t)C^*(\mathbf{z}_2,t)|_{\mathbf{k}} \int d\delta J_{\mathbf{k}}\, d\Delta\phi\, e^{i(\Delta S_{\mathbf{k}}+\Phi_{\beta\alpha,\mathbf{k}})/\hbar} \end{aligned} \tag{4.21}$$

where the sum over $\mathbf{k}$ indicates a sum over all possible recurrence topologies. As discussed by Berry and Tabor [138] for the Van Vleck density of states and in Chapters 2 and 3 for the linear and nonlinear semiclassical response functions, the integral over small deviations from the stationary point $\delta J_{\mathbf{k}}$ will result in a time decay that is canceled by the time divergence of the magnitude of the HK prefactor. As in the density of states, the $\Delta\phi$ integral simply yields an overall constant. $G_{\beta\alpha}$ is then given approximately by

$$G_{\beta\alpha} \approx \sum_{\mathbf{k}} e^{i(\Delta S_{\mathbf{k}}/\hbar+\Phi_{\beta\alpha,\mathbf{k}})} \tag{4.22}$$

where $(\Delta S_{\mathbf{k}} + \Phi_{\mathbf{k}})/\hbar$ is the total accumulated phase at the recurrence with the topology labeled $\mathbf{k}$.

The classical action S grows with time and is given in Eq. (4.6). We can therefore write the action difference $\Delta S(t)$ for a pair of trajectories $\{\mathbf{z}_1, \mathbf{z}_2\}$ as

$$\Delta S(t) = \sum_{\epsilon} \left(J_{\epsilon,1}(t)\lambda_\epsilon(\mathbf{J}_1)\omega_\epsilon t - E_1 t\right) - \left(J_{\epsilon,2}(t)\lambda_\epsilon(\mathbf{J}_2)\omega_\epsilon t - E_2 t\right) . \tag{4.23}$$

At each recurrence given by Eq. (4.20), $J_{\epsilon,i}(t) = J_{\epsilon,i}$ for $i = 1, 2$, and

$$\Delta S(t) = \sum_{\epsilon} \left(J_{\epsilon,1}\lambda_\epsilon(\mathbf{J}_1)\omega_\epsilon - E_1 - J_{\epsilon,2}\lambda_\epsilon(\mathbf{J}_2)\omega_\epsilon + E_2\right) t . \tag{4.24}$$

For a one-dimensional harmonic oscillator system, $\lambda = 1$, and $J\omega = E$. So, for harmonic systems, no phase is accumulated between recurrences, and integration over trajectory differences in $G_{\beta\alpha}$ will not quantize the mean actions $\mathbf{N}$. The accumulated phase from ΔS is therefore entirely due to anharmonic contributions, which for one-dimensional Morse or cubic oscillators are quadratic in action.

For a coupled anharmonic oscillator system within the independent oscillator approximation of Eq. (2.58), we previously derived an expression for the linear divergence of $\Delta S(t)$, which can be rewritten as

$$\Delta S(t)/\hbar \approx \prod_{\epsilon} N_\epsilon \left(\frac{-\Delta J_\epsilon \omega_\epsilon}{2D_\epsilon} \right) \omega_\epsilon t = N_\epsilon \Delta\lambda_\epsilon \omega_\epsilon t \, . \tag{4.25}$$

At each recurrence topology $\mathbf{k}$, $\Delta\lambda_\epsilon\omega_\epsilon t = 2\pi k_\epsilon$, and the accumulated phase is

$$\Delta S_{\mathbf{k}}/\hbar = \sum_{\epsilon} 2\pi k_\epsilon N_\epsilon \, . \tag{4.26}$$

Similarly, for the Morse oscillator, the phase $\Phi_{\beta\alpha}$ is given by

$$\Phi_{\beta\alpha}(t)/\hbar = \Delta\lambda_\beta\omega_\beta t + \sum_{\epsilon\neq\beta} \Delta\lambda_\epsilon\omega_\epsilon t/2 \quad \Longrightarrow \quad \Phi_{\beta\alpha,\mathbf{k}}/\hbar = 2\pi\mathbf{k}\cdot\mathbf{y} \tag{4.27}$$

where y_ϵ is equal to 1 for $\epsilon = \beta$ and equal to 1/2 for all other modes ϵ. Our expression for $G_{\beta\alpha}$ is then finally

$$G_{\beta\alpha}(\mathbf{N}) = \sum_{\mathbf{k}} \exp\left(2\pi i\, \mathbf{k}\cdot(\mathbf{N}+\mathbf{y})\right) \tag{4.28}$$

where the sum over $\mathbf{k}$ in Eq. (4.28) is for all recurrence topologies that are possible at time t. In the long time limit, $G_{\beta\alpha}$ becomes the sum of delta functions in Eq. (4.17).

Even though the expression for $G_{\beta\alpha}$ looks very like the density of states derived from the Van Vleck propagator, there are several important differences to note. Quantization in the Van Vleck density of states occurs through a Fourier transform and a sum over all possible windings (topologies) of a single trajectory. The quantization condition for mean actions however has no such Fourier transform. Instead, the quantization is due to an integral over action differences $\Delta\mathbf{J}$. As discussed in Chapter 2, $\Delta\mathbf{J}$ and the time t occur as a pair in the semiclassical phase for an anharmonic oscillator system, $\Delta S(\Delta\mathbf{J}, t) \approx \Delta S(\Delta\mathbf{J}t)$. Therefore the integral over $\Delta\mathbf{J}$ plays a similar role to the time integral in the density of

states and generates a sum over recurrences. The role of the Maslov index in the Van Vleck propagator is replaced by the phase of the HK prefactor in the response calculation,

$$C(\mathbf{z}_1,t)C^*(\mathbf{z}_2,t) \approx |C(\mathbf{z}_1,t)C^*(\mathbf{z}_2,t)| \prod_{\epsilon} e^{i\Delta\lambda_\epsilon \omega_\epsilon t/2} \,. \tag{4.29}$$

This prefactor phase, along with the phase associated with the coherent state matrix element of $\hat{x}$, results in an integer or half-integer offset in the $\mathbf{N}$ quantization condition.

4.4 The HK density of states

We now wish to calculate the density of states defined in Eq. (4.1) using the Herman-Kluk semiclassical propagator. It is well known [68, 79, 91] that the Herman-Kluk propagator becomes equivalent to the Van Vleck propagator in the stationary phase limit. Rather than simply take the stationary phase limit however, we wish to analyze the HK density of states for the specific cases of the harmonic and Morse oscillators and see explicitly how quantization of energy in the density of states occurs. This analysis will enable us to make comparisons to the response function calculation described in the previous section. Note that the Herman-Kluk approximation to the density of states has been successfully applied numerically to the Henon-Heiles potential by Kay [94] and McQuarrie and Brumer [95], and it is expected to be exact in the harmonic limit.

The trace of the propagator within the HK approximation for a system with

f degrees of freedom is given by

$$\begin{aligned}\left(\mathrm{Tr}\, e^{-i\hat{H}t/\hbar}\right)_{HK} &= \int d\mathbf{x}\ \langle \mathbf{x}|K_{HK}(t)|\mathbf{x}\rangle \\ &= \int \frac{d\mathbf{z}}{(2\pi\hbar)^f}\,\langle \mathbf{z}|\mathbf{z}(t)\rangle\, C(\mathbf{z},t)e^{iS(\mathbf{z},t)/\hbar} \\ &\equiv \int \frac{d\mathbf{z}}{(2\pi\hbar)^f} C(\mathbf{z},t)e^{F(\mathbf{z},t)} \end{aligned} \tag{4.30}$$

where F is a complex exponent. Eq. (4.30) can be evaluated numerically, and it is quantitatively accurate for both a harmonic and Morse oscillator system. This is demonstrated in Figure 4.1, where panel (a) compares the Herman-Kluk expression for the density of states to the exact quantum frequencies for a system of one-dimensional Morse oscillators. The semiclassical frequencies are quantitatively accurate, though the peak amplitudes decay for high frequencies due to the finite range of possible actions N in Eq. (4.30). In panel (b), the semiclassical and quantum results are compared for a more complicated double well, with the potential given by

$$V(q) = \frac{m\omega^2}{8q_0^2}\Big(q - q_0\Big)^2\Big(q + q_0\Big)^2 . \tag{4.31}$$

While the HK density of states is quantitatively accurate for both low and high energies where the potential is locally either harmonic or quartic respectively, the semiclassical result qualitatively fails to capture the quantum tunneling splitting near $\Omega = 5\omega$. This is consistent with previous applications of semiclassical propagators to barrier problems. [98, 105]

For a harmonic system, we can also evaluate this expression analytically by expressing the coordinates and momenta in action-angle variables,

$$\begin{aligned} q(t) &= \sqrt{\frac{2J}{m\omega}}\cos(\phi + \omega t) \\ p(t) &= -\sqrt{2m\omega J}\sin(\phi + \omega t). \end{aligned} \tag{4.32}$$

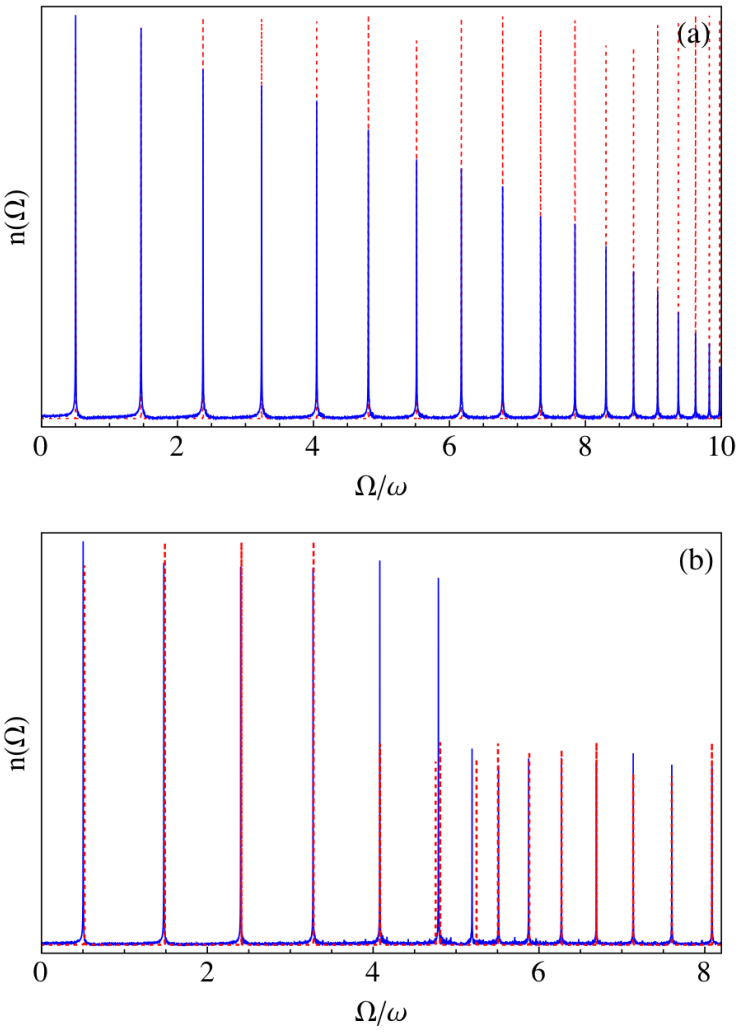

Figure 4.1: The quantum (red, dashed) and semiclassical (blue) density of states are plotted in panel (a) for a one-dimensional Morse oscillator system with $\hbar\omega/D = 0.1$, and in panel (b) for the double-well system given by Eq. (4.31) for $(m\omega q_0^2/\hbar) = 10$. The semiclassical peak positions are quantitatively accurate for the Morse oscillator system, as well as for the double-well system for both low and high energies. Near the top of the potential barrier in panel (b), the semiclassical results are incorrect.

The prefactor and exponent F are then given exactly by

$$C(z,t) = e^{-i\omega t/2} \tag{4.33}$$

$$S(z,t) = -J\sin(\omega t)\cos(2\phi + \omega t) \tag{4.34}$$

$$F(z,t) = -N\left(1 - e^{-i\omega t}\right) \tag{4.35}$$

where $N \equiv J/\hbar$. Note that F is independent of the angle variable ϕ for harmonic systems. We now perform the trivial angle integral as well as the action integral to obtain the trace of the HK propagator,

$$\begin{aligned}\left(\mathrm{Tr}\, e^{-i\hat{H}t/\hbar}\right)_{HK} &= \int dN\ \exp\left[-N\left(1 - e^{-i\omega t}\right) - i\omega t/2\right] \\ &= \frac{e^{-i\omega t/2}}{1 - e^{-i\omega t}} = \sum_{k=0}^{\infty} e^{-i(k+1/2)\omega t}.\end{aligned} \tag{4.36}$$

The expression for the trace in Eq. (4.36) has Fourier components at frequencies $(k + 1/2)\omega$ for integer k. These frequencies correspond to the eigenvalue spectrum of the quantum harmonic oscillator, as expected. We should notice that the quantization of frequency in the above expression has nothing to do with a quantization condition on the action N. We must integrate over the action in order to generate the series of Fourier components in Eq. (4.36), but the quantization of frequency condition only occurs after taking the Fourier transform of the trace of the propagator. This is in contrast to the case of the semiclassical response functions, where action was quantized after performing an integral over action differences.

We can evaluate the harmonic density of states in Eq. (4.30) in an alternate manner by switching the order of the time and action integrals. We start by expanding the (periodic) exponential of F in a Fourier series,

$$e^{F(J,t)} = \sum_{k=0}^{\infty} c_k(J) e^{-ik\omega t} \tag{4.37}$$

$$c_k(J) = \frac{N^k}{k!} e^{-N}. \tag{4.38}$$

It is important to note that the frequency components of e^F are completely independent of action. The real, positive Fourier coefficients $c_k(J)$ depend on action, are peaked at $N = k$, and decay to zero for large k. We can then write the density of states as

$$\begin{aligned} n(\Omega) &\propto \frac{1}{\hbar} \int dJ \int dt \sum_{k=0}^{\infty} c_k(J) \exp\left[i \left(\Omega - (k + 1/2)\omega\right) t\right] \\ &= \sum_{k=0}^{\infty} \delta\left(\Omega - (k + 1/2)\omega\right) \int dN \, \frac{N^k}{k!} e^{-N} \\ &= \sum_{k=0}^{\infty} \delta\left(\Omega - (k + 1/2)\omega\right). \end{aligned} \tag{4.39}$$

As expected, we obtain a harmonically quantized distribution of frequencies Ω. The integral over action only serves to cancel a $k!^{-1}$ factor. If we were to only integrate over a limited range of actions, the frequency components of $n(\Omega)$ would be unchanged; only the weight of each component would be altered.

In the Van Vleck treatment of the density of states in Section 2, only quantized values for the action N contribute after summing over all possible windings. In the harmonic case presented above, there is no quantization condition on the action, just as there is no action quantization for semiclassical response functions for harmonic systems. For an anharmonic system such as the Morse or quartic oscillator or a system of bilinearly coupled oscillators, we therefore might expect a qualitative difference from the harmonic case, as the frequency Ω should be anharmonically quantized. To see this, we once again start with the approximate forms for the coordinates and momenta in action-angle variables given in Eq. (2.24). For a system of one-dimensional Morse oscillators, we can

write the complex exponent $F(z,t)$ from Eq. (4.30) as

$$S(J,t) = -J\sin(\lambda\omega t)\cos(2\phi + \lambda\omega t) - i\varepsilon^2 J^2\omega^2 t/4D\hbar + \cdots \tag{4.40}$$

$$\begin{aligned} F(J,t) &= -N(1-\cos(\lambda\omega t)) - iN\sin(\lambda\omega t) - i\varepsilon^2 J^2\omega^2 t/4D\hbar + \cdots \\ &\approx -N\left(1 - e^{-i\lambda(J)\omega t}\right) - \varepsilon^2 iJ^2\omega^2 t/4D\hbar \end{aligned} \tag{4.41}$$

where we have ignored oscillating terms that are of order ε and ε^2. The linear time divergence of the imaginary part of F is due to the divergence of the action with time for anharmonic systems. We will also make the approximation

$$C(z,t) = \sqrt{\frac{J\omega^2 t}{2D}} e^{-i\lambda(J)\omega t/2} \tag{4.42}$$

as described in Eq. (2.33) of Chapter 2. Numerical simulations of $n(\Omega)$ using Eqs. (4.41) and (4.42) indicate that these approximations are sufficient to capture the anharmonic quantization of Ω. Note that within these approximations, the exponent F is again independent of angle ϕ but unlike for the harmonic case, the imaginary component of F diverges linearly with time. We have also numerically found that the approximation

$$\langle z|z(t)\rangle \to 1 \tag{4.43}$$

does not qualitatively change the anharmonic quantization of Ω. This confirms that, as in the Van Vleck density of states, a trajectory only contributes to $n(E)$ at times when it returns to its initial conditions,

$$z(t) \approx z(0) \implies \phi(t) \approx \phi(0) \implies \lambda(J)\omega t \approx 2\pi k \tag{4.44}$$

for integer k. This is similar to the case of correlation and response functions discussed in Section 3, when a trajectory pair only contributes at times when the phase space separation $\Delta z(t)$ between the trajectory pair is minimized.

Rather than now taking the stationary phase approximation, we instead expand the exponential of F in a Fourier series as in Eq. (4.37), yielding

$$\begin{aligned} C(z,t)e^{F(J,t)} &= \sqrt{\frac{J\omega^2 t}{2D}}\, e^{-iJ^2\omega^2 t/4D\hbar} \sum_{k=0}^{\infty} \frac{N^k}{k!} e^{-N} e^{-i(k+1/2)\lambda(J)\omega t} \\ &\equiv \sum_k A_k(t)\,. \end{aligned} \tag{4.45}$$

Unlike the harmonic Fourier expansion of Eq. (4.37), the frequency spectrum in Eq. (4.45) is strongly action dependent. For fixed action J, only certain frequencies will contribute to the density of states, but these frequencies will not be the correct anharmonic frequencies Ω_k. Instead, each value of the action will contribute harmonically spaced frequencies with a spacing determined by $\lambda(J)$. This is shown as the dashed, red curve in Figure 4.2 for a one-dimensional Morse oscillator with N constrained to be $N_0 = 2.5$. In order for the correct anharmonic frequencies to appear, we must integrate over a range of actions. This is demonstrated by the blue curve in Figure 4.2, where N is integrated in a small range ΔN about $N_0 = 2.5$. It is evident that only Fourier components with the correct anharmonic frequencies survive integration over action, while incorrect frequency components decay to zero. This should be contrasted with the harmonic case where any value of the action contributes the correct harmonic frequencies to the density of states.

We now will integrate the kth component of $n(\Omega)$ over initial angles,

$$B_k(N) \equiv \int_0^{2\pi} \frac{d\phi}{2\pi} A_k = \frac{1}{k!}\left(\frac{\hbar\omega^2 t}{2D}\right)^{1/2} N^{\kappa} e^{-N} e^{-i\omega t(\kappa\lambda(N)+\hbar\omega N^2/4D)} \tag{4.46}$$

where $\kappa \equiv k + 1/2$. We cannot analytically integrate B_k with respect to action N, but we will be able to make a simplifying assumption that generates a simple

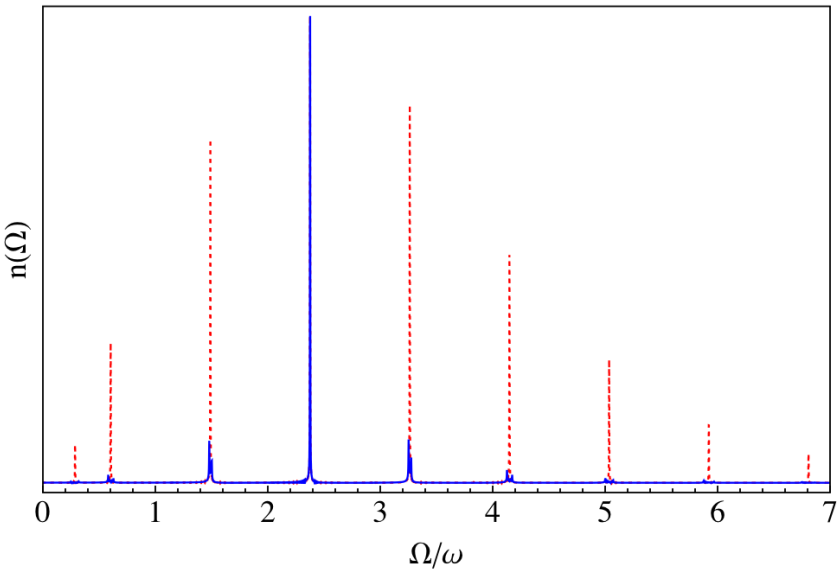

Figure 4.2: The semiclassical density of states for a one-dimensional Morse oscillator with the same parameters as in Figure 4.1 is plotted. The red, dashed curve shows $n(\Omega)$ for fixed action $N_0 = 2.5$, while in the blue curve, the action has been integrated over a small range ΔN about N_0.

result. We first complete the square for the phase of B_k,

$$\begin{aligned}\Psi &\equiv -i\omega t(\kappa\lambda(N) + \hbar\omega N^2/4D) \\ &= -i\omega t(\kappa(1 - \hbar\omega N/2D) + \hbar\omega N^2/4D) \\ &= -i\omega t(\kappa - \kappa^2\hbar\omega/4D) - i\omega t\frac{\hbar\omega}{4D}(N-\kappa)^2 \,. \end{aligned} \tag{4.47}$$

The integral of B_k with respect to action is then given by

$$\begin{aligned} n_k(t) &\equiv \int_0^\infty dN\, B_k(N;t) \\ &= \frac{1}{k!}\left(\frac{\hbar\omega^2 t}{2D}\right)^{1/2} e^{-i\omega t(\kappa-\kappa^2\hbar\omega/4D)} \int_0^\infty dN\, N^\kappa e^{-N} e^{-i\omega t\frac{\hbar\omega}{4D}(N-\kappa)^2} \\ &\equiv g_k(t) e^{-i\omega t(\kappa-\kappa^2\hbar\omega/4D)} \,. \end{aligned} \tag{4.48}$$

We will next calculate g_k by noting that we only get a large contribution to the action integral in Eq. (4.48) when the action is approximately quantized, $N \approx \kappa$.

Thus we expand N around κ and perform the action integral by stationary phase,

$$\begin{aligned} g_k(t) &\approx \frac{1}{k!}\left(\frac{\hbar\omega^2 t}{2D}\right)^{1/2} \kappa^\kappa e^{-\kappa} \int_{-\infty}^{\infty} d\delta N \; e^{-i\omega t \frac{\hbar\omega}{4D}\delta N^2} \\ &= \frac{\kappa^\kappa e^{-\kappa}}{k!}\left(\frac{\hbar\omega^2 t}{2D}\right)^{1/2} \frac{(1-i)\sqrt{2D\pi}}{\sqrt{\hbar\omega^2 t}} \\ &\approx e^{-i\pi/4}. \end{aligned} \tag{4.49}$$

Thus, g_k is essentially independent of both time and k, and is just equal to a constant. The magnitude of the HK prefactor is completely canceled by the action integral, as was the case for the $\Delta\mathbf{J}$ integral in the linear response function, Eq. (2.37). We have therefore shown that the trace of the Herman-Kluk propagator for a Morse oscillator can be written as,

$$\text{Tr } K_{HK}(t) \propto \sum_k e^{-i\omega t(\kappa - \kappa^2\hbar\omega/4D)}, \tag{4.50}$$

and performing the Fourier transform of Eq. (4.50) leads to the correct anharmonic density of states. The analysis which led to Eq. (4.50) can be easily generalized to a system of weakly interacting anharmonic oscillators, as discussed for the linear and nonlinear response functions. Half-integer quantization of the good action variables $\mathbf{N}$ generates peaks in the density of states, while all other frequency components decay to zero upon integration over a range in action.

For the harmonic density of states, there is no quantization condition on the action variable. Each value of the action contributes to the density of states with the same frequency components but different weights. For the anharmonic case, this is qualitatively changed. For the kth component of the trace of the propagator $n_k(t)$, only one set of values for the actions, $N = \kappa$, contributes to the final density of states. However, it is important to realize that these quantized values for the action only contribute to this one component of the density of states, and that we must integrate over a range of action N in order to remove incorrect

frequency components. We cannot simply take Eq. (4.30), insert a quantization condition $N = \kappa$ for all half-integer κ, and obtain the correct anharmonic frequencies. Therefore, there is a quantization condition on the action variables in the HK density of states, but it is a different sort of quantization condition from that discussed in Section 3 for response functions.

4.5 HK wavepacket propagation

The time propagation of vibrational wavepackets is necessary for the theoretical treatment of a variety of spectroscopic and photochemical processes. [140, 141] In this section we will investigate wavepacket propagation within the Herman-Kluk approximation to the propagator. This semiclassical propagation has been shown to be accurate for relatively short times, though for anharmonic systems, the HK approximation is not quantitatively accurate for very long times, and it is numerically challenging to implement for classically chaotic systems. [94,106] However, for weakly anharmonic oscillator systems, we will show that within the Herman-Kluk approximation, an initial wavepacket is propagated with frequency components that correspond to the correct quantum frequencies. The origin of this frequency quantization is very similar to the frequency quantization in the HK density of states.

We define our wavepacket (superposition state) of interest $|\Psi\rangle$ as

$$|\Psi\rangle = \sum_n c_n |n\rangle \tag{4.51}$$

where $|n\rangle$ is the nth energy eigenfunction of the harmonic oscillator, and $c_n \equiv \langle n|\Psi\rangle$, as discussed in Appendix A. In a harmonic potential with frequency ω, the time dependence of $|\Psi\rangle$ and thus the time-dependent wavepacket overlap is

then given by

$$\langle\Psi|\Psi(t)\rangle = \sum_n |c_n|^2 e^{-i(n+1/2)\omega t} \tag{4.52}$$

$$|\langle\Psi|\Psi(t)\rangle|^2 = \sum_{n,m} |c_n|^2 |c_m|^2 e^{i(n-m)\omega t} \,. \tag{4.53}$$

For general wavepackets, we will get contributions at all frequencies $n\omega$ for integer n.

Within the Herman-Kluk approximation to the propagator, the time-dependent wavepacket overlap for a general system is given by

$$\langle\Psi|\Psi(t)\rangle_{HK} = \int \frac{d\mathbf{z}}{(2\pi\hbar)^f} \langle\Psi|\mathbf{z}(t)\rangle \, C(\mathbf{z},t) e^{iS(t)/\hbar} \langle\mathbf{z}|\Psi\rangle \,. \tag{4.54}$$

In order to analyze this result, we must first calculate the overlap between coherent states and harmonic energy eigenstates. We will focus in this section on one-dimensional systems, though the generalization to f weakly coupled degrees of freedom follows as for response functions. The nth harmonic eigenstate in the coherent state basis is given analytically by

$$\langle z|n\rangle = \langle z|0\rangle \frac{(m\omega q - ip)^n}{\sqrt{n!(2m\hbar\omega)^n}} \tag{4.55}$$

$$\langle z|0\rangle = \exp\left[-\frac{1}{4m\hbar\omega}(p^2 + m^2\omega^2 q^2) + \frac{i}{2\hbar}pq\right]. \tag{4.56}$$

The total phase due to the action integral and $\langle z|0\rangle\langle 0|z_t\rangle$ overlaps is defined as

$$\Lambda(t) = \frac{1}{\hbar}\left(S(t) + \frac{1}{2}(pq - p_t q_t)\right) . \tag{4.57}$$

There will be additional phases due to the HK prefactor and $(m\omega q - ip)$ terms in Eq. (4.55). Note that Λ is not the same phase as for the HK density of states. However as was the case with the density of states and response functions, it is the linear divergence of the action for anharmonic systems that generates a quantization condition for the frequency components of the wavepacket.

In action-angle variables, we can write the phase and coherent state-wavepacket overlap exactly for a harmonic system as

$$\Lambda(t) = 0 \tag{4.58}$$

$$|\langle z|0\rangle| = e^{-J/2\hbar} \tag{4.59}$$

$$(m\omega q_t \mp i p_t) = \sqrt{2m\omega J} e^{\pm i(\phi+\omega t)} \,. \tag{4.60}$$

Note that as for harmonic response functions, the phase Λ is equal to zero. There are no stationary points in time, and thus there is no quantization condition on the action variables J. We now plug these pieces into the wavepacket overlap calculation,

$$\begin{aligned} A_{mn} &\equiv \langle m|z(t)\rangle\, C(z,t) e^{iS(t)/\hbar}\, \langle z|n\rangle \\ &= \sqrt{\frac{J^{n+m}}{n!m!\hbar^{n+m}}} e^{-i\omega t/2} e^{-J/\hbar} e^{i(n-m)\phi} e^{-im\omega t} \end{aligned} \tag{4.61}$$

and integrate over the actions and initial angles,

$$\int \frac{dJd\phi}{2\pi\hbar} A_{mn}(J,\phi) = e^{-i(m+1/2)\omega t}\delta_{n,m} \,. \tag{4.62}$$

As each coherent state overlap carries a factor of $e^{\pm in\phi}$, the angle integral of A_{mn} will equal zero unless $n = m$ and the angle-dependence of these phases cancels. As stated above, there is no quantization of action, but integration over J instead yields a constant factor. The time-dependence in Eq. (4.62) is carried by a phase factor that derives from the phase of the HK prefactor as well as the mth eigenstate in the coherent state basis at time t. This time dependent factor is independent of actions and angles, and thus comes outside of the integrals in Eq. (4.62). For superposition wavepackets, the final wavepacket overlap with HK dynamics is then identical to the quantum result,

$$\langle\Psi|\Psi(t)\rangle_{HK} = \sum_n |c_n|^2 e^{-i(n+1/2)\omega t} = \langle\Psi|\Psi(t)\rangle_{QM} \,. \tag{4.63}$$

Therefore, for harmonic systems, the frequency components $n\omega$ in the wavepacket overlap stem from the phase factor in the coherent state overlap $\frac{\langle z|n\rangle}{\langle z|0\rangle}$. The $\omega/2$ term in Eq. (4.63) is derived from the phase of the HK prefactor, similar to the role of the prefactor phase in response function calculations and in the density of states.

For weakly anharmonic systems at short times, we can approximate the oscillator dynamics as

$$q(t) \approx \sqrt{\frac{2J}{m\omega}} \cos\left(\phi + (1 + \epsilon\omega J)\omega t\right) \tag{4.64}$$

where ϵ^{-1} has units of energy. Within this approximation, the phase Λ is not exactly equal to zero, but it does not diverge with time. As such, we do not expect a quantization condition on the actions N. Integrating $A_{mn}(J,\phi)$ in analogy to Eq. (4.62) results in the irreversible decay of the nth component of the magnitude of the wavepacket overlap,

$$\int \frac{dJd\phi}{2\pi\hbar} A_{mn}(J,\phi) \approx e^{-i(n+1/2)\omega t}\delta_{n,m}\left(\frac{1}{1 + i(n+1/2)\epsilon\omega^2\hbar t}\right)^{n+1}. \tag{4.65}$$

This is demonstrated graphically in Figure 4.3 for an initial wavepacket $|\Psi\rangle = (|0\rangle + |1\rangle)/\sqrt{2}$. The time decay derives from the action-dependence of the frequency in Eq. (4.64). Including additional anharmonic terms in the approximate dynamics, as was done for the Morse oscillator previously, results in the quantization of action variables, and thus no long time decay.

As with the density of states, wavepacket propagation is somewhat more complicated for anharmonic systems compared to the harmonic case. As before, we shall focus on the one-dimensional Morse oscillator system, though a very similar analysis is possible for bound states of a generic anharmonic oscillator. The bound quantum eigenstates and energies of the one-dimensional Morse

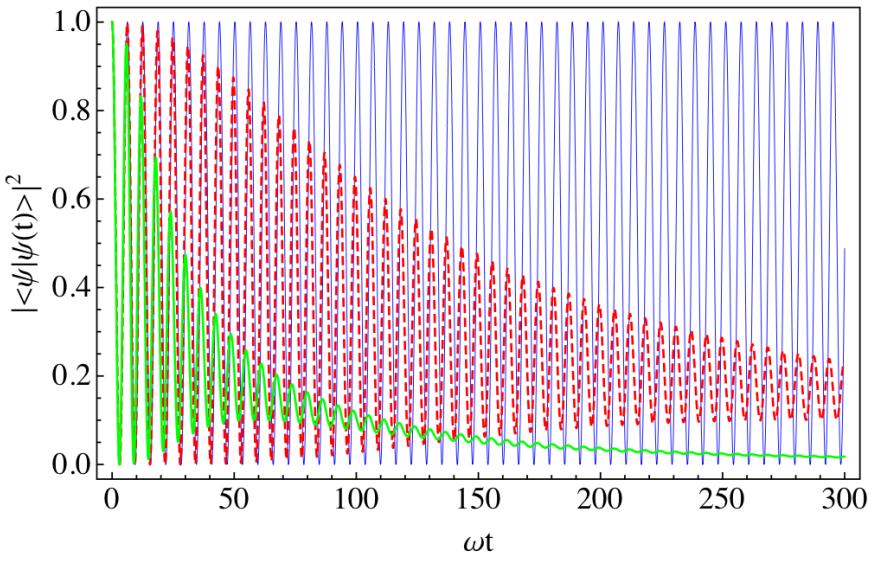

Figure 4.3: The square magnitude of the wavepacket overlap is plotted vs. time for the harmonic $\epsilon/\omega\hbar = 0$ case (blue), $\epsilon/\omega\hbar = 2$ (red, dashed), and $\epsilon/\omega\hbar = 10$ (green). The initial state is a superposition state of the ground and first excited harmonic oscillator states, $|\Psi\rangle = (|0\rangle + |1\rangle)/\sqrt{2}$.

oscillator are given by

$$\hat{H}\,|\varphi_n\rangle = \epsilon_n\,|\varphi_n\rangle \tag{4.66}$$

$$\epsilon_n = \hbar\omega(n+1/2) - \frac{(\hbar\omega(n+1/2))^2}{4D} \tag{4.67}$$

and the eigenstates for a harmonic system can be expanded in this basis as

$$|n\rangle = \sum_k d_{k,n}\,|\varphi_k\rangle\,. \tag{4.68}$$

For an initial wavepacket $|\Psi\rangle$ defined in Eq. (4.51), the wavepacket overlap at time t is then

$$\langle\Psi|\Psi(t)\rangle = \sum_{m,n} c_m^* c_n \sum_k d_{k,m}^* d_{k,n} e^{-i\epsilon_k t/\hbar}. \tag{4.69}$$

The wavepacket overlap will contain anharmonic frequency components in general at values $\Omega_k = \epsilon_k/\hbar$.

The Herman-Kluk propagator can also be applied to this anharmonic system. This is shown in Figure 4.4, where the red curve displays the wavepacket overlap with quantum dynamics, and the blue curve is the semiclassical approximation. In panel (a), the initial wavepacket is the harmonic oscillator ground state, $|\Psi\rangle = |0\rangle$, while in panel (b) the initial state is a superposition state of the ground and first excited harmonic oscillator states, $|\Psi\rangle = (|0\rangle + |1\rangle)/\sqrt{2}$ as in Figure 4.3. While not quantitatively accurate for either case, the HK approximation appears to capture the correct quantum frequencies, though the wavepacket overlap tends to unphysically increase beyond unity for long times. This long time growth is due to the divergence of the magnitude of the HK prefactor with time. While the prefactor acts as a normalization constant for the propagating wavepacket, it is only exact for harmonic systems or within a linearization approximation to the dynamics, as noted in Appendix B. [82]

As a more demanding test of the HK approximation, we can also propagate wavepackets in a potential with multiple degrees of freedom. As an example, we consider the Henon-Heiles potential defined as

$$V_{HH}(x,y) = \frac{m_x\omega_x^2}{2}x^2 + \frac{m_y\omega_y^2}{2}y^2 + c\left(x^2y - y^3/3\right) \tag{4.70}$$

where we will take $m_x = m_y$ and $\omega_x = \omega_y$. This potential has a three-fold symmetry, and for large anharmonicitiy c or large energies, trajectories display classically chaotic motions. [92, 94, 95, 142] We will only consider energies such that ergodic trajectories are irrelevant to the wavepacket dynamics. For an initial Gaussian state given by

$$\langle x,y|\psi\rangle = \sqrt{\frac{m\omega}{\pi\hbar}}\exp\left(-\frac{m\omega}{2\hbar}\Big((x-x_0)^2 + (y-y_0)^2\Big)\right) \tag{4.71}$$

we can calculate the time propagation using both quantum and semiclassical dynamics. In Figure 4.5, we plot the square magnitude of the semiclassical

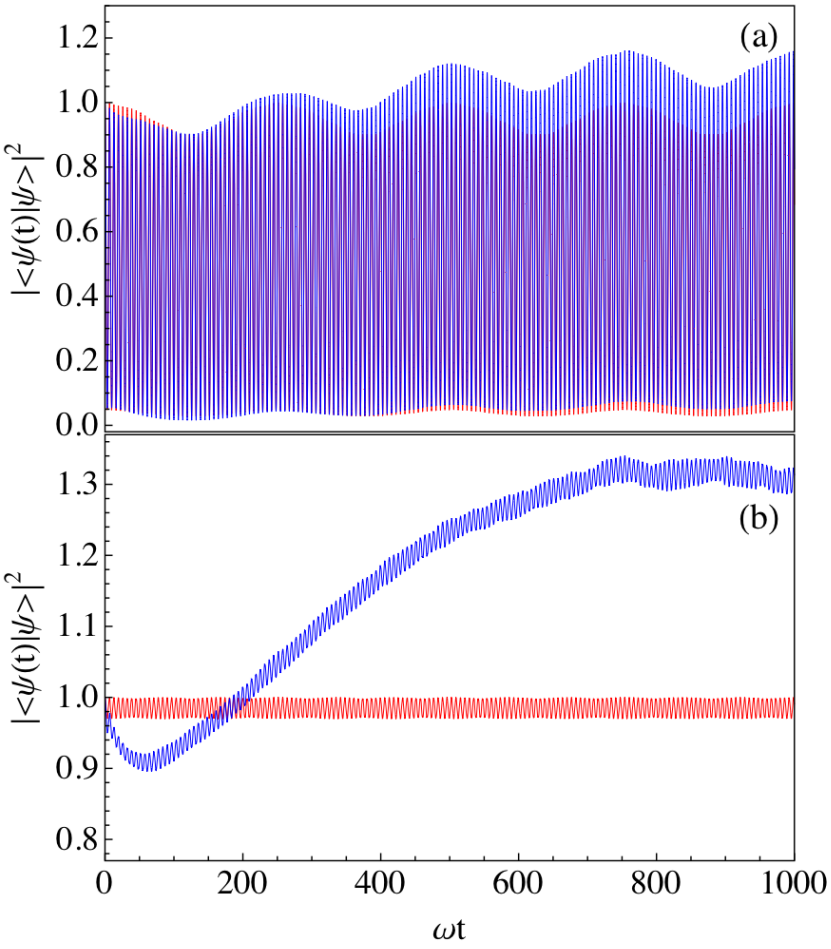

Figure 4.4: The square magnitude of the wavepacket overlap for a Morse oscillator system with $\omega\hbar/D = 0.1$ is compared for both quantum (red) and semiclassical (blue) time propagation. The semiclassical result accurately reproduces the quantum frequency components, though it also contains an incorrect slow growth with time due to inaccurate normalization for the HK wavepacket for long times.

wavepacket as a function of propagation time. For short times, quantum and semiclassical results agree, though the accuracy declines for long times. [94]

In order to analyze how the HK propagator functions for one-dimensional anharmonic oscillators, we will again adopt approximate dynamics in action-angle variables. The phase Λ, defined in Eq. (4.57), can be expanded to second order in anharmonicity ε. Λ contains both oscillatory and linear components in time, where the dominant linear growth is approximately given by

$$\Lambda(t) = -\varepsilon^2 \frac{\omega}{4D\hbar} J^2 \omega t. \tag{4.72}$$

Numerical calculations with this approximation to Λ result in qualitatively correct wavepacket dynamics. We can also approximate the HK prefactor as in Eq. (4.42). This expression for the prefactor is incorrect for short times, but is qualitatively correct for longer times, and again results in qualitatively correct wavepacket dynamics. Making the approximations

$$|\langle z|0\rangle\langle 0|z_t\rangle| \quad \rightarrow \quad |\langle z|0\rangle\langle 0|z\rangle| \quad \text{or} \quad |\langle z_t|0\rangle\langle 0|z_t\rangle| \tag{4.73}$$

also qualitatively retains the anharmonic frequencies in the wavepacket evolution. This is consistent with the stationary phase condition described for the Van Vleck density of states. A classical trajectory only contributes to the wavepacket propagation for times where $z \approx z_t$

Using our approximate forms for the HK prefactor, phase, and the coherent state overlaps from Eqs. (4.59) and (4.60), we can write the integrand for wavepacket propagation in Eq. (4.54) as

$$\begin{aligned} A_{mn} &\equiv \langle m|z(t)\rangle\, C(z,t) e^{iS(t)/\hbar}\, \langle z|n\rangle \\ &= \sqrt{\frac{\hbar\omega^2 t}{2D\, n!m!}}\, N^{(n+m+1)/2} e^{-N} e^{-i(m+1/2)\lambda\omega t} e^{i(n-m)\phi} e^{-i\frac{\omega}{4D\hbar}J^2\omega t}. \end{aligned} \tag{4.74}$$

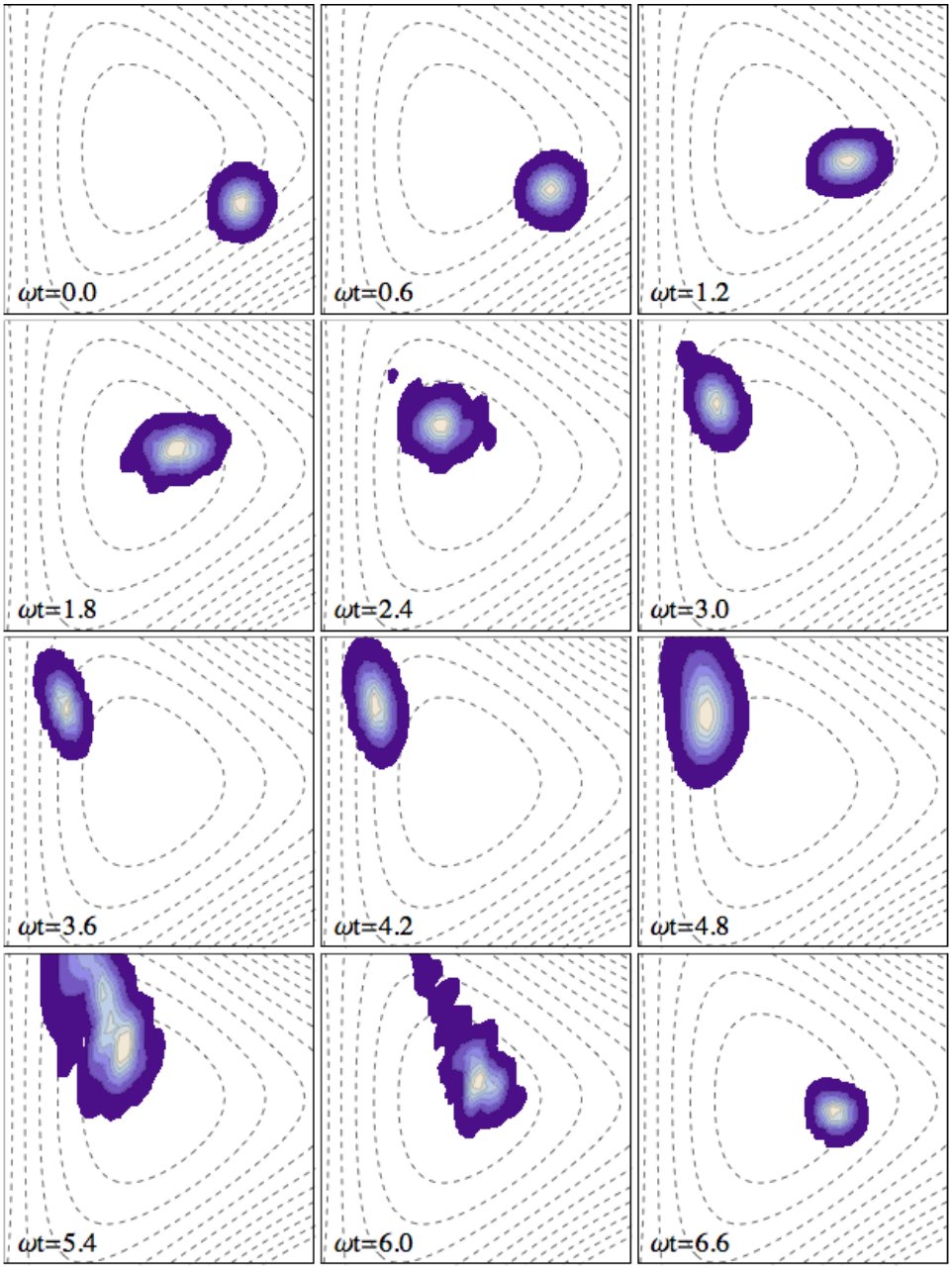

Figure 4.5: The square magnitude of a wavepacket propagating in a Henon-Heiles potential with parameters $(m_x^3\omega_x^5/c^2\hbar) = 320$, $m_x = m_y$, $\omega_x = \omega_y$ is plotted as a function of coordinates x and y. The initial state is a Gaussian centered at $cx_0/m_x\omega_x^2 = -0.19$, $cy_0/m_y\omega_y^2 = 0.38$, and the time propagation is carried out within the Herman-Kluk approximation. The dashed lines indicate contours of equal potential energy.

As for the harmonic case, the angle integral forces $n = m$. If we add in higher order terms in anharmonicity to Eq. (4.60), this $n = m$ constraint will be relaxed, and cross terms in A_{mn} will contribute to the wavepacket propagation. This is to be expected, as the harmonic initial states are not stationary states for the Morse oscillator system. Performing the angle integral of A_{mn} thus yields an expression that is identical to B_n for the HK density of states in Eq. (4.46). We can therefore integrate over action to generate a frequency component to the wavepacket overlap with the correct anharmonic frequency $\Omega_k = \epsilon_n/\hbar$. Therefore, we have shown how the frequency components of the wavepacket overlap (and thus the propagating wavefunction) are anharmonically quantized for a Morse oscillator system. As in the density of states, the actions are subject to a quantization condition, where only trajectories with $N = (n + 1/2)$ contribute to the nth component of the wavepacket overlap.

4.6 Summary

In this Chapter, we have reinterpreted the semiclassical quantization of action condition for response functions, derived in Chapters 2 and 3, in terms of a sum over all recurrence topologies. This is compared to Berry and Tabor's [137, 138] interpretation of the density of states within the Van Vleck approximation to the propagator in terms of a topological sum over periodic trajectories. In addition, we have investigated the mechanism by which the Herman-Kluk propagator generates anharmonically quantized frequency components for both the density of states and for the propagation of wavepackets. For harmonic systems, each value of the action N generates the correct frequency components for the density of states. For anharmonic systems, as for response functions, the time

divergence of the classical action $S(t)$ results in a quantization condition on the action variables and thus anharmonic quantization of frequencies. Our goal in this chapter has been to tie our analysis of semiclassical response functions into the broader context of semiclassical quantization and semiclassical propagators. For every case considered, it is the behavior of the classical action $S(t)$ which dictates how the semiclassical propagators are able to generate quantum results from only classical information.

CHAPTER 5

VIBRATIONAL ECHO SPECTROSCOPY OF HORSERADISH PEROXIDASE

5.1 Introduction

Protein dynamics occur on a wide range of time scales, from fast sub-picosecond local vibrations to large-scale conformational fluctuations that take place in nano or even microseconds, to folding on even longer time scales. These complex dynamics, along with the protein structure, are vital components to an understanding of how proteins function. For example, substrate binding or catalysis in an enzyme may be mediated by a conformational change. Nonlinear NMR techniques such as the spin echo [10] and other multiple-pulse techniques can be used to provide structural information on a protein, but these methods are limited to microsecond time resolution. Infrared spectroscopic techniques such as vibrational echo measurements allow the investigation of dynamics on the femto to nanosecond time scale. [14] Such experiments have been used to probe protein equilibrium fluctuations, dynamics in membranes, and protein unfolding, among others. [9, 13, 143–146] As the femto to picosecond time scale is accessible to molecular dynamics simulations, we seek to use such simulations to calculate vibrational echo spectra within a mixed quantum/classical model and thus connect the experimental spectra to particular molecular motions.

In this chapter we shall focus on heme-containing enzymes such as globins and peroxidases. Carbon monoxide (CO), among other ligands such as O_2, CN^-, and NO, binds strongly to the heme iron in, for example, myoglobin and horseradish peroxidase, and the CO stretching vibrational mode is well resolved

in the infrared spectrum. The CO stretch has a strong transition dipole, and unlike infrared features such as the extended normal mode vibrations in the amide I band, the CO stretch is localized. Furthermore, the CO stretching frequency ν_{CO} is strongly influenced by the local environment in the protein active site. As such, the CO chromophore has been extensively used as a probe of the dynamics of heme proteins. [52,147,148] In both wild-type and mutant myoglobins, vibrational echo measurements along with molecular dynamics simulations have been used by the Fayer and Loring groups to determine the time scales of dephasing and the identities of several spectroscopic states of CO evident in the absorption spectrum. The simulations utilized the MOIL [149] force field and were able to accurately describe the vibrational echo spectrum. In this chapter, we wish to determine whether this accuracy extends to other force fields such as the Amber force fields [150] and to other systems such as the heme-containing protein horseradish peroxidase isoenzyme C.

This chapter is organized as follows. In Section 2, we review the vibrational echo experiment and introduce a mixed quantum/classical model for the calculation of the echo signal. The chromophore CO is treated as a three-level quantum system weakly coupled to an off-resonance classical bath (the protein) within a second-order cumulant approximation. In Section 3, previous applications of this method to vibrational echo measurements in wild-type and mutant myoglobin are discussed. The horseradish peroxidase protein and its spectroscopic features are described in Section 4, while the results of our simulations for this enzyme and comparison to experiment are presented in Section 5. Computational details are provided in Section 6, and we summarize our findings in Section 7.

5.2 Calculating the vibrational echo

For general coupled oscillator systems, exact quantum calculation of the vibrational response functions is challenging. In Chapters 2 and 3, we discussed a semiclassical approximation to $R^{(n)}(t_n, \cdots, t_1)$ that treated each degree of freedom equivalently. This treatment was shown to be accurate for both one-dimensional anharmonic systems as well as coupled oscillator systems. For large coupled systems with many degrees of freedom, determining the good action variables necessary to implement the mean trajectory approximation in Eq. (3.26) is difficult. For systems that naturally separate into a quantum subsystem coupled to a bath of classical motions due to a separation of time scales, an alternative "mixed quantum / classical" method is useful for the calculation of nonlinear response functions. In this procedure, we treat the quantum subsystem exactly, and incorporate the relatively weak effects of the classical modes in an approximate manner.

Consider a three-level quantum system at zero temperature, as shown in Figure 1.2. The energy spacing between the ground and first excited states is defined as $\hbar\omega_{10} \equiv \hbar\omega$, while the energy level spacing between the first and second excited states is $\hbar\omega_{21} \equiv \hbar\omega(1 - \Delta)$. This quantum subsystem is weakly coupled to a classical, off-resonance bath such that no energy transfers between the three-level system and the bath (the pure dephasing limit). The classical bath will induce time-dependent fluctuations in the energy level spacing of the quantum subsystem, $\hbar\omega(t)$. Within a second-order cumulant approximation, [2] the system dynamics can be described by the frequency fluctuation autocorrelation

function $C(t)$,

$$C(t) \equiv \left\langle \delta\omega(t)\, \delta\omega(0) \right\rangle \tag{5.1}$$

where $\delta\omega(t) \equiv \omega(t) - \langle\omega\rangle$ is the frequency fluctuation at time t, and the brackets $\langle\rangle$ indicate an equilibrium ensemble average over bath degrees of freedom. This correlation function in turn generates a line-broadening function $g(t)$,

$$g(t) = \int_0^t d\tau_1 \int_0^{\tau_1} d\tau_2\, C(\tau_2)\,. \tag{5.2}$$

For this mixed quantum/classical model, the time-domain linear absorption spectrum is given by [50, 147]

$$I(t) = |\mu_{10}|^2\, e^{-i\omega t}\, e^{-t/2T_1}\, e^{-g(t)} \tag{5.3}$$

where μ_{10} is the transition dipole moment, and we have included the effects of lifetime broadening through T_1, the lifetime of the first excited state. The usual frequency domain absorption spectrum is obtained from the real part of the Fourier transform of Eq. (5.3). Note that the second cumulant approximation that generated Eq. (5.3) is exact for Gaussian fluctuations in the frequency $\omega(t)$ or when the classical system can be treated as a harmonic bath.

As discussed in Chapter 1, there are two limiting cases for line-broadening mechanisms. When each molecule in a sample experiences a range of frequencies on a time scale that is fast compared to the experiment, the sample is homogeneously broadened, and the frequency fluctuation autocorrelation function $C(t)$ is essentially a delta function at $t = 0$. In this case, the line-broadening function $g(t)$ is linear in time, and the resulting absorption lineshape is Lorentzian,

$$C(t) = 2\lambda\, \delta(t) \quad \Longrightarrow \quad g(t) = \lambda t \tag{5.4}$$

$$I(\Omega) \propto \frac{\lambda}{(\omega - \Omega)^2 + \lambda^2}\,. \tag{5.5}$$

In the static or inhomogeneous limit, each molecule experiences a slightly different local environment, resulting in a range of frequencies that change slowly on the time scale of the experiment. In this case, $C(t)$ is a constant in time, and the resulting absorption spectrum is Gaussian,

$$C(t) = \Lambda^2 \quad \Longrightarrow \quad g(t) = \Lambda^2 t^2/2 \,. \tag{5.6}$$

$$I(\Omega) \propto \exp\Big(- (\omega - \Omega)^2/2\Lambda^2 \Big) \,. \tag{5.7}$$

In general, $C(t)$ will contain time scales intermediate between the homogeneous and static limits, and the resulting absorption spectrum will be a convolution of a Gaussian and Lorentzian peak shape (a Voigt profile). [2]

While the linear absorption spectrum technically contains information on system dynamics and time scales through its dependence on $g(t)$, it can be challenging to differentiate static from homogeneous broadening merely by looking at the absorption lineshape. This is demonstrated in Figure 5.1, where $I(\Omega)$ is plotted for three different line-broadening functions $g(t)$. Note that each absorption spectrum has been normalized to unity at $\Omega = \omega$. The blue curve is dominated by homogeneous broadening with $\lambda = 11\omega/100$, $\Lambda = 0$, the green curve is dominated by static broadening, $\lambda = \omega/100$, $\Lambda = \omega/10$, and the red curve is intermediate between these other two cases, with $\lambda = \omega/20$, $\Lambda = \omega/10\sqrt{2}$. The overall lineshape in each case, however, is essentially identical, except near the tails of each peak. Therefore, in order to determine the time scales which contribute to the vibrational lineshape, we must use nonlinear spectroscopic techniques.

The nonlinear method which we shall focus on in this chapter is the vibrational echo experiment, a technique determined within the rotating wave approximation by the rephasing component of the third-order response function. [15] One representative term which contributes to the vibrational echo is

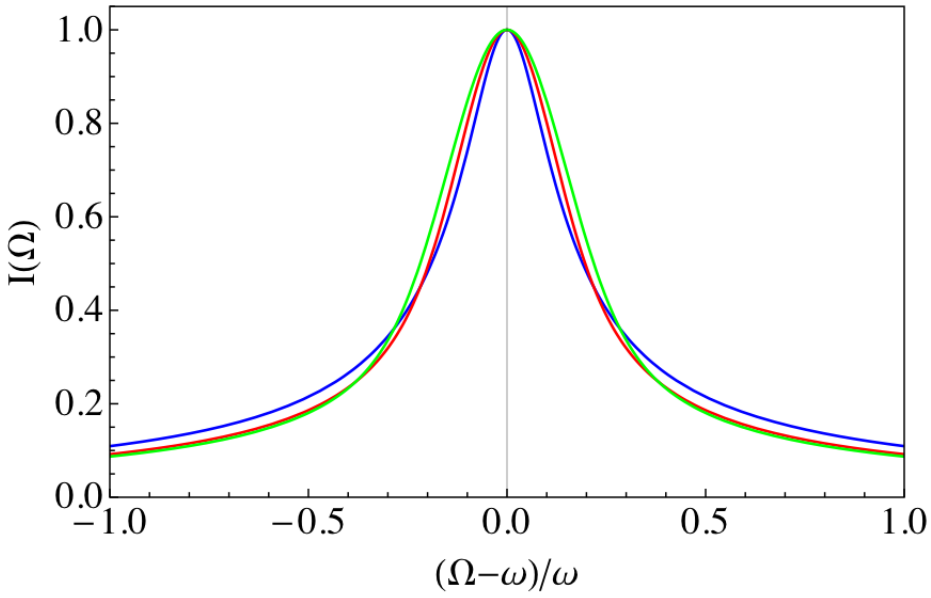

Figure 5.1: Absorption spectra calculated from the Fourier transform of Eq. (5.3) are depicted for various line-broadening functions $g(t)$ with $T_1 \to \infty$. The blue curve is dominated by homogeneous broadening with $\lambda = 11\omega/100$, $\Lambda = 0$, while the green curve is dominated by static broadening, $\lambda = \omega/100$, $\Lambda = \omega/10$. The red curve is intermediate between these other two cases, with $\lambda = \omega/20$, $\Lambda = \omega/10\sqrt{2}$. These absorption spectra are very similar in appearance.

represented by the double-sided Feynman diagram in the third column and third row of Figure D.2 of Appendix D. In this contribution to the echo, the initial interaction with the applied radiation field induces a transition in the bra side of the density matrix. As the system starts in the vibrational ground state at $T = 0$, the result of the first interaction is to put the density matrix into the $0,1$ coherence. During time t_1, the system then evolves a phase $e^{-i\omega_{01}t_1}$. After the second laser pulse, the density matrix is back in the $0,0$ ground state population, and no phase is accumulated during time t_2. The third interaction with the field puts the density matrix into the $1,0$ coherence, with an evolved phase of $e^{i\omega_{01}t_3}$ during time t_3. The total phase of the density matrix for this process is thus

$e^{-i\omega_{01}(t_1-t_3)}$. For $t_1 = t_3$, the system therefore has a total phase of zero.

For a statically broadened system, the coherence frequency ω_{01} varies slightly for each molecule. As a result, the signal rapidly dephases in time, resulting in a broadened absorption peak. In a vibrational echo experiment, however, the total phase for each molecule is small when $t_1 = t_3$. Therefore, the system rephases for this particular combination of time arguments, and the measured signal has a recurrence. This recurrence or "echo" decays as a function of $t = t_1 = t_3$ due to homogeneous broadening which is not rephased. Thus, the vibrational echo experiment allows for the separation of homogeneous and static line-broadening. [14] Note that this type of echo measurement is strongly analogous to the spin echo technique of NMR spectroscopy. [10]

The vibrational echo signal is calculated from the rephasing component of the third-order polarization, $P^{(3)}$, which in turn is found from the convolution of the applied fields with the appropriate nonlinear response function,

$$P^{(3)}(t, T_w, \tau) \propto \int_0^\infty dt_3 \int_0^\infty dt_2 \int_0^\infty dt_1 \sum_{i=1}^{3} R_i(t_3, t_2, t_1)\, E_3(t - t_3) \times E_2(T_2 + t - t_3 - t_2)\, E_1^*(\tau + T_w + t - t_3 - t_2 - t_1)\,. \tag{5.8}$$

The three contributions to the response in Eq. (5.8) correspond to the rephasing double-sided Feynman diagrams in the top three rows of Figure D.2. Within the same second cumulant approximation that generated Eq. (5.3) for the linear absorption spectrum, these three components of the response function are given by

$$\begin{aligned} R_1 &= R_2 = |\mu_{10}|^4 e^{-i\omega(t_3-t_1)}\, e^{-(t_1+2t_2+t_3)/2T_1}\, e^{G(t_1,t_2,t_3)} \\ R_3 &= -|\mu_{10}|^2|\mu_{21}|^2 e^{-i\omega(t_3-t_1)}\, e^{i\omega\Delta t_3}\, e^{-(t_1+2t_2+t_3)/2T_1}\, e^{G(t_1,t_2,t_3)} \end{aligned} \tag{5.9}$$

where $G(t_1, t_2, t_3)$ is defined as a combination of line-broadening functions at different times,

$$G(t_1, t_2, t_3) \equiv -g(t_1) + g(t_2) - g(t_3) - g(t_1 + t_2) - g(t_2 + t_3) + g(t_1 + t_2 + t_3) \qquad (5.10)$$

and T_1 is the excited state lifetime, as in Eq. (5.3). Furthermore, Eq. (5.9) assumes that $C(t)$ in Eq. (5.1) is equal to the frequency fluctuation autocorrelation function of one-quantum coherences,

$$C(t) = \left\langle \delta\omega_{10}(t)\omega_{10}(0) \right\rangle = \left\langle \delta\omega_{21}(t)\omega_{21}(0) \right\rangle = \frac{1}{4}\left\langle \delta\omega_{20}(t)\omega_{20}(0) \right\rangle . \qquad (5.11)$$

We shall also assume that the second excited state lifetime is one-half of the first excited state lifetime T_1, and that the transition dipole moment $|\mu_{21}| = \sqrt{2}\,|\mu_{10}|$ as is appropriate for a nearly harmonic vibration.

The experimental echo signal is calculated from the magnitude of the Fourier transform of $P^{(3)}(\tau, T_w, t)$ with respect to t. If we assume the applied field pulses are short on the timescale of the experiment, we may approximate them as delta function pulses (the impulsive limit). In this limit, $\tau = t_1$, $T_w = t_2$, and $t = t_3$, and the signal P_{echo} is given by

$$\begin{aligned} P_{echo}(\tau; T_w, \Omega) &\propto \left| \int_0^\infty dt\, P^{(3)}(t, T_w, \tau)\, e^{i\Omega t} \right|^2 \\ &\approx \left| \int_0^\infty dt \sum_{i=1}^{3} R_i(t, T_w, \tau)\, e^{i\Omega t} \right|^2 . \end{aligned} \qquad (5.12)$$

Typically, P_{echo} is measured for fixed waiting time $T_w = t_2$ at a particular frequency $\Omega \approx \omega_{10}$. The shape and time decay of P_{echo} gives us a way to determine the static and homogeneous contributions to the lineshape of a system, and thus vibrational echo spectroscopy allows for the investigation of system dynamics on fast (femtosecond to picosecond) time scales.

In Figure 5.2, the vibrational echo signal is plotted for the same model as in Figure 5.1. Panel (a) shows the time dependence of the rephasing response

functions in Eq. (5.9) for three different values of $\tau = t_1$. In each case, the echo pulse is centered at $t_3 = t_1$, with a width and height determined by the line-broadening function $g(t)$. The decay of the pulse height with τ seen in panel (a) reflects the homogeneous component of $g(t)$. In panel (b), the echo signal $P_{echo}(\tau; 0, \omega)$ is plotted as a function of τ for the same line-broadening functions as in Figure 5.1. While the resulting absorption spectra in these three cases are essentially identical, the echo spectra are qualitatively different. When static line-broadening is unimportant (blue curve), the echo spectrum is largest for $\tau = 0$ and then decays essentially exponentially. As the static contribution to $g(t)$ becomes large, the maximum in the echo signal shifts to longer times. Thus, analysis of the echo spectrum allows for the determination of $g(t)$ and thus the frequency fluctuation autocorrelation function $C(t)$. Note that in Figure 5.2(b), each spectrum has been normalized such that its maximum is unity.

In order to calculate either the linear absorption spectrum or the vibrational echo for a system of interest, we need to determine the fundamental frequency and anharmonicity ω and Δ of the three-level quantum subsystem, as well as the excited state lifetime T_1 and the frequency fluctuation autocorrelation function $C(t)$. The quantum subsystem parameters can be obtained either from a quantum calculation on the subsystem or just taken directly from experiment. The excited state lifetime is typically found from, for example, pump-probe spectroscopy. [50] The correlation function $C(t)$ on the other hand can be obtained approximately from molecular dynamics simulations of the entire system by assuming a Stark shift model for the fluctuating frequency $\omega(t)$. [147]

We shall be concerned with the case of a quantum vibrational mode (the diatomic molecule carbon monoxide, CO) bound in the active site of a protein

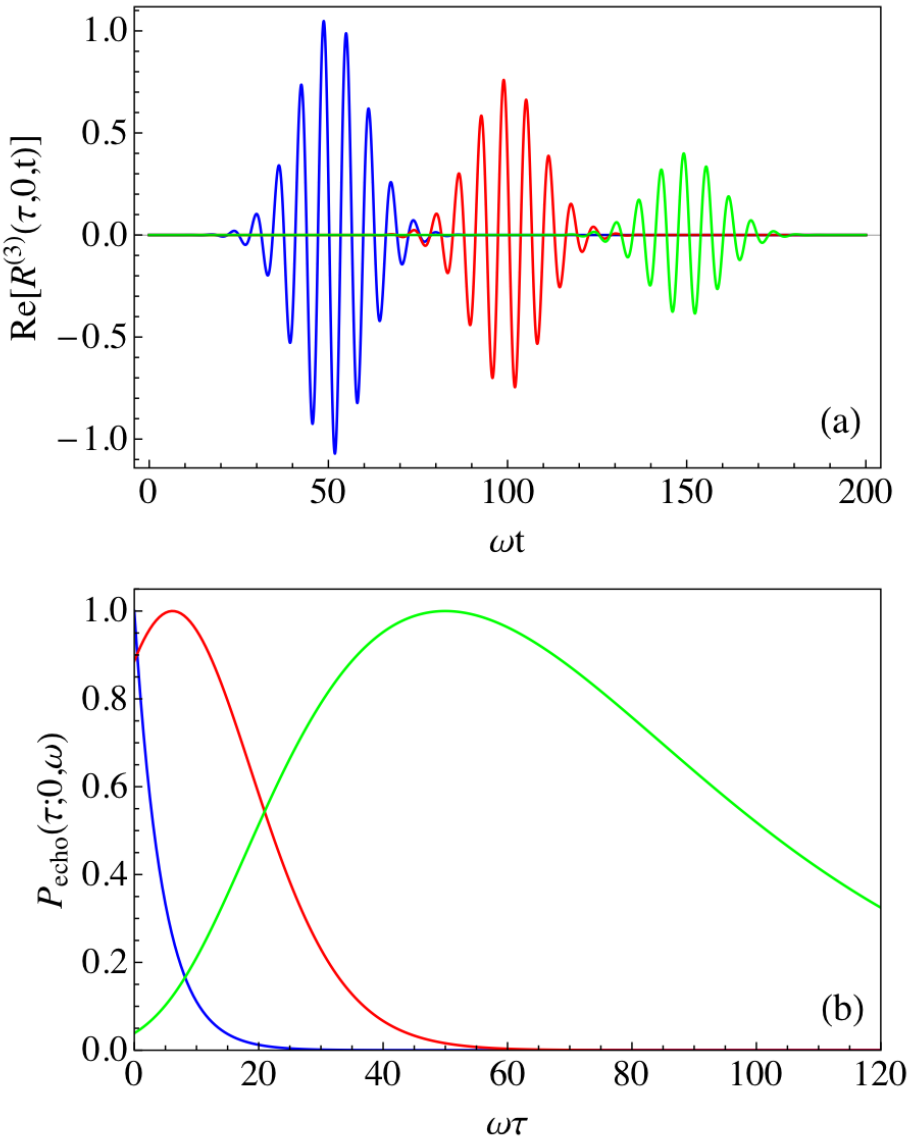

Figure 5.2: In panel (a), the real part of the rephasing component of the third-order response function is plotted vs. $t = t_3$ for $\omega\tau = \omega t_1 = 50$ (blue), $\omega\tau = 100$ (red), and $\omega\tau = 150$ (green). Each curve is calculated from Eq. (5.9) with $\Delta = 1/100$, $T_w = t_2 = 0$, $T_1 \to \infty$, $\lambda = \omega/100$, and $\Lambda = \omega/10$. In panel (b), the echo signal calculated from Eq. (5.12) is shown vs. $\tau = t_1$ for $\Delta = 1/100$, $T_w = t_2 = 0$, and $\Omega = \omega$. Each echo curve corresponds to the absorption curve of the same color in Figure 5.1.

that is in turn surrounded by water. The frequency of the CO stretching mode is sensitive to the electric field generated by the motions of the surrounding atoms. Therefore, we model the frequency of the CO vibration to be proportional to the component of the surrounding electric field along the CO dipole $\vec{u}$,

$$\delta\omega(t) = \lambda\Big(\vec{u}(t)\cdot\vec{E}(t) - \langle\vec{u}\cdot\vec{E}\rangle\Big) \tag{5.13}$$

where λ is the Stark coupling constant and $\vec{E}(t)$ is the instantaneous electric field at the midpoint of the CO bond. The constant λ can either be fit to experiment or obtained using vibrational Stark spectroscopy. [15, 151] The angular brackets in Eq. (5.13) indicate an ensemble average over the motions of the protein and solvent. The correlation function is then given by

$$C(t) = \Big\langle \delta\omega(t)\,\delta\omega(0)\Big\rangle = \lambda^2\Big(\Big\langle(\vec{u}(t)\cdot\vec{E}(t))\,(\vec{u}(0)\cdot\vec{E}(0))\Big\rangle - \langle\vec{u}\cdot\vec{E}\rangle^2\Big). \tag{5.14}$$

We fit $C(t)$ to a multiexponential form

$$C(t) = \sum_{i=1}^{n} \Delta_i^2\, e^{-t/\tau_i} \tag{5.15}$$

where typically $n = 3$. Our computational strategy is thus to calculate the component of the electric field along the CO dipole as a function of time, and then to compute $C(t)$ from an ensemble average and find the parameters Δ_i and τ_i in Eq. (5.15). Using $C(t)$, the line-broadening function $g(t)$ and therefore the resulting echo spectrum can be obtained.

5.3 Echo spectroscopy of myoglobin

Myoglobin (Mb) is a small heme-containing protein comprised primarily of alpha helices that is found in muscle tissue in mammals and can bind ligands such

as O_2 and CO. As the crystal structure has been known for several decades, myoglobin is among the best studied proteins in nature. The heme pocket of myoglobin contains both a proximal histidine residue bound directly to the heme iron, as well as a distal histidine (His64) on the other face of the heme which can interact with bound ligands. The infrared absorption spectrum of CO bound to wild-type myoglobin contains at least three absorption bands denoted A_0, A_1, and A_3 with frequencies of 1965 cm^{-1}, 1944 cm^{-1}, and 1932 cm^{-1} respectively. Many experiments have suggested that these absorption bands correspond to different conformations of amino acids in the heme pocket. [51, 147, 152–154] Studies on mutant myoglobins such as H64V (the distal histidine replaced by a valine) indicate that the frequency of the CO stretch is strongly influenced by the distal histidine. [153, 155, 156] Crystallographic and pH-dependent studies suggest that the A_0 state corresponds to a doubly protonated distal histidine that has swung out of the heme pocket. [157, 158] Interconversion between the A_0 and A_1/A_3 states takes place on the microsecond time scales, while recent 2D-IR chemical-exchange measurements have determined that the A_1 and A_3 states interconvert on the 50 picosecond time scale. [18]

Vibrational echo measurements on the CO vibrational modes of both wild-type and H64V mutant myoglobin have been performed as a function of temperature and solvent conditions and find that the lineshape is dominated by pure dephasing processes rather than population decay. [52, 155, 159] In wild-type myoglobin at room temperature, the vibrational echo of the A_3 state decays more rapidly as a function of time than that of the A_1 state, indicating that the two states have different dephasing rates. [50, 147] In order to determine the origin of these differences, the vibrational echo has been calculated from molecular dynamics simulations in the Loring group and compared to the ex-

perimental results. [15,52,147,155,156] These simulations utilize the MOIL force field [149] and are in quantitative agreement with the wild-type results with one adjustable parameter λ, the Stark coupling constant. The simulated echo spectrum for the H64V mutant is not quantitatively accurate but is still in qualitative agreement with experiment.

Furthermore, the molecular dynamics simulations on wild-type myoglobin have demonstrated two-state behavior that is in good agreement with the A_1 and A_3 states of the CO spectrum. These two states occur for the distal histidine protonated at the ϵ nitrogen, and correspond to a rotation of the histidine ring in the active site. [147] In the A_3 state, the N_ϵ hydrogen points towards the CO ligand, while in the A_1 state, the histidine has rotated around the C_β–C_δ bond, and the N_ϵ hydrogen points away from the CO. Simulations with the δ nitrogen protonated instead of the ϵ nitrogen also reveal two states, but the vibrational echoes for these states do not agree well with the experimental echoes for the A_1 and A_3 states. [15] As is observed experimentally, simulations on the H64V mutant only show one state behavior. [52]

We have repeated these vibrational echo calculations on both wild-type and H64V myoglobin using the Amber force fields, [150] as described in Section 6. Our goal was to determine whether the computational results obtained from MOIL were specific to that force field, or whether other force fields could obtain qualitatively similar results. Simulations on wild type myoglobin with bound CO were performed with both the Amber 94 and 03 force fields with both the TIP3P and SPC/E models for water molecules. [160,161] Starting protein coordinates were obtained from Protein Data Bank (PDB) structures 1BZR and 1A6G, [162,163] and the charge on the CO molecule was set to $q_C = 0.17$,

$q_O = -0.17$ in units of the electron charge, as was done by Anselmi et.al. in recent simulations of carbonmonoxy neuroglobin. [164] Structure 1A6G starts near the A_0 spectroscopic state with the distal histidine swung out of the heme pocket. As a result, no two-state behavior is observed on the time scale of the simulation. Structure 1BZR on the other hand begins near the A_1/A_3 state, and simulations with the Amber 03 force field with SPC/E water reveal the same two-state behavior as observed previously. [147] Simulations with the Amber 94 force field also contain two states, though the A_1 state occurs very infrequently.

The results of one sample simulation run on wild-type myoglobin (Amber 03 force field, SPC/E water) are presented in Figure 5.3. Panel (a) shows the time-dependent frequency fluctuations $\delta\omega(t)$, with the Stark coupling constant set to $\lambda = 1.0\frac{cm^{-1}}{MV/cm}$. Two distinct states are evident, with the higher frequency state corresponding to the A_3 spectroscopic state. In panel (b), the frequency fluctuation autocorrelation functions for each state are plotted. As is observed both experimentally and in MOIL simulations, [147] $C(t)$ at $t = 0$ for the A_3 state is larger than $C(0)$ for the A_1 state, and A_3 dephases more rapidly than A_1. In the third panel, the distal histidine configurations that generate each state are shown. In the A_3 state, the CO interacts strongly with the hydrogen bound to the ϵ nitrogen atom of the histidine. In the A_1 state, the distal histidine has rotated, disrupting this close interaction.

Ben Nebgen in the Loring group has also run simulations on wild-type myoglobin with the Amber 99SB and 03 force fields, starting from structure 1AJG (myoglobin with bound CO). [165] With the same CO charges as in the previous Amber 94 and 03 calculations, he again observed two state behavior. When the CO partial charges were changed to the gas-phase values of $q_C = 0.021$,

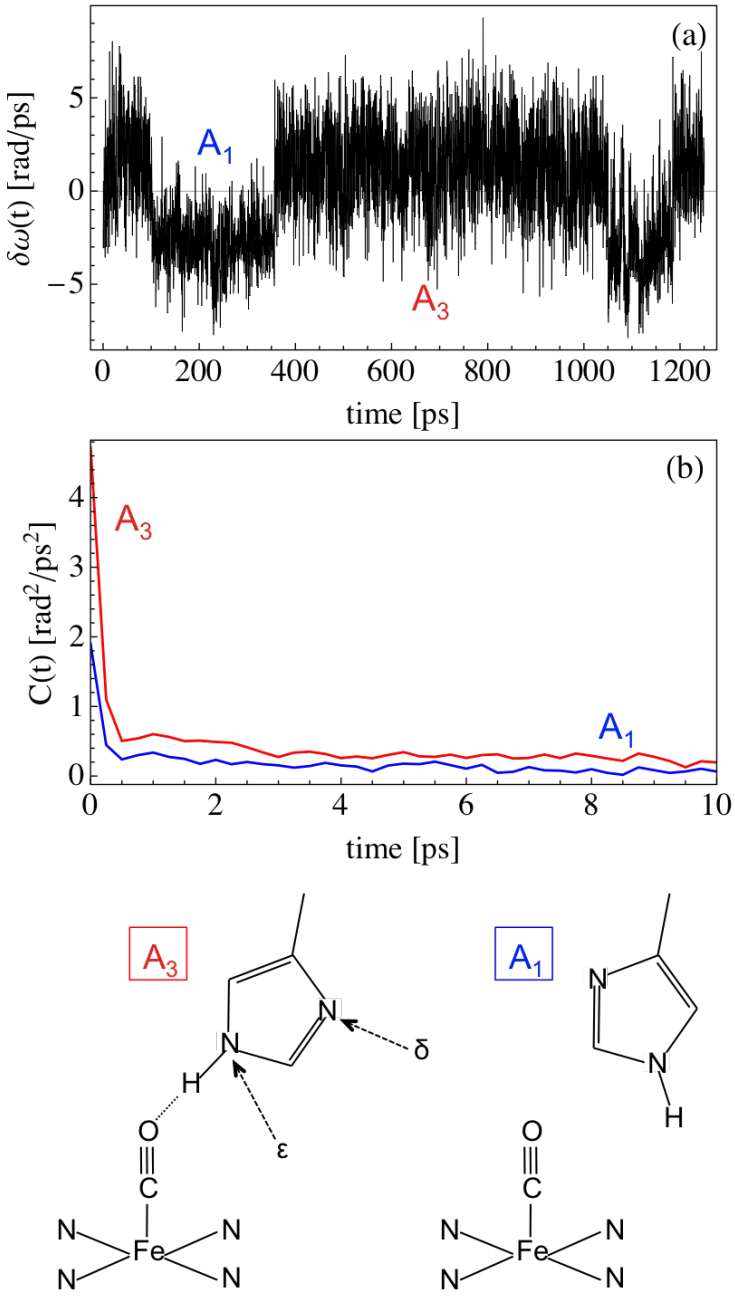

Figure 5.3: In panel (a), the frequency fluctuations $\delta\omega(t)$ are shown for a simulation of wild type myoglobin with the Amber 03 force field and SPC/E water, starting from structure 1BZR. The presence of two spectroscopic states A_1 and A_3 are evident from the fluctuations. Panel (b) displays the correlation function $C(t)$ calculated from the frequency fluctuations in panel (a) for each state. The bottom panel depicts the arrangement of the distal hisidine in the active site for each state.

$q_O = -0.021$ in units of the electron charge, the frequency of flipping between the two states increased. Note that these gas-phase partial charges were also used in MOIL. Finally, simulations were performed on the H64V mutant of myoglobin using the Amber 94, 99SB, and 03 force fields and CO partial charges $q_{CO} = \pm 0.17$. Starting structures were obtained from PDB file 2MGJ [166] and from 1BZR, with the distal histidine manually mutated into a valine and then equilibrated. In all cases, only one state was observed, and the calculated vibrational echo decayed more slowly than for wild type myoglobin, consistent with the previous MOIL results. [52]

5.4 Horseradish peroxidase

Horseradish peroxidase isoenzyme C (HRP) is a heme-containing glycoprotein which oxidizes various organic substrates in the presence of hydrogen peroxide. HRP is the most common member of the peroxidase family found in horseradish roots, and it has been widely studied as a model peroxidase. [167, 168] The ~308 amino acid enzyme is primarily composed of alpha helices, and four disulfide bonds as well as a buried salt bridge provide structural support. Two seven-coordinate calcium ions are present on the proximal and distal sides of the enzyme active site, and loss of either calcium ion results in a decrease in enzyme activity. The active site contains a solvent exposed iron-heme unit which is bound to the protein through a proximal histidine residue, His170, as in myoglobin. The structure of carbonmonoxy HRP from PDB structure 1W4Y [169] is shown in Figure 5.4.

The catalytic cycle of HRP begins with the heme iron in the ferrous Fe(III)

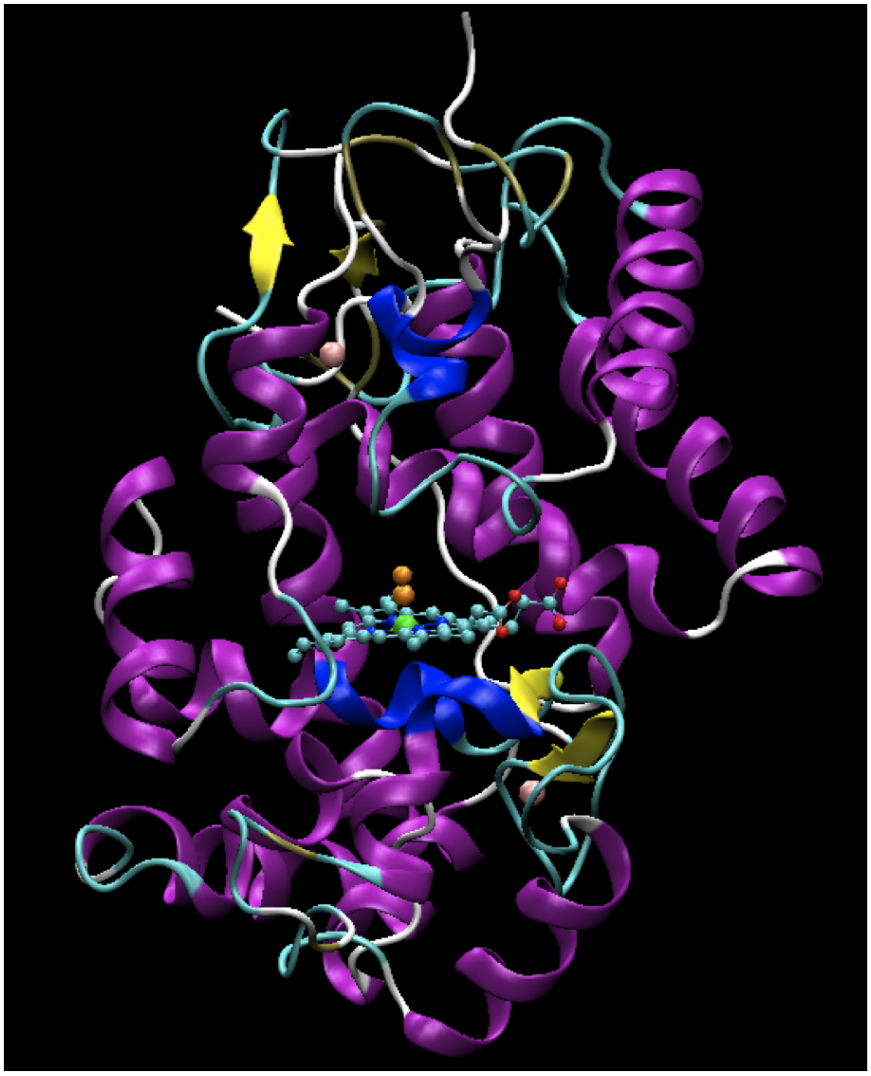

Figure 5.4: Horseradish peroxidase isoenzyme C from PDB structure 1W4Y is shown with the bound CO depicted in orange and the heme iron atom in green. The protein is primarily composed of alpha helices, shown in purple. The two calcium ions are depicted in pink.

resting state. Addition of hydrogen peroxide and elimination of water results in an oxyferryl Fe(IV) species along with a cation radical on the porphyrin ring, referred to as compound I. Two one-electron reductions of substrate molecules return the enzyme to its resting state. Mechanistic studies along with crystal structure data suggest that two amino acids play a vital role in the catalytic cyle — a distal histidine, His42, and a distal arginine, Arg38. [168,170,171] The distal histidine is similar to that in myoglobin, and myoglobin mutants with an active site threonine replaced with an arginine (T67R mutant) have shown catalytic peroxidase activity. [172, 173] The distal histidine is hydrogen bonded through its δ nitrogen to an asparagine, Asn70, which restricts rotations of His42. A phenylalanine residue, Phe41, is also present in the HRP active site.

As in myoglobin and other heme proteins, the HRP heme iron can bind O_2, CO, NO, and CN^-. As described in Section 3, bound CO can be used as a spectroscopic probe of dynamics in the active site. HRP in addition binds a variety of substrates such as the tight-binding inhibitor benzhydroxamic acid (BHA). BHA is held in the active site through hydrogen bonding interactions with His42 and Arg38 as well as with a distal proline residue, Pro139, and it displaces a water molecule that interacts with His42 in the absence of substrate. [174] Upon BHA binding, several hydrophobic amino acid residues move to interact with the BHA aromatic ring, and in doing so block off the active site from the solvent. The active site structure of HRP with bound CO is shown in Figure 5.5 both with and without bound BHA. The top panel without BHA comes from PDB structure 1W4Y, [169] while the bottom panel with BHA comes from structure 2ATJ. [174] Figure 5.6 shows the structure of the distal arginine and histidine, as well as the BHA substrate, and certain atoms are labeled for future reference.

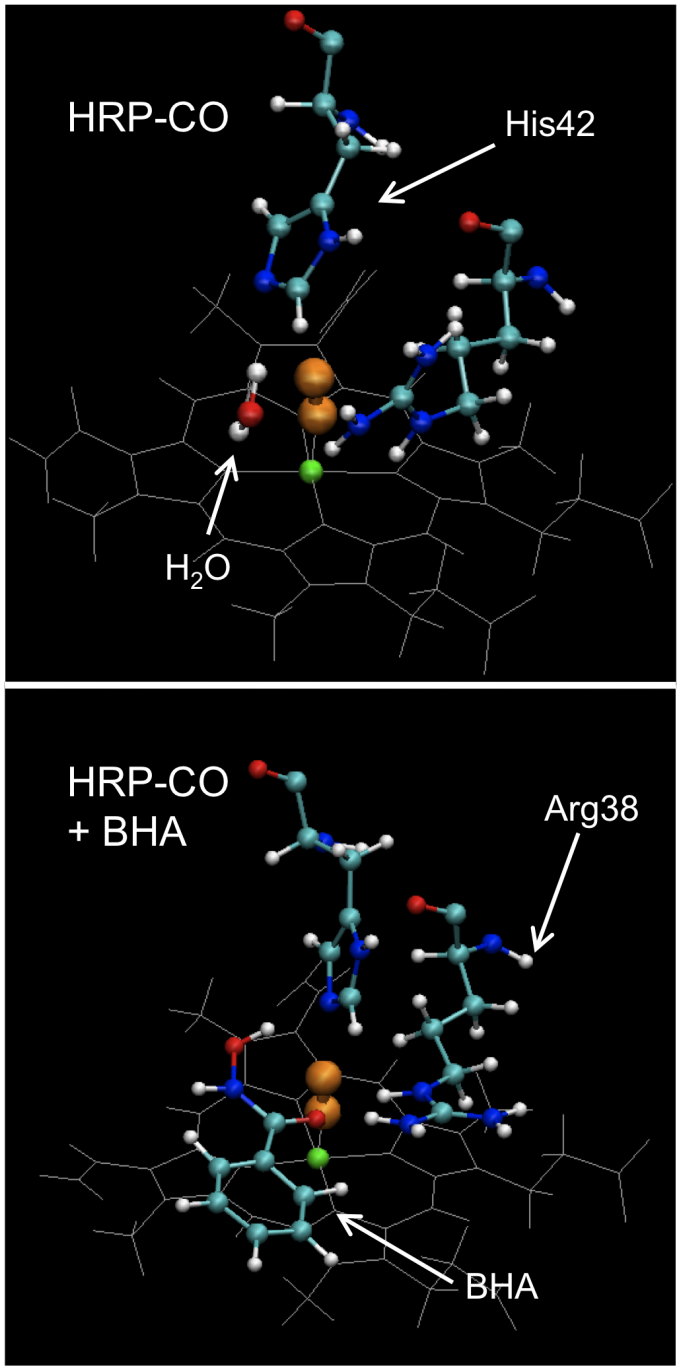

Figure 5.5: The active site of HRP with bound CO is depicted both without (top) and with (bottom) bound BHA. The CO is shown in orange, while the heme iron is in green and the porphyrin ring is in grey. The distal histidine and arginine, as well as BHA and an active site water molecule, are also shown.

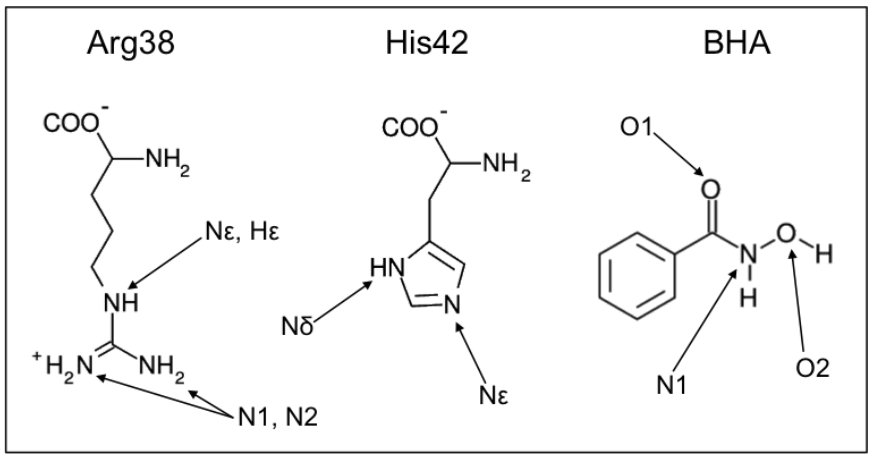

Figure 5.6: The structures of the distal arginine, distal histidine, and benzhydroxamic acid (BHA) are shown, and several important nitrogen and oxygen atoms are labeled for future reference.

Infrared absorption spectroscopy on the CO stretch in HRP without bound BHA shows two distinct spectroscopic states labeled red and blue, with absorption maxima at 1903.7 and 1932.7 cm^{-1} respectively. [175] Resonance Raman experiments suggest that in the red state, the CO is normal to the heme ring and interacts strongly with the distal histidine and only weakly with the distal arginine. In the blue state, the CO is slightly bent from normal with the heme plane, and it interacts more strongly with Arg38 and weakly with His42. [176, 177] As the red state disappears at high pH, this state is thought to correspond to a doubly protonated distal histidine, while the blue state corresponds to a singly protonated histidine. [178] The red peak is also observed to disappear for HRP mutants with Arg38 replaced by a leucine. [179] The absorption spectrum of the CO stretch in HRP has also been studied as a function of temperature, solvent viscosity, and in the absence of the calcium ions. [180–182]

When BHA binds to HRP, the absorption spectrum of the CO stretch simplifies into a single, relatively narrow Gaussian peak centered at 1909.0 cm^{-1}.

A variety of other similar substrates generate comparable absorption spectra. [148, 183] The CO absorption peak with BHA is close in frequency to the red peak without BHA, and the relatively narrow lineshape suggests that the presence of BHA constrains protein motions near the active site. In order to investigate the dynamics of HRP both with and without substrate, Finkelstein et.al. [148] performed 2D-IR and vibrational echo measurements on carbonmonoxy HRP, as discussed in Section 3 for myoglobin. The frequency fluctuation autocorrelation function parameters Δ_i and τ_i from Eq. (5.15) were fit from the experimental data and are compiled in Table 5.1. The fast time scale, motionally narrowed component of $C(t)$ cannot be experimentally decomposed into τ_1 and Δ_1, but instead contributes a Lorentzian lineshape with width $\Gamma^* = \pi\Delta_1^2\tau_1$. The vibrational lifetime parameters T_1 were determined by IR pump-probe experiments. [148]

The active site dynamics in each state of HRP are reflected in the $C(t)$ parameters in Table 5.1. The blue state contains only fast, motionally narrowed dynamics and motions that are slow on the time scale of the experiment. The red state, on the other hand, includes contributions from an intermediate 1.5 ps time scale. With bound BHA, the inhomogeneous broadening parameter Δ_3 is significantly reduced from the red and blue states, resulting in a narrower absorption peak. The linear absorption and vibrational echo spectra obtained from these experimental fits to $C(t)$ are shown in Figure 5.7, where the red and blue curves correspond to the red and blue states, and the green curve indicates bound BHA. The echo spectra are calculated using Eq. (5.8) with $T_w = 0$ and Ω set to the peak absorption frequency for each state. The anharmonicity Δ for each state was estimated from 2D-IR spectroscopy as in Figure 3 of Ref. [148]. As can be seen, with BHA bound, the CO stretch undergoes slower dephasing

Table 5.1: Spectroscopic parameters are shown for the red and blue states of HRP, as well as for BHA bound to HRP. These experimental data are reproduced from Tables 1 and 2 of Finkelstein, et.al., [148] and were obtained by fitting the absorption spectrum and vibrational echo spectrum with a frequency fluctuation autocorrelation function of the form in Eq. (5.15).

	Red	Blue	BHA
ν_{CO} [cm^{-1}]	1903.7	1932.7	1909.0
FWHM [cm^{-1}]	13.0	9.0	7.3
Γ^* [cm^{-1}]	0.76	1.40	1.40
Δ_2 [cm^{-1}]	3.1	3.2	2.3
Δ_3 [cm^{-1}]	5.6	2.4	1.9
τ_2 [ps]	1.5	15.0	4.4
τ_3 [ps]	21	∞	∞
T_1 [ps]	8.0	12.0	–

than in the blue state, while the red state experiences the fastest dephasing of the three.

In order to better understand the spectroscopic states of HRP, Kaposi et.al. [183] have performed molecular dynamics simulations on carbonmonoxy HRP with and without bound BHA for both singly and doubly protonated His42. Their molecular dynamics calculations utilized the CHARMM 22 force field, and they constrained all protein backbone atoms to remain near the starting structures 1ATJ and 2ATJ. [167, 174] In addition, all bond lengths were constrained, and the solvent was treated as a continuum. Within these approximate dynamics, they found that for the singly protonated (high pH) case both with and without BHA, the His42 – Arg38 distance was smaller than in the doubly protonated case. Without bound BHA, the high pH (blue) state has a smaller

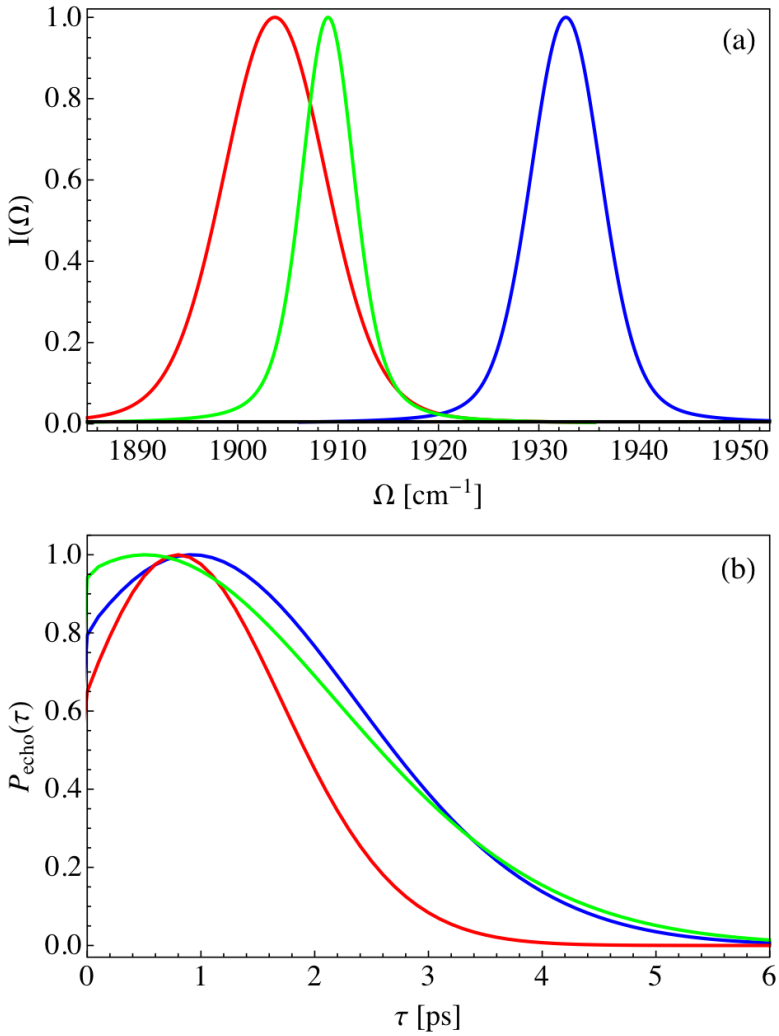

Figure 5.7: The absorption spectrum and vibrational echo for CO bound to HRP are shown in panels (a) and (b) respectively. In each panel, the red curve indicates the red spectroscopic state, the blue curve is the blue state, and the green curve indicates the spectrum when BHA is bound in the active site of HRP. The vibrational echo signal is calculated for $T_w = 0$ and at the dominant frequency ν_{CO} for each state.

CO – Arg38 distance and a larger CO – His42 distance than in the low pH (red) state. When BHA binds for either protonation state, the CO – Arg38 distance decreases, while the CO – His42 distance stays approximately constant. Finally, by monitoring the amino acid RMSD fluctuations, they determined that BHA binding results in a decrease in active site fluctuations. These results are consistent with the experimental findings in Table 5.1 and Figure 5.7. However, Kaposi et.al. [183] did not calculate vibrational echo spectra from their simulations, and due to the constraints placed on bond lengths and backbone atoms, the calculated fluctuations are likely smaller than they would have been without these constraints. Therefore, we wish to use simulations with the Amber force fields to calculate vibrational echo and absorption spectra for each state of HRP, and by doing so increase our understanding of the protein motions in the active site that contribute to the experimentally determined dephasing time scales.

5.5 Results and discussion

In order to calculate the absorption and vibrational echo spectra for carbonmonoxy HRP with the Amber force fields, a number of molecular dynamics simulations were performed where the force field, CO partial charge, and protonation state of the distal histidine were varied. For each simulation, the component of the electric field along the CO dipole was monitored, and the resulting frequency fluctuation autocorrelation function calculated and fit to the multi-exponential form in Eq. (5.15). Several simulations showed multi-state behavior, and an independent correlation function $C(t)$ was calculated for each state. In addition, a number of distances between atoms in the protein active site were monitored for each observed state. The results of our Amber simulations on

HRP without bound BHA are summarized in Table 5.2. The Stark coupling constant has been set to $\lambda = 1.0\frac{cm^{-1}}{(MV/cm)}$ in this table, though we shall later fit λ to the linear absorption spectrum.

Table 5.2 displays the results of MD simulations with seven different combinations of the force field, CO charges, and His42 protonation state. In each case, the initial starting structure was taken to be PDB structure 1W4Y, HRP with bound CO. Simulations A–D correspond to gas phase CO partial charges of $q_{CO} = \pm 0.021$ in units of the electron charge, while simulations E, F, and G correspond to the charges of Anselmi et.al., $q = \pm 0.17$. [164] All simulations other than C and D were performed with the Amber 03 force field, while C and D utilized the 94 force field. Finally, simulations A, C, and E were carried out for doubly protonated His42, thought to correspond to the red spectroscopic state. Simulations B, D, and F had the distal histidine only protonated at the δ nitrogen, while simulation G protonated His42 at the ϵ nitrogen only. Simulation G likely does not correspond to an experimental state of the system, as the protonated ϵ nitrogen of His42 is hydrogen bonded to an asparagine, Asn70.

In simulations A–E, we observe only one spectroscopic state as determined through analysis of the fluctuating frequency $\omega(t)$. Simulation G consists of at least two poorly differentiated states that result from rotations of the distal histidine in the active site. Though such a rotation results in the A_1/A_3 states in wild-type myoglobin as discussed in Section 3, it is unlikely to occur in HRP, as a hydrogen bond between His42 and Asn70 restricts histidine movement. In simulation F, we observe at least four states, though state F1 dominates in most calculated trajectories. As in simulation G, state F2 is the result of a His42 rotation in the active site. States F3 and F4 result from various rotations of the distal

Table 5.2: The results of MD simulations on carbonmonoxy HRP starting from structure 1W4Y are shown, where FF denotes the Amber force field used, q_{CO} is the partial charge on CO, H42 prot. denotes the protonation state of the distal histidine, and all simulations are run with SPC/E water. The parameters Δ_i and $\langle \vec{E} \cdot \vec{u} \rangle$ have units of [rad/ps], while τ_i has units of [ps]. The final five columns give the distance in Angstroms between the CO oxygen atom and the active site atom denoted. The Stark coupling constant has been set to $\lambda = 1.0 \frac{cm^{-1}}{(MV/cm)}$.

Name	FF	q_{CO}	H42 prot.	$\langle \vec{E} \cdot \vec{u} \rangle$	C(0)	τ_1	τ_2	Δ_0	Δ_1	Δ_2	H42 Nϵ	H42 Nδ	A38 Nϵ	A38 Hϵ	A38 N1
A	03	±0.021	δ, ϵ	-11.9	3.62	0.029	14.7	0.43	1.75	0.62	3.0	4.3	3.1	2.8	3.6
B	03	±0.021	δ	-4.4	4.83	0.038	16.5	0.20	2.05	0.78	3.0	4.6	3.1	2.8	3.7
C	94	±0.021	δ, ϵ	-11.3	4.43	0.033	1.66	0.83	1.85	0.57	3.2	4.4	3.1	2.9	3.7
D	94	±0.021	δ	-5.9	6.34	0.044	4.47	0.94	2.13	0.97	3.1	4.9	3.1	2.8	3.9
E	03	±0.17	δ, ϵ	-12.9	3.98	0.042	6.77	0.37	1.89	0.52	3.0	4.3	3.0	2.8	3.6
F1	03	±0.17	δ	-5.6	4.94	0.059	7.10	0.49	2.08	0.63	3.1	4.6	3.0	2.7	3.5
F2	03	±0.17	δ	-9.9	5.60	–	–	–	–	–	3.8	4.1	3.0	2.8	3.4
F3	03	±0.17	δ	-11.7	9.41	0.064	8.39	0.94	2.76	0.95	3.0	5.0	3.0	2.1	3.9
F4	03	±0.17	δ	-8.7	12.3	0.075	6.10	1.21	3.06	1.20	3.2	4.9	3.0	2.3	4.0
G	03	±0.17	ϵ	-10.3	11.3	0.089	5.61	1.39	2.57	1.65	–	–	–	–	–

arginine, Arg38. Though the ϵ nitrogen of Arg38 is relatively stable for each F state, in F3 and F4, the hydrogen atom bound to Nϵ rotates closer to the CO. In states A–E and F1, the orientation of the plane formed by the nitrogen atoms Nϵ and N1, N2 of Arg38 is roughly perpendicular to the heme plane, while in states F3 and F4, the two planes are nearly parallel.

The active site distances measured in Table 5.2 are in only partial agreement with the previous results of Kaposi, et.al. and with experimental observations on the HRP red and blue states. [183] Simulation pairs A/B, C/D, and E/F1 each correspond to simulations with the same force field and CO charge, but different His42 protonation states. Therefore we expect each pair to possibly correlate with the red and blue spectroscopic states of HRP. For each pair, the distance between the CO and the Nϵ and N1 nitrogen atoms of the distal arginine was essentially invariant upon changing the protonation state of His42. In the doubly protonated cases A, C, and E, the δ nitrogen of His42 is slightly closer to the CO than in the singly protonated simulations. This is consistent with previous simulations and experimental evidence, though the effect is smaller than that observed by Kaposi et.al. with the CHARMM force field. In addition, in all simulations we analyzed, the Fe-C-O unit is essentially perpendicular to the heme plane. While this is consistent with the experimental interpretation of the spectroscopic red state, we did not observe any bending associated with the blue state. Furthermore, in each simulation, a water molecule was located on the distal side of the heme unit approximately 3Å from the CO, independent of the force field or CO charges used.

The linear absorption spectra for simulations A–F1 were computed from $C(t)$ as discussed in Section 2, and are shown in Figure 5.8. The solid red and

blue curves indicate the experimental red and blue states, respectively, while the dashed magenta and green curves correspond to simulations A and B, the dot-dashed orange and purple curves correspond to simulations C and D, and the dotted brown and cyan curves correspond to simulations E and F1. The Stark coupling parameter was fit for each simulation pair in order to correctly obtain the experimental frequency difference between the red and blue states. The resulting fits for λ are $\lambda = 0.73$, $\lambda = 1.01$, and $\lambda = 0.75 \frac{cm^{-1}}{(MV/cm)}$ for the simulation pairs A/B, C/D, and E/F1 respectively. We could also have fit λ to obtain the best fit to the absorption spectrum lineshape, or to the vibrational echo spectrum. Note that the value for λ used in previous MOIL simulations on myoglobin, $\lambda \approx 2.1 \frac{cm^{-1}}{(MV/cm)}$, is in better agreement with experiment. [147, 151]

Several of the simulated absorption spectra presented in Figure 5.8 are in good agreement with the experimental results. The red state is well described by simulation C, while the lineshape predicted by simulations A and E is significantly too narrow. In contrast, the blue state is well described by simulations B and F1, while D results in a lineshape that is too broad. No single pair of simulations A/B, C/D, or E/F1 results in qualitative agreement with both experimental peaks. We have not shown spectra for simulations F2, F3, or F4 because the average component of the electric field along the CO dipole, $\langle \vec{E} \cdot \vec{u} \rangle$, is significantly shifted from simulations B, D, and F1. As $\langle \vec{E} \cdot \vec{u} \rangle$ determines the central frequency of the absorption peak, simulations F2, F3, and F4 fall near the red state rather than the blue state. It is possible that one or more of these states contribute to the experimental red peak, as this peak is rather broad.

The vibrational echo spectra with $T_w = 0$ were also calculated for simulations A–F1 using the same values for λ as in Figure 5.8. Panel (a) of Figure 5.9 shows

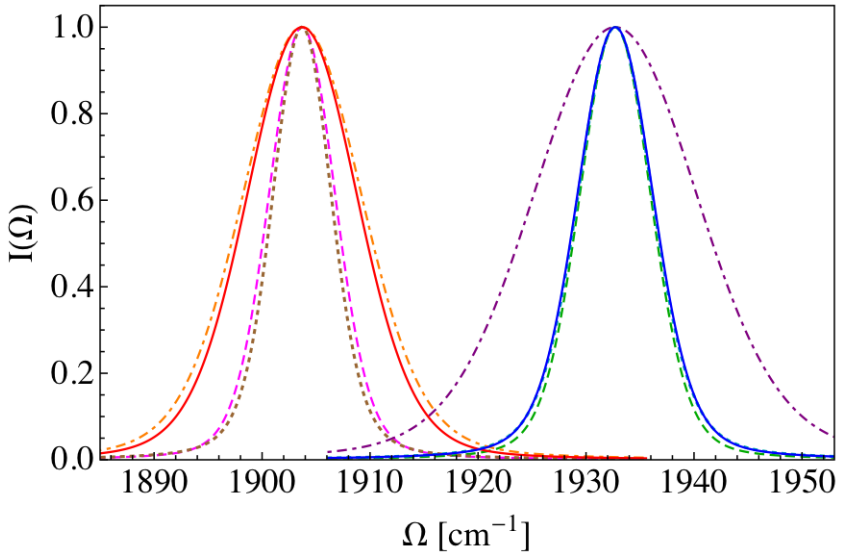

Figure 5.8: The linear absorption spectrum of carbonmonoxy HRP is shown for both the red and blue states. The solid red and blue curves indicate the experimental result, the dashed magenta and green curves correspond to simulations A and B from Table 5.2 respectively, the dot-dashed orange and purple curves correspond to simulations C and D, and the dotted brown and cyan curves correspond to simulations E and F1. For each pair of simulations, the Stark coupling constant λ was fit to the experimental frequency difference $\nu_{CO,blue} - \nu_{CO,red}$. The resulting values for λ are $\lambda = 0.73$, $\lambda = 1.01$, and $\lambda = 0.75 \frac{cm^{-1}}{(MV/cm)}$ for the simulation pairs A/B, C/D, and E/F1 respectively. Note that the cyan curve is almost indistinguishable from the experimental blue curve.

the "red" experimental and simulated results, while panel (b) shows the "blue" experimental and simulated spectra. Each curve in Figure 5.9 corresponds to the absorption spectrum curve of the same color and pattern in Figure 5.8. As was the case for the absorption spectrum, the experimental vibrational echo for the red state is accurately described by the orange curve, simulation C. The echo spectra for simulations A and E decay more slowly than the experimental result, and the peak for simulation A (magenta curve) is shifted to longer times τ. For the blue state, simulations B and F1 again are in qualitative agreement with

experiment, while simulation D decays far too quickly and is peaked at a time τ that is shorter than the experimental result. As we concluded for the absorption spectra, no single pair of simulations adequately describes both the red and blue spectroscopic states of HRP. Instead, the calculated vibrational echoes in Figure 5.8 appear to be nearly independent of the protonation state of His42, but rather depend primarily on the force field and CO charges used. In both panels (a) and (b), the dot-dashed curves corresponding to simulations C and D decay the fastest, while the dashed curves of simulations A and B decay the slowest. This suggests that the HRP active site dynamics are more constrained with the 03 force field and gas phase CO charges, while for the 94 force field and CO charges of $q_{CO} = \pm 0.17$, the active site dynamics undergo larger fluctuations.

We can further analyze the contributions to the simulated vibrational echo spectra by breaking the frequency fluctuation autocorrelation function $C(t)$ up into contributions from subsets of atoms. If we partition the system into two sets of atoms labeled a and b, $C(t)$ is given by

$$\begin{aligned} C(t) &= \langle \delta\omega(t)\, \delta\omega(0) \rangle = \langle (\delta\omega_a(t) + \delta\omega_b(t))\, (\delta\omega_a(0) + \delta\omega_b(0)) \rangle \\ &= C_{aa}(t) + C_{bb} + C_{ab}(t) + C_{ba}(t) \equiv \tilde{C}_a(t) + \tilde{C}_b(t) \end{aligned} \tag{5.16}$$

where the correlation functions for the subsystems are defined as

$$C_{ij}(t) \equiv \langle \delta\omega_i(t)\, \delta\omega_j(0) \rangle \tag{5.17}$$

$$\tilde{C}_j(t) \equiv C_{jj}(t) + \frac{1}{2} \sum_{i \neq j} C_{ij}(t) + C_{ji}(t)\,. \tag{5.18}$$

The correlation function $\tilde{C}_a(t)$ thus contains the direct contributions to the full correlation function from subsystem a as well as one-half of the cross correlations between a and the other atoms in the system.

We have measured $\tilde{C}_a(t)$ for a defined to be all protein amino acids, all water

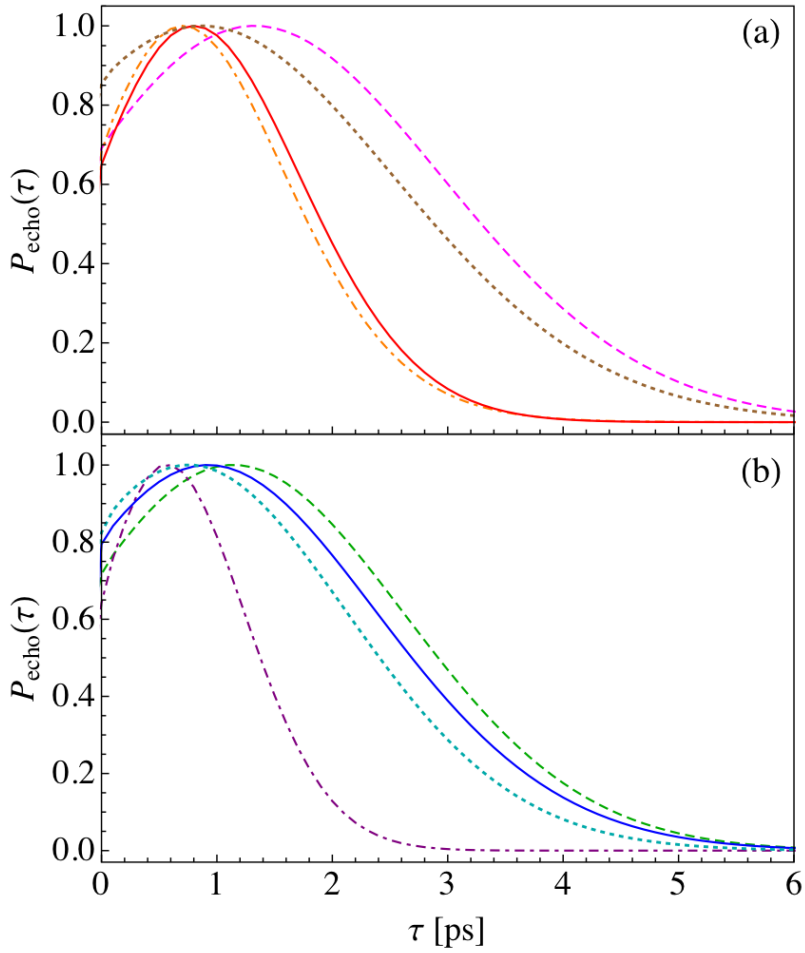

Figure 5.9: The experimental and simulated vibrational echos are compared for both the red state (a) and blue state (b). Each curve corresponds to the same color and pattern as in the absorption spectra in Figure 5.8. The echo calculations are carried out for $T_w = 0$ and for $\Omega = \omega_{CO}$ for each state.

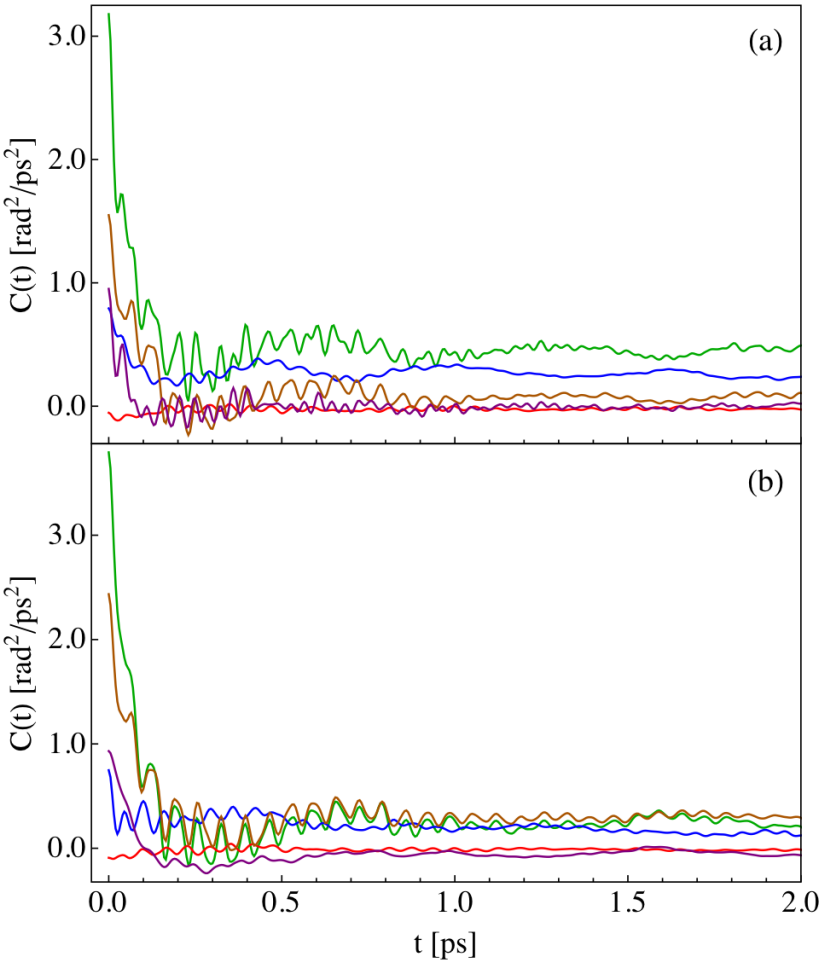

Figure 5.10: The contributions to the frequency fluctuation autocorrelation function $C(t)$ are shown for simulation A in panel (a) and for simulation B in panel (b). The green curve corresponds to the contribution from the protein, the blue curve gives the contribution from all water molecules, and the red curve corresponds to the heme unit. The contributions from the distal arginine and histidine are given in brown and purple respectively. The sum of the protein, water, and heme contributions generates the total correlation function $C(t)$.

molecules, the heme unit, and the distal arginine and histidine. The resulting components of the correlation function are shown in Figure 5.10 for both the doubly and singly protonated His42 cases, simulations A and B. In both cases, contributions from the protein (green) dominate $C(t)$, and the distal arginine (brown) accounts for a large percentage of the short time behavior of the correlation function. This is especially evident for the singly protonated case in panel (b), where the protein and Arg38 contributions are almost identical after about one-fourth of a picosecond. In the doubly protonated case in panel (a), contributions from water molecules (blue) are important on the single picosecond time scale. The relatively slow oscillations in the water curve in panel (a) are a result of librations in the water molecule bound near the CO in the HRP active site, as seen in the top panel of Figure 5.6. Note that in both simulations A and B, the distal histidine (purple) only contributes to the correlation on the very short time scale. This is a result of its relative immobility due to a hydrogen bond to Asn70. In no case did we observe any sizable contribution to the time dependence of $C(t)$ from the heme unit (red).

We now wish to investigate the effect of BHA binding in carbonmonoxy HRP. Experimental evidence suggests that upon binding BHA, the HRP active site dynamics slow down due to the hydrogen bonding network of BHA. This results in less inhomogeneous broadening, and thus a narrower absorption spectrum. We have examined the effect of BHA binding by running a number of Amber simulations using the 03 force field and CO partial charges of $q_{CO} = \pm 0.17$. As no crystal structure exists for carbonmonoxy HRP with bound BHA, we started from two different structures: carbonmonoxy HRP without BHA (1W4Y) and HRP with BHA but without CO (2ATJ). [169,174] Each starting structure was modified to add the missing element and then extensively equi-

librated. Various equilibration procedures including constraints on the BHA position in the active site were tested. The results of these simulations are summarized in Table 5.3, where the top half of the table shows the fitted parameters for $C(t)$ and the bottom half of the table displays distances between the CO and various active site residues.

As can be seen from Table 5.3, multiple states are obtained for simulations with protonation at only the δ nitrogen of His42. While double protonation of His42 only leads to a single state (case H), the mean value for the component of the electric field along the CO dipole is significantly red shifted. As was the case without BHA, ϵ-only protonation of His42 is unlikely to be experimentally relevant. As only a single, Gaussian absorption peak is measured upon BHA binding, it is likely that many or most of the observed simulated states are not present experimentally. An insufficiently accurate force field or an initial structure that is not at equilibrium is most likely the cause of these incorrect states. States J1–J4 result from shifts in the orientation and position of BHA in the HRP active site. States K1 and K2 result from a rotation of the distal histidine, as was observed in wild-type myoglobin.

Kaposi et.al. [183] observed that BHA binding decreases the distance between the distal arginine and CO. Comparing distances in Tables 5.2 and 5.3, we see that for δ protonated His42, the ϵ nitrogen of Arg38 is essentially unaffected by BHA, but the hydrogen atom bound to this nitrogen rotates closer to the CO in simulations J1 and J2 than in simulation F1. In simulations J1 and J2, the δ nitrogen of His42 also moves slightly further from the CO. The Arg38 and His42 orientations in simulations J1 and J2 are thus quite similar to those in simulations F3 and F4, with the plane formed by the Arg38 nitrogens nearly

Table 5.3: Simulation results for carbonmonoxy HRP with bound BHA are presented, where in each case the Amber 03 force field is used along with SPC/E water and CO partial charges of ±0.17. Units are defined as in Table 5.2, and λ is set to $1.0\frac{cm^{-1}}{(MV/cm)}$. The bottom half of this table lists the distance between the CO oxygen and the defined atom, though the final column gives the distance between the BHA carbonyl oxygen O1 and the distal arginine nitrogen N1.

Name	Struct.	H42 prot.	$\langle \vec{E} \cdot \vec{u} \rangle$	C(0)	τ_1	τ_2	Δ_0	Δ_1	Δ_2
H	2ATJ	δ, ϵ	-18.1	7.71	0.043	11.6	0.69	2.61	0.63
I	2ATJ	ϵ	-13.4	6.94	0.037	8.69	0.55	2.53	0.48
J1	2ATJ	δ	-9.1	6.67	0.024	10.8	0.83	2.39	0.53
J2	2ATJ	δ	-9.1	6.57	0.038	5.82	0.82	2.31	0.76
J3	2ATJ	δ	-4.5	5.21	0.055	8.95	0.24	2.22	0.47
J4	2ATJ	δ	-11.7	4.48	0.040	10.3	0.19	2.03	0.57
K1	1W4Y	δ	-6.5	5.62	0.067	9.61	0.40	2.15	0.69
K2	1W4Y	δ	-10.7	4.22	0.085	11.9	0.51	2.90	0.59

Name	H42 Nϵ	H42 Nδ	A38 Nϵ	A38 Hϵ	A38 N1	BHA N1	BHA O1	BHA O2	BHA O1 A38 N1
H	2.9	4.7	3.0	2.3	4.1	4.1	3.0	3.4	2.1
I	3.0	4.9	3.0	2.1	4.0	4.0	3.0	3.2	1.8
J1	3.1	5.0	3.0	2.1	4.1	4.2	3.3	3.3	1.8
J2	3.1	5.0	3.1	2.3	4.1	4.3	4.1	3.2	1.7
J3	3.2	5.0	3.1	2.8	3.2	4.8	5.1	3.5	3.2
J4	3.1	5.0	2.9	2.2	4.2	4.4	3.4	3.5	1.8
K1	3.2	4.7	3.0	2.7	3.5	4.7	5.0	3.3	2.1
K2	4.4	3.8	3.0	2.8	3.4	4.5	4.3	3.3	2.2

parallel to the heme plane. In simulations K1 and K2 on the other hand, the Arg38 occupies the same position and orientation as in simulation F1 without BHA. We have also analyzed the correlation function $C(t)$ for simulations with bound BHA, as was done in Figure 5.10. It is observed that the BHA substrate is not an important contributor to the time dependence of $C(t)$, though it does induce a static shift in $\langle \vec{E} \cdot \vec{u} \rangle$ that results in a red-shifted absorption peak.

The experimental and simulated absorption spectra and vibrational echo spectra for carbonmonoxy HRP with bound BHA are compared in panels (a) and (b) of Figure 5.11. In each panel, the solid green curve indicates the experimental result, while the dotted dark green curve corresponds to simulation J1 from Table 5.3, the dot-dashed blue curve corresponds to simulation J2, and the dashed dark yellow curve corresponds to simulation K2. The Stark coupling constant was fixed as determined previously for HRP without BHA with the 03 force field and CO charges $q_{CO} = \pm 0.17$, $\lambda = 0.75 \frac{cm^{-1}}{(MV/cm)}$. Note that none of the calculated spectra are qualitatively accurate. In addition to a frequency shift, all calculated absorption spectra in panel (a) are too broad. The calculated echoes are similarly not accurate. These results suggest that either we were unable to properly simulate HRP with bound BHA, or that the Amber 03 force field incorrectly models the primarily hydrogen-bonded interactions of the BHA substrate with the HRP active site.

One source of concern for the simulations with bound BHA is that the precise location and orientation of BHA in the HRP active site depends on both the starting structure as well as how the system was equilibrated. If the system becomes stuck in a metastable state, it might take many nano or even microseconds of simulation time to reach equilibrium. If the force field inadequately

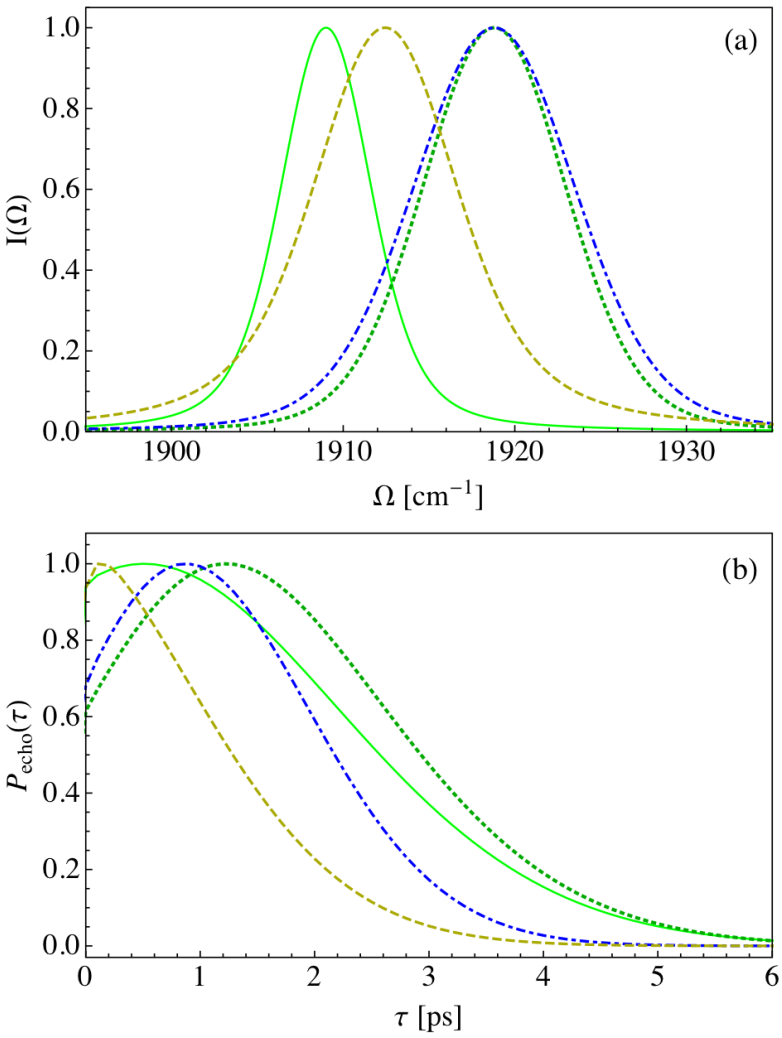

Figure 5.11: The experimental and simulated absorption spectra and vibrational echo spectra for carbonmonoxy HRP with bound BHA are compared in panels (a) and (b) respectively. The solid green curve indicates the experimental spectrum, while the dotted dark green curve corresponds to simulation J1 from Table 5.3, the dot-dashed blue curve corresponds to simulation J2, and the dashed dark yellow curve corresponds to simulation K2. The Stark coupling constant $\lambda = 0.75 \frac{cm^{-1}}{(MV/cm)}$ fit from simulations E and F1 in Table 5.2 was used in these BHA calculations.

models the true active site interactions, a molecular dynamics simulation may never sample the true experimentally relevant regions of phase space. A starting crystal structure with both BHA and CO bound to HRP would thus greatly enhance the reliability of the simulated active site dynamics. In addition, as the vibrational echo spectrum is determined primarily by protein motions around the bound CO, any simulation which generates incorrect short time dynamics will result in an unreliable echo spectrum. Since most force fields are not optimized based on dynamics, it is unclear which force fields (if any) are best for such simulations. Simulations on myoglobin with the MOIL dynamics package resulted in more accurate predictions for the absorption and vibrational echo spectra than did Amber calculations on HRP.

5.6 Computational details

Molecular dynamics simulations were performed with the Amber 10 simulation package using standard Amber force fields. [150] The Amber potential energy is given by the functional form

$$\begin{aligned} V(\mathbf{r}) = & \sum_{bonds} K_b(b - b_0)^2 + \sum_{angles} K_\theta(\theta - \theta_0)^2 \\ & + \sum_{dihedrals} (V_n/2)(1 + \cos(n\phi + \delta)) \\ & + \sum_{nonbonded} \frac{A_{ij}}{r_{ij}^{12}} - \frac{B_{ij}}{r_{ij}^{6}} + \frac{q_i q_j}{r_{ij}} \end{aligned} \tag{5.19}$$

where the specification of all parameters for various atom types defines the force field. Most calculations in this Chapter use the Amber 03 force field, though the 94 and 99SB force fields were also used where indicated. The 99SB force field uses different dihedral angle parameters than the 94 force field, while the

03 force field uses a different charge model from 99SB. We use the parameters of Giammona and Bayly [184] for the atoms of the heme unit. Partial charges for the CO ligand were either taken to be the gas phase values $q_C = 0.021$, $q_O = -0.021$ in units of the electron charge, or taken from Anselmi et.al. [164] to be $q_C = 0.17$, $q_O = -0.17$. Small molecule ligands such as BHA were simulated using the generalized Amber force field (GAFF). We primarily used the extended simple point charge model (SPC-E) for water molecules, though the transferable intermolecular potential 3 point water model (TIP3P) was also used when indicated. Both of these models treat water as a rigid molecule with three interaction sites. [160, 161]

Each simulation began with a crystal structure obtained from the Protein Data Bank (PDB) and then suitably modifed with the xleap package of Amber. Modifications included inserting CO into the heme pocket and changing the protonation state of certain amino acids such as the distal and proximal histidines. Either chloride or sodium ions were added to bring the system to electrical neutrality, and the protein was solvated with typically five Angstroms of water in a truncated octahedral box, around 6000 water molecules. The energy of the system was minimized, and then the system was heated from 0 to 300 Kelvin over 10 picoseconds at fixed volume and with harmonic constraints on protein backbone atoms. Periodic boundary conditions were used, and the particle-mesh Ewald procedure was used to calculate long-range electrostatic interactions. In most cases, the nonbonded cutoff was set to around 9 Å. Equilibration was performed at constant pressure and temperature for around 100 picoseconds, though in some cases the equilibration time was extended to several hundred picoseconds. Temperature was controlled with a Langevin thermostat, while pressure was fixed through weak-coupling isotropic position scal-

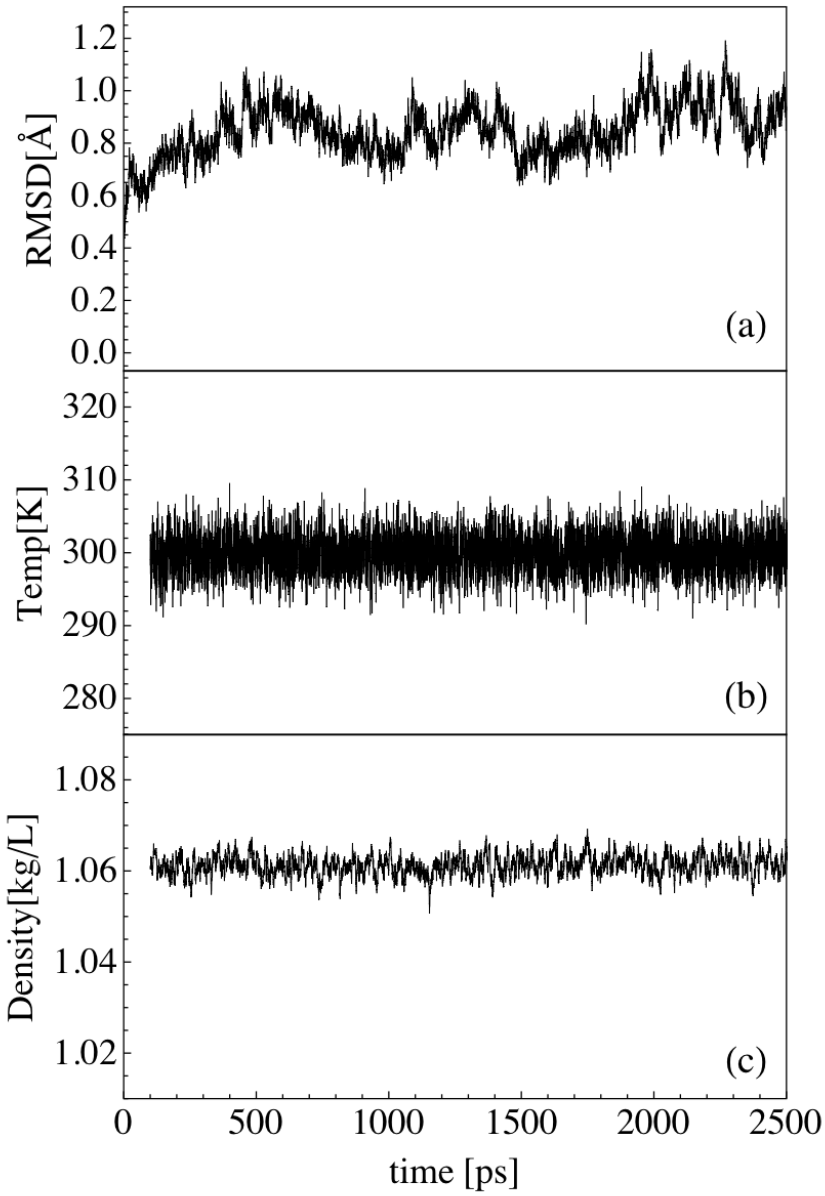

Figure 5.12: The root mean squared displacement of protein backbone atoms, the temperature, and the density are shown in panels (a), (b), and (c) respectively for an example trajectory from a simulation of wild-type myoglobin with the Amber 03 force field and SPC/E water.

ing. [150] During all simulations, the SHAKE algorithm was used to constrain all protein and solvent hydrogen vibrational motions, allowing the time step for the integration of trajectories to be set at one femtosecond. After equilibration, the system was simulated for several nanoseconds, and data was collected every 5 to 25 femtoseconds.

Before calculating the frequency fluctuations $\delta\omega(t)$, the simulation trajectory was checked to ensure the energy, temperature, and density were stable, and that the root mean squared displacement of the protein backbone atoms had equilibrated. This is shown for an example molecular dynamics trajectory in Figure 5.12, where the root mean squared displacement of the backbone is depicted in panel (a), the temperature is plotted in panel (b), and the density is shown in panel (c). For equilibrated trajectories, the positions and partial charges for each atom of the system were used to compute the component of the electric field along the CO bond. This electric field component was then used to compute the frequency fluctuations, as described in Section 2. The ensemble average $\langle \vec{u} \cdot \vec{E} \rangle$ in Eq. (5.14) was assumed to be equal to the time average of $\vec{u}(t) \cdot \vec{E}(t)$, as per the ergodic hypothesis.

5.7 Summary

The vibrational echo measurement provides information unobtainable from a typical linear absorption spectrum and allows for the discrimination between homogeneous and static contributions to the vibrational lineshape. Carbon monoxide bound in the active site of heme proteins is an effective probe of its local environment, and by analyzing its absorption and vibrational echo spec-

tra, we can gain insight into the time scales of protein dynamics nearby the CO. Using a mixed quantum / classical model that treats the chromophore CO as a three level quantum system and the protein motions as an off-resonance classical bath, we can theoretically compute echo spectra using the results of molecular dynamics simulations. Such simulations may give additional insight into the particular motions and amino acids that contribute to the echo spectrum. This procedure was previously performed for myoglobin using the MOIL force field, with accurate results. [147] In this chapter, we sought to extend these calculations to the protein horseradish peroxidase isoenzyme C with the Amber force fields. [148]

We have analyzed a wide variety of simulations of carbonmonoxy HRP both without and with the substrate BHA, created by varying the Amber force field, the partial charge on CO, the starting structure, and the protonation state of the distal histidine. For each simulation, we calculated the frequency fluctuation autocorrelation function, and from $C(t)$ generated the absorption and echo spectra. Though analysis of several distances between the CO and active site residues did qualitatively agree with previous calculations, [183] the predicted echo spectra for the red, blue, and bound BHA spectroscopic states were not in good agreement with experiment. The experimental red state absorption peak is broader than the blue peak due to less constrained active site dynamics. However, we observed no difference in dynamics upon changing the protonation state of His42. The simulated spectra with bound BHA were also significantly broader than the experimental spectrum, and the simulated vibrational echo spectra decayed too rapidly. This poor agreement may reflect underlying inaccuracies in the dynamics generated by the Amber force fields, or it may be a result of not sampling the experimentally relevant regions of phase space due

to an initial structure that was not at equilibrium. In either case, our analysis suggests that while molecular dynamics simulations may be potentially valuable in the interpretation of linear and nonlinear vibrational spectra, great care must be taken due to many potential sources of error and uncertainty.

APPENDIX A

QUANTUM AND CLASSICAL ANHARMONIC OSCILLATORS

A.1 Review of quantum oscillator systems

In this appendix we will review the quantum and classical harmonic and Morse oscillator systems. These results will be used in the calculation of linear and nonlinear response functions in other chapters. In addition, we review classical action-angle variables, as well as the action-angle perturbation theory which will allow us to develop approximate dynamics for coupled anharmonic systems. In many molecular systems, the low-energy vibrational motions of nuclei can be well approximated as harmonic oscillators. In systems with multiple vibrational modes, the harmonic stretching motions of each bond are coupled, but the normal modes of vibration are still harmonic to a first approximation. Therefore we first review the quantum harmonic oscillator, the Hamiltonian for which is

$$\hat{H} = -\frac{\hbar^2}{2m}\frac{d^2}{dx^2} + \frac{m\omega^2}{2}x^2 \tag{A.1}$$

where m is the mass and ω the frequency. The energy eigenstates are given by $|n\rangle$, with

$$\hat{H}|n\rangle = E_n|n\rangle \tag{A.2}$$

$$E_n = (n + 1/2)\hbar\omega\,. \tag{A.3}$$

The set of states $|n\rangle$ form a complete and convenient basis for calculations of the eigenstates for anharmonic oscillator systems. The energy eigenstate matrix

elements of $\hat{x}$ are given by

$$\langle m|\hat{x}|n\rangle = \sqrt{\frac{\hbar}{2m\omega}}\left(\sqrt{n+1}\,\delta_{m,n+1} + \sqrt{n}\,\delta_{m,n-1}\right). \tag{A.4}$$

The coordinate operator $\hat{x}$ thus only couples adjacent states with quantum numbers that differ by one.

At high energies and for large amplitude stretches, molecular vibrations can no longer be accurately described as harmonic oscillators. If a bond is stretched far enough, it will break, and so the true potential energy surface should have a finite dissociation energy. One model Hamiltonian that is often used to more accurately describe vibrations is the Morse potential given by

$$\hat{H} = -\frac{\hbar^2}{2m}\frac{d^2}{dx^2} + D\left(1 - e^{-\alpha x}\right)^2 \tag{A.5}$$

where $\alpha = \sqrt{m\omega^2/2D}$, and D is the dissociation energy, m is the mass, and ω is the frequency at the bottom of the potential well. The bound energy eigenstates $|\varphi_n\rangle$ of the Morse Hamiltonian can be found exactly in terms of the Laguerre polynomials, along with the energy eigenvalues

$$\hat{H}|\varphi_n\rangle = \epsilon_n|\varphi_n\rangle \tag{A.6}$$

$$\epsilon_n = (n+1/2)\hbar\omega - (n+1/2)^2\frac{\hbar^2\omega^2}{4D}\,. \tag{A.7}$$

Unlike the harmonic oscillator, there are only a finite number of bound states in the Morse system. The maximum bound quantum number is given by

$$(n_{max} + 1/2) \approx 2D/\hbar\omega\,. \tag{A.8}$$

As with the harmonic system, there are analytic formulae for the matrix elements of the Morse oscillator, as discussed in detail by Shirts. [130]

For anharmonic potentials, an alternate way to generate accurate eigenstates and energies is to use the harmonic oscillator states as a basis and then perform

a variational calculation. The approximate eigenstates can then be used to calculate any necessary matrix elements. The harmonic reference potential is defined to fit the anharmonic potential near the bottom of the well, and the number of basis states is increased until numerical convergence is achieved. This method is used for most quantum calculations in this dissertation. For several coupled degrees of freedom, this variational method is practical and generates reliable results. For many degrees of freedom such as for an anharmonic solute mode interacting with a bath of off-resonance modes, other methods must be used to approximately solve the Schrödinger equation.

A.2 Review of classical oscillator systems

In the Hamiltonian formulation of classical mechanics, we wish to solve Hamilton's equations for the coordinates $\mathbf{q}$ and momenta $\mathbf{p}$,

$$\dot{\mathbf{p}} = -\frac{\partial H}{\partial \mathbf{q}} \ , \quad \dot{\mathbf{q}} = \frac{\partial H}{\partial \mathbf{p}} \tag{A.9}$$

where the dot above either $\mathbf{q}$ or $\mathbf{p}$ indicates the total derivative with respect to time. By a canonical transformation with generating function S, the classical Hamiltonian can be transformed into [121]

$$H\left(\mathbf{q}, \frac{\partial S}{\partial \mathbf{q}}; t\right) + \frac{\partial S}{\partial t} = 0. \tag{A.10}$$

Eq. (A.10) is known as the Hamilton-Jacobi equation, and it is a central equation of classical mechanics. The generating function (action) S is Hamilton's principal function, and is equal to

$$S = \int L \, dt \tag{A.11}$$

where L is the classical Lagrangian. For time-independent Hamiltonians, the energy E is conserved and the action S can be written as

$$S = W(\mathbf{q}) - Et \tag{A.12}$$

where W is called Hamilton's characteristic function. W serves as the generating function for a useful set of variables known as the angle ϕ and its generalized momentum (also called the action) J. The actions $\mathbf{J}$ are constants of motion and play a central role in many semiclassical quantization schemes. [53, 54]

For periodic and quasiperiodic systems with separable generalized coordinates and momenta q_k and p_k, the kth action variable is given by

$$J_k = \oint p_k dq_k = \int_0^{T_k} p_k \frac{dq_k}{dt} dt \tag{A.13}$$

$$\frac{\partial}{\partial t} J_k = 0 \tag{A.14}$$

where the integral in Eq. (A.13) is performed over all possible q_k for fixed energy E, and T_k is the kth period of motion. The Hamiltonian is a function of only the actions $\mathbf{J}$, and the time-dependence of the angle variables gives the frequency associated with the periodic motion of q_k,

$$\frac{\partial}{\partial t}\phi_k = \frac{\partial H(\mathbf{J})}{\partial J_k} = \lambda_k(\mathbf{J})\omega_k. \tag{A.15}$$

For systems with f degrees of freedom and f action variables, trajectory motion in the $2f$ dimensional phase space takes place on an f-dimensional surface of constant action called an invariant torus. Such systems are called integrable. For systems of coupled anharmonic modes at high enough energy, there may not exist f constants of motion, and thus there will not be f action variables. In this non-integrable case, there will exist regions of phase space that exhibit chaotic motion, and in these regions we cannot write trajectory dynamics in terms of action-angle variables.

The classical trajectories for the harmonic oscillator with mass m and frequency ω can be solved for explicitly in action-angle coordinates,

$$q(t) = q(0)\cos(\omega t) + \frac{p(0)}{m\omega}\sin(\omega t) = \sqrt{\frac{2J}{m\omega}}\cos(\phi + \omega t) \tag{A.16}$$

$$p(t) = p(0)\cos(\omega t) - m\omega q(0)\sin(\omega t) = -\sqrt{2m\omega J}\sin(\phi + \omega t) \tag{A.17}$$

where J is the action and ϕ is the initial angle. For harmonic systems, the relation between the action and the energy E is $J = E/\omega$, while the time-dependence of the angle is given by $\phi(t) = \phi + \omega t$. Associated with the trajectories $q(t)$ and $p(t)$ is the monodromy (stability) matrix $\mathbf{M}$,

$$\mathbf{M}(t) = \begin{pmatrix} M_{qq}(t) & M_{qp}(t) \\ M_{pq}(t) & M_{pp}(t) \end{pmatrix} \tag{A.18}$$

where, for example

$$M_{qp}(t) \equiv \left(\frac{\partial q(t)}{\partial p}\right)_q \quad , \quad M_{qq}(t) \equiv \left(\frac{\partial q(t)}{\partial q}\right)_p . \tag{A.19}$$

The monodromy matrix is symplectic with a determinant equal to unity. The harmonic monodromy matrix elements are given by

$$\begin{aligned} M_{qq}(t) &= \cos\omega t \quad , \quad M_{pp}(t) = \cos\omega t \\ M_{pq}(t) &= -m\omega\sin\omega t \ , \quad M_{qp}(t) = \frac{1}{m\omega}\sin\omega t \end{aligned} \tag{A.20}$$

and $M_{qq}M_{pp} - M_{qp}M_{pq} = 1$ as expected.

The classical Morse oscillator system is also explicitly solvable in action-angle variables,

$$q(t) = \sqrt{\frac{2D}{m\omega^2}}\ \ln\left(\frac{1 + b\cos\phi(t)}{\lambda^2}\right) \tag{A.21}$$

$$p(t) = -\sqrt{2Dm}\ \ \left(\frac{\lambda b\sin\phi(t)}{1 + b\cos\phi(t)}\right) \tag{A.22}$$

$$b \equiv \sqrt{E/D} \tag{A.23}$$

$$\lambda \equiv \sqrt{1 - E/D} \tag{A.24}$$

where the energy and action are related by

$$E = \omega J - \frac{\omega^2 J^2}{4D} \tag{A.25}$$

and the time-dependence of the angle is

$$\phi(t) = \phi + \lambda(J)\omega t = \phi + \left(1 - \frac{\omega J}{2D}\right)\omega t. \tag{A.26}$$

The Morse oscillator phase space dynamics in Eqs. (A.21) and (A.22) reduce to the harmonic dynamics in Eq. (A.16) and (A.16) in the limit of infinite dissociation energy, $D \to \infty$. The monodromy matrix elements are in general complicated functions of the action and angle for anharmonic systems, but as with the harmonic oscillator,

$$M_{qq}(0) = M_{pp}(0) = 1 \ , \quad M_{qp}(0) = M_{pq}(0) = 0 \tag{A.27}$$

and $\det \mathbf{M}(t) = 1$. It can also be shown that for regular (non-chaotic) anharmonic systems such as the Morse oscillator, the magnitude of the monodromy matrix elements grows linearly with time. For chaotic systems, the monodromy matrix grows exponentially with time. [37–39]

A.3 Classical action-angle perturbation theory

Here we review classical action-angle perturbation theory for one-dimensional anharmonic oscillators. [121,126] This perturbation theory will be used to calculate approximate dynamics for $q(t)$ and $p(t)$ and is easily generalizable to multiple coupled degrees of freedom. For systems with the Hamiltonian

$$\begin{aligned} H =& \frac{1}{2m}p^2 + \frac{m\omega^2}{2}q^2 + \varepsilon\gamma_3 q^3 + \varepsilon^2\gamma_4 q^4 + \cdots \\ =& \frac{1}{2m}p^2 + \frac{m\omega^2}{2}q^2 + V_{anh}(q) \end{aligned} \tag{A.28}$$

approximate dynamics for q and p can be computed in powers of the dimensionless anharmonicity ε. Zeroth-order harmonic action and angle variables, I and θ, are related to coordinates and momenta by

$$q = \sqrt{\frac{2I}{m\omega}} \cos\theta \tag{A.29}$$

$$p = -\sqrt{2Im\omega} \sin\theta. \tag{A.30}$$

The good action and angle variables are denoted J and ϕ. The harmonic action I and angle θ can be written in terms of good actions and harmonic angles, [126]

$$I = J + \sum_n{}' A_n \, n \, e^{in\cdot\theta} \tag{A.31}$$

$$\theta = \phi + i \sum_n{}' \frac{\partial A_n}{\partial J} \, e^{in\cdot\theta} \tag{A.32}$$

where A_n is related to the Fourier expansion of the anharmonic potential

$$A_n = -\frac{1}{\omega \cdot n} \int \frac{d\theta}{2\pi} \, e^{-in\cdot\theta} \, V_{anh}(J, \theta) \tag{A.33}$$

where n is an integer, and the prime in the summation indicates $n \neq 0$. A_n is next expanded in powers of the anharmonicity ε and inserted into Eqs. (A.29)–(A.32) to give a perturbation expansion for q and p. The time dependence of the angle variable is given by

$$\phi(t) = \phi + \lambda(J)\omega t \tag{A.34}$$

$$\lambda(J)\omega = \frac{\partial H}{\partial J} \tag{A.35}$$

where the first corrections to λ enter at second order in ε.

For a one-dimensional Morse oscillator, the Hamiltonian can be expanded in powers of the anharmonicity $\sqrt{1/D}$ as

$$V_{anh}(q) = -\varepsilon \frac{m^{3/2}\omega^3}{\sqrt{8D}} q^3 + \varepsilon^2 \frac{7m^2\omega^4}{48D} q^4 + \cdots . \tag{A.36}$$

To first order in the dimensionless anharmonicity ε, the Morse oscillator coordinate and momentum are given by

$$\begin{aligned} q(t) &= \sqrt{\frac{2J}{m\omega}}\cos\phi(t) - \varepsilon\frac{J}{\sqrt{8mD}}\Big(\cos(2\phi(t)) - 3\Big) \\ p(t) &= -\sqrt{2m\omega J}\sin\phi(t) + \varepsilon\frac{\sqrt{2m}\omega J}{\sqrt{D}}\cos\phi(t)\sin\phi(t) \end{aligned} \tag{A.37}$$

where $\phi(t)$ is taken to be the exact angle for a Morse oscillator given by Eq. (A.24). Because of this, Eq. (A.37) is not truly a perturbative result. These approximate dynamics will be used to analyze the Herman-Kluk semiclassical approximation to response functions and wavepacket propagation.

APPENDIX B

THE HK APPROXIMATION TO THE RESPONSE FUNCTION

B.1 Derivation of the HK response function

In this appendix, the Herman-Kluk expression for the nonlinear vibrational response function, Eq. (2.7), is derived from the quantum nonlinear response function in Eq. (2.1) and the general form for the Herman-Kluk semiclassical propagator, Eq. (2.2). This derivation follows that of Noid, Ezra, and Loring, 2003, [27] and further details can be found there. As discussed in Chapter 1, the nth-order vibrational response function $R^{(n)}(t_n, \cdots, t_1)$ describes coherent n-photon processes on a single electronic surface and is defined as

$$\begin{aligned} R^{(n)}(t_n, \ldots, t_1) &= \left(\frac{i}{\hbar}\right)^n \mathrm{Tr}\left\{\hat{x}\hat{K}(t_n)\Big[\hat{x}, \hat{K}(t_{n-1})\Big[\hat{x}, \cdots \right. \\ &\times \left. \Big[\hat{x}, \hat{K}(t_1)\Big[\hat{x}, \hat{\rho}\Big]\hat{K}^\dagger(t_1)\Big] \cdots \Big]\hat{K}^\dagger(t_{n-1})\Big]\hat{K}^\dagger(t_n)\right\} \end{aligned} \tag{B.1}$$

where $\hat{K}(t)$ is the quantum propagator and $\hat{\rho}$ is the statistical density matrix. We have assumed that the system is coupled to the field through an electric dipole interaction proportional to the coordinate $\hat{x}$.

The Herman-Kluk propagator for f degrees of freedom has the form

$$\hat{K}_{HK}(t) = (2\pi\hbar)^{-f} \int d\mathbf{z}\, |\mathbf{z}(t)\rangle\, C(\mathbf{z}, t) e^{iS(\mathbf{z},t)/\hbar} \langle \mathbf{z}| \tag{B.2}$$

where $C(\mathbf{z}, t)$, $S(\mathbf{z}, t)$, and the coherent states $\langle \mathbf{x}|\mathbf{z}\rangle$ are defined in Eqs. (2.3), (2.4), and (2.5). In order to evaluate the coherent state matrix element of a commutator of $\hat{x}$ and $\hat{A}$, we make use of the identity

$$\langle \mathbf{z}_1|[\hat{x}, \hat{A}]|\mathbf{z}_2\rangle = i\hbar\langle \mathbf{z}_1|\mathbf{z}_2\rangle \frac{\partial}{\partial \bar{p}_{12}} \left(\frac{\langle \mathbf{z}_1|\hat{A}|\mathbf{z}_2\rangle}{\langle \mathbf{z}_1|\mathbf{z}_2\rangle}\right) \tag{B.3}$$

where $\bar{p}_{12}$ is the mean momentum of trajectories $\mathbf{z}_1$ and $\mathbf{z}_2$ in the active degree of freedom. Inserting the Herman-Kluk propagator into Eq. (B.1) and evaluating the commutators with Eq. (B.3) yields

$$\begin{aligned} R^{(n)}(t_n,\cdots,t_1) &= (-1)^n \int \frac{d\mathbf{z}_1}{(2\pi\hbar)^f} \int \frac{d\mathbf{z}_2}{(2\pi\hbar)^f} \cdots \int \frac{d\mathbf{z}_{2n}}{(2\pi\hbar)^f}\, C(\mathbf{z}_1,t_1)\cdots C^*(\mathbf{z}_{2n},t_n) \\ &\times\ e^{iS(\mathbf{z}_1,t_1)}\, e^{-iS(\mathbf{z}_2,t_1)} \cdots e^{iS(\mathbf{z}_{2n-1},t_n)} e^{-iS(\mathbf{z}_{2n},t_n)}\ Q^*_{2n-1,2n}(t_n) \\ &\times\ \langle \mathbf{z}_{2n}(t_n)|\mathbf{z}_{2n-1}(t_n)\rangle \langle \mathbf{z}_{2n-1}|\mathbf{z}_{2n}\rangle \cdots \langle \mathbf{z}_3|\mathbf{z}_4\rangle \langle \mathbf{z}_1|\mathbf{z}_2\rangle \\ &\times\ \left[\frac{\partial}{\partial \bar{p}_{2n-1,2n}} \left(\frac{\langle \mathbf{z}_{2n-2}(t_{n-1})|\mathbf{z}_{2n}\rangle \langle \mathbf{z}_{2n-1}|\mathbf{z}_{2n-3}(t_{n-1})\rangle}{\langle \mathbf{z}_{2n-1}|\mathbf{z}_{2n}\rangle} \right)\right] \cdots \\ &\times\ \left[\frac{\partial}{\partial \bar{p}_{34}} \left(\frac{\langle \mathbf{z}_2(t_1)|\mathbf{z}_4\rangle \langle \mathbf{z}_3|\mathbf{z}_1(t_1)\rangle}{\langle \mathbf{z}_3|\mathbf{z}_4\rangle} \right)\right] \cdot \left[\frac{\partial}{\partial \bar{p}_{12}} \left(\frac{\langle \mathbf{z}_1|\,\hat{\rho}\,|\mathbf{z}_2\rangle}{\langle \mathbf{z}_1|\mathbf{z}_2\rangle} \right)\right] \end{aligned} \tag{B.4}$$

where Q_{jk} is defined as the coherent state matrix element of $\hat{x}$,

$$Q_{jk} \equiv \frac{\langle \mathbf{z}_j|\,\hat{x}\,|\mathbf{z}_k\rangle}{\langle \mathbf{z}_j|\mathbf{z}_k\rangle} = \bar{q}_{jk} - i\frac{\Delta p_{jk}}{2\gamma\hbar}\ . \tag{B.5}$$

The momentum derivatives in Eq. (B.4) are given by

$$\frac{\partial}{\partial \bar{p}_{jk}} \left(\frac{\langle \mathbf{z}_a|\mathbf{z}_j\rangle \langle \mathbf{z}_k|\mathbf{z}_b\rangle}{\langle \mathbf{z}_j|\mathbf{z}_k\rangle} \right) = \frac{1}{i\hbar} \left(Q_{kb} - Q^*_{ja} \right) \frac{\langle \mathbf{z}_a|\mathbf{z}_j\rangle \langle \mathbf{z}_k|\mathbf{z}_b\rangle}{\langle \mathbf{z}_j|\mathbf{z}_k\rangle}\ . \tag{B.6}$$

The difference between complex coordinates Q_{jk} can be rearranged in terms of the coherent state matrix elements of the momentum operator, P_{jk},

$$Q_{kb} - Q^*_{ja} = -\frac{i}{m\omega}(P_{ab} - P^*_{jk})\,. \tag{B.7}$$

Using Eqs. (B.6) and (B.7), the terms in Eq. (B.4) can be simplified to yield the result for the Herman-Kluk nth-order response function given in Eq. (2.7).

B.2 Linearization of the HK response function

In the classical limit, the only pairs of trajectories which contribute to a response function are those that start very close together in phase space. In this case, the

time dependent difference variables $\Delta\mathbf{q}_{jk}(t)$ and $\Delta\mathbf{p}_{jk}(t)$ can be linearized as

$$\begin{aligned}\Delta\mathbf{q}_{jk}(t) &= \mathbf{M}_{\mathbf{qq}}(\bar{\mathbf{z}}_{jk},t)\cdot\Delta\mathbf{q}_{jk} + \mathbf{M}_{\mathbf{qp}}(\bar{\mathbf{z}}_{jk},t)\cdot\Delta\mathbf{p}_{jk}\\ \Delta\mathbf{p}_{jk}(t) &= \mathbf{M}_{\mathbf{pq}}(\bar{\mathbf{z}}_{jk},t)\cdot\Delta\mathbf{q}_{jk} + \mathbf{M}_{\mathbf{pp}}(\bar{\mathbf{z}}_{jk},t)\cdot\Delta\mathbf{p}_{jk}\end{aligned} \tag{B.8}$$

where $\mathbf{M}_{\mathbf{qq}}(\bar{\mathbf{z}}_{jk},t)$ is a monodromy matrix element for the mean trajectory $\bar{\mathbf{z}}_{jk}$. This linearization approximation is exact for harmonic systems, but fails qualitatively at long times for anharmonic systems. Within the linearization approximation, the action difference $\Delta S(t)$ is given explicitly by

$$\begin{aligned}S(\mathbf{z}_j,t) - S(\mathbf{z}_k,t) = &\left(\bar{\mathbf{p}}_{jk}(t)\,\mathbf{M}_{\mathbf{qq}}(\bar{\mathbf{z}}_{jk},t) - \bar{\mathbf{p}}_{jk}\right)\cdot\Delta\mathbf{q}_{jk}\\ &+ \bar{\mathbf{p}}_{jk}(t)\,\mathbf{M}_{\mathbf{qp}}(\bar{\mathbf{z}}_{jk},t)\cdot\Delta\mathbf{p}_{jk}\,.\end{aligned} \tag{B.9}$$

This linearized action difference cancels the phase of the coherent state overlaps, resulting in a total semiclassical phase of zero,

$$\psi_{jk} = \left[S(\mathbf{z}_j,t) - S(\mathbf{z}_k,t) + \bar{\mathbf{p}}_{jk}(t)\cdot\Delta\mathbf{q}_{jk}(t) - \bar{\mathbf{p}}_{jk}\cdot\Delta\mathbf{q}_{jk}\right]_{lin} = 0\,. \tag{B.10}$$

As discussed in Chapter 2, it is the structure of the phase for an anharmonic system that quantizes the mean action variables in the linear response calculation. Thus, the linearized approximation to the phase results in the loss of all quantum coherence information.

As is shown in detail by Noid et.al., [27] the integral of $A_{12}(t)$ from Eq. (2.8) over difference variables within the linearization approximation can be evaluated analytically. Rather than result in a quantization condition on the mean action, this integral over difference variables is simply unity,

$$\int\frac{d\Delta\mathbf{z}_{12}}{(2\pi\hbar)^f}\left[C(\mathbf{z}_1,t)C^*(\mathbf{z}_2,t)\,e^{i\Delta S(t)/\hbar}\,\langle\mathbf{z}_2(t)|\mathbf{z}_1(t)\rangle\langle\mathbf{z}_1|\mathbf{z}_2\rangle\right]_{lin} = 1\,. \tag{B.11}$$

Therefore the classical limit to the linear response function results from the linearization of difference variables. In order to derive the classical limit for nonlinear response functions, an addition approximation is necessary. The ratio of

coherent state overlaps, $O_{jklm}(t)$, becomes sharply peaked about $\bar{\mathbf{z}}_{lm} \approx \bar{\mathbf{z}}_{jk}(t)$ for small $\hbar$. Thus we approximate this ratio as

$$O_{jklm}(t) \equiv \frac{\langle \mathbf{z}_k(t)|\mathbf{z}_m\rangle\langle \mathbf{z}_l|\mathbf{z}_j(t)\rangle}{\langle \mathbf{z}_k(t)|\mathbf{z}_j(t)\rangle\langle \mathbf{z}_l|\mathbf{z}_m\rangle} \longrightarrow (2\pi\hbar)^f \, \delta(\bar{\mathbf{z}}_{lm} - \bar{\mathbf{z}}_{jk}(t)) \, . \tag{B.12}$$

Within the linearization approximation and Eq. (B.12), the quantum nonlinear response function $R^{(n)}(t_n, \cdots, t_1)$ reduces to the correct classical limit, Eq. (1.36).

APPENDIX C

SEMICLASSICAL QUANTIZATION

The semiclassical WKB (Wentzel, Kramers, and Brillouin) method has its roots in the old quantum theory, which holds that a quantum system obeys classical mechanics, except that only classical trajectories which satisfy a certain condition on the classical action are allowed. [53] The WKB method approximately solves for the wavefunction of a one-dimensional system in the limit of small $\hbar$, and is thus expected to become correct in the large quantum number, small wavelength, or semiclassical limit. The requirement that the wavefunctions be normalizable results in the condition

$$\frac{1}{2\pi}\int p\,dq = n\hbar \tag{C.1}$$

where the integral in Eq. (C.1) goes over one period of motion, and n is an integer. This condition is valid for one-dimensional or separable systems and is referred to as the Bohr-Sommerfeld quantization condition. Eq. (C.1) can also be written in terms of the classical action variable J,

$$\frac{1}{2\pi}\int p\,dq = \frac{1}{2\pi}\int_0^T p(\tau)\,\dot{q}(\tau)\,d\tau = J \tag{C.2}$$

and thus the Bohr-Sommerfeld condition is a quantization condition on the classical action.

A generalization of the Bohr-Sommerfeld condition to non-separable systems is given by the EBK (Einstein, Brillouin, and Keller) quantization theory,

$$J_k = \frac{1}{2\pi}\oint_{C_k}\mathbf{p}\cdot d\mathbf{q} = \frac{1}{2\pi}\oint_{C_k}\sum_i p_i dq_i = (n_k + \alpha_k/4)\hbar \tag{C.3}$$

where the C_k are k independent closed loops of the invariant torus in k dimensions, J_k is the kth good action variable, and α_k is an integer (the Maslov index) which depends on the topology of contour C_k. [54,56] For example, for the

bound states of a one-dimensional oscillator, a classical trajectory encounters two turning points, and $\alpha = 2$. The C_k closed loops do not need to be classical trajectories but may instead be chosen for convenience. As first noted by Einstein, Eq. (C.3) only applies to regions of phase space with periodic or quasiperiodic classical motions. For an f-dimensional system, invariant tori and thus f good action variables exist in such regions, and EBK quantization makes sense. In regions with ergodic (chaotic) motion, EBK quantization is not generally applicable.

This distinction between quasiperiodic and chaotic motion is depicted graphically as a surface of section plot in Figure C.1 for a Henon-Heiles system at both low and high energies with the potential energy given in Eq. (4.70). A surface of section is a two-dimensional cut through the full four-dimensional phase space for this coupled oscillator system, where we plot y vs. p_y such that x is zero and p_x is non-negative. Each plot shows a selection of trajectories at a fixed energy, and quasiperiodic trajectories appear as a smooth curve. Chaotic trajectories on the other hand appear as a scattering of points. Truly periodic trajectories are similar to quasiperiodic orbits, but they do not trace out a full curve, but instead only appear on the surface of section as a series of isolated points. Surface of section plots provide an easy way to determine the behavior of phase space for a system as a function of the energy.

Semiclassical quantization in the chaotic or non-integrable regime can be done through the periodic orbit theory of Gutzwiller. [57, 58, 185] Even for chaotic regions of phase space, there typically exist isolated and rare periodic orbits, and each of these orbits contributes a sinusoidal oscillation to the total density of states. The Gutzwiller trace formula for the density of states is then

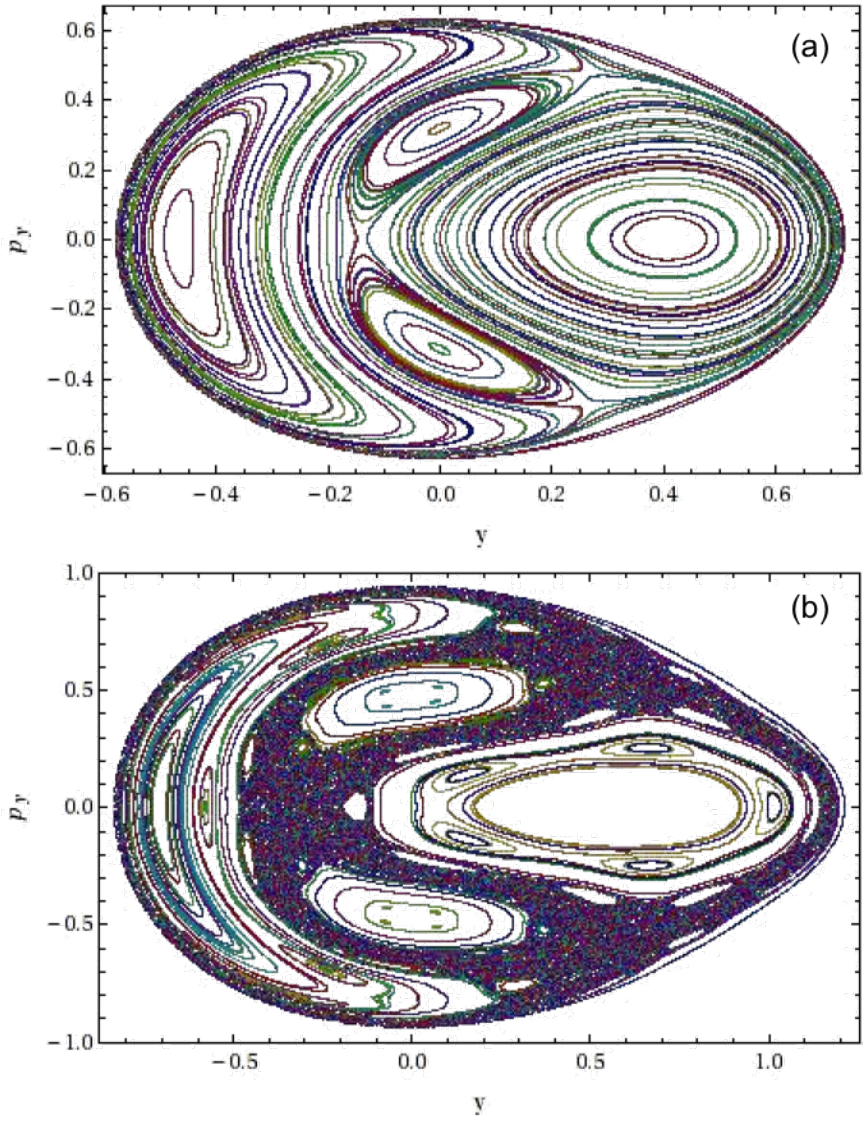

Figure C.1: Surface of section plots of y vs. p_y for $x = 0$ and $p_x \geq 0$ are shown for a Henon-Heiles system with the same parameters as in Figure 4.5. Panel (a) consists of a collection of trajectories at a low energy, while in panel (b), the trajectory energy is increased past the chaotic threshold. Regions consisting of smooth curves indicate quasiperiodic motion, while a scatter pattern indicates an ergodic region of phase space.

given by

$$n(E) = \bar{n}(E) + \frac{1}{\pi\hbar} \sum_r T_r A_r \cos\left(S_r/\hbar - \alpha_r \pi/2\right) \tag{C.4}$$

where $\bar{n}(E)$ is the Thomas-Fermi density of states, [138] and the sum over r indicates a sum over all periodic orbits. S_r is the classical action $\oint p\, dq$ along periodic orbit r, α_r is an integer, T_r is the period of the orbit, and A_r is a function of the monodromy matrix elements. Summing over all orbits of a single periodic trajectory results in a peak in the density of states. Eq. (C.4) assumes that all such periodic trajectories are isolated, and it is thus not applicable to multiply periodic systems. [138] More recent work by Takatsuka, et.al. [186, 187] has also investigated semiclassical quantization in the chaotic regime and has demonstrated that constructive and destructive interference in a semiclassical phase is sufficient to quantize the density of states.

In order to use the EBK method to calculate the semiclassical energy eigenvalue spectrum, it is first necessary to find the good action variables for a system. In the one-dimensional case, this is typically easy, and we have made use of action variables for various one-dimensional anharmonic oscillator systems in this dissertation. For weakly coupled systems with f degrees of freedom, classical perturbation theory can be used to find approximate good actions. [126] However, for more strongly coupled systems, or for systems near a resonance where the frequency of two unperturbed oscillator modes is comparable, finding the good action variables can be a challenge. [188, 189] Marcus et.al. [125, 190–192] have calculated actions through integration in the surface of section, while Percival calculates invariant tori through a variational principal. [193, 194] As discussed in Chapter 4, the Fourier transform of semiclassically propagated wavepackets can also generate quantized actions. [76] Finally, Martens and Ezra [127, 128, 195] and Sorbie and Handy [132, 133, 196] among

others have used Fourier analysis methods for quasiperiodic trajectories to find action and angle variables in these general cases. These methods are numerically practical and can be applied to strongly resonant systems.

APPENDIX D

DOUBLE-SIDED FEYNMAN DIAGRAMS

As discussed in Chapters 1 and 3, coherent nonlinear vibrational signals are generally emitted at distinct wavevectors $\mathbf{k}_s$ that correspond to linear combinations of the wavevectors of the incoming radiation field. For a general four-wave mixing experiment as depicted in Figure 1.1,

$$\mathbf{k}_s = y_1\mathbf{k}_1 + y_2\mathbf{k}_2 + y_3\mathbf{k}_3 \tag{D.1}$$

where $y_i = \pm 1$, and $\mathbf{k}_1$, $\mathbf{k}_2$, and $\mathbf{k}_3$ label the wavevectors for the fields that interact with the sample. When the incoming laser pulses are sufficiently broad compared to the fundamental carrier frequency Ω, and when this frequency is near resonance with the chromophore oscillator frequency, $\omega \approx \Omega$, we can invoke the rotating wave approximation. [2, 15] Within this approximation, the nonlinear signal with wavevector $\mathbf{k}_s$ will be generated by one spatially phase-matched component to the response function as in Eq. (3.30).

The quantum response along a given wavevector is conveniently represented as a sum of double-sided Feynman diagrams. [2, 13] These diagrams consist of a pair of vertical lines which represent the time evolution of the ket (left) and bra (right) sides of the density matrix. Time is displayed vertically, and along the vertical lines the system evolves according to the material Hamiltonian in the absence of radiation. Over a time t, each element of the density matrix ρ_{nm} will evolve with a phase proportional to the energy difference between eigenstates n and m,

$$\rho_{nm}(t) = e^{i(E_n - E_m)t/\hbar}\,\rho_{nm} = e^{i\omega_{nm}t}\,\rho_{nm}\,. \tag{D.2}$$

Interactions with the radiation field are indicated by arrows pointing either into or out of the left or right (ket or bra) lines. For the third-order response function, the first three arrows indicate interactions with the applied field, while the final arrow corresponds to the emission of the signal. Each of the first three arrows carries a weight $\pm(i/\hbar)\mu E$ where μ is the dipole and E is the electric field, with the plus or minus sign depending on if they interact on the left or right sides respectively. The final arrow carries only a weight μE. Arrows that point into the diagram represent absorption of energy, while arrows that point away indicate emission. Within the rotating wave approximation, arrows pointing to the right carry a phase factor $\exp(i\mathbf{k}\cdot\mathbf{r})$, while arrows pointing to the left have a phase factor $\exp(-i\mathbf{k}\cdot\mathbf{r})$

In Figure D.1, a sample double-sided Feynman diagram is shown. In this example, the first interaction with the field results in an absorption on the ket side of the density matrix, while the second interaction indicates an absorption on the bra side. The third interaction induces an emission from the bra side, while finally the emitted signal corresponds to an emission from the ket. During times t_1 and t_3, this diagram is in a one-quantum coherence, while during time t_2 it is in a population. As the coherences during times t_1 and t_3 enter with the same sign, this diagram is of the nonrephasing type, and the signal is emitted along a wavevector $\mathbf{k}_s = \mathbf{k}_1 - \mathbf{k}_2 + \mathbf{k}_3$. Finally, note that the diagram both starts and ends in a population, in this case the ground state.

As discussed in Chapter 3, each double-sided Feynman diagram is an intrinsically quantum mechanical object without a well-defined classical limit. Rather, collections of diagrams corresponding to the total signal propagating in a particular wavevector combine to have a finite classical limit. [33] In Figure D.2, a

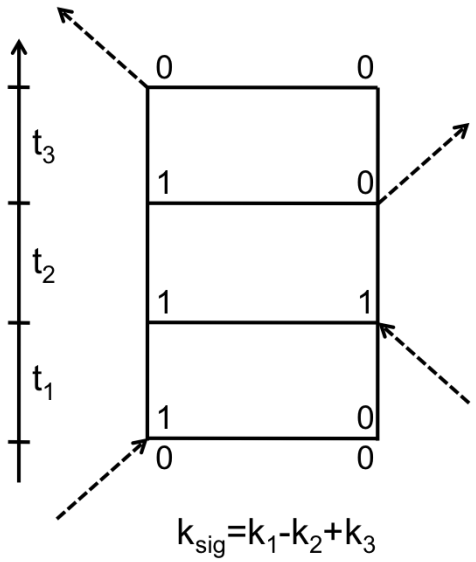

Figure D.1: An example double-sided Feynman diagram which contributes to the third-order response function is displayed. The two sides of the diagram represent the time evolution of the ket and bra sides of the density matrix, and arrows pointing into and out of the diagram represent interactions with the field. The time delay between field interactions is shown on the vertical axis.

collection of diagrams is shown, the columns of which represent different phase-matched components, while each row corresponds to a different mean trajectory path. For example, the third column contains only rephasing diagrams that contribute to $R^{++-}(t_3, t_2, t_1)$, and the fourth row contributes to the "down-down" path in Figure 3.1. The total third-order response function consists of a sum over all starting states for these twelve diagrams as well as their complex conjugates. In addition, there are also diagrams where the first interaction with the field results in emission rather than absorption of energy. Note that at zero temperature, some of these twelve diagrams do not contribute to the response, as they would seem to contain an emission from the ground state. The fourth row, as well as the first (nonrephasing) diagram in the third row, should not contribute when the system starts in the ground state. It is in fact this nonrephasing di-

agram in the third row (the "down-up" path) which incorrectly contributes to the mean trajectory approximation to the third-order response function, as seen in Figure 3.8.

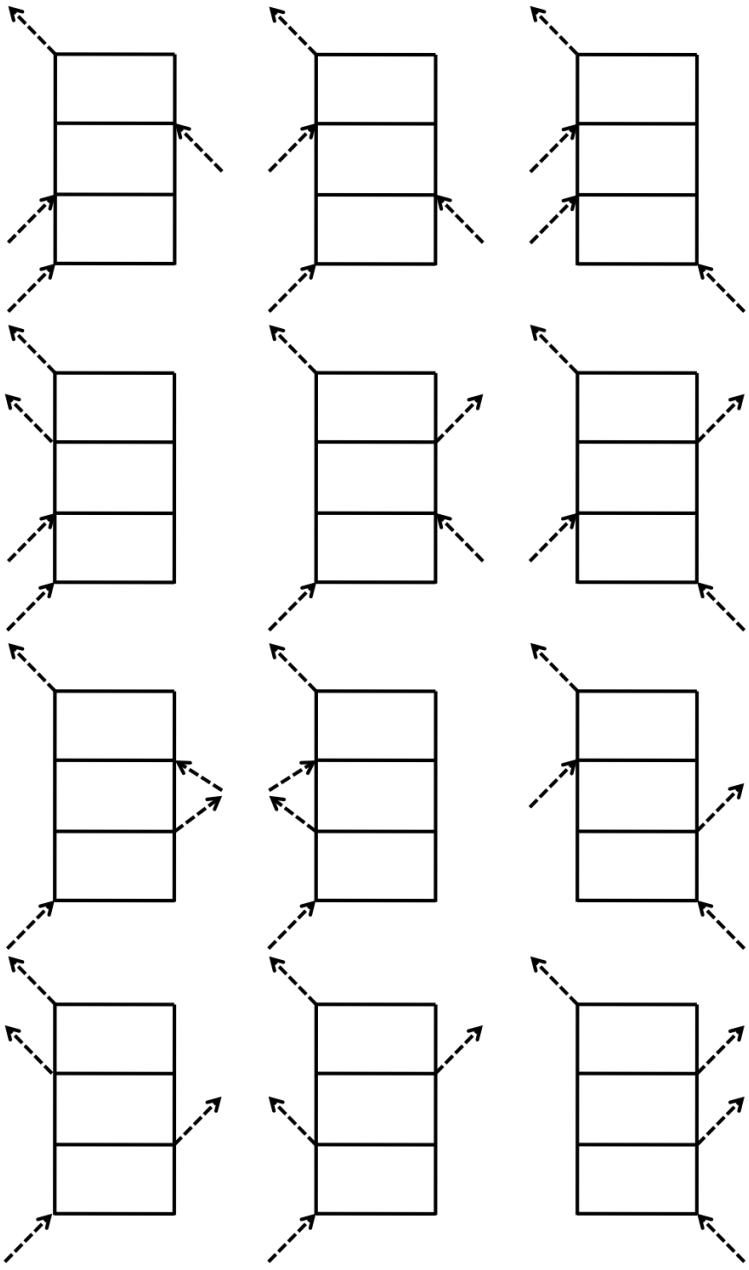

Figure D.2: Twelve possible double-sided Feynman diagrams that contribute to the third-order response functions are displayed. The first two columns correspond to nonrephasing diagrams, while the third column contains rephasing diagrams. The first column is in a two-quantum coherence during time t_2, while the second and third columns are in populations during this time interval. Each row of diagrams corresponds to a different mean trajectory path, as discussed in Figures 3.1 and 3.2.

BIBLIOGRAPHY

[1] Tannor, D. *Introduction to Quantum Mechanics: A Time-Dependent Perspective;* University Science Books: Sausalito, CA, 2006.

[2] Mukamel, S. *Principles of Nonlinear Optical Spectroscopy;* Oxford University Press: New York, 1995.

[3] Loudon, R. *The Quantum Theory of Light, 2nd ed.;* Clarendon Press: Oxford, 1983.

[4] Mukamel, S.; Piryatinski, A.; Chernyak, V. *Acc. Chem. Res.* **1999**, *32*, 145–154.

[5] Bagchi, S.; Kim, Y. S.; Charnley, A. K.; Smith, A. B.; Hochstrasser, R. M. *J. Phys. Chem. B* **2007**, *111*, 3010–3018.

[6] Zheng, J. R.; Fayer, M. D. *J. Am. Chem. Soc.* **2007**, *129*, 4328–4335.

[7] Kolano, C.; Helbing, J.; Kozinski, M.; Sander, W.; Hamm, P. *Nature* **2006**, *444*, 469–472.

[8] Smith, A. W.; Tokmakoff, A. *J. Chem. Phys.* **2007**, *126*, 045109.

[9] Mukherjee, P.; Kass, I.; Arkin, I. T.; Zanni, M. T. *Proc. Natl. Acad. Sci. U. S.* **2006**, *103*, 3528–3533.

[10] Hahn, E. L. *Physics Today* **1953**, *6*, 4.

[11] Scheurer, C.; Mukamel, S. *J. Chem. Phys.* **2002**, *116*, 6803–6816.

[12] Ge, N.-H.; Hochstrasser, R. M. *Phys. Chem. Comm.* **2002**, *5*, 17–26.

[13] Hamm, P.; Lim, M.; Hochstrasser, R. M. *Phys. Rev. Lett.* **1998**, *81*, 5326–5329.

[14] Fayer, M. D. *Annu. Rev. Phys. Chem.* **2001**, *52*, 315–356.

[15] Noid, W. G. *The (semi-) classical vibrational echo ;* Ph. D. thesis: Cornell University, 2005.

[16] Massari, A. M.; Finkelstein, I. J.; McClain, B. L.; Goj, A.; Wen, X.; Bren, K. L.; Loring, R. F.; Fayer, M. D. *J. Am. Chem. Soc.* **2005**, *127*, 14279–14289.

[17] Naraharisetty, S. R. G.; Kasyanenko, V. M.; Rubtsov, I. V. *J. Chem. Phys.* **2008**, *128*, 104502.

[18] Ishikawa, H.; Kwak, K.; Chung, J. K.; Kim, S.; Fayer, M. D. *PNAS* **2008**, *105*, 8619–8624.

[19] Gelin, M. F.; Egorova, D.; Domcke, W. *J. Chem. Phys.* **2005**, *123*, 164112.

[20] Gelin, M. F.; Egorova, D.; Domcke, W. *Acc. Chem. Res.* **2009**, *42*, 1290–1298.

[21] Sun, X.; Miller, W. H. *J. Chem. Phys.* **1999**, *110*, 6635–6644.

[22] Shao, J.; Makri, N. *J. Phys. Chem. A* **1999**, *103*, 9479–9486.

[23] Wright, N. J.; Makri, N. *J. Chem. Phys.* **2003**, *119*, 1634–1642.

[24] Wright, N. J.; Makri, N. *J. Phys. Chem. B* **2004**, *108*, 6621–6624.

[25] Makri, N. *J. Phys. Chem. A* **2004**, *108*, 806–812.

[26] Liu, J.; Nakayama, A.; Makri, N. *Chem. Phys.* **2006**, *322*, 1267–1274.

[27] Noid, W. G.; Ezra, G. S.; Loring, R. F. *J. Chem. Phys.* **2003**, *119*, 1003–1020.

[28] Leegwater, J. A.; Mukamel, S. *J. Chem. Phys.* **1995**, *102*, 2365–2371.

[29] Mukamel, S.; Khidekel, V.; Chernyak, V. *Phys. Rev. E* **1996**, *53*, R1–R4.

[30] Williams, R. B.; Loring, R. F. *J. Chem. Phys.* **2000**, *113*, 1932–1941.

[31] Williams, R. B.; Loring, R. F. *J. Chem. Phys.* **2000**, *112*, 3104–3105.

[32] Noid, W. G.; Ezra, G. S.; Loring, R. F. *J. Phys. Chem. B* **2004**, *108*, 6536–6543.

[33] Noid, W. G.; Loring, R. F. *J. Chem. Phys.* **2004**, *121*, 7057–7069.

[34] Ma, A.; Stratt, R. M. *J. Chem. Phys.* **2002**, *116*, 4692–4971.

[35] Dellago, C.; Mukamel, S. *Phys. Rev. E* **2003**, *67*, 035205.

[36] Saito, S.; Ohmine, I. *Phys. Rev. Lett.* **2002**, *88*, 207401.

[37] Malinin, S. V.; Chernyak, V. Y. *Phys. Rev. E* **2008**, *77*, 025201(R).

[38] Malinin, S. V.; Chernyak, V. Y. *Phys. Rev. E* **2008**, *77*, 056201.

[39] Malinin, S. V.; Chernyak, V. Y. *Phys. Rev. E* **2008**, *77*, 056202.

[40] Kryvohuz, M.; Cao, J. *Phys. Rev. Lett.* **2006**, *96*, 030403.

[41] Sahrapour, M. M.; Makri, N. *J. Chem. Phys.* **2010**, *132*, 134506.

[42] Kryvohuz, M.; Cao, J. *J. Chem. Phys.* **2005**, *122*, 024109.

[43] Kryvohuz, M.; Cao, J. *Phys. Rev. Lett.* **2005**, *95*, 180405.

[44] Kryvohuz, M.; Cao, J. *Chem. Phys.* **2006**, *322*, 41–45.

[45] Noid, W. G.; Ezra, G. S.; Loring, R. F. *J. Chem. Phys.* **2004**, *120*, 1491–1499.

[46] Goj, A.; Loring, R. F. *J. Chem. Phys.* **2006**, *124*, 194101.

[47] Gruenbaum, S. M.; Loring, R. F. *J. Chem. Phys.* **2009**, *131*, 204504.

[48] Akiyama, R.; Loring, R. F. *J. Chem. Phys.* **2002**, *116*, 4655–4664.

[49] Akiyama, R.; Loring, R. F. *J. Phys. Chem. A* **2003**, *107*, 8024–8028.

[50] Merchant, K. A.; Thompson, D. E.; Xu, Q.-H.; Williams, R. B.; Loring, R. F.; Fayer, M. D. *Biophys. J.* **2002**, *82*, 3277–3288.

[51] Merchant, K. A.; Noid, W. G.; Thompson, D. E.; Akiyama, R.; Loring, R. F.; Fayer, M. D. *J. Phys. Chem. B* **2003**, *107*, 4–7.

[52] Finkelstein, I. J.; Goj, A.; McClain, B. L.; Massari, A. M.; Merchant, K. A.; Loring, R. F.; Fayer, M. D. *J. Phys. Chem. B* **2005**, *109*, 16959–16966.

[53] Berry, M. V.; Mount, K. E. *Rep. Prog. Phys.* **1972**, *35*, 315–397.

[54] Einstein, A. *Verh. Dtsch. Phys. Ges.* **1917**, *19*, 82.

[55] Brillouin, M. L. *J. Phys.* **1926**, *7*, 353–368.

[56] Keller, J. B. *Ann. Phys.* **1958**, *4*, 180–188.

[57] Gutzwiller, M. C. *J. Math. Phys.* **1967**, *8*, 1979–2000.

[58] Gutzwiller, M. C. *J. Math. Phys.* **1971**, *12*, 343–358.

[59] Gutzwiller, M. C. *Chaos in Classical and Quantum Mechanics;* Springer-Verlag: New York, 1990.

[60] Feynman, R. P. *Rev. Mod. Phys.* **1948**, *20*, 367–387.

[61] Littlejohn, R. G. *J. Stat. Phys.* **1992**, *68*, 7–50.

[62] Vleck, J. H. V. *Proc. Nat. Acad. Sci.* **1928**, *14*, 178–188.

[63] Kay, K. G. *Chem. Phys.* **2006**, *322*, 3–12.

[64] Liu, J.; Miller, W. H. *J. Chem. Phys.* **2007**, *126*, 114506.

[65] Heller, E. J. *J. Chem. Phys.* **1991**, *94*, 2723–2729.

[66] Miller, W. H. *J. Chem. Phys.* **1991**, *95*, 9428–9430.

[67] Liu, J.; Miller, W. H. *J. Chem. Phys.* **2007**, *126*, 234110.

[68] Kay, K. G. *Annu. Rev. Phys. Chem.* **2005**, *56*, 255–280.

[69] Hochman, G.; Kay, K. G. *Phys. Rev. A* **2006**, *73*, 064102.

[70] Campolieti, G.; Brumer, P. *J. Chem. Phys.* **1998**, *109*, 2999–3003.

[71] Wang, H.; Manolopoulos, D. E.; Miller, W. H. *J. Chem. Phys.* **2001**, *115*, 6317–6326.

[72] Ankerhold, J.; Saltzer, M.; Pollak, E. *J. Chem. Phys.* **2002**, *116*, 5925–5932.

[73] Makri, N.; Miller, W. H. *J. Chem. Phys.* **2002**, *116*, 9207–9212.

[74] Mukamel, S.; Maddox, J. B. *J. Chem. Phys.* **2004**, *121*, 36–43.

[75] Heller, E. J. *Acc. Chem. Res.* **2006**, *39*, 127–134.

[76] Heller, E. J. *J. Chem. Phys.* **1981**, *75*, 2923–2931.

[77] Heller, E. J. *J. Chem. Phys.* **1975**, *62*, 1544–1555.

[78] Turi, L.; Rossky, P. J. *J. Chem. Phys.* **2004**, *120*, 3688–3698.

[79] Herman, M. F.; Kluk, E. *Chem. Phys.* **1984**, *91*, 27–34.

[80] Kluk, E.; Herman, M. F.; Davis, H. L. *J. Chem. Phys.* **1986**, *84*, 326–334.

[81] Klauder, J. R.; Skagerstam, B. *Coherent States: Applications in Physics and Mathematical Physics;* World Scientific: Singapore, 1985.

[82] Herman, M. F. *J. Chem. Phys.* **1986**, *85*, 2069–2076.

[83] Baranger, M.; de Aguiar, M. A. M.; Keck, F.; Korsch, H. J.; Schellhaass, B. *J. Phys. A* **2001**, *34*, 7227–7286.

[84] Grossmann, F.; Herman, M. F. *J. Phys. A* **2002**, *35*, 9489–9492.

[85] Miller, W. H. *Mol. Phys.* **2002**, *100*, 397–400.

[86] Child, M. S.; Shalashilin, D. V. *J. Chem. Phys.* **2003**, *118*, 2061–2071.

[87] Grossmann, F.; Xavier, A. L. *Phys. Lett. A* **1998**, *243*, 243–248.

[88] Miller, W. H. *J. Phys. Chem. B* **2002**, *106*, 8132–8135.

[89] Deshpande, S. A.; Ezra, G. S. *J. Phys. A* **2006**, *39*, 5067–5078.

[90] Deshpande, S. A. *Quantum and semiclassical aspects of chemical dynamics;* Ph. D. thesis: Cornell University, 2007.

[91] Kay, K. G. *J. Chem. Phys.* **1994**, *100*, 4377–4392.

[92] Sklarz, T.; Kay, K. G. *J. Chem. Phys.* **2004**, *120*, 2606–2617.

[93] Kay, K. G. *J. Chem. Phys.* **1994**, *100*, 4432–4446.

[94] Kay, K. G. *J. Chem. Phys.* **1994**, *101*, 2250–2260.

[95] McQuarrie, B. R.; Brumer, P. *Chem. Phys. Lett.* **2000**, *319*, 27–44.

[96] Herman, M. F. *Chem. Phys. Lett.* **1997**, *275*, 445–452.

[97] Walton, A. R.; Manolopoulos, D. E. *Chem. Phys. Lett.* **1995**, *244*, 448–455.

[98] Hochman, G.; Kay, K. G. *J. Chem. Phys.* **2009**, *130*, 061104.

[99] Herman, M. F. *J. Chem. Phys.* **1995**, *103*, 8081–8097.

[100] Wu, Y.; Herman, M. F. *J. Chem. Phys.* **2005**, *123*, 144106.

[101] Wu, Y.; Herman, M. F. *J. Chem. Phys.* **2006**, *125*, 154116.

[102] Herman, M. F.; Coker, D. F. *J. Chem. Phys.* **1999**, *111*, 1801–1808.

[103] Gruenbaum, S. M.; Loring, R. F. *J. Chem. Phys.* **2008**, *128*, 124106.

[104] Gruenbaum, S. M.; Loring, R. F. *J. Chem. Phys.* **2008**, *129*, 124508.

[105] Kay, K. G. *J. Chem. Phys.* **1997**, *107*, 2313–2328.

[106] Walton, A. R.; Manolopoulos, D. E. *Mol. Phys.* **1996**, *87*, 961–978.

[107] Guerin, B. E.; Herman, M. F. *Chem. Phys. Lett.* **1998**, *286*, 361–368.

[108] Li, S. Z.; Schmidt, J. R.; Corcelli, S. A.; Lawrence, C. P.; Skinner, J. L. *J. Chem. Phys.* **2006**, *124*, 204110.

[109] DeVane, R.; Space, B.; Perry, A.; Neipert, C.; Ridley, C.; Keyes, T. *J. Chem. Phys.* **2004**, *121*, 3688–3701.

[110] Ishizaki, A.; Tanimura, Y. *J. Phys. Chem. A* **2007**, *111*, 9269–9276.

[111] Choi, J. H.; Cheon, S.; Cho, M. *Chem. Phys.* **2007**, *337*, 81–92.

[112] Zhuang, W.; Abramavicius, D.; Mukamel, S. *Proc. Nat. Acad. Sci. U. S.* **2006**, *103*, 18934–18938.

[113] Miller, W. H. *J. Chem. Phys.* **2006**, *125*, 132305.

[114] Miller, W. H. *J. Phys. Chem. A* **2001**, *105*, 2942–2955.

[115] Pollak, E.; Liao, J. L. *J. Chem. Phys.* **1998**, *108*, 2733–2743.

[116] Poulsen, J. A.; Nyman, G.; Rossky, P. *J. Chem. Phys.* **2003**, *119*, 12179.

[117] Shi, Q.; Geva, E. *J. Chem. Phys.* **2004**, *120*, 10647.

[118] Liu, J.; Miller, W. H. *J. Chem. Phys.* **2006**, *125*, 224104.

[119] Yonei, K. *J. Phys. A: Math. Gen.* **1990**, *23*, 1705–1715.

[120] Kryvohuz, M.; Cao, J. *J. Chem. Phys.* **2009**, *130*, 234107.

[121] Goldstein, H. *Classical mechanics;* Addison-Wesley: Reading, Mass., 1950.

[122] Karplus, M.; Porter, R. N.; Sharma, R. D. *J. Chem. Phys.* **1965**, *43*, 3259–3287.

[123] Schatz, G. C.; Moser, M. D. *J. Chem. Phys.* **1978**, *68*, 1992–1994.

[124] Chirikov, B. V. *Phys. Rep.* **1979**, *52*, 263–379.

[125] Noid, D. W.; Koszykowski, M. L.; Marcus, R. A. *Ann. Rev. Phys. Chem.* **1981**, *32*, 267–309.

[126] Schatz, G. C.; Mulloney, T. *J. Phys. Chem.* **1979**, *83*, 989–999.

[127] Martens, C. C.; Ezra, G. E. *J. Chem. Phys.* **1987**, *86*, 279–307.

[128] Martens, C. C.; Ezra, G. E. *J. Chem. Phys.* **1985**, *83*, 2990–3001.

[129] Noid, D. W.; Marcus, R. A. *J. Chem. Phys.* **1977**, *67*, 559–567.

[130] Shirts, R. B. *J. Phys. Chem.* **1987**, *91*, 2258–2267.

[131] M uller, M.; Heiss, W. D. *J. Phys. A* **2000**, *33*, 93–111.

[132] Sorbie, K. S. *Mol. Phys.* **1976**, *32*, 1577–1590.

[133] Sorbie, K. S.; Handy, N. C. *Mol. Phys.* **1976**, *32*, 1327–1347.

[134] Thoss, M.; Wang, H. B. *Annu. Rev. Phys. Chem.* **2004**, *55*, 299–332.

[135] Sun, X.; Miller, W. H. *J. Chem. Phys.* **1998**, *108*, 8870–8877.

[136] Batista, V.; Zanni, M. T.; Greenblatt, B. J.; Neumark, D. M.; Miller, W. H. *J. Chem. Phys.* **1999**, *110*, 3736–3747.

[137] Berry, M. V.; Tabor, M. *Proc. R. Soc. Lond. A* **1976**, *349*, 101–123.

[138] Berry, M. V.; Tabor, M. *J. Phys. A: Math. Gen.* **1977**, *10*, 371–379.

[139] VanVleck, J. H. *Proc. Nat. Acad. Sci.* **1928**, *14*, 178–188.

[140] Sklarz, T.; Kay, K. G. *J. Chem. Phys.* **2002**, *117*, 5988–5997.

[141] Tannor, D. J.; Garashchuk, S. *Annu. Rev. Phys. Chem.* **2000**, *51*, 553–600.

[142] Brewer, M. L. *J. Chem. Phys.* **1999**, *111*, 6168–6170.

[143] Bredenbeck, J.; Helbing, J.; Kumita, J. R.; Woodlley, G. A.; Hamm, P. *PNAS* **2005**, *102*, 2379–2384.

[144] Chung, H. S.; Khalil, M.; Smith, A. W.; Ganim, Z.; Tokmakkoff, A. *PNAS* **2005**, *102*, 612–617.

[145] Wang, J.; Chen, J.; Hochstrasser, R. M. *J. Phys. Chem. B* **2006**, *110*, 7545–7555.

[146] Massari, A. M.; Finkelstein, I. J.; Fayer, M. D. *J. Am. Chem. Soc.* **2006**, *128*, 3990–3997.

[147] Merchant, K. A.; Noid, W. G.; Akiyama, R.; Finkelstein, I. J.; Goun, A.; McClain, B. L.; Loring, R. F.; Fayer, M. D. *J. Am. Chem. Soc.* **2003**, *125*, 13804–13818.

[148] Finkelstein, I. J.; Ishikawa, H.; Kim, S.; Massari, A. M.; Fayer, M. D. *PNAS* **2007**, *104*, 2637–2642.

[149] Elber, R.; Roitberg, A.; Simmerling, C.; Goldstein, R.; Li, H.; Verkhivker, G.; Keasar, C.; Zhang, J.; Ulitsky, A. *Comput. Phys. Commun.* **1994**, *91*, 159–189.

[150] Case, D. A.; Darden, T. A.; III, T. E. C.; Simmerling, C. L.; Wang, J.; Duke, R. E.; Luo, R.; Crowley, M.; Walker, R. C.; Zhang, W.; Merz, K. M.; Wang, B.; Hayik, S.; Roitberg, A.; Seabra, G.; Kolossvry, I.; F.Wong, K.; Paesani, F.; Vanicek, J.; Wu, X.; Brozell, S. R.; Steinbrecher, T.; Gohlke, H.; Yang, L.; Tan, C.; Mongan, J.; Hornak, V.; Cui, G.; Mathews, D. H.; Seetin, M. G.; Sagui, C.; Babin, V.; Kollman, P. A. *AMBER 10;* University of California: San Francisco, 2008.

[151] Park, E. S.; Boxer, S. G. *J. Phys. Chem. B* **2002**, *106*, 5800–5806.

[152] Kushkuley, B.; Stavrov, S. S. *Biophys. J.* **1996**, *70*, 1214–1229.

[153] Jr., G. N. P.; Teodoro, M. L.; Li, T.; Smith, B.; Olson, J. S. *J. Phys. Chem. B* **1999**, *103*, 8817–8829.

[154] Franzen, S. *J. Am. Chem. Soc.* **2002**, *124*, 13271–13281.

[155] Goj, A.; Loring, R. F. *Chem. Phys.* **2007**, *341*, 37–44.

[156] Goj, A. *Vibrational dephasing in a mutant myoglobin;* Ph. D. thesis: Cornell University, 2007.

[157] Zhu, L.; Sage, J. T.; Rigos, A. A.; Morikis, D.; Champion, P. M. *J. Mol. Biol.* **1992**, *224*, 207–215.

[158] Yang, F.; Jr., G. N. P. *J. Mol. Biol.* **1996**, *256*, 762–774.

[159] Rector, K. D.; Jiang, J. W.; Berg, M. A.; Fayer, M. D. *J. Phys. Chem. B* **2001**, *105*, 1081–1092.

[160] Jorgensen, W. L.; Chandrasekhar, J.; Madura, J.; Impey, R. W.; Klein, M. L. *J. Chem. Phys.* **1983**, *79*, 926–935.

[161] Berendsen, H. J. C.; Grigera, J. R.; Straatsma, T. P. *J. Phys. Chem.* **1987**, *91*, 6269–6271.

[162] Kachalova, G. S.; Popov, A. N.; Bartunik, H. D. *Science* **1999**, *284*, 473–476.

[163] Vojtechovsky, J.; Chu, K.; Berendzen, J.; Sweet, R. M. *Biophys.* **1999**, *77*, 2153–2174.

[164] Anselmi, M.; Brunori, M.; Vallone, B.; Nola, A. D. *Biophys. J.* **2007**, *93*, 434–441.

[165] Teng, T. Y.; Srajer, V.; Moffat, K. *Nat. Struct. Bio.* **1994**, *1*, 701–705.

[166] Quillin, M. L.; Arduini, R. M.; Olson, J. S.; Jr., G. N. P. *J. Mol. Biol.* **1993**, *234*, 140–155.

[167] Gajhede, M.; Schuller, D. J.; Henriksen, A.; Smith, A. T.; Poulos, T. L. *Nat. Struct. Biol.* **1997**, *4*, 1032–1038.

[168] Veitch, N. C. *Phytochemistry* **2004**, *65*, 249–259.

[169] Carlsson, G. H.; Nicholls, P.; Svistunenko, D.; Berglund, G. I.; Hajdu, J. *Biochemistry* **2005**, *44*, 635–642.

[170] Filizola, M.; Loew, G. H. *J. Am. Chem. Soc.* **2000**, *122*, 18–25.

[171] Rodríguez-López, J. N.; Lowe, D. J.; Hernández-Ruiz, J.; Hiner, A. N. P.; García-Cánovas, F.; Thorneley, R. N. F. *J. Am Chem. Soc.* **2001**, *123*, 11838–11847.

[172] Redaelli, C.; Monzani, E.; Santagostini, L.; Casella, L.; Sanangelantoni, A. M.; Pierattelli, R.; Banci, L. *Chem. Bio. Chem.* **2002**, *3*, 226–233.

[173] Roncone, R.; Monzani, E.; Nicolis, S.; Casella, L. *Eur. J. Inorg. Chem.* **2004**, *2004*, 2203–2213.

[174] Henriksen, A.; Schuller, D. J.; Meno, K.; Welinder, K. G.; Smith, A. T.; Gajhede, M. *Biochemistry* **1998**, *37*, 8054–8060.

[175] Barlow, C. H.; Ohlsson, P.-I.; Paul, K.-G. *Biochemistry* **1976**, *15*, 2225–2229.

[176] Evangelista-Kirkup, R.; Smulevich, G.; Spiro, T. G. *Biochemistry* **1986**, *25*, 4420–4425.

[177] Hashimoto, S.; Takeuchi, H. *Biochemistry* **2006**, *45*, 9660–9667.

[178] Holzbaur, I. E.; English, A. M.; Ismail, A. A. *J. Am. Chem. Soc.* **1996**, *118*, 3354–3359.

[179] Dalosto, S. D. *J. Phys. Chem.* **2003**, *107*, 1884–1892.

[180] Kaposi, A. D.; Fidy, J.; Manas, E. S.; Vanderkooi, J. M.; Wright, W. W. *Biochim. Biophys. Acta* **1999**, *1435*, 41–50.

[181] Kaposi, A. D.; Vanderkooi, J. M.; Wright, W. W.; Fidy, J.; Stavrov, S. S. *Biophys. J.* **2001**, *81*, 3472–3482.

[182] Kaposi, A. D.; Wright, W. W.; Fidy, J.; Stavrov, S. S.; Vanderkooi, J. M.; Rasnik, I. *Biochemistry* **2001**, *40*, 3483–3491.

[183] Kaposi, A. D.; Prabhu, N. V.; Dalosto, S. D.; Sharp, K. A.; Wright, W. W.; Stavrov, S. S.; Vanderkooi, J. M. *Biophys. Chem.* **2003**, *106*, 1–14.

[184] Giammona, D. A. *;* Ph. D. thesis: University of California, Davis, 1984.

[185] Robbins, J. M. *Nonlinearity* **1991**, *4*, 343–363.

[186] Takatsuka, K.; Takahashi, S.; Koh, Y. W.; Yamashita, T. *J. Chem. Phys.* **2007**, *126*, 021104.

[187] Takahashi, S.; Takatsuka, K. *J. Chem. Phys.* **2007**, *127*, 084112.

[188] Jaffe, C.; Reinhardt, W. P. *J. Chem. Phys.* **1979**, *71*, 1862–1869.

[189] Miller, W. H. *J. Chem. Phys.* **1984**, *81*, 3573–3575.

[190] Eastes, W.; Marcus, R. A. *J. Chem. Phys.* **1974**, *61*, 4301–4306.

[191] Noid, D. W.; Marcus, R. A. *J. Chem. Phys.* **1975**, *62*, 2119–2124.

[192] Noid, D. W.; Koszykowski, M. L.; Marcus, R. A. *J. Chem. Phys.* **1977**, *67*, 404–408.

[193] Percival, I. C. *J. Phys. A* **1974**, *7*, 794–802.

[194] Percival, I. C.; Pomphrey, N. *Mol. Phys.* **1976**, *31*, 97–114.

[195] Martens, C. C.; Ezra, G. E. *J. Chem. Phys.* **1987**, *87*, 284–302.

[196] Sorbie, K. S.; Handy, N. C. *Mol. Phys.* **1977**, *33*, 1319–1334.